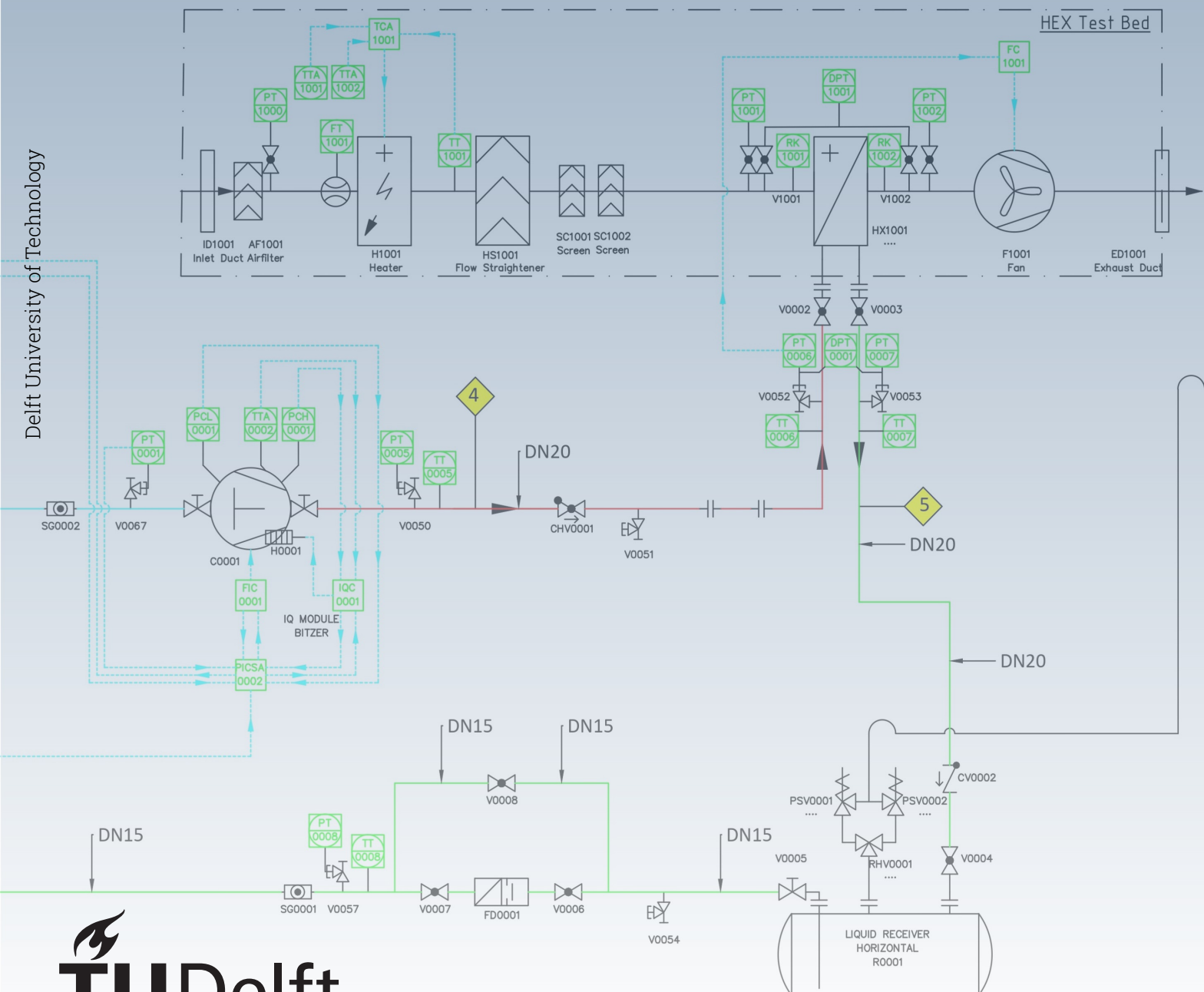


Modelling and Control of Novel Environmental Control Systems

Centrifugal Compressor Testing in the Inverse Organic Rankine Cycle Integrated System

C.J. Luiten

Delft University of Technology



Modelling and Control of Novel Environmental Control Systems

Centrifugal Compressor Testing in the Inverse
Organic Rankine Cycle Integrated System

by

C.J. Luiten

to obtain the Individual Double Degree of Master of Science for
Systems & Control and Aerospace Engineering
at the Delft University of Technology,
to be defended publicly on Thursday the 27th of February 2025 at 14:30.

Project duration:	February, 2024 - February, 2025
Thesis committee:	Prof. P. Colonna Chair
	Dr. C. De Servi Supervisor AE
	Dr. D. Boskos Supervisor ME
	Dr. L. Laurenti External Examiner

Cover: Detailed Process & Information Diagram of the Inverse organic Rankine cycle Integrated System (modified). Published with permission from Dr. De Servi.

Preface

The contents of this thesis report represent the conclusion of my Individual Double Degree (IDD) journey at the Mechanical Engineering and Aerospace Engineering faculties at TU Delft. During this three and a half year period, I have been introduced to many very interesting topics within both control and aerospace engineering that, instead of saturating my initial fascination, have sparked only more interest in what lies beyond the borders of the educational programmes. Although completing these programmes posed numerous significant obstacles, overcoming them has allowed me to grow tremendously, both on a professional and personal level, for which I am very grateful. As a result of this, I can confirm that my expectations of the IDD being a challenging but extremely rewarding program were exactly right, and I sincerely recommend any student to follow their curiosity and expand their academic path wherever possible.

The material of this report covers a research project contributing to the improvement of Environmental Control System (ECS) technology aboard future aircraft. Within this context, the aim of the research is to obtain a better understanding of the transient behaviour of Vapour Compression Cycle (VCC) systems used for cooling in aeronautical applications. To this end, a dynamic model of a novel VCC-based ECS test facility was developed, and a control system was designed for consistent testing of the compressor. Since the dynamic model and control system are inextricably linked, the thesis highlights the importance of a multi-disciplinary approach in addressing the complex and interrelated nature of next-generation ECSs. It follows that extensive knowledge of both thermodynamics and control theory is required to unlock the full potential of VCC technology. Therefore, this report aims to demonstrate the potential of combining the expertise of Power & Propulsion and Systems & Control and encourage additional collaborative projects between the two groups in future research.

Over the last three years, and especially during the thesis, I have been fortunate to connect with many inspiring individuals in academia. Above all, I want to thank my supervisors, Carlo and Dimitris, for the many hours they dedicated to following and, when necessary, adjusting the course of my project. I have been deeply impressed by their ability to identify future challenges and determine the best steps forward through a combination of expertise and instinct. I would also like to thank Federica for her help in the early stages of the project. Without her insights, I would still be struggling to get my Modelica code to work. Lastly, I want to thank Rúben for stepping in after Federica's PhD project ended. I greatly appreciate his patience and informal attitude in the face of my endless questions during meetings that ran far beyond the scheduled time.

On a social level, I have also received a great deal of support from those around me. For the many hours spent tackling the challenging courses in Systems & Control together, I want to thank my fellow Goonies: Berend, Bob, Emiel, and Gijs. Being able to share the experiences of the first, and perhaps toughest, year of the master's with friends made all the difference. I also want to thank Guillaume and Job for their companionship during the Power & Propulsion year. Without the extensive coffee breaks and the occasional visits to the Skihut, I most likely would not have made it through the year.

Finally, I want to thank my family. Despite the distance between us, my parents and sister have guided me through difficult times and we have celebrated successes together. In particular, I want to thank Lauren. In times of intense stress, she has always been able to support me like no one else, and without her unwavering encouragement, I would not be where I am today. Thank you.

*C.J. Luiten
Delft, February 2025*

Summary

Aviation's growing contribution to greenhouse gas (GHG) emissions has intensified research into More Electric Aircraft (MEA) concepts, where electrically powered non-propulsive systems replace traditional ones to improve efficiency and reduce environmental impact. The Environmental Control System (ECS) is the main consumer of non-propulsive power, traditionally relying on the Air Cycle Machine (ACM) powered by bleed air from the main engine. In lieu of electrifying the ACM, utilization of the Vapour Compression Cycle (VCC) offers a promising alternative for the refrigeration tasks of the ECS, primarily for its higher thermodynamic efficiency. However, the implementation of VCCs in aviation remains a challenge due to excessive system weight, the environmental impact of refrigerants, and high control complexity. To address these challenges, at Delft University of Technology (TU Delft), the Inverse Organic Rankine Cycle Integrated System (IRIS) test facility was developed to investigate the performance of a novel VCC-based ECS configuration and support research on integrated design optimization methods for the preliminary design of next-generation ECSs. Two key innovations are of particular interest in the IRIS: the use of a high-speed electric centrifugal compressor and the use of the low Global Warming Potential (GWP) refrigerant R-1233zd(E). Given these innovations, the main goals of the facility are threefold: evaluating the performance of centrifugal VCCs for aviation applications, investigating the aerothermal behaviour of heat exchangers in the VCC, and analysing the refrigeration cycle using R-1233zd(E) and other low-GWP refrigerants.

The literature study in this thesis examines the background of ECS technology, the historical development of VCC-based cooling in aviation, and the modelling and control approaches commonly used in research. It highlights that while existing steady-state models are widely used for ECS design, they do not capture the transient behaviour of VCC systems, which is crucial for understanding thermal responses, control dynamics, and component interactions. To address this, a review of dynamic modelling approaches is presented, focusing on Moving Boundary (MB) and Finite Control Volume (FCV) methods for heat exchangers and the use of steady-state performance maps for compressor modelling. Additionally, different VCC control strategies, ranging from conventional PID methods to advanced model-based and intelligent control techniques, are assessed for their suitability in the IRIS.

Building on this foundation, the scientific paper presents the core research contributions of this thesis. The first objective was to develop a dynamic model of the IRIS facility, using a modular approach in Modelica to construct individual component models before integrating them into a full system representation. This framework allows for transient simulations to analyse system behaviour under varying external conditions. The second objective was to design a control strategy that ensures stable and consistent operation of the IRIS, particularly for compressor testing. Unlike conventional ECS control strategies that focus on optimizing efficiency, the IRIS control system was designed to enable precise and repeatable test conditions to support future research on high-speed centrifugal compressors.

The predictions of the dynamic model were found to be reliable, as they were successfully verified against steady-state experimental data and physical reasoning. This confirms the model's ability to accurately represent the system's transient behaviour, providing a valuable tool for further research on VCC-based cooling systems. The controller demonstrated its capability to maintain the system at desired operating conditions, ensuring stable and repeatable compressor testing. This allows for the full evaluation of the centrifugal compressor across different operating scenarios. More broadly, the model presented in this thesis provides valuable insights into the performance of VCC-based cooling equipment for aircraft applications. Additionally, the developed control methodology offers a structured approach to assess the operation of centrifugal compressors, supporting their integration into next-generation aircraft ECSs.

Contents

Preface	i
Summary	ii
Nomenclature	viii
I Scientific Paper	1
II Literature Study	57
II.1 Introduction	59
II.2 Environmental Control System	62
II.2.1 Flying at Altitude: The Need for an ECS	62
II.2.2 Historical Development	63
II.2.3 Air Cycle Machine	64
II.2.4 More Electric Aircraft and the ACM	66
II.3 Vapour Compression Cycle Technology	67
II.3.1 Thermodynamic Principles	67
II.3.2 Historical Development in Aviation	69
II.3.3 Challenges in Future ECS Design	69
II.4 Novel ECS Designs: From Theory to Practice	71
II.4.1 Key Advancements	71
II.4.2 The IRIS Experimental Facility	73
II.4.2.1 Typical Helicopter ECS	74
II.4.2.2 Deviations from the Conceptual Design	75
II.5 Dynamic Modelling of VCC Systems	77
II.5.1 History of VCC Modelling	77
II.5.2 Modelling Paradigms	79
II.5.2.1 Modularity	79
II.5.2.2 Causal versus Non-causal	80
II.5.3 Modelica	81
II.5.4 Individual Component Modelling	82
II.5.4.1 Heat Exchangers	82
II.5.4.2 Compressor	88
II.5.4.3 Expansion Valve	91
II.5.4.4 Liquid Receiver	92
II.6 Control	94
II.6.1 Classifying VCC Control Methods	94
II.6.1.1 Conventional Methods	95
II.6.1.2 Advanced Controls	96
II.6.1.3 Intelligent Controls	99
II.6.2 Suitability for the IRIS	100
II.7 Research Objectives	102
II.7.1 Relevance for the IRIS	102
II.7.2 Methodological Considerations	103

II.7.3 Refined Research Objectives 103

III Supporting Material 104

III.1 IRIS Detailed System Architecture 105

III.2 References Literature Study 107

List of Figures

II.1.1 Projections of global Greenhouse Gas (GHG) emission pathways, adapted from [1]. The red range assumes policies as implemented by the end of 2020. The green and blue ranges show pathways that limit global warming to 2 °C and 1.5 °C respectively.	59
II.2.1 Atmospheric conditions at altitude, based on the International Standard Atmosphere [18].	62
II.2.2 Illustration of the first pressurized cabin concept in the Popular Science Monthly magazine, October 1932 [21].	63
II.2.3 Ideal reverse open Brayton cycle, adapted from [11].	64
II.2.4 Schematic representation of a simple-cycle ACM architecture for the ECS of an aircraft, adapted from [11].	65
II.2.5 Typical power distribution of an aero-engine [8].	66
II.3.1 Schematic representation of the Carnot cycle for refrigeration and corresponding temperature-entropy diagram, adapted from [27].	68
II.3.2 Schematic representation of the vapour compression cycle for refrigeration and corresponding temperature-entropy diagram, adapted from [27]. For the temperature-entropy diagram, the dashed black lines indicate irreversible processes.	69
II.4.1 Three-dimensional rendering of a centrifugal compressor impeller, adapted from [30], with isometric and side views shown on the left and right, respectively. The rotational direction of the impeller is shown with a black arrow, the blue region indicates the meridional flow channel, and the red arrow denotes the mean flow direction.	72
II.4.2 Typical layout of a VCC-based ECS for large rotorcraft and corresponding temperature-entropy diagram [50].	73
II.4.3 Configuration of the IRIS, based on the typical helicopter ECS in Figure II.4.2, adapted from [52]. The shaded components are to be implemented in a later phase of the project.	74
II.4.4 Schematic representation of the component architecture of the IRIS at the time of commissioning, including the corresponding temperature-entropy diagram [13].	75
II.5.1 Moving Boundary model of a horizontal evaporator, based on the approach developed by Wedekind [63].	78
II.5.2 Finite Control Volume model of the heat pump heat exchanger, as proposed by MacArthur and Grald [61].	78
II.5.3 Graphical representation of modelling approaches for the dynamic modelling of VCC systems, based on the review of Rasmussen [57].	79
II.5.4 Volume associated with a two-phase liquid-vapour mixture flow. The length of the volume ζ is defined along the flow direction.	83
II.5.5 Experimental results from Lee et al. [96] for the evaporation heat transfer coefficient as a function of the vapour quality. The effects of changing the mass flux (left), heat flux (middle), and evaporation temperature (right) are included in the diagrams.	86
II.5.6 Temperature profiles along an evaporator for the FCV model (a), and the MB model (b) [97].	88
II.5.7 Off-design performance map of a centrifugal compressor stage, adapted from Giuffr� [30]. Solid lines represent speed lines obtained from a mean-line model, while the dots correspond to mass-averaged CFD calculations. The percentages at the dots indicate the isentropic efficiency.	89
II.5.8 Simplified corrected compressor map showing the effects of increased inlet temperature at constant pressure ratio (red) relative to the design point, marked by a black dot. . . .	90
II.6.1 Classification of control methods for VCC systems in literature, adapted from [58]. . . .	94

II.6.2	Schematic representation of a thermostatic expansion valve [116].	95
II.6.3	Minimal Stable Superheat line, as proposed by Huelle [121], adapted from [119].	96
II.6.4	Schematic of an Artificial Neural Network, adapted from [131].	99
II.6.5	Graphical representation of fuzzy sets, from the original paper of Zadeh in 1965 [134].	100
III.1.1	Simplified P&ID of the IRIS facility, where the heating loop (indicated in blue) provides heat to the refrigeration loop (indicated in red) at the evaporator and heat is rejected to the cooling loop (indicated in green) at the condenser [13].	105

List of Tables

II.5.1 Operating range for the experimental results presented by Lee et al. [96]. 86

Nomenclature

Abbreviations

Abbreviation	Definition
ACARE	Advisory Council for Aeronautic Research in Europe
ACM	Air Cycle Machine
AEA	All Electric Aircraft
AI	Artificial Intelligence
ANN	Artificial Neural Network
ARMA	Autoregressive Moving-Average
CAMD	Computer Aided Molecular Design
CFD	Computational Fluid Dynamics
CoMT	Continuous Molecular Targeting
COP	Coefficient of Performance
DAE	Differential-Algebraic Equation
ECS	Environmental Control System
EEV	Electronic Expansion Valve
FAA	Federal Aviation Administration
FCV	Finite Control Volume
FD	Finite Difference
GHG	Greenhouse Gas
GWP	Global Warming Potential
HEA	Hybrid Electric Aircraft
HEM	Homogeneous Equilibrium Model
HTC	Heat Transfer Coefficient
IPCC	Intergovernmental Panel on Climate Change
IRIS	Inverse organic Rankine cycle Integrated System
LQG	Linear Quadratic Gaussian
MB	Moving Boundary
MEA	More Electric Aircraft
MIMO	Multiple Input Multiple Output
MPC	Model Predictive Control
MSS	Minimal Stable Superheat
ODE	Ordinary Differential Equation
ORC	Organic Rankine Cycle
P&ID	Process & Information Diagram
PID	Proportional Integral Derivative
RGA	Relative Gain Array
SISO	Single Input Single Output
TEV	Thermostatic Expansion Valve
TU Delft	Delft University of Technology
VCC	Vapour Compression Cycle

Symbols

Symbol	Definition	Unit
A	Area	m^2
C	Cooling load	W
C_d	Discharge coefficient	-
COP	Coefficient of Performance	-
COP_{max}	Maximum Coefficient of Performance	-
D	Diameter	m
f	Membership function	-
F_F	Critical pressure ratio factor	-
F_L	Recovery factor	-
g	Gravitational acceleration	m/s^2
G	Mass flux	$kg/(s\ m^2)$
h	Specific enthalpy	J/kg
$J_{VCS,II}$	Objective function from Jain and Alleyne	-
k	Thermal conductivity	W/(m K)
\dot{m}	Mass flow rate	kg/s
M	Mass	kg
P	Pressure	bar
P_{atm}	Atmospheric pressure	bar
p_r	Reduced pressure	bar
Pr	Pradtl number	-
\dot{Q}	Heat flow	W
R	Gas constant	J/(kg K)
Re	Reynolds number	-
s	Specific entropy	J/(kg K)
T	Temperature	K
t	Time	s
T_{evap}	Evaporation temperature	K
u	Velocity	m/s
V	Volume	m^3
v	Specific volume	m^3/kg
\dot{W}_c	Compressor work	W
\dot{W}_t	Turbine work	W
x	Vapour quality	-
\dot{X}_{dest}	Exergy destruction rate	W
Z	Shah's parameter	-
α	Convective heat transfer coefficient	W/(m^2 K)
η	Efficiency	-
γ_{Pv}	Isentropic volume exponent	-
γ_A	Cross-sectional void fraction	-
γ_V	Volumetric void fraction	-
λ	Objective function tuning parameter	-
μ	Dynamic viscosity	kg/(m s)
ω	Compressor speed	RPM
ϕ	Flow coefficient	-
ρ	Density	kg/m^3
ρ^ℓ	Saturated liquid density	kg/m^3
ρ^v	Saturated vapour density	kg/m^3
ζ	Two-phase region length	m

Part I

Scientific Paper

Modelling and Control of a Vapour Compression Cycle for Centrifugal Compressor Testing in a Novel Environmental Control System

C.J. Luiten

Delft University of Technology, 2628 CD Delft, the Netherlands

The adoption of Vapour Compression Cycle (VCC) refrigeration technology in aircraft Environmental Control Systems (ECS) presents efficiency advantages over conventional Air Cycle Machine (ACM) architectures. However, the implementation of VCCs in aviation remains a challenge due to excessive system weight, negative environmental impact of refrigerants, and high control complexity. This study focuses on the Inverse organic Rankine cycle Integrated System (IRIS) at TU Delft, which investigates electrically driven VCC systems with novel refrigerant types for aircraft applications. A dynamic model of the IRIS refrigeration loop is developed to assess transient behaviour and evaluate the performance of a high-speed centrifugal compressor to be integrated into the system. The model employs a modular, physics-based approach using the Modelica/Dymola environment, incorporating the Moving Boundary method for heat exchangers and steady-state performance maps for the compressor. Model verification is performed through steady-state and transient analyses. Subsequently, a linear decentralized control strategy is designed to regulate the compressor inlet and outlet conditions, ensuring stable operation across varying test conditions. Simulation results demonstrate that the controller successfully regulates the refrigeration loop of the IRIS to reach the desired setpoints for full compressor testing, while keeping inputs within operational limits. Additionally, it is shown that key system dynamics are correctly captured by the model, providing valuable insights into the operational feasibility of centrifugal VCCs in aerospace ECS applications.

Nomenclature

Acronyms

ACARE	Advisory Council for Aeronautic Research
ACM	Air Cycle Machine
AEA	All Electric Aircraft
DAE	Differential-Algebraic Equation
ECS	Electronic Expansion Valve
ECS	Environmental Control System
EoS	Equation of State
GHG	Greenhouse gas
GWP	Global Warming Potential
HEA	Hybrid Electric Aircraft
HEM	Homogeneous Equilibrium Model
IPCC	Intergovernmental Panel on Climate Change
IRIS	Inverse Rankine Cycle Integrated System
ISA	International Society of Automation
LTC	Lumped Thermal Capacity
LTI	Linear Time Invariant
MB	Moving Boundary
MEA	More Electric Aircraft
MIMO	Multiple Input Multiple Output
P&ID	Process & Information Diagram
PI	Proportional Integral

RGA	Relative Gain Array
SISO	Single Input Single Output
VCC	Vapour Compression Cycle

Symbols

\dot{Q}	Heat transfer rate per unit length
\dot{m}	Mass flow rate
\dot{Q}	Heat transfer rate
\dot{W}_c	Compressor work
C	Perimeter
A	– Area
	– State-space state matrix
A_c	Cross-sectional area
A_v	Nominal valve flow area
B	State-space input matrix
C	State-space output matrix
C_p	Heat capacity at constant pressure
c_w	Specific heat capacity
COP	Coefficient of Performance
D	State-space direct feed-through matrix
d	Non-controlled input vector
D_h	Hydraulic diameter
E	Energy
F_F	Critical pressure ratio factor

F_L	Recovery factor	Ω	Rotational speed
f_p	Petukhov's friction factor	ω_B	Bandwidth frequency
G	– Mass flux	ω_I	Integral action frequency
	– Linear transfer function	Φ	System matrix heat exchanger working fluid equations
g	Valve opening characteristic	ϕ	System vector heat exchanger working fluid equations
h	Specific enthalpy	ρ	Density
h_{2s}	Isentropic enthalpy compressor outlet	Σ	Relative difference
I	Identity matrix	σ	Singular value
i	Index	τ_f	Time constant first order filter
j	Colburn factor	τ_I	Integral time constant
K	Controller	θ	Valve opening percentage
k	Thermal conductivity	Ξ	Constant for Chang and Wang correlation
K_P	Proportional gain		
L	– Length		
	– Open-loop transfer function		
L_a	Length air flow path perpendicular to refrigerant stream	Subscripts	
L_p	Louver pitch	$(\cdot)_h$	Partial derivative at constant specific enthalpy
M	Mass	$(\cdot)_P$	Partial derivative at constant pressure
N_T	Corrected compressor speed	a	Air side
Nu	Nusselt number	C	Condenser
P	Pressure	d	Non-controlled inputs
PI	Proportional Integral control element	E	Evaporator
PR	Pressure ratio	f	Refrigerant
Pr	Prandtl number	h	Heat transfer
q	Vapour quality	s	Glycol-water side
r	Reference vector	v	Expansion valve
Re	Reynolds number	w	Wall
S	Sensitivity function	$cond$	Condensation
s	– Entropy	cor	Corrected
	– Laplace transform variable	$crit$	Critical
SH	Degree of superheating	c	Compressor
T	– Temperature	$down$	Downstream
	– Complementary sensitivity function	eff	Effective
t	Time	fin	Fin
u	– Velocity along spatial direction x	$init$	Initial
	– Input vector	int	Intermediate boundary glycol-water
V	Volume	in	Inlet
x	– One-dimensional spatial coordinate	max	Maximum
	– Dynamic state vector	mid	Centre value
y	Output vector	nom	Nominal
Z	Scaling matrix	nor	Normalized
z	Vector of unknowns	out	Outlet
\mathbf{n}	Normal direction pointing out of control volume	$pass$	Heat exchanger pass
α	Heat transfer coefficient	ref	Reference
β	Position along corrected speed line	sat	Partial derivative along saturation line
δ	Deviation from steady-state	$sink$	Sink
ϵ	Relative error	ss	Steady-state
η_s	Isentropic efficiency	tot	Total
η_t	Total area efficiency	up	Upstream
η_{fin}	Fin efficiency	Superscripts	
γ	Void fraction	ℓ	Saturated liquid
Λ	Relative gain array	v	Saturated vapour
μ	Dynamic viscosity	$*$	Critical conditions
		$+$	Positive maximum deviation
		$-$	Negative maximum deviation

1 Introduction

Global warming is expected to continue increasing Earth’s surface temperature unless global policies to reduce greenhouse gas (GHG) emissions undergo substantial changes. The 2023 synthesis report by the Intergovernmental Panel on Climate Change (IPCC) indicates that rising GHG emissions from human activities have already driven an average global temperature increase of approximately 1.1 °C between the time periods 1850–1900 and 2011–2020 [1]. Current policies are unfortunately insufficient to flatten this trend enough to limit global warming to a maximum of 2 °C and pursue the more ambitious goal of staying below 1.5 °C, as outlined in the 2015 Paris Agreement [2]. Consequently, catastrophic weather events, such as the recent flooding in the Valencia region in Spain, are likely to occur more frequently and with an increased intensity [3]. To mitigate these consequences, it is imperative to take action to reduce GHG emissions wherever possible, minimizing our collective negative impact on the environment.

GHG emissions are distributed across various sectors, with aviation currently contributing approximately 2% [4]. Alarmingly, this share is expected to rise as passenger air travel grows at an annual rate of 4%, while other sectors continue to reduce their carbon footprints [5]. A 2015 study by the European Parliament projected that the CO₂ emissions from international aviation could reach 22% of global emissions by 2050 [6]. In response to these concerning trends, the Advisory Council for Aeronautic Research in Europe (ACARE) developed the FlightPath 2050 roadmap, outlining environmental goals for aviation. These include reducing perceptible aircraft noise by 65%, cutting NO_x emissions by 90%, and lowering CO₂ emissions by 75%, all relative to a typical new aircraft from the year 2000 [7]. To meet these targets, research in both industry and academia has shifted toward aircraft electrification, with a focus on minimizing weight and specific fuel consumption. The initial step in this transition is the More Electric Aircraft (MEA) concept, which replaces non-propulsive onboard systems with electrical alternatives while maintaining fossil-fuel-powered propulsion. This approach enhances the efficiency of the main engine and auxiliary systems but introduces unique challenges in the generation, distribution, and utilization of electrical power [8]. By focussing on overcoming these challenges, the MEA concept paves the way for the integration of hybrid and fully electric propulsion systems. The corresponding aircraft concepts are called Hybrid Electric Aircraft (HEA) and All Electric Aircraft (AEA) ,

respectively.

The Environmental Control System (ECS) is the largest consumer of non-propulsive power in an aircraft, responsible for approximately 5% of the total specific fuel consumption [9]. By regulating temperature, pressure, and humidity, the ECS ensures cabin conditions that provide passenger comfort. Recent research has focused on the design and optimization of ECS architectures, as improving their efficiency can lead to significant fuel savings for the aircraft [10]. Traditionally, ECS designs for large aircraft rely for cabin cooling on the Air Cycle Machine (ACM) , which uses high-pressure bleed air from the main engines as its power source [11]. Following a reverse open Brayton cycle, this air is compressed, cooled in a heat exchanger, and expanded through a turbine to produce low-temperature air. The cooled air is then mixed with hot bleed air that bypassed the ACM to maintain the desired conditions. Although the ACM is simple and reliable, its reliance on bleed air presents challenges for the MEA framework, where bleed air is no longer available. To address this, additional electric compressors must be integrated. These modifications have promoted the investigation of alternative thermodynamic cycles that may be more suitable for electric aircraft.

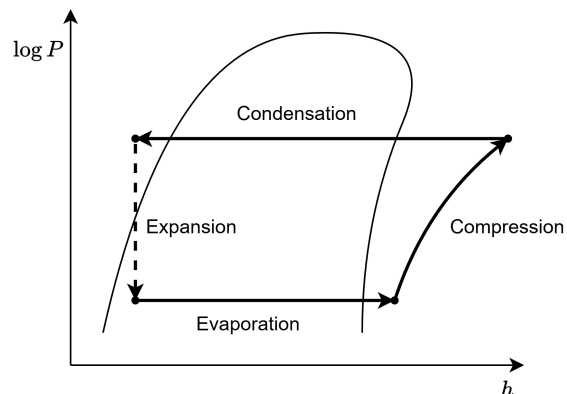


Figure 1: Pressure-enthalpy diagram of an ideal single-stage inverse organic Rankine cycle.

One promising option is the Vapour Compression Cycle (VCC) , which is based on the inverse Rankine cycle, as shown in Figure 1. A working fluid is circulated through system undergoing four main processes: Evaporation, compression, condensation, and expansion [12]. The desired cooling capacity is achieved through the evaporation process. Here cabin air passes through a heat exchanger, where heat is transferred to the working fluid, causing it to evaporate. Subsequently, the fluid is compressed from low to high pressure, increasing its temperature correspondingly. Sub-

sequently, the vapour is condensed by rejecting thermal energy to a cooling medium, typically ram air. Finally, the fluid is throttled through an expansion valve back to the evaporation pressure. By exploiting the phase transitions of the working fluid, the VCC achieves a much higher Coefficient of Performance (*COP*) compared to the ACM [11]. Additionally, since the VCC is not directly connected to the main engine, the cycle can be controlled independently, allowing for more flexibility. However, implementing the VCC requires almost the realization of a new technology in the case of aircraft ECS, including the development of specialized compressors, heat exchangers, and valves for the working fluid. This added complexity, along with an increase in volume and mass of the ECS, may offset the VCC’s performance benefits. Consequently, the suitability of the VCC for future more electric aircraft remains an active area of research.

1.1 The IRIS

At Delft University of Technology, an ongoing research project investigates novel ECS designs based on the adoption of an electrically driven VCC system to enhance efficiency and reduce environmental footprint [13]. Although this technology has already been implemented in the ECS of rotorcraft and small aircraft [11, 14], its suitability for larger aircraft is constrained by several factors, including excessive system volume and weight, safety concerns about refrigerant flammability and toxicity, and a lack of research dedicated to airborne applications [15]. Two key innovations are pursued in the project. Firstly, the traditional scroll compressor used in existing VCC-based ECS designs is replaced with an electrically powered high-speed centrifugal compressor. These centrifugal compressors are not only highly compact and lightweight, but also feature foil bearings. The use of these bearings eliminates the need for an oil system, thereby preventing fluid contamination and further reducing weight. Secondly, low-Global Warming Potential (GWP) working fluids are assessed as replacement of the conventional R-134a refrigerant, significantly reducing the environmental impact if the working fluid is released into the atmosphere.

During the project’s initial phase, several numerical studies on centrifugal VCC design were carried out, as documented in the dissertations of Giuffr  [15] and Ascione [13]. These studies involved developing multi-objective design optimizations to determine the optimal thermodynamic state of the VCC and to size the compressor and heat exchangers accordingly [16–18]. In addition, the impact of the use of differ-

ent refrigerants was evaluated [19]. The IRIS test facility (Inverse Organic Rankine Cycle Integrated System) was developed to support this research by providing an experimental platform to validate the numerical models and test components [20]. More specifically, the IRIS features test sections for compressor systems and air-to-refrigerant heat exchangers, bridging the gap between theory and practical implementation and offering insights into system performance under real-world conditions.

However, the IRIS was not initially designed as a fully versatile test platform. Instead, the facility was built to mimic the ECS of a helicopter, with its components sized for the critical conditions of that kind of application [21]. Although this design provides a starting point for the test rig, it also introduces significant limitations: The system is not fully adaptable to test a wide range of operating conditions and does not fully reflect the configuration of the system it aims to represent. For example, the original plan called for an intercooler paired with a high-speed centrifugal compressor. However, due to the unavailability of the compressor, a reciprocating compressor was temporarily installed, which led to changes in the system architecture. Since reciprocating compressors cannot operate safely at very low suction pressures, the intercooler was removed to increase the evaporation temperature, further deviating from the intended design. Consequently, the IRIS configuration is the result of a trade-off between two opposites; it serves as both a test facility for specific VCC components and a prototype that loosely mirrors a future ECS for larger aircraft. This dual role means that while the IRIS can test up to certain operating conditions, it cannot offer the full flexibility of a purpose-built test rig, nor does it provide a perfect representation of a VCC as implemented in a real ECS.

Despite these limitations, the IRIS remains a valuable tool in the advancement of novel ECS research. The variety of measurement equipment of the facility allows the acquisition of crucial experimental data that complement the numerical optimization studies, aiding in the refinement of theoretical models. Although it may not be fully adaptable to every possible VCC configuration, the IRIS is particularly effective in enabling testing conditions that closely resemble those found in actual aircraft operations. This capability helps address knowledge gaps in the behaviour of components such as the high-speed centrifugal compressor, which has not been extensively tested in airborne applications.

Furthermore, the modular nature of the IRIS means that it can be continuously updated and

improved as the project progresses. The planned replacement of the reciprocating compressor with the high-speed centrifugal compressor, for example, will bring the test rig closer to the specifications of a fully functional ECS, thus enhancing its relevance and accuracy in simulating future systems for electric aircraft. Additionally, the flexibility of the facility allows for further adaptations, such as the integration of an intercooler or other critical components that could expand its testing capabilities. By enabling these updates, the IRIS serves not only as a current test bed but also as a dynamic research platform capable of supporting the ongoing development and optimization of environmentally sustainable ECS designs.

1.1.1 Component Architecture

To provide a clearer overview of its system layout, Figure 2 presents a schematic of the Process & Information Diagram (P&ID) for the IRIS test facility. This diagram illustrates three distinct loops: the heating loop, cooling loop, and refrigeration loop, each corresponding to a subsystem in the ECS of a helicopter [18]. The following paragraphs will describe these loops in more detail.

The heating loop supplies heat to the system and simulates the heat sources found in an aircraft, such as passengers in the cabin or avionics. Instead of air, the loop uses an antifreeze mixture of ethylene glycol and water to enable more precise temperature control, due to its greater heat capacity and lower compressibility compared to air. As shown in the diagram, the fluid is heated by an electric heater and stored in a large insulated tank. A constant speed pump ensures a

constant volumetric flow rate, pushing the fluid through the evaporator. To maintain the desired temperature at the inlet of the evaporator, a three-way mixing valve blends hot fluid from the storage tank with colder fluid from the evaporator's outlet. This method offers more effective temperature control than using the heater directly, as it avoids delays caused by the thermal capacity of the heater or the fluid stored in the tank. By preheating the fluid in the tank and regulating its flow through the mixing valve, the desired temperature can be maintained more efficiently.

The cooling loop functions as a heat sink, similar to the ram air system in an aircraft. In the IRIS system, the cooling loop operates as an open cycle, using air as the cooling medium. Fresh air is drawn from the environment by a variable-speed fan located just upstream of the exit duct. After passing through a filter, the air is heated to the desired temperature using an electric heater. It then flows through a straightener and screen before reaching the condenser, where it is heated up. Subsequently, the air moves through the fan and exits the duct.

The refrigeration loop represents the core of the ECS. Its layout mirrors that of the VCC in an aircraft and incorporates five main components: the evaporator, compressor, condenser, liquid receiver, and Electronic Expansion Valve (EEV). The working fluid in the refrigeration loop is the low-GWP haloolefin R-1233zd(E) [22]. Starting at the outlet of the evaporator, indicated as point 1 in the diagram, the refrigerant (now a superheated vapour) moves through the compressor, where both its temperature and pressure are increased. Between points 3 and 4, the refrigerant

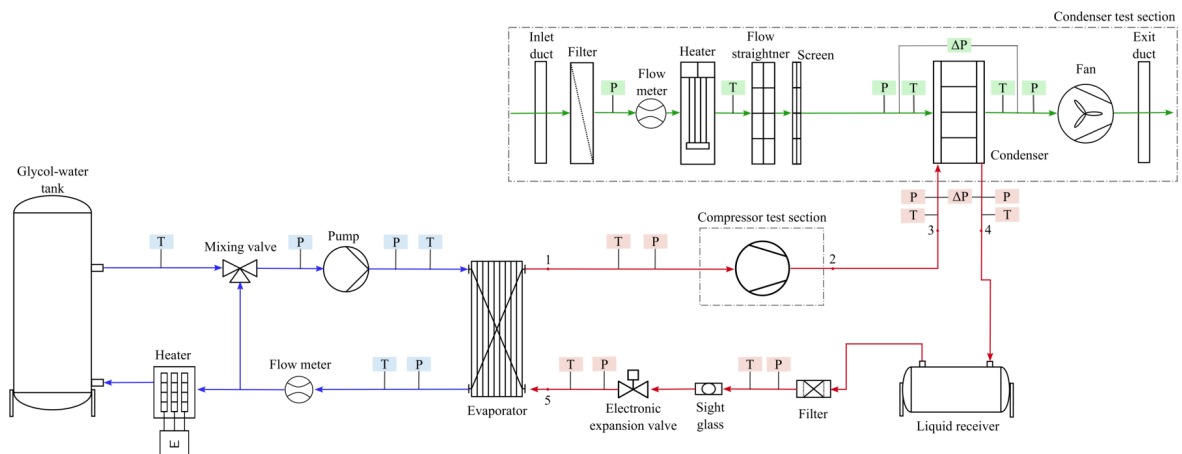


Figure 2: Schematic representation of the P&ID of the IRIS, adapted from [20]. The heating loop is shown with blue process lines, the cooling loop with green, and the refrigeration loop with red. Temperature and pressure sensors are indicated with ‘T’ and ‘P’ labels respectively.

ant passes through the condenser, where heat is rejected until it reaches saturated vapour conditions first and then condensation occurs. Further cooling brings the working fluid to subcooled liquid conditions at point 4. From points 4 to 5, the liquid flows through the liquid receiver, which acts as the main refrigerant storage. This component sets the active charge in the cycle and can also store refrigerant when the system undergoes maintenance. Finally, the high-pressure liquid is expanded through the EEV, reducing the pressure and thereby causing flash evaporation. This process creates a two-phase stream at point 5. In the evaporator, the remaining liquid in the two-phase stream evaporates. The vapour is further heated to prevent liquid droplets from entering the compressor.

The evaporator and condenser consist in a counterflow brazed-plate heat exchanger and a microchannel cross-flow heat exchanger with multi-louvred fins on the air side, respectively. The compressor is currently a semi-hermetic reciprocating piston compressor, but in a near future, this machine will be replaced by a twin-stage high-speed centrifugal machine.

1.2 Research Objectives

The goal of this research is to develop a dynamic numerical model of the refrigeration loop of the IRIS test facility. This model will be instrumental in assessing the off-design performance of existing components and predicting the behaviour of the system once the high-speed centrifugal compressor is integrated into the rig. Given the susceptibility of centrifugal compressors to stall phenomena in certain operating ranges [23], the model will also serve as a foundation for developing a control strategy to regulate the operating conditions of the compressor. With this controller, the operational range of the centrifugal compressor may be assessed effectively, avoiding instabilities at the edges of its performance envelope.

From these goals, the following two research objectives are formulated:

1. **Develop a dynamic model** of the refrigeration cycle of the IRIS to simulate transient behaviour under varying external conditions. The model assumes the future integration of the centrifugal compressor in the working fluid loop.
2. **Design and implement a control system** to regulate critical process variables for the operation of the compressor, specifically temperatures and pressures at the inlet and outlet. The control system will

maintain stable and consistent conditions for the compressor, enabling its reliable testing.

The scope of the dynamic model is limited to the refrigeration loop, given the time available for this project. Consequently, the thermodynamic variables at the interfaces with the heating and cooling loops, such as temperatures, pressures, and mass flow rates, are treated as time-varying inputs or outputs of the model. In the context of control system design and the future integration of the dynamic model in integrated design optimization frameworks, the dynamic order of the model should be kept as low as possible, while retaining a physical interpretation of the variables. In other words, the number of dynamic states in the model should be minimized to ensure low simulation times, allowing for quicker development and verification of controllers.

Ultimately, by offering a way to assess the performance of the facility under off-design conditions, the dynamic model enables faster and more cost-effective evaluations than modifying the physical setup. Additionally, the controller streamlines the compressor testing process by automatically adjusting appropriate inputs. These contributions are vital for improving the functionality of the IRIS and advancing the next generation of environmentally sustainable ECS designs.

1.3 Outline

To address the research objectives outlined in the previous section, this report is organized as follows:

Chapter 2 introduces the modelling methodologies, divided into three parts. Section 2.1 outlines the employed modelling paradigms. Section 2.2 provides detailed descriptions of the individual component models, including the assumptions and methods used. Section 2.3 explains the integration of these component models within the Dymola environment, highlighting the use of auxiliary submodels and simplifications for successful implementation.

Chapter 3 focuses on verifying the developed model. Section 3.1 presents the model's steady-state prediction, which serves as the basis for initialisation for dynamic simulations. Section 3.2 analyses transient simulation results for three scenarios, assessing the trends for their physical validity. Finally, Section 3.3 evaluates the model's integrity, with particular emphasis on the conservation of mass and energy.

Chapter 4 addresses the design of the control system for compressor testing. Section 4.1 defines

the control problem, specifying the plant, inputs, outputs, and disturbances. Section 4.2 describes the linearization of the model around the steady-state initialisation point, followed by scaling and a comparison between the linearized approximation and the full nonlinear model. Section 4.3 details the development and tuning of a decentralized controller using established linear control methods. In Section 4.4, the performance of the closed-loop system is evaluated for three distinct cases, using both the full nonlinear model and the closed-loop linearized system.

Finally, Chapter 5 presents the conclusions, discussing key implications of the methodologies employed and suggesting potential directions for future research.

2 VCC Modelling

This chapter focuses on the transient modelling of the Vapour Compression Cycle (VCC) in the Inverse organic Rankine cycle System (IRIS). The chapter begins with the selection of an appropriate modelling paradigm, which serves as the foundation for the entire modelling process. Next, the individual component models, i.e. heat exchangers, compressor, and expansion valve, are described in detail. Finally, the integration of these component models into a complete VCC model within the Dymola environment is addressed, including the incorporation of necessary auxiliary components.

2.1 Modelling Paradigm

Modelling complex thermodynamic systems can be approached in various ways, each with its own advantages and limitations. A modular approach was chosen to derive the model equations. Unlike a monolithic method, which considers the full system as a single entity, modular modelling involves dividing the system into submodels and deriving the dynamic equations for each part. This method is particularly well-suited for the VCC of the IRIS facility, as it allows for easy updates or model extensions in response to evolving requirements. For example, components can be replaced, or the submodels can be refined to better fit experimental data, without the need to reconstruct the entire model.

Interactions between the various submodels occur through ports, which use specific variables to exchange information. In physical modelling, it is often convenient to select pairs of connecting variables that represent energy when multiplied together [24]. These variables, referred to as effort and flow, enable seamless integration of submodels across various physical domains, such

as translational, rotational, electrical, hydraulic, and thermal systems. When two submodels are connected, equality equations enforce that all effort variables at the ports are equal and that the sum of all flow variables is zero. The total system model can then be represented as a system of Differential-Algebraic Equations (DAEs), which can be solved using specialized numerical methods [25].

The chosen modelling environment for this work is Dymola, a commercial simulation tool that uses the Modelica language [26]. A key strength of Modelica is its non-causal modelling approach, which eliminates the need to predefine inputs and outputs for submodels. Instead, equations are written symbolically, and the solver determines the inputs and outputs automatically, based on the boundary conditions of the overall system model. This flexibility greatly reduces the modeller’s workload and allows any type of submodel to connect with another provided that the connecting ports are compatible. However, the approach also has drawbacks. Careless connections or poorly chosen boundary conditions can introduce unnecessary sets of implicit nonlinear algebraic equations or high-index DAEs [27]. Such difficulties increase computational cost or solvability of the model, and careful attention is therefore required to avoid complications.

To address these challenges, a causal modelling method was employed. In causal modelling, inputs and outputs are predefined in a way that ensures convenient and computationally efficient connections between submodels. This approach minimizes the index of the DAE system and avoids unnecessary algebraic loops. Two fundamental module types are used: storage modules and flow modules.

- **Storage modules** accept flow variables as inputs and provide effort variables as outputs. The effort variables follow from dynamic states within the module. These states govern the behaviour of the system over time, and result from the integration of time-differential equations.
- **Flow modules**, on the other hand, are static. They take effort variables as inputs and compute the resulting flow variables based on their difference.

Storage and flow modules can be directly connected, as their inputs and outputs are compatible. By connecting storage and flow modules in an alternating pattern, the components of complex systems can thus be modelled systematically and efficiently.

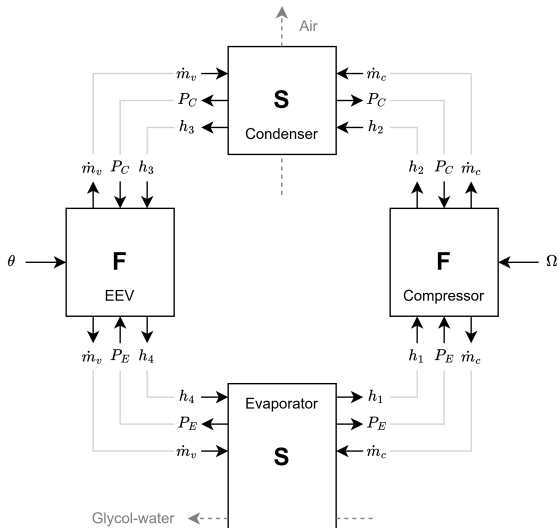


Figure 3: Causality diagram of refrigerant cycle in VCC of the IRIS.

Applying the causal modelling method to derive the dynamic model of the IRIS working fluid loop involves a key assumption: the dynamics of the compressor and expansion valve are significantly faster than those of the heat exchangers [28]. This assumption enables time-scale decoupling, where the fast components can be modelled as static, while the dynamic states of the model represent only the slower transients of the system. Consequently, the compressor and expansion valve are treated as flow modules, while the heat exchangers are represented as storage modules. The interactions between these modules are illustrated using a causality diagram, shown in Figure 3. While this diagram resembles the representation of the refrigeration loop in Figure 2, the arrows in the causality diagram indicate the flow of information rather than the flow of mass. Each module's ports correspond to the inlets and outlets of the associated component, with pressure and mass flow rate serving as the effort and flow variables, respectively. To account for the convection of energy, specific enthalpy is also included as a port variable. Its direction aligns with the flow of refrigerant, which is assumed to not change during operation. For improved readability, the causality diagram is only shown for the working fluid.

Notably, the liquid receiver is excluded from the model for simplicity. Doing so results in a constant refrigerant charge in the model and implies the additional assumption of negligible mass and thermal inertia of the receiver. Although some authors have reported on the importance of including a liquid receiver model to appropriately account for the varying refrigerant charge at off-design conditions [30–32], it was decided to

neglect the modelling of this component as the variation of the active charge of fluid in the operating range of the IRIS setup is expected to be small. Future studies will assess the validity of this hypothesis, as mentioned in more detail in Section 5.2.

2.2 Components

Each of the submodels in Figure 3 requires specialized modelling approaches and will therefore be discussed in separate sections. Given the complexity of the heat exchanger models, their description is further divided into sections covering the working fluid equations, glycol-water side equations, air side equations, and wall temperature equations. Additionally, the heat transfer correlations used for the various convective heat transfer processes are addressed in a dedicated subsection.

2.2.1 Heat Exchangers

For the heat exchanger models, the Moving Boundary (MB) method is used, since it provides a good balance between accuracy and computational efficiency in comparison with alternative methods [33, 34]. The MB method relies on the following simplifying assumptions:

- The heat exchanger can be modelled as a long, horizontal tube.
- The flow in the heat exchanger is one-dimensional, meaning properties are uniform over the cross-sectional area.
- The cross-sectional area of the flow is constant.
- Pressure drop along the heat exchanger is negligible.
- Axial heat conduction through the fluid and solid material of the heat exchanger is negligible.

These assumptions simplify the differential conservation equations governing flow dynamics, reducing them to their one-dimensional form [35]:

$$\frac{\partial \rho}{\partial t} + \frac{\partial \rho u}{\partial x} = 0 \quad (1)$$

$$\frac{\partial \rho h}{\partial t} + \frac{\partial \rho u h}{\partial x} = \frac{\partial P}{\partial t} + \frac{\dot{Q}}{A_c}. \quad (2)$$

Equation (1) and (2) represent conservation of mass and energy, respectively, where ρ is the fluid density, t represents time, x is the one-dimensional spatial direction, u is the velocity along this direction, h is the specific enthalpy, P is the pressure, \dot{Q} is the heat transfer rate per unit length, and A_c is the cross-sectional area of the flow. As pressure is assumed uniform along

the length of the heat exchanger, the momentum equation is omitted. These conservation equations apply to all fluids in the heat exchanger, including refrigerant, glycol-water, and air, although the relations between the thermodynamic properties in (1) and (2) and their effect on the dynamic states differ for each fluid.

Working Fluid

The key principle of the MB method is to integrate (1) and (2) according to the phase of the working fluid [29]. For instance, in the evaporator illustrated in Figure 4, the refrigerant enters as a two-phase flow and exits as superheated vapour (this transition is also depicted in Figure 1). As the fluid moves through the heat exchanger, the liquid evaporates until the fluid reaches saturated vapour conditions, where all liquid has evaporated. The MB method assumes that this phase transition point can be represented by a one-dimensional position within the heat exchanger, denoted as L_1 in Figure 4. Changes in pressure, mass flow rate, and heat transfer to the refrigerant over time alter the characteristics of the evaporation process, causing the position of this phase transition boundary to shift dynamically along the heat exchanger length. Consequently, the evaporator is divided into two regions whose sizes fluctuate based on the flow conditions. Similarly, the condenser is divided into three distinct regions. As shown in Figure 1, the refrigerant entering the condenser is first desuperheated in a single-phase vapour region, then fully condensed in a two-phase region, and finally subcooled in a single-phase liquid region. It is assumed that no phase regions (dis)appear in the two heat exchangers during operation: the evaporator always contains a two-phase and superheating region, while the condenser consistently features desuperheating, two-phase, and subcooling regions.

Building on this approach, the model equations can be found by integrating (1) and (2) with respect to the spatial coordinate x for each phase region. In the context of the causal modelling approach, the goal is to arrive at a system of equations that can be solved explicitly for the time derivatives of dynamic states, preferably with no implicit algebraic loops. As will become clear in the following derivation, the choice for the dynamic states is not fixed, and suitable variables must be selected based on the structure of the conservation equations.

The integral conservation equations are derived from (1) and (2) by applying the divergence theorem and the Leibniz rule [36]. For instance, the dynamics of the two-phase region in the evaporator, indicated with the $_1$ subscript, are described by

$$A_{c,E} \left(L_{1,E} \frac{d\bar{\rho}_{1,E}}{dt} + \bar{\rho}_{1,E} \frac{dL_{1,E}}{dt} \right) = \dot{m}_v - \dot{m}_E^v \quad (3)$$

$$A_{c,E} \left(L_{1,E} \left(\frac{d(\overline{\rho h})_{1,E}}{dt} - \frac{dP_E}{dt} \right) + \overline{\rho h}_{1,E} \frac{dL_{1,E}}{dt} \right) = \dot{m}_v h_4 - \dot{m}_E^v h_E^v + \dot{Q}_{f,1,E}, \quad (4)$$

where \dot{m} indicates the mass flow rate and \dot{Q} is the heat transfer rate. The subscripts $_E$, $_v$, and $_f$ respectively represent variables for the evaporator, expansion valve, and refrigerant. The superscript v indicates variables at the saturated vapour boundary. The bar notation is used to denote the average of a property throughout the region, e.g. $\overline{\rho h}$ indicates the average of the product of density and specific enthalpy in the volume. The definitions of these average properties depend on the phase of the fluid in the region.

For two-phase flow, the Homogeneous Equilibrium Model (HEM) is used, stating that the

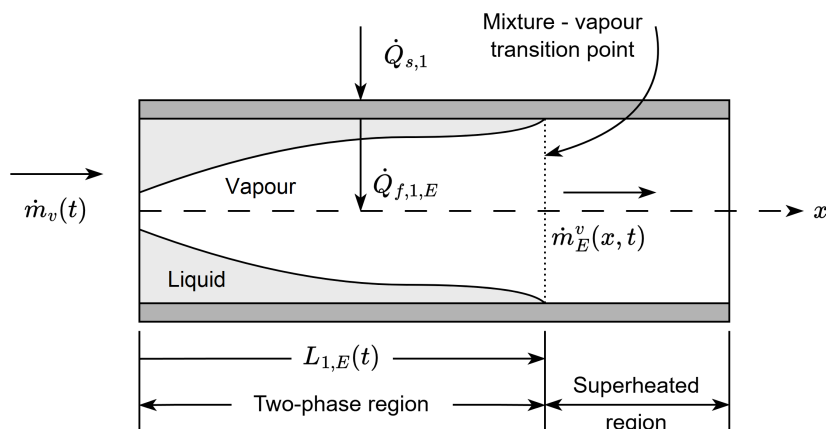


Figure 4: Schematic drawing of the refrigerant flow through the evaporator, adapted from [29].

two phases have equal velocity and are in thermodynamic equilibrium. The average density then follows from the void fraction γ , which represents the local ratio between the area occupied by vapour and the total cross-sectional area. Following the assumptions of the HEM, it is a function of the vapour quality, q , and saturation densities [37] through

$$\gamma = \frac{1}{1 + \frac{1-q}{q} \left(\frac{\rho^v}{\rho^\ell} \right)}, \quad (5)$$

where the superscript ℓ denotes saturated liquid conditions. The average void fraction can be determined through integration with respect to the spatial coordinate. For simplicity, it is assumed that the vapour quality varies linearly along the length of the two-phase region, resulting in

$$\bar{\gamma} = \frac{1}{q_{out} - q_{in}} \int_{q_{in}}^{q_{out}} \gamma \left(q, \frac{\rho^v}{\rho^\ell} \right) dq, \quad (6)$$

with in and out indicating the inlet and outlet respectively. It is additionally assumed that the average void fraction is time-invariant [38]. This means that its value for the evaporator and condenser can be computed once and then used as fixed parameters for the models. Given the configuration of the phase regions in the condenser, the inlet and outlet quality of its two-phase region will always be 1 and 0 respectively. Similarly, the outlet quality of the two-phase region in the evaporator will always be equal to 1. As a result, the average void fraction of the condenser is a function of only the pressure. In the evaporator, the average void fraction is a function of the pressure and inlet quality. To compute the values of the average void fractions, the pressures and evaporator inlet quality at the design point of the IRIS are used. For the evaporation region, again denoted by the $_1$ subscript, the average density is then given by

$$\bar{\rho}_{1,E} = \bar{\gamma}_E \rho_E^v + (1 - \bar{\gamma}_E) \rho_E^\ell. \quad (7)$$

Similarly, the average of the product between density and specific enthalpy can also be expressed using the average void fraction:

$$\overline{(\rho h)}_{1,E} = \bar{\gamma}_E \rho_E^v h_E^v + (1 - \bar{\gamma}_E) \rho_E^\ell h_E^\ell. \quad (8)$$

Since the average void fraction is assumed constant, the time derivatives of these average properties are a function of only the evaporation pressure and its time derivative. For example, the time derivative of the mean density of evapora-

tion is given by

$$\frac{d\bar{\rho}_{1,E}}{dt} = \left(\bar{\gamma}_E \left(\frac{\partial \rho_E^v}{\partial P} \right)_{sat} + (1 - \bar{\gamma}) \left(\frac{\partial \rho_E^\ell}{\partial P} \right)_{sat} \right) \frac{dP_E}{dt}, \quad (9)$$

where the partial derivatives along the saturation lines are indicated with the sat subscript. These partial derivatives are functions of only the evaporation pressure, and can be found in an external package used to calculate the thermodynamic properties of R-1233zd(E), namely REFPROP [39], that is called in the Modelica environment through the ExternalMedia package [40].

For single-phase regions, the average properties in the conservation equations are computed using the pressure and average specific enthalpy in the region. In contrast with the two-phase regions, where the mean void fraction is used, the single-phase regions require the inlet and outlet enthalpy to determine the average enthalpy. It is assumed that the enthalpy profile within the single-phase region is linear. For example, in the superheating region of the evaporator, indicated with the $_2$ subscript, the average specific enthalpy is given by

$$\bar{h}_{2,E} = \frac{h_E^v + h_1}{2}. \quad (10)$$

All other fluid properties in the region can then be determined from the pressure and average enthalpy by calling the appropriate Equation of State (EoS) through ExternalMedia, e.g.

$$\bar{\rho}_{2,E} = f(P_E, \bar{h}_{2,E}), \quad (11)$$

and for the average of the product of density and enthalpy it is assumed that $(\rho h) \approx \bar{\rho} \cdot \bar{h}$. The time derivatives of the average properties are then a function of the time derivatives of the pressure and average specific enthalpy, resulting in

$$\begin{aligned} \frac{d\bar{\rho}_{2,E}}{dt} &= \left(\frac{\partial \bar{\rho}_{2,E}}{\partial P} \right)_h \frac{dP_E}{dt} + \left(\frac{\partial \bar{\rho}_{2,E}}{\partial h} \right)_P \frac{d\bar{h}_{2,E}}{dt} \\ \frac{d\bar{h}_{2,E}}{dt} &= \frac{1}{2} \left(\left(\frac{\partial h_E^v}{\partial P} \right)_{sat} \frac{dP_E}{dt} + \frac{dh_1}{dt} \right), \end{aligned} \quad (12)$$

where the $_h$ and $_P$ subscripts indicate that the partial derivatives are computed with respect to a constant specific enthalpy and pressure, respectively.

After combining the conservation equations of each phase region the evaporator model consists of a total of four conservation equations in the following seven unknowns: P_E , $L_{1,E}$, h_1 , \dot{m}_E^v , $\frac{dP_E}{dt}$,

$\frac{dL_{1,E}}{dt}$, $\frac{dh_1}{dt}$. From this, it follows that an appropriate selection of the dynamic states of the evaporator includes the pressure P_E , phase transition position $L_{1,E}$, and the outlet enthalpy h_1 . Doing so results in a system of 4 conservation equations and 4 unknowns. Combining the unknowns into a vector $z_E = \left[\frac{dP_E}{dt} \quad \frac{dL_{1,E}}{dt} \quad \frac{dh_1}{dt} \quad \dot{m}_E^v \right]^T$, the final form of the evaporator equations can be written as [36]

$$z_E = \Phi_E^{-1} \phi_E, \quad (13)$$

where the matrix Φ_E and vector ϕ_E are uniquely determined by the model inputs and dynamic states. Recalling the assumption that no phase regions (dis)appear, matrix Φ_E will always be invertible, and the unknowns of the working fluid equations can thus be found explicitly, guaranteeing a minimal index and proving that no implicit algebraic loops have to be solved.

For the condenser, indicated with subscript C , a total of six conservation equations result from combining the three phase regions. Similar to the evaporator model, the dynamic states are selected as P_C , $L_{1,C}$, $L_{2,C}$ and h_3 , resulting in a total of six unknowns; $z_C = \left[\frac{dP_C}{dt} \quad \frac{dL_{1,C}}{dt} \quad \frac{dL_{2,C}}{dt} \quad \frac{dh_3}{dt} \quad \dot{m}_C^v \quad \dot{m}_C^\ell \right]^T$. The equations can be written similarly to the evaporator system in (13), and a minimal index and absence of algebraic loops is therefore also ensured for the working fluid equations of the condenser. More details on the derivation of the working fluid equations can be found in Appendix A.

Glycol-water Side

The glycol-water side of the evaporator, denoted with subscript s is divided into two regions, corresponding to the phase regions of the working fluid. As the phase transition point of the working fluid shifts, the boundary separating the two glycol-water regions moves accordingly. Similar to the working fluid, the glycol-water flow is assumed to have uniform pressure throughout. The resulting integral mass and energy conservation equations resemble (3) and (4). However, since the position of the phase transition, $L_{1,E}$, is determined solely by the conservation equations of the working fluid, this variable and its time derivative are treated as outputs of the working fluid equations and inputs to the glycol-water equations.

The glycol-water average thermodynamic properties are calculated using the pressure and specific enthalpy, as was done for the single-phase regions of the working fluid. For this, a linear enthalpy profile is again assumed between the boundaries of each region. However, due to limi-

tations in defining the EoS for mixtures in the ExternalMedia framework, the glycol-water mixture is approximated by using a water fluid model, which is available in the Modelica Standard Library [41].

The dynamics of the glycol-water side of the evaporator are described by a total of four conservation equations, and the variables selected as dynamic states are the pressure P_s , the intermediate enthalpy at the boundary between the regions $h_{s,int}$, and the outlet enthalpy $h_{s,out}$, yielding a total of four unknowns. Note, however, that the evaporator has a counter-flow orientation, resulting in the inlet and outlet boundaries to be geometrically opposite to those of the working fluid. In vector form, the unknowns are given by $z_s = \left[\frac{dP_s}{dt} \quad \frac{dh_{s,int}}{dt} \quad \frac{dh_{s,out}}{dt} \quad \dot{m}_{s,int} \right]$. The unknown vector can be computed explicitly using an approach similar to that adapted for solving the working fluid equations in (13). More details on the glycol-water side equations are provided in Appendix A.

Air Side

The air side of the condenser, indicated by subscript a , is modelled analogously to the glycol-water flow in the evaporator, splitting the air flow into three volumes corresponding to the phase regions of the working fluid. However, to minimize the number of dynamic states and thereby improve computational efficiency, only the dynamics of the storage of energy in the air are considered. As a result, the pressure is assumed uniform and constant, and the air mass flow rate through the condenser is equal to the specified inlet flow rate. Since the condenser has a cross-flow configuration, the total air mass flow rate must be split in accordance with the sizes of each of the three volumes, which depend on the lengths of their respective fluid phase regions. This results in a slightly different formulation of the conservation of energy in the volumes of the air flow in comparison with the glycol-water equations, where a counter-flow stream is modelled. For example, in the desuperheating region of the condenser, the conservation of energy equation is given by

$$\frac{A_{c,a}L_a}{L_{tot,C}} \left(L_{1,C} \frac{d(\overline{\rho h})_{a,1}}{dt} + (\overline{\rho h})_{a,1} \frac{dL_{1,C}}{dt} \right) = \dot{m}_a \frac{L_{1,C}}{L_{tot,C}} (h_{a,in} - h_{a,out,1}) - \dot{Q}_{a,1}, \quad (14)$$

where L_a is the length of the air flow path perpendicular to the refrigerant stream, $A_{c,a}$ denotes the total cross-sectional area of the air flow, and the $_{tot}$ subscript denotes the total heat exchanger

length in the direction of the refrigerant flow. The boundary position $L_{1,C}$ and its time derivative are inputs of the energy equation for the airflow, following from the working fluid equations. Similar to the single-phase regions of the working fluid and glycol-water flows, the enthalpy profile is assumed linear, and the average properties of the air are determined at the pressure and average air enthalpy of the respective volumes. The EoS of dry air contained in the Modelica Standard Library is used for this. In total, the equations for the air side of the condenser include three dynamic states: the outlet enthalpies of each region, $h_{a,out,1}$, $h_{a,out,2}$, and $h_{a,out,3}$. The time derivatives of these states follow explicitly after substitution of the average property equations in the energy equations. More details on the derivation of the air side equations are provided in Appendix A.

Wall Temperature

To account for the thermal capacitance of the metal interface between the hot and cold streams, a wall element is included in the heat exchanger model, indicated with subscript w . Similar to the approach used for the secondary flows, the wall is divided into sections corresponding to the phase regions of the working fluid, with its thermal properties lumped and averaged within each region. For example, referring to the schematic representation of the evaporator in Figure 4, the integral energy equation describing the average wall temperature in the two-phase region of the evaporator is given by

$$L_{1,E} \frac{d\bar{T}_{w,1,E}}{dt} = \frac{dL_{1,E}}{dt} (T_{w,E}^v - \bar{T}_{w,1,E}) + \frac{\dot{Q}_{s,1} - \dot{Q}_{f,1,E}}{\rho_{w,E} c_{w,E} A_{c,w,E}}, \quad (15)$$

where c_w is the specific heat capacity of the wall. The first term on the right-hand side of this equation accounts for the change in energy of the wall section caused by the movement of the working fluid's phase transition boundary. To ensure energy conservation, the value of $T_{w,E}^v$ has to be adapted depending on which direction the boundary moves. This is achieved through a switching policy for the boundary wall temperature [42]. When the phase transition boundary moves downstream, the wall temperature at the boundary is set equal to the average wall temperature of the superheating region. Conversely, if the boundary moves upstream, it is set to the average wall temperature of the two-phase region.

The physical reasoning behind this switching strategy lies in the interaction between the two regions of the wall. When the boundary

moves downstream, the two-phase wall section effectively absorbs part of the superheating wall section. Since the average wall temperatures of these regions typically differ, the energy of the two-phase wall section must adjust (either increasing or decreasing) depending on the average temperature of the neighbouring section. Similarly, when the boundary moves upstream into the two-phase region, the effect is reversed, altering the energy of the superheating wall section. This process ensures that no energy is lost, hence guaranteeing conservation across the entire wall. For the evaporator, this switching strategy is mathematically expressed as

$$T_{w,E}^v = \begin{cases} \bar{T}_{w,2,E} & \frac{dL_{1,E}}{dt} \geq 0 \\ \bar{T}_{w,1,E} & \frac{dL_{1,E}}{dt} < 0 \end{cases}. \quad (16)$$

A similar switching strategy is applied for the wall energy equations of the condenser. However, since the condenser contains two phase transition boundaries, two wall boundary temperatures are defined. The wall section of the condenser corresponding with the two-phase region thus contains two boundary movement terms, one for each phase transition boundary. A more detailed derivation of the wall energy equation can be found in Appendix A.

Heat Transfer

To complete the heat exchanger models, it is essential to define expressions for the heat transfer rate. In general, these expressions take the following form:

$$\dot{Q}_f = \bar{\alpha} A_h (\bar{T}_w - \bar{T}_f), \quad (17)$$

with $\bar{\alpha}$ as the average convective heat transfer coefficient. The heat transfer rate is considered positive when directed towards the refrigerant. Note that the average temperature of the fluids follows from the average enthalpy and pressure. For internal flows, the heat transfer area is expressed as $A_h = LC$, where L is the length of the region and C represents the perimeter of the flow channel. On the air side, the heat transfer area for the i th region depends on the region's length and the fin efficiency η_f , resulting in

$$A_{h,a,i} = \eta_t \frac{L_{i,C}}{L_{tot,C}} A_{h,a} \quad (18)$$

$$\eta_t = 1 - \frac{A_{fin}}{A_{h,a}} (1 - \eta_{fin}).$$

The average convective heat transfer coefficient $\bar{\alpha}$ is determined separately for each phase region on both the refrigerant and secondary fluid sides. These coefficients are typically obtained

from empirical correlations that account for the geometrical characteristics of the heat exchanger and thermodynamic properties of the fluids. Such correlations often rely on dimensionless numbers, e.g. Reynolds, Prandtl, and Nusselt, which are defined as

$$\begin{aligned} Re_{D_h} &= \frac{GD_h}{\mu} \\ Pr &= \frac{C_p \mu}{k} \\ Nu_{D_h} &= \frac{\alpha D_h}{k}. \end{aligned} \quad (19)$$

Here, D_h denotes the hydraulic diameter, i.e. $D_h = \frac{4A_c}{C}$, μ is the dynamic viscosity, C_p is the heat capacity at constant pressure, and k is the thermal conductivity. To avoid algebraic loops, the mass flux $G = \dot{m}/A_c$ is calculated from the average of the inlet and outlet mass flow rates, which are model inputs for all fluids. Since the flow characteristics differ significantly for each fluid, particularly in the two-phase regions, the heat transfer correlations for each scenario are discussed individually.

For heat transfer between the wall and the refrigerant, three different correlations are applied, depending on the fluid's phase. In single-phase regions, when the Reynolds number is below 3000, a constant Nusselt number of $Nu_{D_h} = 3.66$ is assumed. For Reynolds numbers above 3000, Gnielinski's correlation is used, along with Petukhov's friction factor [43], given by

$$\begin{aligned} Nu_{D_h} &= \frac{\frac{f_p}{8} (Re_{D_h} - 1000) Pr}{1 + 12.7 \left(\frac{f_p}{8}\right)^{\frac{1}{2}} \left(Pr^{\frac{2}{3}} - 1\right)} \\ f_p &= (0.790 \ln(Re_{D_h}) - 1.64)^{-2}. \end{aligned} \quad (20)$$

The average heat transfer coefficient is then determined by evaluating this correlation at the average fluid properties: $\overline{Nu}_{D_h} \approx Nu_{D_h}(P, \bar{h})$.

For two-phase flow in the evaporator, the following correlation of Lee et al. [44] is used:

$$\begin{aligned} \overline{Nu}_{D_h} &= 0.9243 Re_\ell^{0.6151} Pr_\ell^{0.33} \\ Re_\ell &= \frac{G_{eq} D_h}{\mu^\ell} \\ Pr_\ell &= \frac{C_p^\ell \mu^\ell}{k^\ell} \\ G_{eq} &= G \left((1 - \bar{q}) + \bar{q} \left(\frac{\rho^\ell}{\rho^v} \right)^{0.5} \right) \\ \bar{q} &= \frac{q_{in} + 1}{2}, \end{aligned} \quad (21)$$

where the inlet quality q_{in} is derived from the inlet enthalpy and evaporator pressure using the EoS, while the Reynolds and Prandtl numbers are calculated based on saturated liquid properties.

In the condenser's condensation region, Shah's correlation [45] is employed. Under the assumption of a linear quality profile between 0 and 1, the local correlation is integrated to compute the average heat transfer coefficient, resulting in

$$\begin{aligned} \bar{\alpha} &= \alpha_\ell \left(1 + \frac{1.128}{1.817} \left(\left(\frac{\rho^\ell}{\rho^v} \right)^{0.3685} \times \right. \right. \\ &\quad \left. \left. \left(\frac{\mu^\ell}{\mu^v} \right)^{0.2363} \left(1 - \frac{\mu^v}{\mu^\ell} \right)^{2.144} Pr_\ell^{-0.1} \right) \right) \\ \alpha_\ell &= 0.023 Re_\ell^{0.8} Pr_\ell^{0.4} \frac{k^\ell}{D_h}, \end{aligned} \quad (22)$$

where the definitions of the Reynolds and Prandtl numbers follow those in (21).

For the glycol-water mixture, the average heat transfer coefficient is assumed constant in both regions. It is calculated based on inlet conditions using Gnielinski's formula and Petukhov's friction factor, as depicted in (20). The thermodynamic properties of the flow follow from the EoS, where the mixture is approximated as pure water.

Finally, for the air side Chang and Wang's correlation [46] is applied in each region, given by

$$\begin{aligned} \bar{\alpha} &= \frac{j C_p G}{Pr^{\frac{2}{3}}} \\ j &= \Xi Re_{L_p}^{-0.49}. \end{aligned} \quad (23)$$

Here, j denotes the Colburn factor, Ξ is a constant dependent on the air-side fin geometry, and L_p is the louver pitch of the fins. The thermodynamic properties of the air are determined from the pressure and average enthalpy of the region.

Table 1: Heat transfer coefficient correlations for each fluid and phase region.

Fluid	Phase Region	Correlation
R-1233zd(E)	Single-phase	Gnielinski with Petukhov [43]
	Evaporation	Lee et al. [44]
	Condensation	Shah [45]
Glycol-water	All	Gnielinski with Petukhov
Air	All	Chang and Wang [46]

To provide an overview, Table 1 summarizes the chosen heat transfer correlations for each fluid and phase region.

2.2.2 Compressor

The compressor model is static, containing no dynamic states. This allows the use of a steady-state performance map to determine the mass flow rate through the centrifugal compressor at a given compressor speed and pressure ratio. Although the compressor consists of two stages connected in series, a combined single-stage performance map is used, which has two important implications.

Firstly, while using performance maps for both independent stages would improve accuracy, the available experimental data only contain measurements at the inlet of the first stage and the outlet of the second stage. Therefore, a single-stage performance map is assumed to approximate the combined behaviour of both stages.

Secondly, the single-stage map inherently accounts for interstage heat transfer from bypass flows used in the bearing system and from cooling the electric motor that powers the compressor. Specifically, refrigerant exiting the first stage flows through a cooling duct near the motor coils before entering the second stage, absorbing some of the heat generated by the motor. In addition, a portion of the refrigerant stream at the compressor inlet bypasses the main flow to lubricate the bearings, where frictions between the static and rotating elements increase the temperature of the fluid before reinjection. The extent of these effects depends on the rotational speed and flow conditions of the compressor. However, due to the lack of detailed thermodynamic data within the compressor, these effects are assumed to be captured adequately in the single-stage performance map.

The performance map itself is constructed using experimental data provided by the compressor manufacturer. During testing, the rotational speed and inlet conditions (temperature and pressure) were held constant, while the discharge pressure was varied. This process generates speed lines; curves of data points corresponding to a specific compressor speed, defined by the suction and discharge pressures and temperatures. The measurement range is constrained by two limits: surge and choke.

- Surge occurs when the pressure ratio becomes too large, causing flow separation and reattachment at a certain frequency. This results in violent oscillations and a significant performance drop. The speed lines are measured just before surge, where the pressure ratio reaches its maximum.
- Choke occurs when the flow reaches the local speed of sound, preventing any further

increase in mass flow rate regardless of pressure difference. The speed lines approach this condition asymptotically.

By performing experiments across a range of compressor speeds (from minimum to maximum rotational speed), the operational regime of the compressor is mapped. The data are obtained at constant inlet conditions, defined by a reference temperature T_{ref} and pressure P_{ref} . However, when the compressor operates in off-design conditions with varying inlet conditions, the speed lines change shape. To address this, the rotational speed and mass flow rate are corrected using the following relations, valid for an ideal gas [47]:

$$\begin{aligned} N_T &= \sqrt{\frac{T_{\text{ref}}}{T_1}} \frac{\Omega}{\Omega_{\text{ref}}} \\ \dot{m}_{\text{cor}} &= \sqrt{\frac{T_1}{T_{\text{ref}}}} \frac{P_{\text{ref}}}{P_E} \dot{m}_c. \end{aligned} \quad (24)$$

Here, N_T is the corrected speed, non-dimensionalized by the reference rotational speed $\Omega_{\text{ref}} = 80$ kRPM, and the subscripts $_{\text{cor}}$ and $_c$ indicate corrected properties and compressor variables respectively.

The corrected compressor map consists of two plots (see Figure 5): one showing the pressure ratio PR as a function of the corrected mass flow rate, and another showing the isentropic efficiency η_s as a function of the corrected mass flow rate. The map can be converted into numerical tables using the β -line method [48], allowing interpolation to determine the required variables for specific input conditions. Three tables are constructed, one for the pressure ratio PR , one for the corrected mass flow rate \dot{m}_{cor} , and one for the isentropic efficiency η_s . The independent variables are the β variable from the β -line method, and the corrected compressor speed N_T .

To compute the mass flow rate and isentropic efficiency in the compressor model, the inlet pressure P_E , outlet pressure P_C , and compressor speed Ω are used as inputs (see Figure 3). The procedure is as follows:

1. Compute the pressure ratio PR as P_C/P_E .
2. Correct the compressor speed N_T using the relation in (24).
3. Initialize an iterative procedure to identify the corresponding β -value for the given PR and N_T . This starts with a guess (half the total number of β -lines) and evaluates the compressor map tables for varying β until convergence.

4. Extract the corrected mass flow rate and isentropic efficiency from the tables at the converged β .
5. Determine the actual mass flow rate using (24).
6. Use the isentropic efficiency to compute the outlet enthalpy h_2 of the compressor with

$$h_2 = h_1 + \frac{1}{\eta_s}(h_{2s} - h_1),$$

where h_{2s} , the isentropic outlet enthalpy, is evaluated from the EoS at the condenser pressure P_C and entropy s_1 , which is determined at the inlet conditions (P_E, h_1) .

Since the procedure requires solving an implicit relation to determine β , the model includes an algebraic loop. Fortunately, a unique solution to this set of equations is always guaranteed as long as the operating point of the compressor remains within the boundaries of the map. This is evident from the speed lines in Figure 5a, where, at a given corrected speed, each point along the line corresponds to a single pressure ratio. Contrarily, if the speed lines were horizontal at low mass flow rates, pressure ratio values near surge could result in multiple valid solutions for β , making the implicit system underdetermined.

2.2.3 Expansion Valve

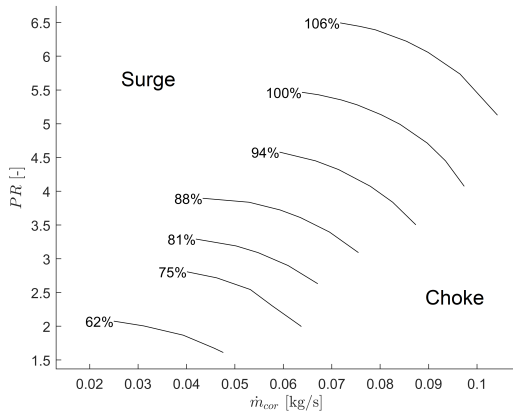
The Electronic Expansion Valve (EEV) model is implemented using the liquid flow valve model with potential choked flow conditions provided in the ThermoPower Modelica library [49]. This

model applies standard valve sizing equations from the International Society of Automation (ISA) [50]. The mass flow through the valve is described by

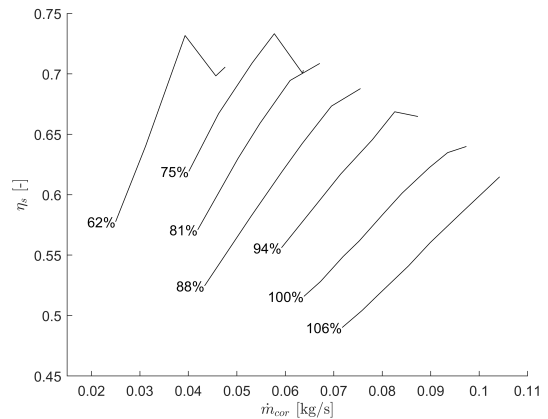
$$\begin{aligned} \dot{m}_v &= A_v g(\theta) \sqrt{\rho_{in} \Delta P_{eff}} \\ \Delta P_{eff} &= \begin{cases} \Delta P & \Delta P < \Delta P_{crit} \\ \Delta P_{crit} & \text{otherwise} \end{cases} \\ \Delta P &= P_C - P_E \\ \Delta P_{crit} &= F_L^2 (P_C - F_F P_{in}^\ell) \\ F_F &= 0.96 - 0.28 \sqrt{\frac{P_{in}^\ell}{P^*}}, \end{aligned} \quad (25)$$

where ΔP_{eff} and ΔP_{crit} are the effective and critical pressure ratios, respectively, and A_v is determined from nominal operating conditions, chosen based on the design point of the IRIS. The opening behaviour of the valve is described by the characteristic equation $g(\theta)$, where θ represents the valve's opening percentage, ranging from 0 % (fully closed) to 100 % (fully open). A linear opening characteristic is adopted based on the valve manufacturer's specification sheets [51].

From the pressure difference equations, it follows that when the pressure drop across the valve exceeds the critical pressure difference, the flow becomes choked, and the effective pressure difference is limited to the critical value. The recovery factor F_L is assumed constant at 0.9. The critical pressure ratio factor F_F is derived using the Homogeneous Equilibrium Model (HEM). Under the assumption that flash evaporation leads to two-phase flow within the valve, the HEM shows that the critical pressure ratio depends solely on



(a) Pressure ratio



(b) Isentropic efficiency

Figure 5: Single-stage compressor performance map of centrifugal compressor, constructed from experimental data provided by the manufacturer. The reference temperature and pressure are $T_{ref} = 25 \text{ }^\circ\text{C}$ and $P_{ref} = 0.72 \text{ bar}$ respectively, and the corrected speed is indicated in the figure as a percentage of the reference speed $\Omega_{ref} = 80 \text{ kRPM}$.

the saturation pressure corresponding to the inlet temperature P_{in}^ℓ and the refrigerant's critical pressure P^* [52]. This dependence is reflected in the given equation for F_F .

To determine the outlet enthalpy, an adiabatic expansion process is assumed, meaning no heat is exchanged with the surroundings as the fluid passes through the valve. It follows that the outlet specific total enthalpy equals the inlet specific total enthalpy, i.e.

$$h_4 = h_3. \quad (26)$$

2.3 Model Implementation

After formulating the model equations for the individual components, the submodels were implemented in Modelica to construct the complete Vapour Compression Cycle (VCC).

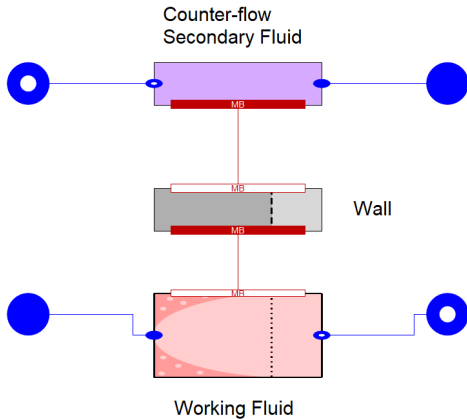


Figure 6: Evaporator model in Modelica.

To connect the submodels, standard connection interfaces were primarily used, taken from the ThermoPower library or the Modelica Standard Library. However, within the heat exchanger models, a custom connection interface was introduced as part of the moving boundary method. This interface extends the standard thermal connection by incorporating the lengths of the phase regions of the working fluid as inputs or outputs.

For instance, in the evaporator model shown in Figure 6, three submodels (working fluid, wall, and secondary fluid) are connected using this custom interface. Two interface variants are employed: the outlet interface, represented by a white-filled connector, outputs the phase region lengths, while the inlet interface, represented by a red-filled connector, takes these lengths as inputs. This setup ensures that the phase region lengths are calculated by the working fluid part of the model and passed directly to the wall and secondary fluid parts as inputs. A similar connection scheme is applied in the condenser model.

The full VCC model, as depicted in Figure 7, consists of 18 dynamic states: 8 within the evaporator model and 10 within the condenser model, summarized in Table 2. The overall model requires six time-dependent input signals: valve opening ratio θ , compressor speed Ω , air inlet temperature $T_{a,in}$, air mass flow rate \dot{m}_a , glycol-water inlet temperature $T_{s,in}$, and glycol-water inlet mass flow rate $\dot{m}_{s,in}$. Additionally, a valve and pressure sink were added at the outlet of the glycol-water stream in the evaporator. The valve opening is controlled based on the inlet mass flow rate, determining the outlet mass flow rate through the linear relation

$$\dot{m}_{s,out} = \frac{P_s - P_{sink}}{P_{s,nom} - P_{sink}} \dot{m}_{s,in}. \quad (27)$$

This approach addresses numerical stability issues. In causal modelling, the glycol-water storage module in the evaporator requires the inlet and outlet mass flow rates as inputs. A simple strategy would be to set the outlet mass flow rate equal to the inlet value, which is a direct input to the overall VCC model. However, because the glycol-water pressure responds rapidly to mass flow rate differences, this would cause significant pressure spikes, leading to numerical instability. By defining the outlet mass flow rate based on the pressure difference between the glycol-water and the pressure sink (held constant), pressure spikes are mitigated, improving the model's numerical robustness.

Table 2: Dynamic states within the heat exchanger models.

Component	Dynamic States		
Evaporator	P_E	$L_{1,E}$	h_1
	$\bar{T}_{w,1,E}$	$\bar{T}_{w,2,E}$	P_s
	$h_{s,int}$	$h_{s,out}$	
Condenser	P_C	$L_{1,C}$	$L_{2,C}$
	h_3	$\bar{T}_{w,1,C}$	$\bar{T}_{w,2,C}$
	$\bar{T}_{w,3,C}$	$h_{a,out,1}$	$h_{a,out,2}$
	$h_{a,out,3}$		

Before verifying the VCC model through steady-state and transient simulations, a final modification to the working fluid submodel in the condenser must be discussed. In the desuperheating region, the working fluid is in a single phase, and the time derivative of the average enthalpy in this region is expressed as

$$\frac{d\bar{h}_{1,C}}{dt} = \frac{1}{2} \left(\frac{dh_2}{dt} + \left(\frac{\partial h_C^v}{\partial P} \right)_{sat} \frac{dP_C}{dt} \right). \quad (28)$$

From this it can be seen that the time derivative of the condenser inlet enthalpy, $\frac{dh_2}{dt}$, must be provided as an input to compute $\frac{dh_{1,C}}{dt}$. However, since the upstream compressor model lacks dynamic states, its outlet enthalpy derivative cannot be directly obtained from the model. Instead, it would have to be derived from the evaporator outlet enthalpy, which is a dynamic state, and any time-varying effects resulting from changes in the compressor speed input. Given that the compressor relies on compressor map tables for outlet enthalpy calculations, determining its time derivative is highly complex, and the current configuration of the model equations prevents Dymola from finding the relation between the compressor outlet enthalpy and the dynamic states of the system. It was therefore decided to modify the expression for the time derivative of the average enthalpy in the first zone of the condenser to

$$\frac{d\bar{h}_{1,C}}{dt} \approx \left(\frac{\partial h_C^v}{\partial P} \right)_{sat} \frac{dP_C}{dt}. \quad (29)$$

This adjustment assumes that changes in the average enthalpy within the desuperheating region depend solely on the condenser's pressure dynamics, excluding the influence of upstream transients. While this assumption has been applied in previous studies [53], it is important to note that it can lead to inaccuracies during rapid compressor speed changes or fast transients at the evaporator outlet.

3 Model Verification

With the model developed in the previous chapter, the next chapter focuses on verifying its predictions. This involves comparing the model's steady-state solution with experimental data obtained during the Inverse organic Rankine cycle Integrated System (IRIS) commissioning phase, as well as evaluating the dynamic trends that arise from variations in the model's input variables. Additionally, the chapter examines the integrity of the model by assessing its adherence to the principles of mass and energy conservation.

3.1 Steady-state

Finding a steady-state solution for the Vapour Compression Cycle (VCC) model equations involves setting all time derivatives to zero and solving for the dynamic states summarized in Table 2. However, with six system inputs that can be set arbitrarily, numerous solutions to this problem are possible, depending on the chosen boundary conditions. To verify the steady-state solution effectively, it is helpful to define these boundary conditions based on experimental steady-state data collected during the commissioning of the IRIS. This data, detailed in the dissertation of Ascione [13], provides a reference for evaluating whether the model produces steady-state conditions similar to those observed experimentally. Since the experimental data was

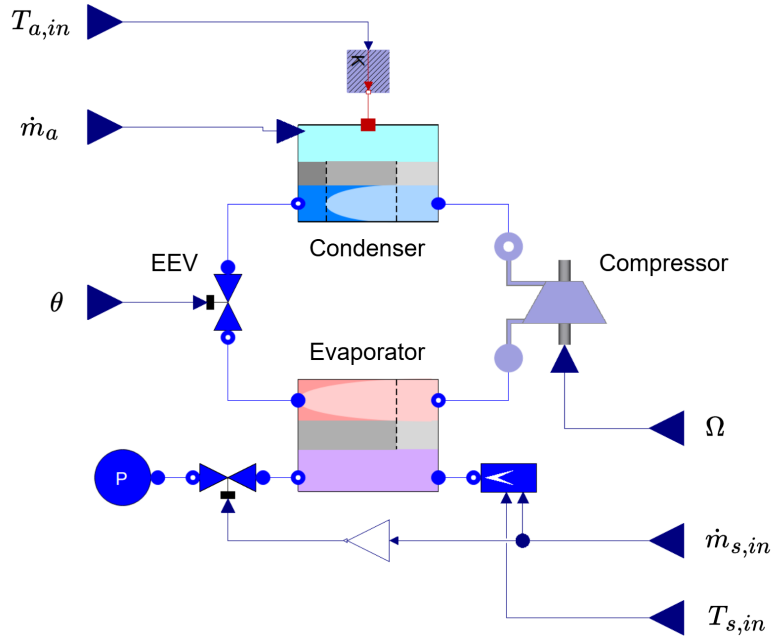


Figure 7: Complete refrigeration loop in Dymola.

obtained using the reciprocating compressor currently installed in the facility, perfect agreement with the model is not expected, but this approach still offers an initial indication of the model’s credibility.

In line with this methodology, an equivalent steady-state model of the complete system was implemented in MATLAB. For this, the equations presented in Chapter 2 were used with all time derivatives equal to zero. The goal is to find the steady-state values of all dynamic states of the model with the boundary conditions set to those of the IRIS during commissioning, listed in Table 3. To this end, the steady-state problem is formulated as a constrained optimization, with the objective of minimizing the difference between the cooling load of the real system during commissioning and the cooling load predicted by the model. Constraints are included to ensure energy conservation and that the lengths of the phase regions within the heat exchangers sum correctly to the total heat exchanger lengths. The outputs of the algorithm are the steady-state values of the dynamic states of the model, which can be used to initialize the dynamic simulation of the model.

Table 3: Boundary conditions of the IRIS during commissioning [13].

Property	Unit	Value
$T_{s,in}$	°C	40.8
P_s	bar	1.01
$\dot{m}_{s,in}$	$\frac{\text{kg}}{\text{s}}$	0.40
$T_{a,in}$	°C	38.0
P_a	bar	1.01
\dot{m}_a	$\frac{\text{kg}}{\text{s}}$	1.30

The results of the optimization problem are shown in Figure 8, with the corresponding model constants reported in Appendix B. The steady-state values of the dynamic states indicate the VCC system model is valid. Additionally, the temperatures and pressures within the heat exchangers are consistent with expectations, as the inlet and outlet temperatures closely match those observed during the facility’s commissioning. A comparison between the experimental data and the steady-state optimization results is provided in Table 4. While some quantitative differences

are apparent, the predicted values remain within a comparable range. Using the relative difference $\Sigma = \frac{|\text{Model}-\text{IRIS}|}{\text{IRIS}}$, all properties in the table show deviations within 12% of the experimental results. This level of agreement is particularly reasonable, given the substantial differences between the compressors in the model and the real setup, and the fact that piping and pressure drops in the heat exchangers were not modelled. To fully validate whether the steady-state predictions of the model align with the actual facility, experimental testing would be required. However, since the centrifugal compressor has not yet been installed in the rig, such validation lies beyond the scope of this work.

Table 4: Comparison between experimental steady-state of the IRIS [13] and model predictions.

Property	Unit	IRIS	Model	$\Sigma(\%)$
T_1	°C	24.4	21.8	0.87
T_2	°C	78.4	74.7	1.05
T_3	°C	56.8	56.3	0.15
T_4	°C	22.6	17.6	1.69
P_E	bar	1.12	0.99	11.7
P_C	bar	4.48	3.95	11.8
\dot{m}_f	$\frac{\text{kg}}{\text{s}}$	0.12	0.11	8.33
\dot{Q}_E	kW	17.9	16.8	6.15
COP	-	3.76	3.84	2.13

3.2 Transient Response

The transient verification of the dynamic model is evaluated through three simulation cases: a change in the Electronic Expansion Valve (EEV) opening percentage, a change in the compressor speed, and a change in the air mass flow rate at the condenser. Each simulation is initiated from the steady-state solution obtained in the previous section. The DASSL solver [54] is employed for all simulations, with a tolerance set at 1e-8 to ensure numerical precision. The primary objective of these simulations is to verify whether the transient responses of the system can be understood and explained based on physical reasoning.

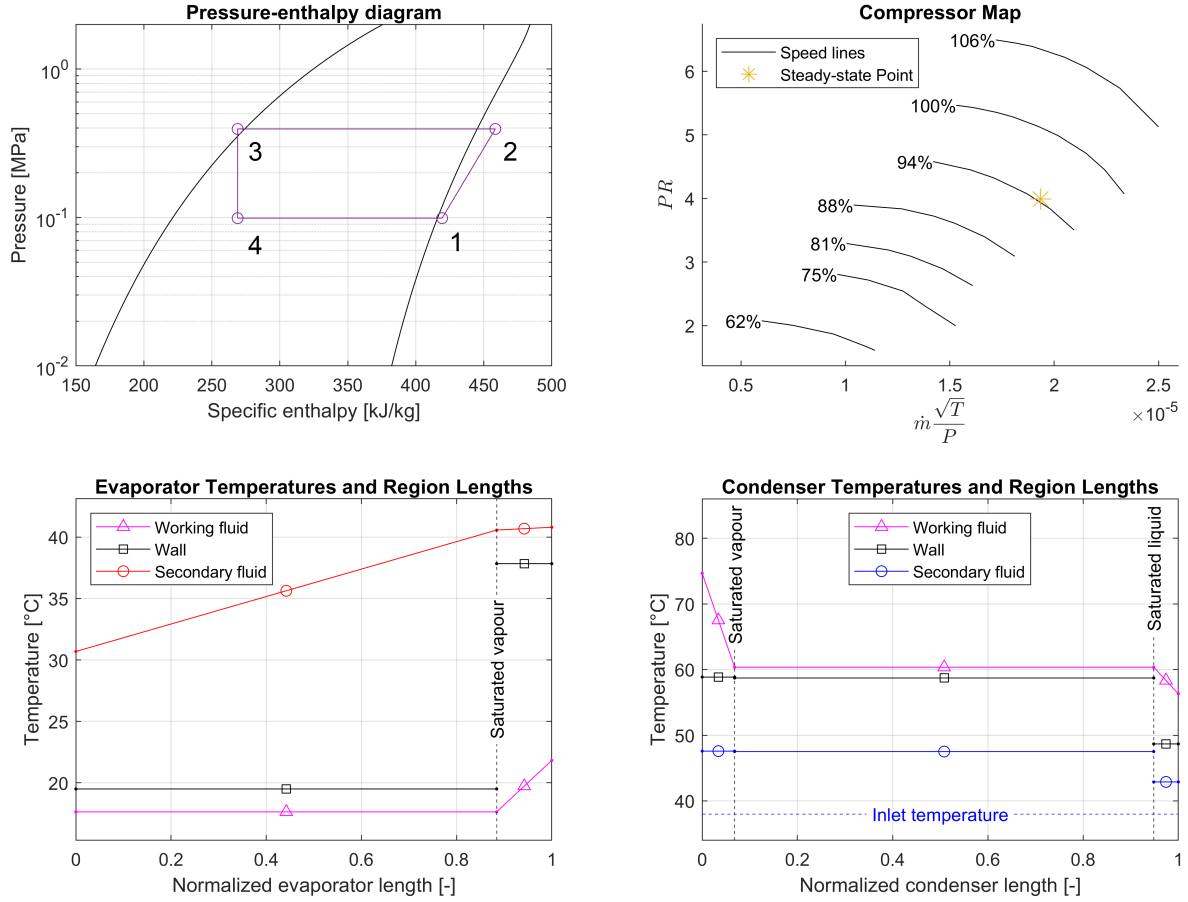


Figure 8: Steady-state solution of the VCC model corresponding to the boundary conditions given in Table 3.

3.2.1 Valve Opening

Starting from steady-state conditions, the first transient simulation investigates the effect of changes in the EEV opening. The valve is initially closed from $\theta_{init} = 30\%$ to $\theta_1 = 25\%$ over 30 seconds using a ramp function. After a delay of 40 seconds, the valve opening is ramped to $\theta_2 = 32\%$ over 30 seconds and held at this position for the remainder of the simulation.

As the EEV is typically used to control the degree of superheating, SH , at the outlet of the evaporator [55], the input signal and the resulting superheating are plotted together in Figure 9. As expected, closing the valve increases the degree of superheating, while opening it reduces it. This behaviour stems from changes in the mass flow rate through the valve: closing the valve reduces the mass flow rate, delivering less, low-temperature, refrigerant from the condenser to the evaporator. Consequently, the point of complete evaporation shifts upstream, leaving more evaporator length available for superheating. This leads to a higher degree of su-

perheating at the outlet. When the valve opens, the reverse occurs, and the degree of superheating decreases.

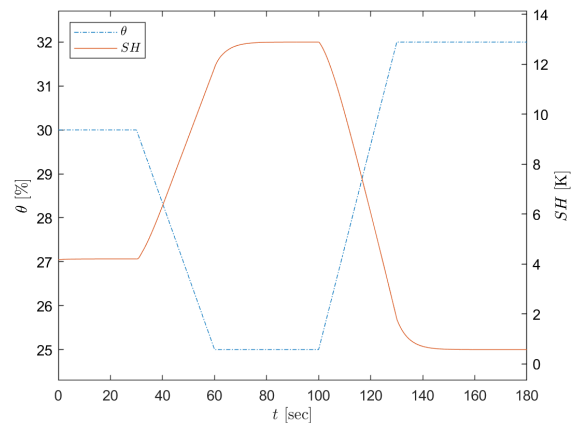


Figure 9: Transient plot of the expansion valve opening θ and the resulting degree of superheating SH .

It is important to note that when the degree of superheating drops to zero, the superheating region in the evaporator vanishes. This makes the Φ_E matrix in Equation 13 singular, preventing the evaporator equations from being solved and ultimately causing the model to crash. Although this singularity is a limitation of the dynamic model, it can serve as a safety indicator from a practical perspective. In standard operation, VCC systems are designed such that the refrigerant entering the compressor is always single-phase. This is crucial because liquid droplets can degrade compressor performance [56] and even damage internal components [57]. Thus, the singularity caused by the disappearance of the vapour region in the evaporator acts as an early warning that liquid refrigerant may enter the compressor, transforming a limitation of the model into a useful diagnostic tool.

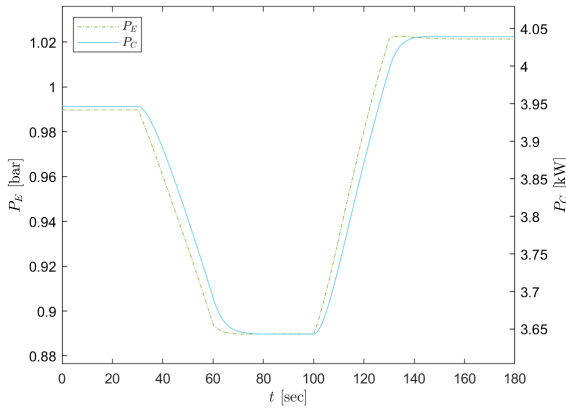


Figure 10: Transient response of evaporator and condenser pressures, P_E and P_C , to the valve opening θ shown in Figure 9.

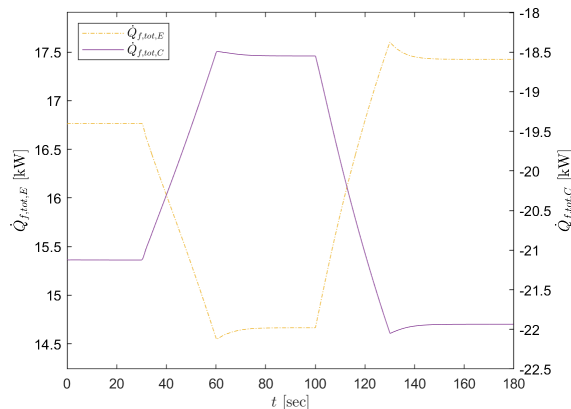


Figure 11: Transient response of refrigerant heat flows, $\dot{Q}_{f,tot,E}$ and $\dot{Q}_{f,tot,C}$, to the valve opening θ shown in Figure 9. Note that the condenser heat flow is negative, since energy is removed from the refrigerant.

Although the cause-effect relationship between valve opening and superheating is relatively straightforward, interpreting the response of other thermodynamic variables in full-cycle simulations is more complex due to the simultaneous occurrence of multiple dynamic effects. For example, closing the expansion valve influences the pressures and mass flow rates in both the condenser and evaporator, but the net effect is not immediately intuitive because two opposing mechanisms are at play:

- *Mass accumulation perspective:* A more restricted valve reduces the mass flow leaving the condenser, causing more refrigerant to accumulate and increasing the condenser pressure. Conversely, less refrigerant enters the evaporator, leading to a pressure drop. This aligns with a simple volume-pressure analogy: pumping air into a tire increases pressure, while releasing air decreases it.
- *Heat transfer perspective:* Closing the valve reduces refrigerant flow through the evaporator, altering the phase distribution. As the two-phase region shrinks and the single-phase region grows, the heat transfer coefficient drops significantly, reducing the overall heat addition to the cycle. This lowers the energy input, which in turn reduces both evaporator and condenser pressures.

The simulation results in Figure 10 show that while the evaporator pressure initially drops and the condenser pressure briefly rises, both eventually follow a downward trend. At the same time, heat transfer in the cycle decreases in magnitude (Figure 11). This suggests that the reduction in heat flow, rather than mass accumulation effects, dominates the overall pressure response.

This example highlights the intricate interrelations between multiple causes and effects, underscoring the value of the dynamic model in enhancing the understanding of system behaviour.

3.2.2 Compressor Speed

The second transient verification involves ramping the compressor speed from $\Omega_{init} = 74.8$ kRPM to $\Omega_1 = 82.8$ kRPM over 15 seconds. In Figure 12 this signal is shown, where Ω is normalized to allow for easier comparison with the corrected compressor speed, N_T (given in (24)). The normalized compressor speed, Ω_{nor} , is given by

$$\Omega_{nor}(t) = \sqrt{\frac{T_{ref}}{T_{1,init}} \frac{\Omega(t)}{\Omega_{ref}}}. \quad (30)$$

The plot reveals that as the compressor speed, Ω_{nor} , increases, the compressor inlet tempera-

ture, T_1 , also rises. This can be attributed to the higher mass flow rate, which extracts more refrigerant from the evaporator. The increased mass flow rate reduces the size of the two-phase region in the evaporator, leaving more of its length available for the single-phase superheating region. Unlike the two-phase region, where the temperature remains constant, the temperature of the single-phase vapour rises as heat is supplied, leading to an increase in the outlet temperature. Additionally, the higher mass flow rate enhances heat transfer, further elevating the outlet temperature.

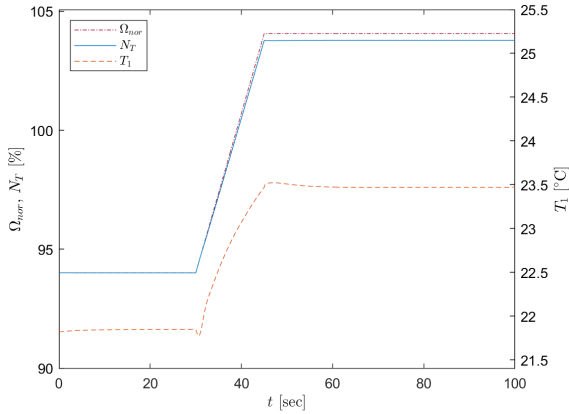


Figure 12: Normalized compressor speed input Ω_{nor} with corresponding transients of the corrected speed N_T and compressor inlet temperature T_1 .

The rise in compressor inlet temperature leads to a slight decrease in the corrected speed, N_T , which reflects the physical effect of reduced refrigerant density at higher temperatures. A lower density reduces the mass flow rate and pressure ratio achievable at a given compressor speed. The correction method captures this behaviour by adjusting the effective speed used to interpolate the compressor maps. This ensures that the pressure ratio and mass flow rate align with the physical principles governing the system, demonstrating that the model provides results consistent with these expectations.

In Figure 13, the compressor map displays the transient trajectory resulting from the compressor ramp up, along with the surge and choke lines, which are necessary for applying the β -line method. A conservative approach was taken when defining these lines to ensure the compressor remains well within its operating range at all times. The trajectory, marked by a triangle at the start and a cross at the end, shows that as the compressor speed increases, the corrected mass flow rate rises. However, the pressure ratio does not rise as fast, resulting in the operating point

to move closer to the choke line, eventually settling near this limit. Similar to the disappearance of the superheating region discussed in Section 3.2.1, β -values exceeding the surge or choke lines violate the assumptions of the compressor model, leading to a crash if these thresholds are crossed. Since modelling surge and choke dynamics is not a primary objective of this work, this limitation is acceptable.

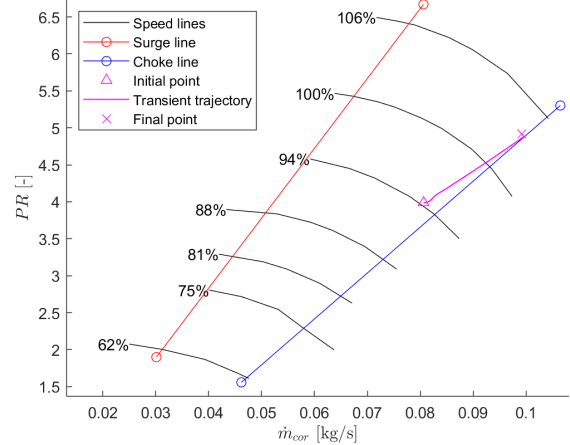


Figure 13: Corrected compressor map with surge and choke lines and the transient trajectory resulting from the compressor ramp up in Figure 12.

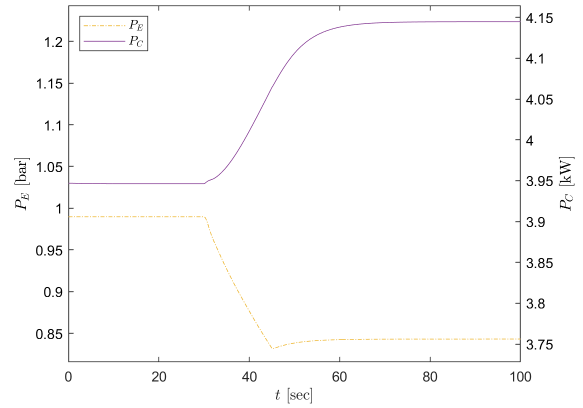


Figure 14: Transient response of evaporator and condenser pressures, P_E and P_C respectively, as a result of the compressor ramp up in Figure 12.

The compressor's tendency to reach choking conditions during the ramp-up is explained by the pressure plots in Figure 14. These plots reveal that the pressures in the heat exchangers, particularly the condenser, respond relatively slowly to the increase in compressor speed. As a result, the pressure ratio does not adjust quickly enough to accommodate the ramp-up, causing the operating point to approach the choke line. This slow pressure response is physically intuitive, as

the large volumes and two-phase dynamics of the heat exchangers dampen the effects of rapid mass flow changes.

3.2.3 Air Mass Flow Rate

In the final verification simulation, the air mass flow rate is varied. Practically, this corresponds to adjusting the speed of the variable-speed fan in the cooling loop. In the simulation, the mass flow rate is increased from an initial value of $\dot{m}_{a,init} = 1.13$ kg/s to $\dot{m}_{a,1} = 1.43$ kg/s over a period of 30 seconds. After being held constant for 40 seconds, it is then reduced to $\dot{m}_{a,2} = 0.93$ kg/s over another 30 seconds.

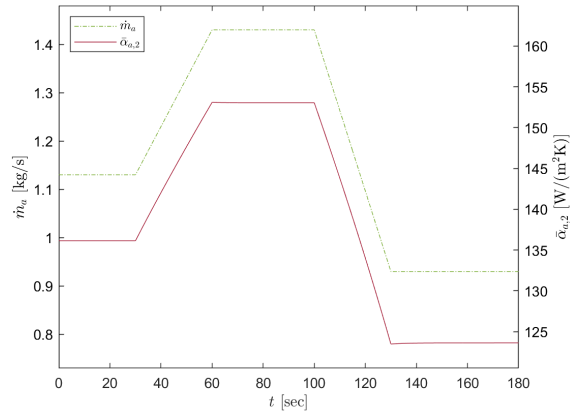


Figure 15: Input signal for the air mass flow rate \dot{m}_a and corresponding average convective heat transfer coefficient on the air side in the two-phase region of the condenser, $\bar{\alpha}_{a,2}$.

Increasing the air mass flow rate directly enhances the heat transfer coefficient. This occurs because the higher flow rate increases air velocity through the condenser fins, promoting turbulence and thereby improving heat transfer. This behaviour is evident in Figure 15, where the heat transfer coefficient rises during the increase in air mass flow rate and falls when the flow rate decreases. Figure 16 and 17 further illustrate that improved heat transfer on the air side leads to a drop in the wall temperature, which, in turn, causes a reduction in condensation temperature. The lower condensation temperature, which is directly related to the refrigerant pressure, reflects greater energy removal from the refrigerant, which reduces overall pressure levels. As the wall temperature and pressure decrease, the temperature difference between the two-phase wall section and refrigerant becomes smaller, diminishing the heat transfer rate.

In Figure 17 the transient behaviour of the air-side heat transfer rate in the two-phase region exhibits non-minimum phase dynamics. Initially, an increase in heat transfer occurs due

to the higher mass flow rate. However, as the wall temperature drops, the temperature difference between the wall and air decreases, eventually counteracting the effect of the increased heat transfer coefficient. This non-minimum phase effect is particularly pronounced during the second phase of the simulation, where the air mass flow rate is changed at a faster rate.

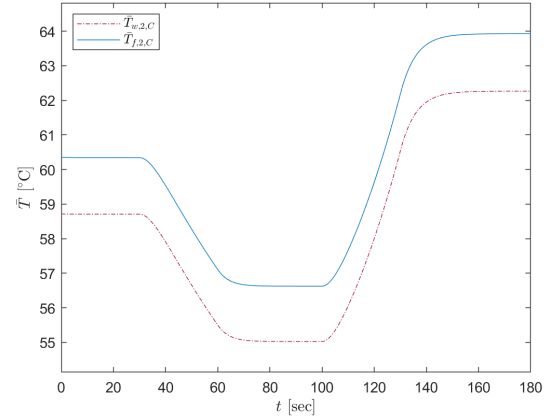


Figure 16: Transient response of the average wall temperature, $\bar{T}_{w,2,C}$, and refrigerant temperature, $\bar{T}_{f,2,C}$, of the two-phase region of the condenser, as a result of the air mass flow rate variation shown in Figure 15.

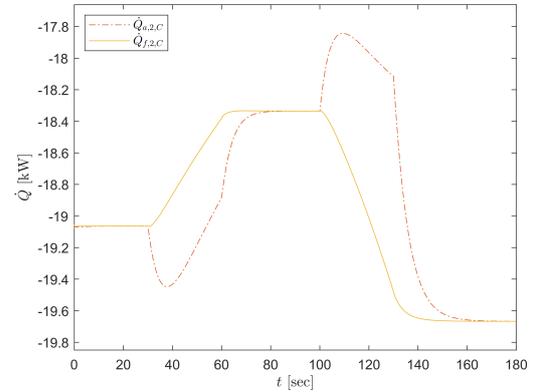


Figure 17: Heat flow rates from the refrigerant, $\dot{Q}_{f,2,C}$, and to the air, $\dot{Q}_{a,2,C}$ in the two-phase region of the condenser, as a result of the air mass flow rate signal in Figure 15.

The discontinuities observed in the air-side heat transfer trend arise from the algebraic dependency of the heat transfer coefficient on the mass flow rate. Since the mass flow rate varies discontinuously as a ramp signal, the resulting heat transfer coefficients on the air side (see Figure 15) also exhibit discontinuities. For instance, at $t = 60$ seconds, when the slope of the heat transfer coefficient abruptly levels off due to the ramp signal, the opposing effects of the de-

ing wall temperature and pressure in the condenser become more pronounced. This causes an immediate change in the slope of the air-side heat flow, with the absolute value decreasing more rapidly as the balance between these competing effects shifts.

The observed variations in heat transfer coefficient, wall and refrigerant temperature, and heat flow rates can be reasonably attributed to changes in air mass flow rate, with trends that align with physical expectations. However, as noted in the EEV response analysis in Section 3.2.1, interpreting these results is challenging due to the interplay of multiple simultaneous effects. Regardless, the overall behaviour observed in this simulation adds confidence in the capability of the model to correctly capture the system dynamics.

3.3 Model Integrity

As a final step, the integrity of the model can be assessed by verifying the conservation of mass and energy throughout the simulations. This involves evaluating whether conservation laws in the heat exchangers are fulfilled during the simulation. In each heat exchanger, the total mass and energy are computed by summing the contributions from individual control volumes. For example, for the evaporator, these summations are given by

$$\begin{aligned} M_E &= \sum_{i=1}^2 A_{c,E} L_{i,E} \bar{\rho}_{i,E} \\ E_E &= \sum_{i=1}^2 L_{i,E} \left(A_{c,E} \overline{(\rho h)}_{i,E} \right. \\ &\quad \left. + \rho_{w,E} c_{w,E} A_{w,E} \bar{T}_{w,i,E} \right). \end{aligned} \quad (31)$$

Here, M_E and E_E represent the mass and energy in the evaporator, respectively. It can be seen that the mass in the evaporator is computed from the volume, i.e. the product of cross-sectional area A_c and length L , and average refrigerant density $\bar{\rho}$ in the control volume. Similarly, the energy follows from the product of refrigerant density and specific enthalpy $\overline{(\rho h)}$. Additionally, the energy contained in the wall is determined from the wall volume, i.e. the product of length and wall cross-sectional area A_w , wall density ρ_w , wall specific heat capacity c_w , and average wall temperature \bar{T}_w . The total mass M and energy E in the system are obtained from combining the contributions of both heat exchangers: $M = M_E + M_C$ and $E = E_E + E_C$. It is worth noting that only the energy of the refrigerant and wall is considered, excluding the energy of secondary fluids.

To verify model integrity throughout dynamic simulation, two variables are introduced:

$$\begin{aligned} \Delta M &= M - M_{init} \\ \Delta E &= E - \left(\int (\dot{Q}_{in} + \dot{W}_c + \dot{Q}_{out}) dt + E_{init} \right). \end{aligned} \quad (32)$$

The heat flows \dot{Q}_{in} and \dot{Q}_{out} represent the heat transferred from the glycol-water to the evaporator wall and from the condenser wall to the air, respectively, while \dot{W}_c denotes the compressor work and M_{init} and E_{init} are the initial mass and energy contained in the system at the start of the simulation. The variable ΔM represents the deviation in total refrigerant mass relative to the initial value, while ΔE quantifies the difference between the change in system energy (calculated using integral equations, as defined in Equation 31) and the added thermal energy and work to the system. Ideally, these variables should remain zero throughout the simulation to satisfy conservation principles. However, due to simplifying assumptions and numerical approximations, small deviations are expected.

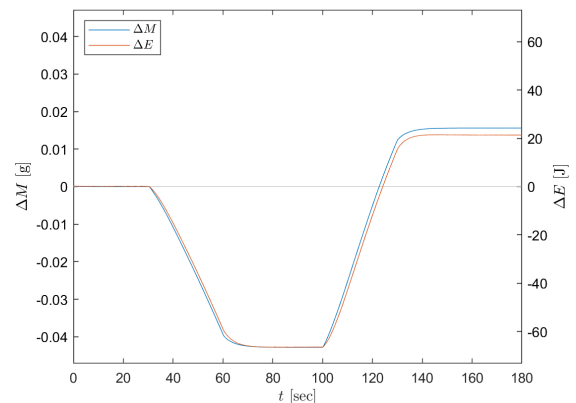


Figure 18: Integrity check for the EEV opening simulation from Section 3.2.1.

As an example, Figure 18 presents the integrity check for the EEV opening simulation from Section 3.2.1. Initially, during steady-state conditions, both ΔM and ΔE are zero, confirming conservation. However, deviations arise when the system dynamics respond to the valve adjustment. These deviations are likely caused by certain assumptions, such as the constant average void fraction in the heat exchangers, which neglects some density dynamics and directly impacts mass changes. Additionally, modifications to the enthalpy derivative in the condenser's desuperheating zone, as discussed in Section 2.3, may also contribute to the deviations.

Fortunately, the maximum deviations in mass and energy are negligible compared to the system's initial values of 183 grams and 2.85 MJ,

respectively. Defining relative errors as $\epsilon_M = \frac{\max(|\Delta M|)}{M_{init}}$ and $\epsilon_E = \frac{\max(|\Delta E|)}{E_{init}}$, Table 5 shows that the deviations remain within 0.3 % across all verification simulations. This demonstrates that the model sufficiently respects conservation principles. However, since these simulations are relatively short, the cumulative effects of deviations over extended periods remain partially hidden. Therefore, care should be taken when performing long-duration simulations, and the integrity of the model should always be verified in such cases.

Table 5: Integrity check of the transient simulation in Section 3.2, with the simulations represented by their respective input symbols (θ , Ω , and \dot{m}_a). Only the maximum relative errors for mass (ϵ_M) and energy (ϵ_E) deviations are shown, each taken from the simulation in which it is largest.

		Units	Mass	Energy
Initial		[kg, MJ]	0.183	2.85
$\max(\Delta M)$ $\max(\Delta E)$	θ	[mg, J]	42.8	66.6
	Ω	[mg,J]	46.5	29.8
	\dot{m}_a	[mg,J]	11.2	63.9
Max ϵ_M and ϵ_E		[%]	0.254	0.0234

4 Control

In this chapter, the design of a control system for the Inverse organic Rankine cycle Integrated System (IRIS) is presented. The chapter begins with formalizing the control problem, defining the plant, with control inputs and outputs. The non-linear Modelica model is then linearized around the steady-state initialization point (outlined in Section 3.1). Based on this linearized model, a decentralized controller is constructed, where three independent control loops are tuned using established linear techniques. Lastly, the chapter presents the results of the closed-loop performance of the decentralized control strategy.

4.1 Problem Formulation

The ultimate goal of the IRIS experiments is to determine the performance maps of the compressor being tested. This can be achieved by setting an operating environment similar to that in the stand-alone compressor test described in Section 2.2.2, where the compressor speed is set to

specific values, the inlet conditions are held constant, and the outlet pressure is varied in a controlled way. However, the implementation of such a control system presents challenges due to the inherent coupling between the compressor inlet and outlet conditions. Disturbances at the outlet propagate through the loop, influencing the inlet, and making it difficult to maintain consistent operating conditions. This coupling and the need to approach surge and choke limits for map construction, where nonlinearities dominate, make manual operation impractical. Therefore, an active control strategy is required to regulate the compressor operating conditions across the desired range, preventing the compressor from entering surge or choke.

From a control engineering perspective, it is crucial to abstract the dynamic model developed in Section 2 into a plant with control inputs and outputs. As shown in the Dymola model in Figure 7, six variables must be provided as model inputs. However, not all of these inputs are equally practical or effective for control purposes. In addition, selecting appropriate outputs is a non-trivial task due to the large number of states and internal variables in the model. To address this, the following section will discuss how to carefully select the inputs and outputs to ensure effective regulation of the system.

4.1.1 Input/Output Selection

To select the outputs of the plant, the computational steps from the compressor model in Section 2.2.2 are recalled, where the operational conditions of the compressor are represented by the instantaneous point on the compressor map. The operating point in the map is determined by the pressure ratio PR and corrected speed N_T , which depends on the actual compressor speed Ω and the compressor inlet temperature T_1 . Therefore, the position on the map is uniquely defined by four variables: the pressures P_E and P_C , the inlet temperature T_1 , and the compressor speed Ω . The first three of these variables are thermodynamic properties that can be measured directly from the physical system, making them suitable candidates for feedback control. In contrast, the compressor speed is a model input variable, which makes it intuitive to use as a control input. However, in typical compressor testing procedures, the compressor speed is set at constant values for each individual speed line, making it impractical for continuously regulating an output. Therefore, the compressor speed is not treated as a control input, but rather as a non-controlled input, unavailable for regulation by the control system. In this approach, during testing, the compressor

speed can be set at an arbitrary value and the control system is tasked with adjusting the other three parameters (P_C , P_E , and T_1) to reach the desired operating conditions at the given compressor speed.

For proper control system design, it is generally recommended that the number of inputs matches or exceeds the number of outputs to be controlled [58]. Consequently, three control inputs are used, resulting in a Multiple Input Multiple Output (MIMO) plant.

The Electronic Expansion Valve (EEV) opening θ is a natural choice for the first control input, since it is the only model input, aside from the compressor speed, that directly influences the internal conditions of the Vapour Compression Cycle (VCC). As such, it is expected to have a significant effect on the outputs P_E , P_C , and T_1 . This expectation is further supported by the fact that the EEV is conventionally used to control the degree of superheat at the evaporator outlet [55], which parallels controlling the outlet temperature T_1 for a given pressure P_E .

The remaining two control inputs must be chosen from the secondary fluid variables at the heat exchangers. These variables depend on the dynamics of the heating and cooling loops of the IRIS and cannot be directly controlled. Instead, external controllers regulate the operation of these loops to achieve the desired conditions at the heat exchanger inlets, introducing additional dynamics and time delays. However, for the scope of this work, it is assumed that the secondary fluid variables can be set instantly, allowing them to be treated as direct control inputs. Under this assumption, the selection of the remaining inputs follows from the following physical reasoning.

Since the refrigerant pressures of both heat exchangers, i.e. P_C and P_E , must be controlled, it is sensible to include one input at each heat exchanger. As discussed in Section 1.1.1, the glycol-water mass flow rate $\dot{m}_{s,in}$ is maintained by a constant-speed pump, which ensures a fixed volumetric flow rate. As a result, the mass flow rate cannot be varied significantly, making it unsuitable for control. However, the glycol-water inlet temperature, regulated by a three-way mixing valve, can be adjusted rapidly, making it a suitable control input. Therefore, $T_{s,in}$ is selected as the second control input.

On the air side, the inlet temperature is controlled by a heater upstream of the condenser, while the air mass flow rate is regulated by a variable-speed fan. Since the mass flow rate responds more quickly to changes in fan speed than the temperature does to changes in heat input,

\dot{m}_a is chosen as the third control input. The choices for the control inputs and outputs are illustrated in Figure 19, where the VCC plant is represented as a 3×3 nonlinear Multiple Input Multiple Output (MIMO) system. The control inputs θ , \dot{m}_a , and $T_{s,in}$ are combined to form input vector u . Similarly, the outputs P_E , P_C , and T_1 are represented by vector y . The input variables of the Dymola model that are not used as control inputs, Ω , $\dot{m}_{s,in}$, and $T_{a,in}$ are indicated with vector d .

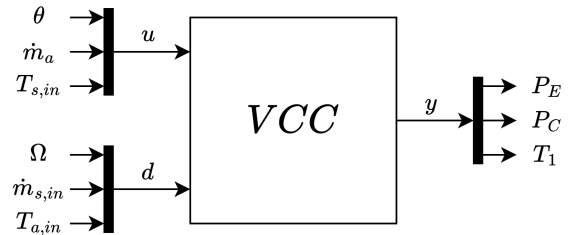


Figure 19: Nonlinear MIMO plant representing the VCC system. The inputs, outputs, and non-controlled inputs are respectively combined in the u , y , and d vectors.

4.2 Linearization

Since the VCC model is nonlinear, analysing its dynamic behaviour is most straightforward when linearizing around a steady-state point. This approach enables the application of well-established linear systems theory and provides access to a wide range of control system design methods. The dynamics of the deviations near the steady-state point can be expressed in the general state-space form as

$$\begin{aligned} \delta \dot{x} &= \tilde{A} \delta x + \tilde{B} \delta u + \tilde{B}_d \delta d \\ \delta y &= \tilde{C} \delta x + \tilde{D} \delta u + \tilde{D}_d \delta d. \end{aligned} \quad (33)$$

Here, δ denotes deviations from the steady-state, while the state-space matrices \tilde{A} , \tilde{B} , \tilde{B}_d , \tilde{C} , \tilde{D} , and \tilde{D}_d correspond to the first-order derivatives (Jacobian matrices) of the nonlinear system with respect to the states, inputs, and non-controlled inputs, evaluated at steady-state. Before the nonlinear model can be approximated in this linear structure, some adjustments are necessary to address the explicit appearance of input derivatives.

4.2.1 Input Derivatives

The dynamics of the VCC plant, depicted in Figure 19, can be expressed as

$$\dot{x} = F(x, u, d, \dot{u}, \dot{d}). \quad (34)$$

This equation explicitly defines the time derivatives of the dynamic states \dot{x} as a function of the states x , inputs u , non-controlled inputs d ,

and the time derivatives of the inputs \dot{u} and non-controlled inputs \dot{d} . The inclusion of input time derivatives arises because the time derivatives of the inlet temperatures of air, $\frac{dT_{a,in}}{dt}$, and glycol-water, $\frac{dT_{s,in}}{dt}$, are needed to calculate the enthalpy change in the initial control volumes of the secondary fluid flows within the heat exchangers. Consequently, the system dynamics cannot be directly transformed into the linear form presented in (33), as that formulation does not account for time derivatives of inputs. To address this issue, two solutions are proposed:

- *Neglecting input transients.* As in Section 2.3, upstream transient effects are omitted from the enthalpy derivative equation in the first control volume of the secondary fluid. If the inlet temperature variations are small, this simplification has little impact on model accuracy.
- *Adding first-order low-pass filters between the temperature signals and model inputs.* The filter adds a dynamic state to the system, defining the time derivative of the input as a function of this state. A small filter time constant allows the filtered temperature to closely track the input, capturing rapid changes like step variations effectively.

To maintain simplicity, the first solution was chosen for the air inlet temperature $T_{a,in}$, as it is expected to remain relatively steady during testing in the physical setup. For the glycol-water inlet temperature $T_{s,in}$, the second solution was selected, since this temperature is a controlled input and its temporal variation is therefore expected to be significant. A filter time constant of $\tau_f = 10^{-5}$ seconds was applied, resulting in an augmented model with one additional state, bringing the total number of states to 19.

With the adjustments to the inlet temperature inputs, the state-space matrices in (33) can be calculated. The built-in linearization feature in Dymola was employed for this purpose. The software first simulates the system up to a predefined time point and then computes the Jacobian matrices with respect to the states, inputs, and outputs.

4.2.2 Scaling

The final step in the linearization process involves scaling the state-space matrices. This step is necessary because the variables have units that differ by several orders of magnitude, which can lead to numerical issues and control challenges [58]. For instance, as shown in the steady-state

solution in Section 3.1, the evaporator outlet temperature is $T_{1,ss} = 295$ K, while the condenser pressure is $P_{C,ss} = 3.95 \cdot 10^5$ Pa, differing by three orders of magnitude. To address these differences and bring the variables to a comparable scale, scaling expressions are applied [58] given by

$$\begin{aligned} x &= \frac{\delta x}{\delta x_{max}} & u &= \frac{\delta u}{\delta u_{max}} \\ y &= \frac{\delta y}{\delta y_{max}} & d &= \frac{\delta d}{\delta d_{max}}, \end{aligned} \quad (35)$$

Here, x , u , y , and d represent the scaled deviation variables, with the δ notation omitted to improve readability. The subscript $_{max}$ denotes the maximum expected deviation from the steady-state nominal conditions. In most cases, the maximum positive and negative deviations, indicated by the superscripts $^+$ and $^-$, are not symmetric. As a result, the worst-case scenario is used, leading to

$$\begin{aligned} \delta x_{max} &= \min(|x^+ - x_{ss}|, |x^- - x_{ss}|) \\ \delta u_{max} &= \min(|u^+ - u_{ss}|, |u^- - u_{ss}|) \\ \delta y_{max} &= \min(|y^+ - y_{ss}|, |y^- - y_{ss}|) \\ \delta d_{max} &= \max(|d^+ - d_{ss}|, |d^- - d_{ss}|). \end{aligned} \quad (36)$$

For instance, for the glycol-water inlet temperature, the upper and lower limits are set to 55 °C and 35 °C, respectively. This results in $\delta(T_{s,in})_{max} = \min(|55 - 40.8|, |35 - 40.8|) = \min(14.2, 5.8) = 5.8$ K. The scaling of the inputs, outputs, and non-controlled inputs can then be represented as a multiplication with diagonal scaling matrices Z :

$$u = Z_u^{-1} \delta u \quad y = Z_y^{-1} \delta y \quad d = Z_d^{-1} \delta d. \quad (37)$$

The scaling matrices have the maximum deviations placed along their diagonal. For example, for the inputs, the scaling matrix is expressed as $Z_u = \text{diag}[\delta(\dot{m}_a)_{max}, \delta(\theta)_{max}, \delta(T_{s,in})_{max}]$. By incorporating these matrices into the linear system described in (33), the state-space matrices are scaled accordingly by

$$\begin{aligned} A &= Z_x^{-1} \tilde{A} Z_x & B &= Z_x^{-1} \tilde{B} Z_u \\ B_d &= Z_x^{-1} \tilde{B}_d Z_d & C &= Z_y^{-1} \tilde{C} Z_x \\ D &= Z_y^{-1} \tilde{D} Z_u & D_d &= Z_y^{-1} \tilde{D}_d Z_d, \end{aligned} \quad (38)$$

and the final linear system can then be formulated in the familiar Linear Time Invariant (LTI) form as

$$\begin{aligned} \dot{x} &= Ax + Bu + B_d d \\ y &= Cx + Du + D_d d. \end{aligned} \quad (39)$$

As previously mentioned, x , u , y , and d represent the scaled deviations from the steady-state nominal conditions around which the linearization was carried out.

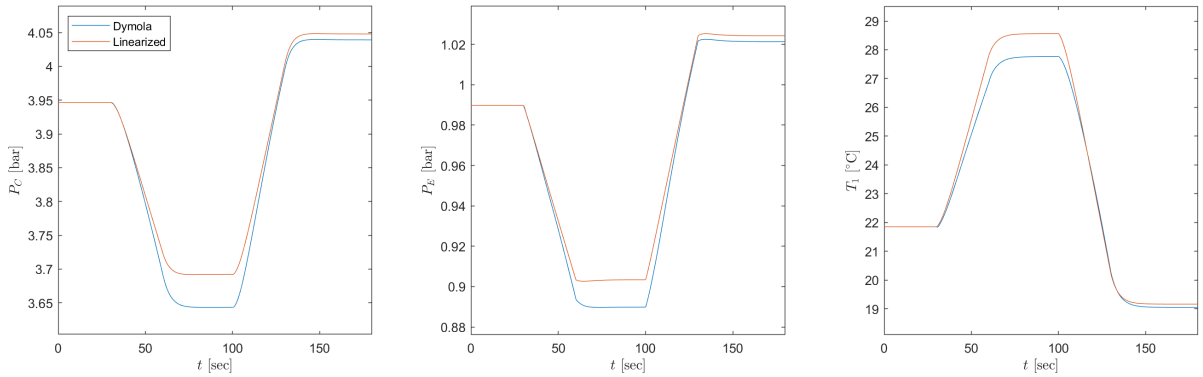


Figure 20: Comparison between the outputs of the linearized model and the full nonlinear model. The input signal of the EEV opening verification in Section 3.2.1 is used.

4.2.3 Comparison with Dymola

To verify that the linearized model aligns with the full nonlinear Dymola model, the linearized system is implemented in Simulink. The model is then integrated over time for a given input signal, and the corresponding outputs are computed. These outputs are subsequently unscaled and added to the steady-state values from the linearization point to obtain the final output transients. As an example, the outputs from the linear model are compared with those from the Dymola model for the input signal used in the EEV opening verification (see Section 3.2.1). In Figure 20, the outputs from both models are plotted. The overall trends and response times of the linearized model are in reasonable agreement with those of the Dymola model. However, the steady-state predictions from the linearized model do not align with the nonlinear model, in this case leading to an absolute error of up to $\sim 16.7\%$ for the condenser pressure deviation from the initial steady-state. These discrepancies suggests significant nonlinearities in the system, limiting the effectiveness of the linearized model for steady-state predictions. Despite these errors, the ability of the linearized model to predict transients accurately makes it suitable for analysing system characteristics during the initial controller design phase.

4.3 Decentralized Control

Building on the linearized model derived in the previous section, the system's characteristics are analysed to evaluate its potential for achieving desirable control performance. As detailed in the following sections, various tools from linear control theory are employed, leading to the selection of a decentralized control strategy. Within this framework, three independent controllers are designed and tuned, and the closed-

loop behaviour of the complete linear MIMO system is subsequently analysed.

4.3.1 Relative Gain Array

To evaluate the feasibility of diagonal control, the Relative Gain Array (RGA) is employed [59]. The RGA is a matrix that quantifies the relative interaction between control input-output pairs in a system. For an ideally diagonal and decoupled system, the RGA equals the identity matrix, implying that independent Single Input Single Output (SISO) controllers are sufficient for each input-output pair, with no additional interactions between the control loops. Deviations from the identity matrix, however, indicate coupling between control loops, which may limit the performance of diagonal control strategies. As such, the RGA of the linearized VCC system serves as a metric for assessing the suitability of these approaches.

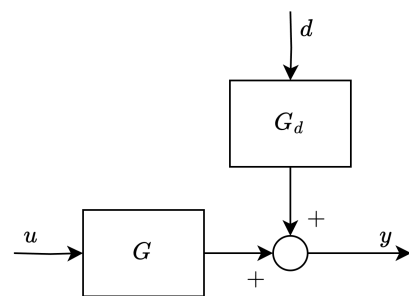


Figure 21: Linear system represented by transfer functions $G(s)$ and $G_d(s)$.

To compute the RGA, the linear system defined in (39) is transformed into the frequency domain using the Laplace transform. This yields

$$y(s) = G(s)u(s) + G_d(s)d(s), \quad (40)$$

where $G(s) = C(sI - A)^{-1}B + D$ represents the input-to-output dynamics of the system, while

$G_d(s) = C(sI - A)^{-1}B_d + D_d$ accounts for the effect of non-controlled inputs. A graphical representation of these transfer functions is provided in Figure 21 for clarity.

Given the transfer function G between the inputs and outputs, the RGA is computed as

$$\Lambda(G) = G \odot (G^{-1})^T, \quad (41)$$

where \odot denotes element-by-element multiplication, also known as the Schur product. Since G depends on the Laplace transform variable s , the RGA is expressed as a function of the complex frequency s . Using the model constants described in Appendix B, the RGA of the linearized VCC system at steady-state is given by

$$\Lambda(G|_{s=0}) = \begin{matrix} \dot{m}_a & \theta & T_{s,in} \\ \begin{bmatrix} 1.78 & -0.58 & -0.19 \\ -0.74 & 1.02 & 0.72 \\ -0.04 & 0.56 & 0.47 \end{bmatrix} & \begin{matrix} P_C \\ P_E \\ T_1 \end{matrix} \end{matrix} \cdot (42)$$

In this matrix, the inputs are displayed above the columns, while the outputs are indicated alongside the rows. Several observations can be made from the computed RGA values.

First, the absolute values of the elements are not excessively large, suggesting that control challenges associated with input uncertainty, such as those arising from neglected actuator dynamics, are unlikely to be critical. Additionally, there are no negative values on the diagonal, which is favourable for stability. Negative diagonal couplings in the RGA can lead to instability when controllers with integral action are employed [58].

Further examining the RGA elements reveals that the interactions between input-outputs pairs align with intuition. For instance, the air mass flow rate \dot{m}_a has the most significant effect on

the condenser pressure P_C . This is logical because the air mass flow rate directly influences the condenser conditions, thereby affecting the working fluid pressure. Similarly, the valve input θ exerts a notable influence on P_C as well, since the valve is positioned directly downstream of the condenser. Finally, the interaction between the glycol-water inlet temperature $T_{s,in}$ and P_C has the smallest absolute value, which makes sense because its influence originates further away from the condenser, resulting in a less direct effect compared to the other inputs.

Despite the interactions indicated by the input-output pairings in the RGA from (42), pursuing a decentralized control approach remains a justified choice. Developing such a control structure offers the following key advantage:

- Diagonal controllers can be designed and tuned relatively quickly using straightforward methods such as Proportional Integral (PI) control and loop shaping.

For this reason, the development of an initial diagonal controller with a PI approach is detailed in the following section.

4.3.2 PI Control and Loop Shaping

With the input-output pairs shown in (42), three independent control loops are established. For each loop, Proportional Integral (PI) controllers are implemented, forming the feedback structure illustrated in Figure 22, where K represents the complete controller. Each diagonal control element, PI_i , is defined as

$$PI_i(s) = K_{P,i} \left(1 + \frac{1}{\tau_{I,i} \cdot s} \right), \quad (43)$$

where $K_{P,i}$ and $\tau_{I,i}$ represent the proportional gain and integral time constant, respectively.

To tune the individual PI controllers, a SISO loop shaping method is applied. The Bode plot

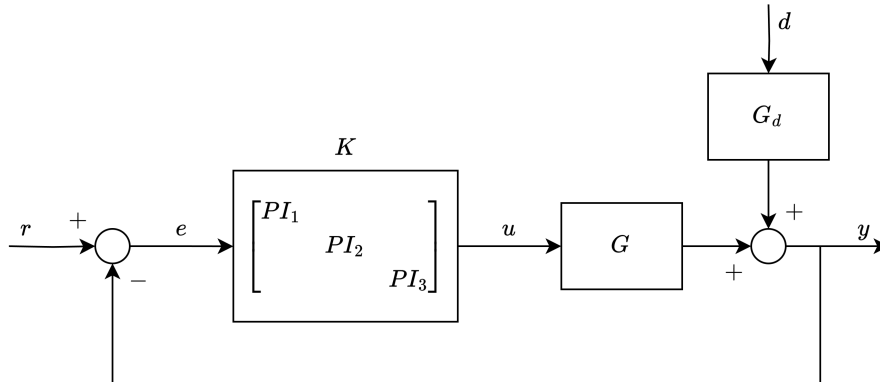


Figure 22: Feedback control for the linearized system using a decentralized PI controller.

of the open loop transfer function $L = GK$ is adjusted to achieve desirable low-frequency performance, adequate high-frequency roll-off, and appropriate gain and phase margins at the cross-over frequency. Further details on the loop shaping method are provided in Appendix C. The resulting controller gains are summarized in Table 6.

Table 6: Controller gains resulting from SISO loop shaping for each individual control loop.

Control loop		K_I	τ_I
\dot{m}_a	$\leftrightarrow P_C$	-10	10
θ	$\leftrightarrow P_E$	0.08	0.1
$T_{s,in}$	$\leftrightarrow T_1$	9	10

4.3.3 Closed-loop Analysis

To evaluate the performance of the decentralized controller, a MIMO closed-loop analysis is necessary. This is because the SISO loop shaping method described in Section 4.3.2 does not consider the interactions between control loops, which can degrade performance when all loops operate simultaneously. For the MIMO analysis, the singular values of the closed-loop sensitivity and complementary sensitivity functions, S and T , are examined across a range of frequencies. These transfer functions are defined as

$$\begin{aligned} S &= (I + L)^{-1} \\ T &= (I + L)^{-1} L, \end{aligned} \quad (44)$$

where I is the identity matrix.

The sensitivity function, S , describes how the effects of non-controlled inputs ($y_d = G_d d$) and disturbances propagate to the output y , while the complementary sensitivity function, T , characterizes the mapping from the reference signal r to the output y . Ideally, the magnitudes of S and T should be very small and close to identity, respectively, meaning that disturbances are completely rejected and the reference signal is tracked perfectly. However, in practice, achieving a low magnitude of S at high frequencies requires large control gains, which can introduce instabilities [58]. Therefore, a low magnitude of S is typically desired only up to a certain bandwidth, beyond which larger magnitudes are allowed at higher frequencies, trading off disturbance rejection for improved stability. Since $S + T = I$, the magnitude of T is then close to identity at

low frequencies and decreases at higher frequencies, indicating good reference tracking at low frequencies, with performance deteriorating as the frequency increases.

Given that S and T represent the closed-loop transfer functions of a MIMO system, interpreting their magnitudes requires a decomposition of the system responses for different combinations of reference and disturbance signals. This is achieved through singular value decomposition. The upper and lower singular values, $\bar{\sigma}$ and $\underline{\sigma}$, of S represent the worst-case and best-case disturbance rejection, respectively, while for T , they indicate the opposite in terms of reference tracking performance. Consequently, the stability margins and bandwidth of the MIMO system are directly related to these singular values.

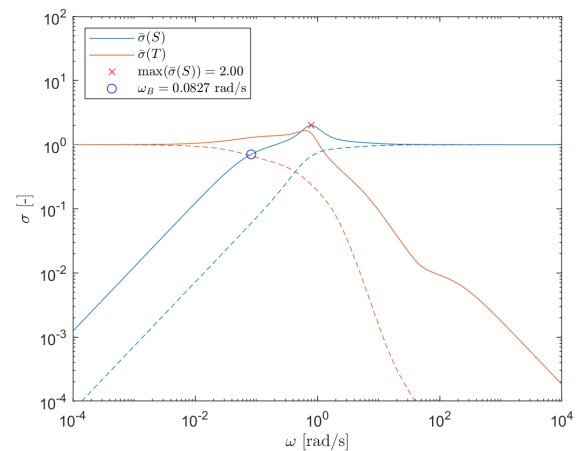


Figure 23: Singular values of closed-loop transfer functions S and T . The solid line and dashed line indicate the upper and lower singular values, $\bar{\sigma}$ and $\underline{\sigma}$, respectively.

In Figure 23, the upper (solid) and lower (dashed) singular values, $\bar{\sigma}$ and $\underline{\sigma}$, of the closed-loop transfer functions are plotted as a function of frequency. The system bandwidth, ω_B , is defined as the frequency at which the sensitivity function first satisfies $S(\omega_B) = \frac{1}{\sqrt{2}}$. For the diagonally controlled system, this corresponds to $\omega_B = 0.0827$ rad/s. The peak of the sensitivity function is $\max(\bar{\sigma}(S)) = 2.00028$. As a general guideline, a sensitivity peak around 2, given the relatively low values of the elements in the RGA, ensures adequate stability and robustness margins [58]. Based on these indicators, i.e. the RGA and upper singular value peaks, the closed-loop MIMO system is expected to exhibit good stability and reference tracking performance up to the bandwidth frequency.

It is important to note that this analysis is applicable only to linear systems. For the full nonlinear model, reference tracking performance

and stability margins may differ. However, near the steady-state linearization point, the analysis provides a useful approach for understanding the system's behaviour.

4.4 Results

This section reports the performance of the controller developed in the previous section for reference tracking and disturbance rejection. To this end, closed-loop simulation results are presented for three scenarios: tracking a single speed line, rejecting a disturbance in the inlet air temperature $T_{a,in}$, and reconstructing the full compressor map.

4.4.1 Single Speed Line Tracking

To trace speed lines on the compressor map, appropriate reference signals must be defined for the outputs: condenser pressure (P_C), evaporator pressure (P_E), and compressor inlet temperature (T_1). For a single speed line, this process follows a method similar to standard compressor testing in an isolated environment. The inlet temperature and pressure of the compressor are kept constant, while the outlet pressure is varied sequentially to reach the surge and choke limits. The simulation is divided into the following steps:

1. Transition from the initial steady-state point to the centre of the nearest speed line, corresponding to $\beta_{mid} = \frac{1}{2} \max(\beta)$.
2. Move to the surge point of the speed line by increasing the outlet pressure.
3. Move to the choke point of the speed line by decreasing the outlet pressure.
4. Return to the centre of the speed line and allow the system to settle back to steady-state.

These steps are illustrated in the compressor map in Figure 24, where the various steady-state operating points reached at the end of each phase are marked by magenta asterisks. The surge and choke limits are represented as straight lines. Given the uncertainty in the performance map, these limits have been defined with a conservative approach. Note that although the compressor inlet temperature and pressure are fixed in this scenario, alternative combinations of outlet pressure and inlet conditions could achieve the same reference points on the compressor map.

In Figure 25 the results of the simulation are shown. For the reference signal of the condenser pressure P_C (shown in the top left panel), a transition time of 5 seconds is used to ramp between the reference points indicated in Figure 24. The

only exception to this is between points 2 and 3, where a ramp time of 10 seconds is used. At each new point, the reference value is kept constant for 75 seconds, while at the final point the reference value is kept constant for an additional 30 seconds.

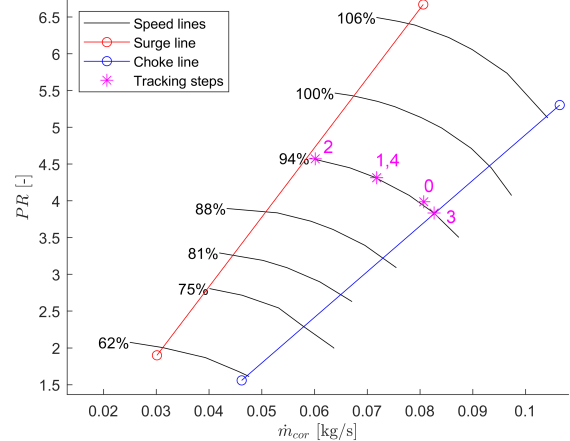


Figure 24: Compressor map with magenta points indicating the various steady-state operating points reached at the end of each test phase. The numbering of the points corresponds to the four distinct steps of the simulation.

The results include the outputs and control inputs of two closed-loop systems: the decentralized controller implemented in the full non-linear Dymola model, and the controller in closed-loop with the linearized model, simulated in the Simulink environment. The first thing to notice in Figure 25 is that the controller is in general capable of tracking the imposed reference signals with an acceptable response time and zero steady-state error. This excellent steady-state performance can be attributed to the integral action in the Proportional Integral (PI) controllers. In addition to this, two other important observations can be made.

First, the interactions between the control loops can be clearly seen in centre left and bottom left panel of Figure 25, where the evaporator pressure P_E and compressor inlet temperature T_1 are shown. If the system would be perfectly diagonal, the condenser pressure reference could be tracked without the need for control in the other loops. However, as the condenser pressure is changed by the first controller, the evaporator pressure and compressor inlet temperature can be seen to change as well and the controllers of the other loops have to adjust for this. Fortunately, the coupling is not too detrimental, since the system can be seen to remain stable and the maximum deviations from the references are approximately 0.05 bars and 1.3 °C for the evapo-

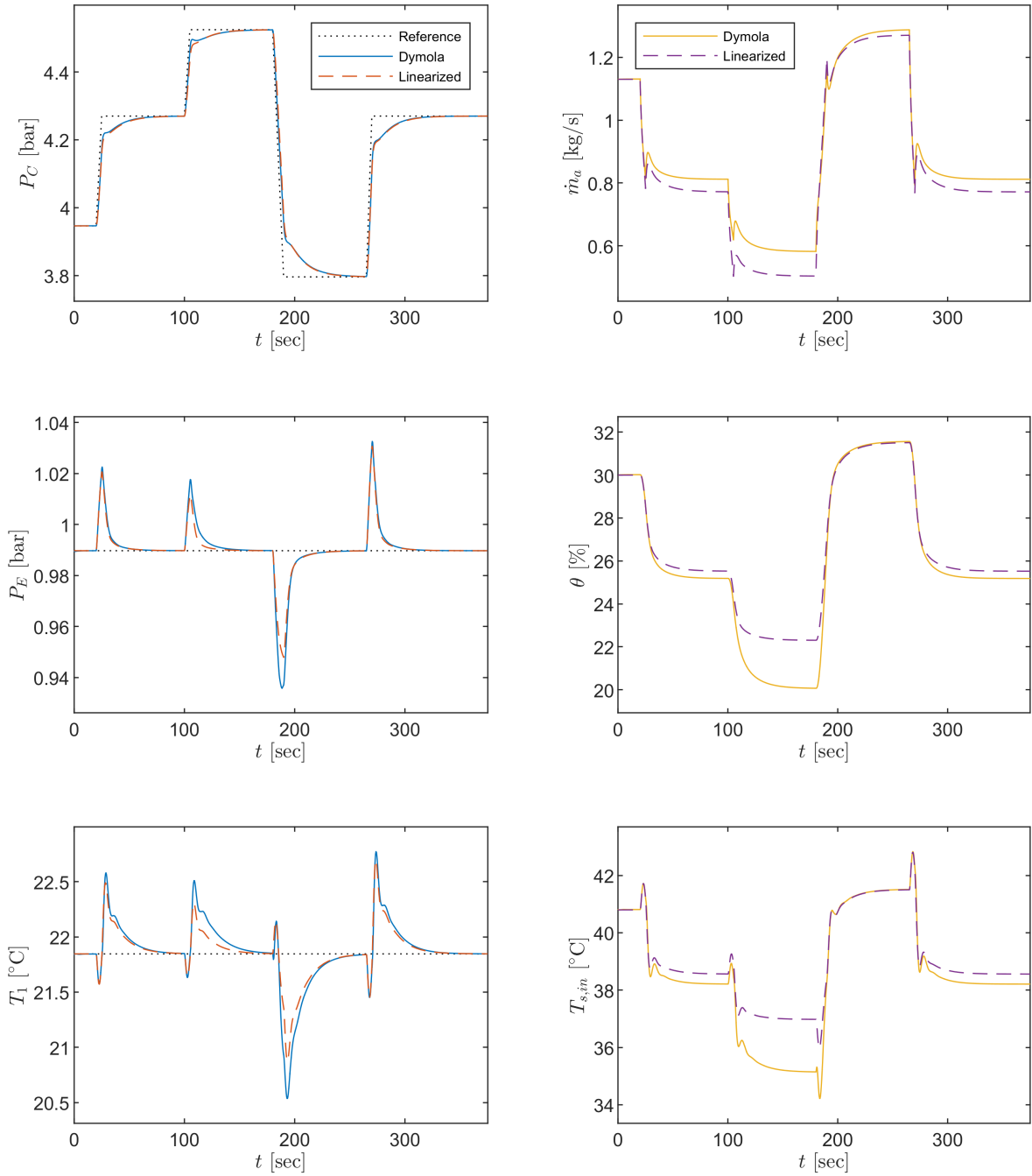


Figure 25: Closed-loop reference tracking results of the nonlinear model and linearized model for the speed line closest to the linearization point. From top to bottom, the panel rows correspond to the control loops of the condenser pressure P_C , evaporator pressure P_E , and compressor inlet temperature T_1 , respectively. The right column panels contain the plots of the control inputs.

rator pressure and compressor inlet temperature respectively, which is considered acceptable for the speed line tracking task.

Second, while the initial responses of both closed-loop systems are very similar, their control inputs, shown in the right column panels of Figure 25, begin to diverge once a new steady state

is reached. This behaviour can be attributed to differences in the steady-state predictions of the nonlinear Dymola model and its linearized approximation, as discussed in Section 4.2.3. However, linking the steady-state differences observed in the closed-loop simulation to those caused by a single input change is not straightforward. For

instance, considering the evaporator pressure in Figure 20, the linear model underestimates the impact of valve closure on the evaporator pressure. Based on this, one might expect the closed-loop simulation of the linearized system to show more valve closure to counteract the increase in evaporator pressure during reference tracking. Yet, the centre right panel of Figure 25 reveals the opposite: the controller closes the valve more when paired with the Dymola model than with the linearized system.

This counter-intuitive result highlights the complex coupled dynamics of the VCC system, especially in closed-loop operation. Interactions between the independent control loops introduce additional dynamic couplings, further complicating the system's behaviour. Regardless, despite the discrepancies arising from unmodelled nonlinearities, the controlled Dymola model outputs demonstrate that the controller delivers performance comparable to the linearized model for which it was designed. This finding is encouraging for the implementation of the designed control system in the IRIS setup, as it suggests that the decentralized PI control strategy can perform effectively even when the steady-state behaviour of the actual system deviates from the models used during controller tuning.

4.4.2 Air Temperature Disturbance Rejection

In the second simulation, the temperature of the air entering the condenser, $T_{a,in}$, is rapidly increased by 10 °C using a ramp signal over 5 seconds. While this scenario may not seem particularly realistic, given that outdoor temperatures in the Netherlands are unlikely to spontaneously rise by 10 °C, the goal is to investigate the controller's response to a sudden and extreme disturbance that reduces the effectiveness of heat rejection at the heat sink.

The inlet temperature disturbance is shown in the top panel of Figure 26. The air temperature ramps from 38 to 48 °C over 5 seconds. For the output response only the condenser working fluid pressure P_C is shown in the middle panel, as it is the output most directly influenced by the inlet air temperature. The sharp increase in air temperature causes an initial pressure peak in the condenser, which gradually decreases once the inlet air temperature stabilizes. For the Dymola model, this pressure peak is significantly larger than for the linearized system, suggesting that the controller has greater difficulty managing the disturbance due to nonlinearities in the heat rejection process. This is confirmed by the air mass flow \dot{m}_a rate computed by the controller, depicted

in the bottom panel, which shows that the non-linear model requires a much larger input to reject the disturbance compared to the linearized system.

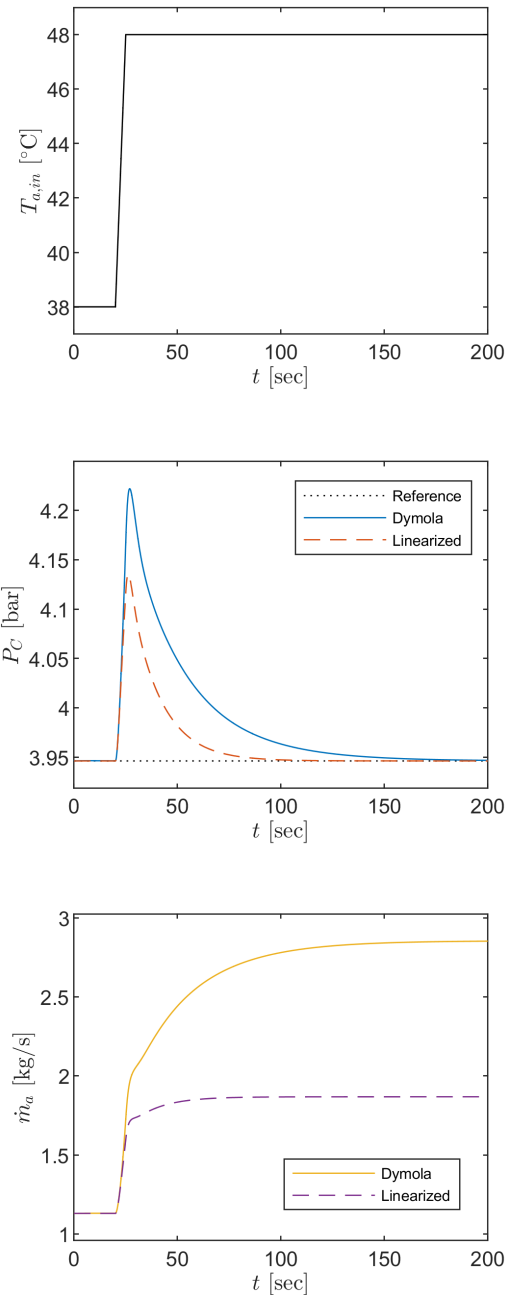


Figure 26: Closed-loop disturbance rejection results of the nonlinear model and linearized model for a sudden change in air inlet temperature $T_{a,in}$.

To understand these nonlinearities, the general expression for heat transfer is recalled as

$$\dot{Q}_a = \bar{\alpha} A_h (\bar{T}_a - \bar{T}_w). \quad (45)$$

Unlike in (17), this formulation considers the temperature difference between the wall and the

air. When the average air temperature, \bar{T}_a , increases due to the inlet air temperature disturbance, the absolute heat transfer from the condenser wall to the air decreases. This reduction in energy removal leads to an increase in condenser pressure, as was also discussed in section 3.2.3. To counteract this, the controller increases the air mass flow rate to enhance the heat transfer coefficient. However, the relationship between air mass flow rate and heat transfer coefficient, based on the correlation from Chang and Wang in (23), is nonlinear. The correlation states that the rate of increase in the heat transfer coefficient diminishes as the mass flow rate rises, limiting the controller’s ability to compensate for the disturbance at higher mass flow rates.

Additionally, the formulation of (45) reveals another source of nonlinearity: the temperature difference between the air and the wall. As the air temperature increases, this difference inevitably decreases, since the maximum wall temperature is directly linked to the working fluid pressure. In the condenser’s two-phase region, where most heat transfer occurs, the condensation temperature is defined by the condenser pressure, which the controller aims to keep constant. As a result, the wall temperature does not increase significantly, as the refrigerant temperature acts as an upper limit. The resulting narrowing temperature difference between the wall and air makes it increasingly difficult to remove sufficient heat from the system by merely increasing the heat transfer coefficient. In the extreme case where the air temperature matches the wall temperature, heat transfer becomes impossible, regardless of the heat transfer coefficient’s value.

Although this simulation examines a large and somewhat unrealistic disturbance, it highlights a fundamental limit in the controllability of the VCC. When extreme disturbances or imposed setpoints reduce the temperature difference between the secondary fluid and refrigerant, the required control input to maintain desired conditions becomes excessively large. This limitation in controllability will be further explored in the next simulation, targeting the reconstruction of the complete compressor map.

4.4.3 Full Map Testing

The final test involves the reconstruction of the complete compressor performance map, as shown in Figure 5a. This is accomplished by providing the decentralized controller with reference signals to sequentially track corrected speed lines ranging from 62% to 106% of the nominal compressor speed (80 kRPM). For each speed line, the approach mirrors the single-speed line

tracking simulation described in Section 4.4.1, where the evaporator pressure and compressor inlet temperature remain constant while the outlet pressure varies. However, transitioning between speed lines to reconstruct the full map introduces additional considerations for the reference signals. Moreover, because the input variables are bounded in the actual IRIS facility, adjustments to the air inlet temperature are necessary to enable complete map reconstruction under realistic conditions.

This section is therefore divided into three parts. First, the procedure for constructing reference signals to track multiple speed lines is explained, where the air inlet temperature of the linearization point is used ($T_{a,in} = 38\text{ }^\circ\text{C}$). Next, the closed-loop simulation results of the Dymola model and linearized approximation are presented, and the limitations of the controller with respect to the input bounds are discussed. Finally, the simulation is repeated with a lower air inlet temperature to improve the feasibility of compressor map reconstruction in the real system.

Constructing Reference Signals

The challenges discussed in the previous section regarding small temperature differences between the air and the condenser wall also arise when reconstructing the full compressor map, particularly at lower corrected speeds. Maintaining a constant evaporator pressure equal to that of the linearization point, $P_E = 0.990\text{ bar}$, throughout the simulation proves infeasible. For instance, consider the condenser pressure required to achieve the lowest pressure ratio in the map ($PR \approx 1.5$) at this evaporator pressure, given by

$$\begin{aligned} \min(P_C)|_{P_E=0.990\text{ bar}} &\approx 1.5\text{ bar} \\ \implies T_{cond} &\approx 29\text{ }^\circ\text{C}. \end{aligned} \quad (46)$$

The corresponding condensation temperature, T_{cond} , is obtained from the fluid properties of R-1233zd(E) at the specified condenser pressure. At the steady-state linearization point, derived from the IRIS commissioning conditions (see Table 3), the air inlet temperature is $T_{a,in} = 38\text{ }^\circ\text{C}$. Since the condensation temperature at the lowest pressure ratio is below the air inlet temperature, the controller cannot achieve this pressure. Therefore, the evaporator pressure and compressor inlet temperature reference signals must be carefully chosen to ensure the condenser pressure remains high enough for effective heat rejection under the boundary condition of $T_{a,in} = 38\text{ }^\circ\text{C}$.

To address this, the evaporator pressure reference signal is defined as an array of linearly

spaced pressures within the range

$$(P_E)_{\text{ref}} \in [0.80, 2.00] \text{ bar.} \quad (47)$$

This approach assigns a specific evaporator pressure to each speed line, with higher evaporator pressures applied to lower corrected speeds and vice versa, ensuring sufficiently high condenser pressures. For pressure ratios ranging from 1.5 to 6.5, the corresponding range of condenser pressures and condensation temperatures is

$$\begin{aligned} (P_C)_{\text{ref}} &\in [3.00, 5.20] \text{ bar} \\ \implies T_{\text{cond}} &\in [50.8, 70.7] \text{ }^\circ\text{C.} \end{aligned} \quad (48)$$

These condensation temperatures are well above the air inlet temperature defined in Table 3, reducing the demands on the controller at these conditions.

For the compressor inlet temperature reference, a unique value is assigned to each speed line as well. The degree of superheat is maintained at its initial steady-state value of approximately $SH \approx 4.20$ K to ensure that no liquid enters the compressor. Using this degree of superheat, the compressor inlet temperature is calculated for each evaporator pressure.

The speed lines of the compressor map represent corrected speeds, requiring the actual compressor speed at each line to be calculated based on the compressor inlet temperature. To determine this, the expression in (24) is rearranged to solve for the actual compressor speed Ω , using the desired corrected speed N_T and the compressor inlet temperature T_1 corresponding to that speed line.

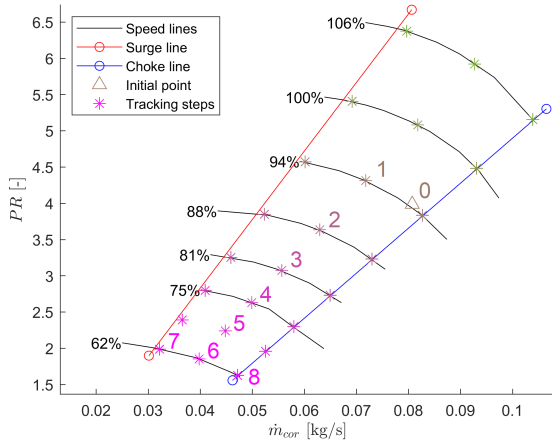


Figure 27: Compressor map with operating set-points for full reconstruction of the machine performance, showing evaporator pressure variations: magenta represents high pressures, and green represents low pressures.

In Figure 27, the reference points used to track the full compressor map are shown. For

each speed line, the procedure follows the steps outlined in Figure 24, with ramp functions ensuring smooth transitions between setpoints. The main difference is that evaporator and compressor inlet temperatures vary across speed lines. These variations are highlighted in Figure 27, where green asterisks indicate low evaporator pressure and magenta asterisks indicate high evaporator pressure. The reference signals for P_C , P_E , and T_1 follow a specific order: they start at the centre of the speed line closest to the initialization point, then shift step by step from one speed line centre to the next, down to the lowest speed line (62% of the nominal compressor speed). From there, the setpoints are imposed as described in Section 4.4.1, and the process repeats for each subsequent speed line. To improve clarity, the first eight steps are numbered in Figure 27, while later steps remain unnumbered for readability.

To demonstrate that the tracking procedure is not limited by the availability of specific speed lines in the experimental map, the 68% speed line is included in the tracking sequence, even though it was not part of the original dataset provided by the compressor manufacturer.

Although it is in theory possible to track any speed line, the robustness of the control system in case the compressor characteristics deviate significantly from those used for its design should be demonstrated. This demonstration is not included in the scope of the current work. However, the methods demonstrated here suggest that an iterative procedure can be used to improve the quality of the compressor performance map and control system simultaneously. The motivation for this procedure is discussed further in Section 5.2.

Simulation Results for Air at 38 °C

In Figure 28, the transient responses and corresponding control inputs for condenser pressure P_C and compressor inlet temperature T_1 are presented with the air inlet temperature set at $T_{a,in} = 38$ °C. Both the closed-loop results from the Dymola model and its linearized approximation are included. The controller effectively tracks the steady-state references, although at lower corrected speeds, the condenser pressure, P_C , shows a slower response compared to speed lines closer to the linearization point, as can be seen in more detail in the close-ups in Figure 29. This slower response is only observed in the Dymola model, suggesting that nonlinearities are responsible for the reduced performance at these lower speeds.

This is further supported by the air mass flow

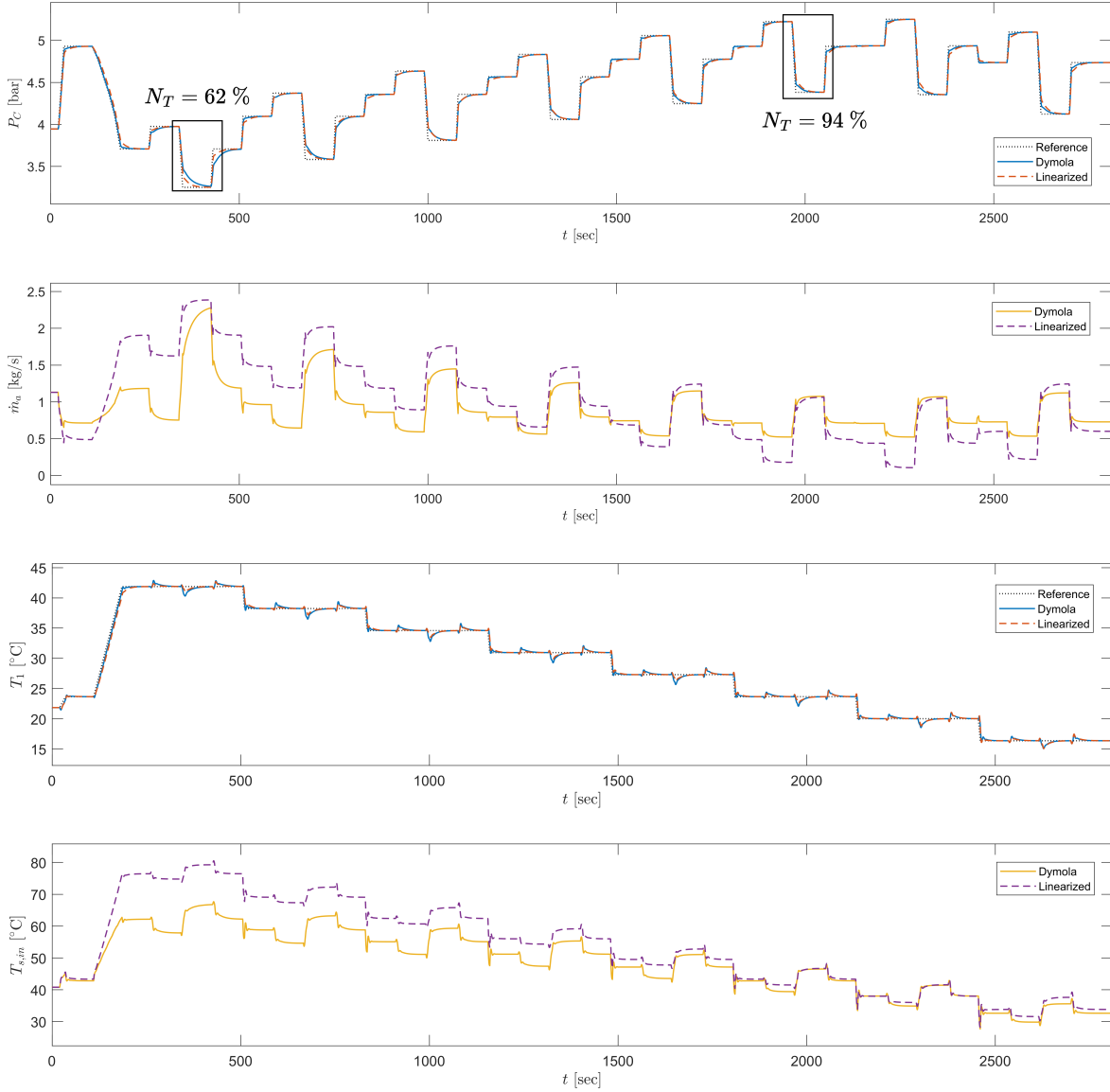


Figure 28: Closed-loop reference tracking results of the nonlinear model and linearized model for the full compressor map reconstruction at $T_{a,in} = 38^\circ\text{C}$. The panels contain from top to bottom the condenser pressure P_C , air mass flow rate \dot{m}_a , compressor inlet temperature T_1 , and glycol-water inlet temperature $T_{s,in}$, respectively. In the top panel, two close-up windows of the lowest corrected speed line, $N_T = 62\%$, and speed line closest to the linearization point, $N_T = 94\%$, are shown in Figure 29.

rate plots, \dot{m}_a , in Figure 28, which show significant divergence in the control inputs computed by the controllers in the two systems at lower corrected speeds. While the controller's response speed remains consistent across all speed lines in the linearized system, the Dymola system exhibits a slower response at lower speeds. This indicates that the fixed control gains lack the ability to compensate for the reduced heat transfer effectiveness, caused by lower mass flow rates and smaller temperature differences with ambient air, as discussed in Section 4.4.2.

For the compressor inlet temperature, T_1 , the closed-loop performance of the Dymola and linearized systems is comparable in Figure 28. This suggests that the system nonlinearities captured in the Dymola model have less impact on the ability of the controller to track the reference signal for the compressor inlet temperature than for the condenser pressure. However, the glycol-water inlet temperature, $T_{s,in}$, computed by the controller shows notable deviations between the Dymola and linearized models, particularly at lower corrected speeds.

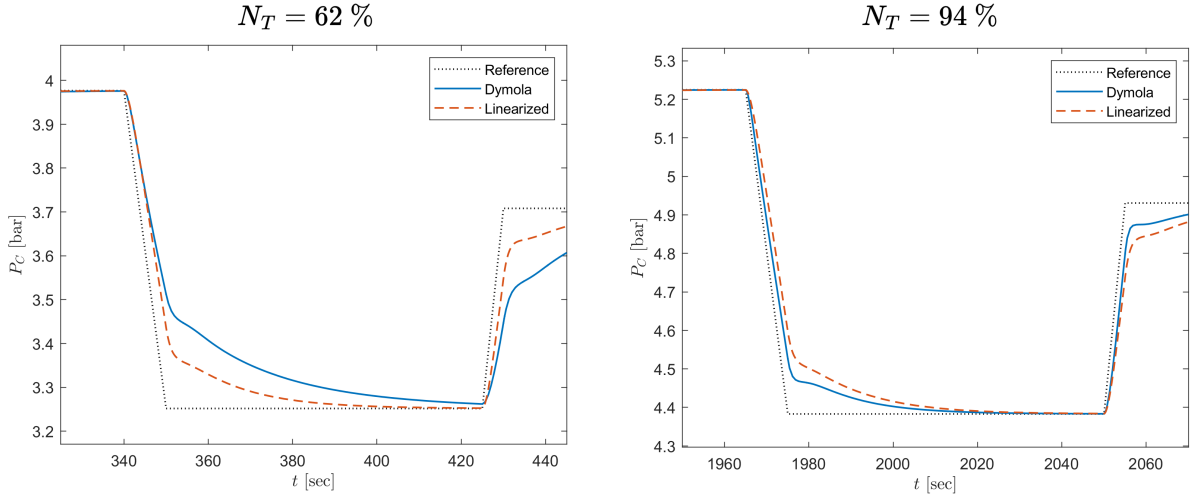


Figure 29: Close-up windows of the $N_T = 62\%$ line (left) and $N_T = 94\%$ line (right) for the closed-loop reference tracking of the condenser pressure P_C from Figure 28.

Although the controller's tracking performance is less effective at lower corrected speeds, it still successfully reaches all steady-state reference points defined by the set points. For testing purposes, achieving the desired set points is more critical than the speed at which they are reached. As such, the controller's tracking performance is considered acceptable for the intended testing applications at $T_{a,in} = 38\text{ }^\circ\text{C}$.

However, a significant issue arises when examining the control inputs, i.e. \dot{m}_a and $T_{s,in}$, in Figure 28. During the commissioning of the IRIS, it was determined that the variable-speed fan of the cooling loop can achieve a maximum air mass flow rate of approximately 1.5 kg/s [20]. Additionally, a safety interlock is in place to shut down the heater if the glycol-water temperature exceeds $50\text{ }^\circ\text{C}$. For the given air temperature of $38\text{ }^\circ\text{C}$, these constraints pose a challenge, as the simulation results indicate that both the air mass flow rate and glycol-water inlet temperature exceeded these limits during the first half of the simulation.

Unfortunately, adjusting only the reference signals for P_C and T_1 does not resolve this issue. Increasing the condenser pressure at lower corrected speeds requires a corresponding increase in evaporator pressure to maintain the lowest pressure ratios. To ensure vapour conditions at the compressor inlet, this would require a higher glycol-water temperature, which exceeds the heater's operating limits. Conversely, lowering the glycol-water inlet temperature would require reducing the evaporator pressure and, consequently, the condenser pressure to maintain the required pressure ratios. This, in turn, would de-

mand a higher air mass flow rate, which exceeds the maximum capacity of the fan.

Therefore, to enable the reconstruction of the full compressor map under the given control input limitations, the inlet temperature of the air, $T_{a,in}$ must be adjusted. In the following paragraph, this scenario is discussed in detail.

Reducing the Air Temperature to $20\text{ }^\circ\text{C}$

To cope with the limitations on the control inputs of the IRIS facility, the simulation from the previous paragraph was repeated with the air inlet temperature reduced to $20\text{ }^\circ\text{C}$. Lowering the air temperature allows heat to be rejected effectively at lower condenser pressures, thereby reducing the overall pressure levels in the system. This adjustment eases the conditions for the controller, making it less challenging to reach the imposed set points while staying within the input limits. However, before discussing the simulation results, additional modifications to the reference signals must be explained. The chosen evaporator pressure range and the corresponding condenser pressure and temperature ranges are as follows:

$$\begin{aligned} (P_E)_{\text{ref}} &\in [0.80, 1.20] \text{ bar} \\ \implies (P_C)_{\text{ref}} &\in [1.80, 5.20] \text{ bar} \\ T_{\text{cond}} &\in [34.5, 70.7] \text{ }^\circ\text{C} \end{aligned} \quad (49)$$

The first key adjustment is the reduction of the highest evaporator pressure reference. This allows for lower glycol-water inlet temperatures, meaning the controller is not required to raise this temperature as much. However, lowering the evaporator pressure reference also necessitates a decrease in the condenser pressure reference to maintain the desired pressure ratio.

At first glance, this reduction in condenser pressure might seem problematic, as it decreases the condenser wall temperature and could limit the heat rejection. However, due to the significantly lower air temperature, the temperature difference at the reduced condensation pressure remains sufficient, with approximately 14.5 °C between the lowest condensation temperature and the air. This ensures effective heat transfer despite the lower pressure levels.

With the adjusted air temperature and reference signals, the simulation is repeated. Starting 20 seconds after initialization, the air temperature is reduced from 38°C to 20°C over a 30-second ramp. At $t = 50$ seconds, the reference signal procedure begins, driving the system toward the tracking points shown in Figure 27.

The simulation results, presented in Figure 30, confirm that the control inputs estimated with the nonlinear model remain feasible ($\dot{m}_a < 1.5$ kg/s and $T_{s,in} < 50$ °C) with tracking performance comparable to that obtained in the higher air inlet temperature scenario. Notably, at lower corrected speeds, the slower condenser pressure setpoint tracking observed in the higher temperature case is slightly improved.

To further illustrate these results, the tracking trajectory of the compressor map reconstruction at $T_{a,in} = 20$ °C is overlaid on the compressor map in Figure 31, showing only the results obtained with the nonlinear model for clarity. The controller successfully tracks all reference points outlined in Figure 27, remaining close to the corrected speed lines during both increases and de-

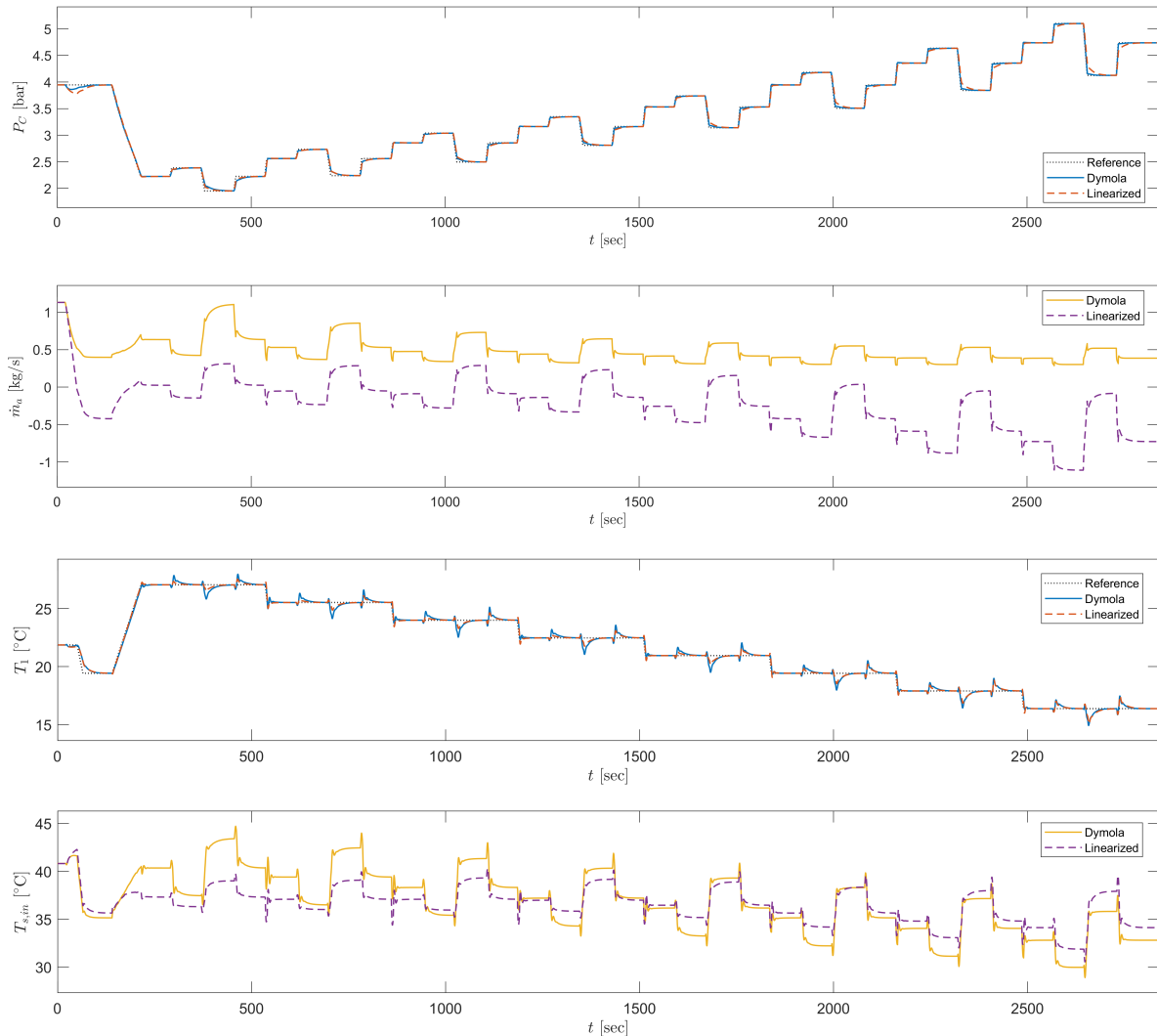


Figure 30: Closed-loop reference tracking results of the nonlinear model and linearized model for the full compressor map reconstruction at $T_{a,in} = 20$ °C. The panels show, from top to bottom, the condenser pressure P_C , air mass flow rate \dot{m}_a , compressor inlet temperature T_1 , and glycol-water inlet temperature $T_{s,in}$, respectively.

creases in outlet pressure. However, at lower corrected speeds, the trajectory covered by the compressor when shifting from one speed line to the other does not end up at the centre of the targeted speed line, as instead achieved at higher rotational speeds. This deviation occurs because the condenser pressure P_C responds more slowly at lower speeds, as observed in Figure 28 and 30.

When shifting to a higher corrected speed, the deviation in Figure 31 leans toward the choke line, while the opposite trend is observed in case the shift is towards a lower corrected speed. Additionally, since the corrected speed lines diverge more at higher pressure ratios and mass flow rates, the relative deviations at lower corrected speeds become more pronounced due to smaller pressure ratios and the shorter distance between speed lines.

Despite these deviations, the controller successfully reaches all reference points while keeping control inputs within bounds. Moreover, the method allows tracking of any corrected speed line, enabling further refinement of the compressor map by reconstructing intermediate speed lines. With a total simulation time of approximately 47 minutes, the full compressor map can be reconstructed efficiently. These results suggest that the proposed control strategy is suitable for

a proper testing of the compressor and it does not require modifications to the current IRIS layout.

However, it is worth noting that as the air inlet temperature decreases, the system moves further away from the linearization point used in the controller design. This can be seen in Figure 30, where small deviations in the reference compressor inlet temperature become more pronounced compared to Figure 28, which is closer to the linearization point. Additionally, in Figure 30, the mass flow rate calculated by the controller in the linear closed-loop system becomes sometimes negative, an unphysical result since flow reversal is not supported in the model.

These deviations highlight that the linear performance indicators of the controlled system, such as the sensitivity and complementary sensitivity functions discussed in Section 4.3.3, may lose accuracy as the system moves too far away from the linearization point. Significant deviations could lead to performance deterioration, and the closed-loop system's stability and robustness may even become insufficient. Nevertheless, as shown in Figure 28, 30, and 31, the controller maintains acceptable performance for the scenarios considered, proving its validity for the operation of the IRIS setup.

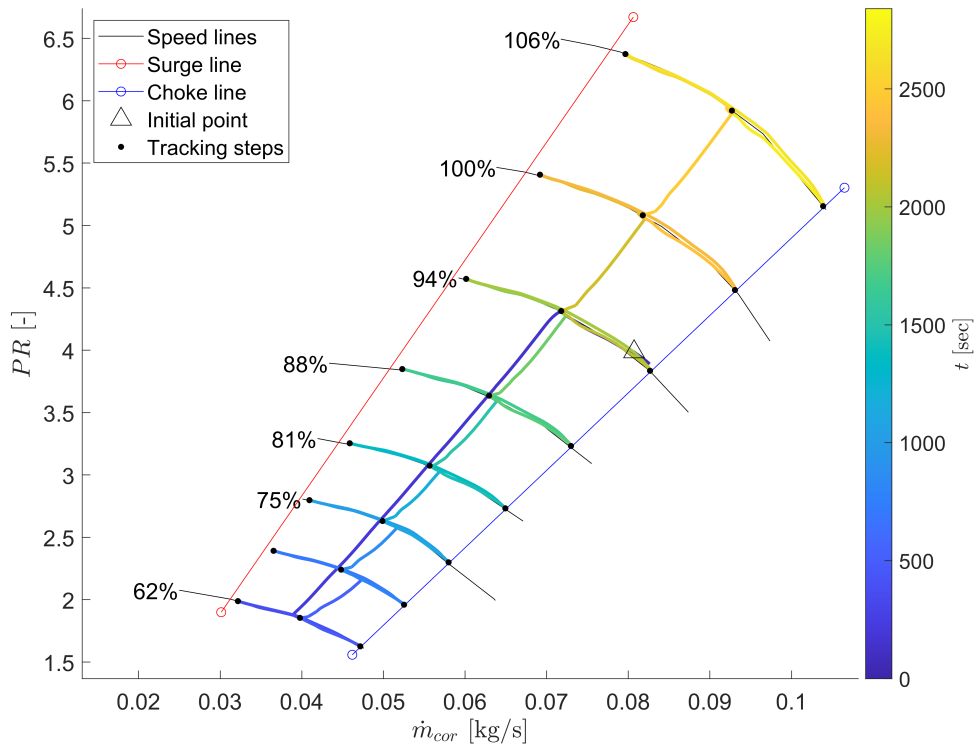


Figure 31: Closed-loop tracking trajectory obtained with the nonlinear model for $T_{a,in} = 20$ °C, where the trajectory's colour reflects the simulation time, as indicated by the colour bar on the right.

5 Conclusions

In this research, a numerical model was developed to investigate the transient operation of the Inverse organic Rankine cycle Integrated System (IRIS) test facility, whose operating principle is based on that of the Vapour Compression Cycle (VCC). Additionally, a control strategy was presented to enable reliable compressor testing with the goal of characterizing its off-design performance maps.

For the dynamic modelling, a modular and causal approach was adopted, with individual submodels developed for each of the main components of the working fluid loop of the setup: evaporator, compressor, condenser, and expansion valve. Leveraging time-scale separation principles, only the dynamics of the heat exchangers were considered, while the compressor and valve were modelled statically. These submodels were then interconnected to form the complete VCC system model.

Heat exchangers were modelled using the Moving Boundary (MB) method, dividing the component into distinct control volumes separated by boundaries where refrigerant phase change occurs. Mass and energy conservation equations were applied within each control volume, with empirical correlations from literature used to model convective heat transfer. It was shown that with the MB formulation of the heat exchanger models a minimal Differential-Algebraic Equation (DAE) index is guaranteed, enabling efficient numerical simulations.

The compressor model reproduces the performance of a two-stage centrifugal compressor that will be installed in the IRIS facility in the next months. Compressor performance maps derived from experimental data were converted into numerical interpolation tables using the β -line method, allowing the computation of mass flow rate and isentropic efficiency from suction and discharge pressures and inlet enthalpy. Surge and choke dynamics were excluded, since operation in these regimes lies outside of the scope of the research.

The submodels were implemented in Dymola, a modelling environment that uses the Modelica language. The complete VCC model includes six inputs: air inlet temperature, air mass flow rate, glycol-water inlet temperature, glycol-water inlet mass flow rate, expansion valve position, and compressor rotational speed.

Verification showed that the steady-state predictions of the model aligned well with experimental data from the facility's commissioning phase, despite differences in the compressor type and neglecting the heat exchanger pressure losses

and piping. Key parameters deviated by less than 12%, which was deemed reasonable. Transient analyses demonstrated the model's ability to capture system responses, such as the effects of changes in valve opening, compressor speed, and airflow rates. The observed trends were consistent with physical reasoning, and the model was shown to conserve mass and energy appropriately, confirming its reliability for studying VCC dynamics.

The control strategy focused on maintaining consistent compressor conditions, with evaporator pressure, condenser pressure, and compressor inlet temperature identified as key outputs. The rotational speed of the compressor was treated as an external disturbance to align with typical testing procedures. From a physical perspective, the appropriate control inputs were selected as the expansion valve position, the air mass flow rate, and the glycol-water inlet temperature. Linearizing the system around a steady-state operating point, a Relative Gain Array (RGA) analysis justified the use of an initial decentralized control design. Three independent Proportional Integral (PI) controllers were tuned using a loop-shaping method. While a full robustness analysis was not performed, the closed-loop transfer functions indicated good stability and robustness properties.

The controller's performance was evaluated through three scenarios. First, it was demonstrated that a single corrected speed line in the compressor map could be tracked effectively by providing appropriate reference signals. The results indicate that the integral action of the PI controllers allows for excellent steady-state performance, even when the steady-state prediction of the model does not fully align with the behaviour of the actual system. Second, the impact of changing the condenser air inlet temperature was analysed, and it was shown that nonlinearities in the system led to degraded performance when the condenser pressure set point was too low. Finally, the reconstruction of the full compressor map was presented. Initial simulations at 38°C ambient air temperature revealed violations of input constraints, prompting additional simulations at 20°C. In both cases, the results indicated that the corrected speed lines could be tracked sequentially, though some degradation in performance was observed at lower speed lines. Overall, the findings showed that the controller enabled the reconstruction of the compressor map within a reasonable time frame and without exceeding inlet constraints.

Based on the results of this research, the developed dynamic model proves to be a valuable tool for analysing the transient behaviour

of the VCC in the IRIS facility. It offers insights into the complex interactions between cycle components, which are challenging to investigate quickly and safely in real-life settings. Furthermore, the tracking performance achieved with the decentralized controller demonstrates that the compressor map can be successfully reconstructed within the existing system architecture.

The modelling and control system development presented in this research involved several simplifications and methodological choices aimed at managing computational demand and addressing practical constraints. These assumptions, while necessary to achieve the objectives within the given scope, introduce limitations that influence the generalizability and interpretation of the conclusions. Therefore, the following section will provide a discussion on these topics.

5.1 Discussion

This section explores the implications of several key simplifications and the potential effects they may have on the findings of the study. Three topics are discussed: active charge predictions, heating effects in the compressor, and control tuning and robustness.

Active Charge Modelling and the Liquid Receiver

In the heat exchanger models developed in this research, the void fractions of the two-phase regions in the condenser and evaporator were assumed to be time-invariant. Their values were determined using the Homogeneous Equilibrium Model (HEM) formulation in (5). However, this assumption is generally valid only for small transients, as highlighted in prior studies [34, 38]. During the construction of the full compressor map, the transients in the simulations may arguably exceed this range, particularly considering the condenser pressure variations illustrated in Figure 30.

As a result, the assumption of time-invariant void fractions introduces inaccuracies in capturing the two-phase transport phenomena, potentially leading to significant deviations in the predicted active refrigerant charge compared to actual system behaviour. In this context, another important simplification is the omission of the liquid receiver, which may further impact active charge predictions. Although dynamic modelling of the liquid receiver has received limited attention in the literature [60], studies suggest that its dynamics are intricately linked with other cycle components [30], and that accurately predicting the active charge may require an integrated mass analysis that considers all system components, including the receiver [31].

To evaluate the effects of these simplifications, validation against experimental results from the IRIS facility is essential. If the heat exchanger models are found to lack predictive accuracy, more elaborate void fraction models that account for time-varying behaviour should be incorporated, as suggested by Qiao et al. [61]. Additionally, if challenges with active charge predictions persist, the model can be expanded to include a dynamic representation of the liquid receiver, although inclusion of this component is rare in open literature [28].

Compressor Interstage Cooling and Secondary Flow

In the compressor submodel, a single-stage performance map was employed to represent the off-design behaviour of the two-stage centrifugal compressor. As discussed in Section 2.2.2, this approach assumes that the effects of interstage cooling and secondary flow to the foil bearings are adequately captured by the equivalent single-stage map. However, since refrigerant heating between stages and in the foil bearings are inherently dynamic phenomena, this assumption may become invalid over large operating ranges, such as those encountered during the reconstruction of the compressor map.

Additionally, the accuracy of the correction method used in the model may be questionable for such a broad operating range, as the ideal gas assumption might not hold under all simulation conditions. Similar to the time-invariant void fraction assumption, the validity of the compressor model's underlying assumptions should be evaluated through comparison with experimental results. However, since the centrifugal compressor is not yet installed in the IRIS facility, such validation can only be performed after the facility's architecture has been updated.

If these assumptions prove inadequate, the current model could be extended by independently modelling the two compression stages, each with its own performance map, while also incorporating the effects associated with interstage cooling and secondary bearing flow.

Controller Tuning and Robustness Analysis

Although the controller performance demonstrated in the simulations is satisfactory, it is important to highlight that the development of the control strategy and its corresponding gains was based on a somewhat heuristic approach. For instance, in the analysis of the RGA in Section 4.3.1, a qualitative assessment determined that the steady-state RGA was sufficiently close to the identity matrix to justify a decentralized con-

trol strategy. Similarly, the loop-shaping process involved manually tuning the gains of the PI controllers to achieve a desirable loop transfer function. Lastly, the evaluation of closed-loop performance relied on the singular values of the sensitivity and complementary sensitivity functions, with a rule of thumb applied to the peak of the sensitivity function as an indicator of stability margins and robustness for the Multi-Input Multi-Output (MIMO) system.

While these well-established methods often yield effective controller designs, as evidenced by the simulation results, more rigorous approaches could be employed to mathematically guarantee specific stability and robustness properties of the closed-loop system. Such methods could account for uncertainties in inputs, outputs, and system dynamics, enabling more precise optimization of the controller for reference tracking, disturbance rejection, and input constraints. However, due to time limitations, these advanced techniques were not pursued in this research. For the purpose of providing an initial understanding of the control challenges associated with compressor testing in the IRIS facility, the heuristic methodology presented here proved to be effective. Further insights into modern and classical methods for robust controller design can be found in the book of Skogestad and Postlethwaite [58].

5.2 Future Work

Based on the findings of the research, several directions for future work were identified. Some of these directions are aimed at addressing the challenges discussed in the previous section. However, additional ideas are presented considering the broader applicability of the dynamic VCC model. In addition, possible alternative approaches for more advanced control system design in later research endeavours are suggested.

Experimental Validation

The most important future step regarding the dynamic model of the VCC is validating its predictions against experimental data from IRIS. System-level properties, such as the distribution of the active charge, can only be validated once the centrifugal compressor is installed. However, component-level validation can already be performed for the heat exchangers and expansion valve, regardless of the compressor installed in the IRIS.

To achieve this, the component models must be provided with appropriate inputs and outputs, as outlined in the causality diagram in Figure 3. For example, validating the evaporator model requires a transient experiment in the real facility,

during which the mass flow rates entering and exiting the heat exchanger are recorded, along with the evaporator pressure, inlet and outlet temperatures, and the properties of the glycol-water streams. These recorded mass flow rates and inlet enthalpies can then serve as inputs to the model, allowing its predicted outputs to be compared with the experimental data. By systematically performing these validation steps, inaccuracies in the submodels can be identified, enabling improvements that bring the models into closer alignment with the actual system behaviour. Potential areas of improvement include the void fraction models incorporated in the two-phase regions of the heat exchangers, the convective heat transfer correlations, and the expansion valve discharge coefficient and opening characteristics.

Including Additional Components

As discussed in Section 5.1, neglecting the liquid receiver in the dynamic model may lead to significant errors in predicting the active charge distribution throughout the cycle. To address this, incorporating a dynamic model of the receiver in a future update would be a logical step. Furthermore, the modular structure of the model allows for the inclusion of additional components as needed. This flexibility aligns with the evolving nature of the IRIS, where changes to the system architecture are anticipated in upcoming project phases.

The conceptual design of the IRIS, as detailed in the dissertations of Ascione and Giuffr  [13, 15], highlights the need for future models to account for additional components, particularly an intercooler and various (three-way) valves. Developing these submodels and integrating them into the full VCC model will be essential to accommodate the facility’s planned extensions.

Expanding Controller Performance Analyses

Another important direction for future development is expanding the controller performance analyses presented in this work. Advanced mathematical tools, such as the structured singular value [58], could be utilized to further evaluate the robust performance of the closed-loop system, accounting for input and output uncertainties as well as unknown system dynamics. Gaining a deeper understanding of these properties could aid in developing more effective controllers for component testing while also enhancing the general applicability of the results presented here. In the long term, rigorous mathematical proofs of system stability and robustness could provide a strong foundation for an effective deployment of VCC-based Environmental Con-

trol System (ECS) technology aboard aircraft. To achieve this, the analysis methods should possibly also include nonlinear approaches, ensuring that performance can be guaranteed over a sufficiently wide operating range.

Iterative Compressor Testing

In Section 4.4.3, the flexibility of tracking any desired speed line was linked to the quality of the compressor performance map and control system, with an iterative testing procedure suggested. The central idea is that the control methodology presented here can be used to reconstruct a more detailed compressor map than the one initially used in the controller design. Once the map is reconstructed, the compressor model can be updated by replacing the original map with the new one. This allows the control system to be refined for the updated model, improving control during compressor testing. In this way, both the control system and compressor map can be enhanced simultaneously. It is important to note that improving the control system goes beyond simply tuning the current PI controllers. As the map becomes more detailed, more advanced control designs can be incorporated into the methodology, enabling tighter control near the surge and choke lines, which can help expand the compressor map close to or even beyond these limits.

Integrated Design Optimization

The integrated design optimizations developed by Ascione and Giuffr  considered only steady-state conditions. However, since ECSs inherently operate under transient conditions during a typical commercial flight mission, optimizing solely for steady-state scenarios may result in conservative system designs that overlook transient phenomena, which could relax design constraints. To address this, the dynamic model developed in this work could be used in future optimizations to extend existing methods and account for dynamic effects. Furthermore, integrating the control system design into the optimization process would allow system components and controllers to be designed simultaneously rather than sequentially, potentially improving both the efficiency and performance of the overall system.

References

[1] K. Calvin et al. *IPCC, 2023: Climate Change 2023: Synthesis Report. Contribution of Working Groups I, II and III to the Sixth Assessment Report of the Intergovernmental Panel on Climate Change [Core Writing Team, H. Lee and J. Romero*

(eds.)]. *IPCC, Geneva, Switzerland*. Ed. by P. Arias et al. July 2023. DOI: 10.59327/ipcc/ar6-9789291691647. URL: <http://dx.doi.org/10.59327/IPCC/AR6-9789291691647>.

- [2] C. A. Horowitz. “Paris Agreement”. In: *International Legal Materials* 55.4 (Aug. 2016), pp. 740–755. ISSN: 1930-6571. DOI: 10.1017/s0020782900004253. URL: <http://dx.doi.org/10.1017/S0020782900004253>.
- [3] W. W. Attribution. *Extreme downpours increasing in Southern Spain as fossil fuel emissions heat the climate*. Nov. 2024. URL: <https://www.worldweatherattribution.org/extreme-downpours-increasing-in-southern-spain-as-fossil-fuel-emissions-heat-the-climate/>.
- [4] H. Ritchie. “Sector by sector: where do global greenhouse gas emissions come from?” In: *Our World in Data* (2020). <https://ourworldindata.org/ghg-emissions-by-sector>.
- [5] V. Grewe et al. “Evaluating the climate impact of aviation emission scenarios towards the Paris agreement including COVID-19 effects”. In: *Nature Communications* 12.1 (June 2021). ISSN: 2041-1723. DOI: 10.1038/s41467-021-24091-y. URL: <http://dx.doi.org/10.1038/s41467-021-24091-y>.
- [6] M. Cames et al. *Emission Reduction Targets for International Aviation and Shipping*. The European Commission, 2015. URL: [https://www.europarl.europa.eu/thinktank/en/document/IPOL_STU\(2015\)569964](https://www.europarl.europa.eu/thinktank/en/document/IPOL_STU(2015)569964).
- [7] O. Zaporozhets, V. Isaienko, and K. Synylo. “PARE preliminary analysis of ACARE FlightPath 2050 environmental impact goals”. In: *CEAS Aeronautical Journal* 12.3 (July 2021), pp. 653–667. ISSN: 1869-5590. DOI: 10.1007/s13272-021-00525-7. URL: <http://dx.doi.org/10.1007/s13272-021-00525-7>.
- [8] G. Buticchi, P. Wheeler, and D. Boroyevich. “The More-Electric Aircraft and Beyond”. In: *Proceedings of the IEEE* 111.4 (Apr. 2023), pp. 356–370. ISSN: 1558-2256. DOI: 10.1109/jproc.2022.3152995. URL: <http://dx.doi.org/10.1109/JPROC.2022.3152995>.

- [9] AC-9 Aircraft Environmental Systems Committee. *Environmental control systems life cycle cost*. Tech. rep. 400 Commonwealth Drive, Warrendale, PA, United States: SAE International, 2017.
- [10] H. Schefer et al. “Discussion on Electric Power Supply Systems for All Electric Aircraft”. In: *IEEE Access* 8 (2020), pp. 84188–84216. DOI: 10.1109/ACCESS.2020.2991804.
- [11] M. Merzvinškas et al. “Air conditioning systems for aeronautical applications: a review”. In: *The Aeronautical Journal* 124.1274 (Dec. 2019), pp. 499–532. ISSN: 2059-6464. DOI: 10.1017/aer.2019.159. URL: <http://dx.doi.org/10.1017/aer.2019.159>.
- [12] S. K. Wang. *Handbook of Air Conditioning and Refrigeration*. en. 2nd Edition. New York: McGraw-Hill Education, 2001. ISBN: 9780070681675. URL: <https://www.accessengineeringlibrary.com/content/book/9780070681675>.
- [13] F. Ascione. “Vapour Compression Cycle Technology for Aviation: Automated Design Methods and a New Experimental Setup”. English. Dissertation (TU Delft). Netherlands: Delft University of Technology, 2024. DOI: 10.4233/uuid:39ef6ce1-d97f-4197-83ab-96d1e766de61.
- [14] K. Linnett and R. Crabtree. “What’s Next in Commercial Aircraft Environmental Control Systems?” In: *SAE Technical Paper Series*. ICES. SAE International, July 1993. DOI: 10.4271/932057. URL: <http://dx.doi.org/10.4271/932057>.
- [15] A. Giuffré. “Integrated Design Optimization of Electrically-Driven Vapor Compression Cycle Systems for Aircraft: Powered by High-Speed Centrifugal Compressors”. English. Dissertation (TU Delft). Delft University of Technology, 2023. DOI: 10.4233/uuid:b4f6a4a4-2e48-4bbe-9093-3f1368282f63.
- [16] A. Giuffré, P. Colonna, and M. Pini. “Design Optimization of a High-Speed Twin-Stage Compressor for Next-Gen Aircraft Environmental Control System”. In: *Journal of Engineering for Gas Turbines and Power* 145.3 (Dec. 2022), p. 031017. ISSN: 0742-4795. DOI: 10.1115/1.4056022. eprint: [https://doi.org/10.1115/1.4056022](https://asmedigitalcollection.asme.org/gasturbinespower/article-pdf/145/3/031017/6958025/gtp\145\03\031017.pdf). URL: <https://doi.org/10.1115/1.4056022>.
- [17] A. Giuffré et al. “Data-driven modeling of high-speed centrifugal compressors for aircraft Environmental Control Systems”. In: *International Journal of Refrigeration* 151 (2023), pp. 354–369. ISSN: 0140-7007. DOI: <https://doi.org/10.1016/j.ijrefrig.2023.03.019>. URL: <https://www.sciencedirect.com/science/article/pii/S0140700723000865>.
- [18] F. Ascione, P. Colonna, and C. De Servi. “Integrated design optimization method for novel vapour-compression-cycle-based environmental control systems”. In: *Applied Thermal Engineering* 236 (2024), p. 121261. ISSN: 1359-4311. DOI: <https://doi.org/10.1016/j.applthermaleng.2023.121261>. URL: <https://www.sciencedirect.com/science/article/pii/S1359431123012905>.
- [19] F. Ascione et al. “Assessment of an Inverse Organic Rankine cycle system for the ECS of a large rotorcraft adopting a high-speed centrifugal compressor and a low GWP refrigerant”. en. In: *Proceedings of the 6th International Seminar on ORC Power Systems*. Ed. by T. U. of Munich. Technical University of Munich, 2021. DOI: 10.14459/2021mp1633127.
- [20] *Design and Commissioning of the IRIS: A Setup for Aircraft Vapour Compression Cycle-Based Environmental Control System Testing*. Vol. Volume 5: Cycle Innovations. Turbo Expo: Power for Land, Sea, and Air. June 2024, V005T06A006. DOI: 10.1115/GT2024-123714. eprint: [https://doi.org/10.1115/GT2024-123714](https://asmedigitalcollection.asme.org/GT/proceedings-pdf/GT2024/87974/V005T06A006/7369301/v005t06a006-gt2024-123714.pdf).
- [21] AC-9 Aircraft Environmental Systems Committee. *Air conditioning, helicopter, general requirements for*. Tech. rep. 400 Commonwealth Drive, Warrendale, PA, United States: SAE International, 2021.
- [22] M. E. Mondéjar, M. O. McLinden, and E. W. Lemmon. “Thermodynamic Properties of trans-1-Chloro-3, 3, 3-trifluoropropene (R1233zd(E)): Vapor Pressure, (p, ρ , T) Behavior, and Speed of Sound Measurements, and Equation of State”. In: *Journal of Chemical & Engi-*

- neering Data 60.8 (July 2015), pp. 2477–2489. ISSN: 1520-5134. DOI: 10.1021/acs.jced.5b00348. URL: <http://dx.doi.org/10.1021/acs.jced.5b00348>.
- [23] X. Xue and T. Wang. “Stall recognition for centrifugal compressors during speed transients”. In: *Applied Thermal Engineering* 153 (May 2019), pp. 104–112. ISSN: 1359-4311. DOI: 10.1016/j.applthermaleng.2019.02.027. URL: <http://dx.doi.org/10.1016/j.applthermaleng.2019.02.027>.
- [24] P. Breedveld. “Concept-Oriented Modeling of Dynamic Behavior”. In: *Bond Graph Modelling of Engineering Systems*. Springer New York, 2011, pp. 3–52. ISBN: 9781441993687. DOI: 10.1007/978-1-4419-9368-7_1. URL: http://dx.doi.org/10.1007/978-1-4419-9368-7_1.
- [25] G. Byrne and P. Ponzi. “Differential-algebraic systems, their applications and solutions”. In: *Computers & Chemical Engineering* 12.5 (May 1988), pp. 377–382. ISSN: 0098-1354. DOI: 10.1016/0098-1354(88)85052-x. URL: [http://dx.doi.org/10.1016/0098-1354\(88\)85052-x](http://dx.doi.org/10.1016/0098-1354(88)85052-x).
- [26] S. E. Mattsson and H. Elmqvist. “Modelica - An International Effort to Design the Next Generation Modeling Language”. In: *IFAC Proceedings Volumes* 30.4 (Apr. 1997), pp. 151–155. ISSN: 1474-6670. DOI: 10.1016/S1474-6670(17)43628-7. URL: [http://dx.doi.org/10.1016/S1474-6670\(17\)43628-7](http://dx.doi.org/10.1016/S1474-6670(17)43628-7).
- [27] R. Gani and I. T. Cameron. “Modelling for dynamic simulation of chemical processes: the index problem”. In: *Chemical Engineering Science* 47.5 (Apr. 1992), pp. 1311–1315. ISSN: 0009-2509. DOI: 10.1016/0009-2509(92)80252-8. URL: [http://dx.doi.org/10.1016/0009-2509\(92\)80252-8](http://dx.doi.org/10.1016/0009-2509(92)80252-8).
- [28] B. P. Rasmussen. “Dynamic modeling for vapor compression systems—Part I: Literature review”. In: *HVAC&R Research* 18.5 (Sept. 2012), pp. 934–955. ISSN: 1938-5587. DOI: 10.1080/10789669.2011.582916. URL: <http://dx.doi.org/10.1080/10789669.2011.582916>.
- [29] G. L. Wedekind and W. F. Stoecker. “Theoretical Model for Predicting the Transient Response of the Mixture-Vapor Transition Point in Horizontal Evaporating Flow”. In: *Journal of Heat Transfer* 90.1 (Feb. 1968), pp. 165–174. ISSN: 1528-8943. DOI: 10.1115/1.3597448. URL: <http://dx.doi.org/10.1115/1.3597448>.
- [30] R. Moradi et al. “Assumption-free modeling of a micro-scale organic Rankine cycle system based on a mass-sensitive method”. In: *Energy Conversion and Management* 245 (Oct. 2021), p. 114554. ISSN: 0196-8904. DOI: 10.1016/j.enconman.2021.114554. URL: <http://dx.doi.org/10.1016/j.enconman.2021.114554>.
- [31] J. Oh, H. Jeong, and H. Lee. “Experimental and numerical analysis on low-temperature off-design organic Rankine cycle in perspective of mass conservation”. In: *Energy* 234 (Nov. 2021), p. 121262. ISSN: 0360-5442. DOI: 10.1016/j.energy.2021.121262. URL: <http://dx.doi.org/10.1016/j.energy.2021.121262>.
- [32] R. Moradi and L. Cioccolanti. “Modelling approaches of micro and small-scale organic Rankine cycle systems: A critical review”. In: *Applied Thermal Engineering* 236 (Jan. 2024), p. 121505. ISSN: 1359-4311. DOI: 10.1016/j.applthermaleng.2023.121505. URL: <http://dx.doi.org/10.1016/j.applthermaleng.2023.121505>.
- [33] S. Bendapudi, J. E. Braun, and E. A. Groll. “A comparison of moving-boundary and finite-volume formulations for transients in centrifugal chillers”. In: *International Journal of Refrigeration* 31.8 (Dec. 2008), pp. 1437–1452. ISSN: 0140-7007. DOI: 10.1016/j.ijrefrig.2008.03.006. URL: <http://dx.doi.org/10.1016/j.ijrefrig.2008.03.006>.
- [34] A. Desideri et al. “Comparison of Moving Boundary and Finite-Volume Heat Exchanger Models in the Modelica Language”. In: *Energies* 9.5 (May 2016), p. 339. ISSN: 1996-1073. DOI: 10.3390/en9050339. URL: <http://dx.doi.org/10.3390/en9050339>.
- [35] J. MacArthur and E. Grald. “Unsteady compressible two-phase flow model for predicting cyclic heat pump performance and a comparison with experimental data”. In: *International Journal of Refrigeration* 12.1 (Jan. 1989), pp. 29–41. ISSN: 0140-7007. DOI: 10.1016/0140-7007(89)90009-1. URL: [http://dx.doi.org/10.1016/0140-7007\(89\)90009-1](http://dx.doi.org/10.1016/0140-7007(89)90009-1).
- [36] X.-D. He, S. Liu, and H. H. Asada. “Modeling of Vapor Compression Cycles for Multivariable Feedback Control of HVAC Systems”. In: *Journal of Dynamic Systems,*

- Measurement, and Control* 119.2 (June 1997), pp. 183–191. ISSN: 1528-9028. DOI: 10.1115/1.2801231. URL: <http://dx.doi.org/10.1115/1.2801231>.
- [37] C. Cai et al. “Assessment of void fraction models and correlations for subcooled boiling in vertical upflow in a circular tube”. In: *International Journal of Heat and Mass Transfer* 171 (2021), p. 121060. ISSN: 0017-9310. DOI: <https://doi.org/10.1016/j.ijheatmasstransfer.2021.121060>. URL: <https://www.sciencedirect.com/science/article/pii/S0017931021001630>.
- [38] B. T. Beck and G. L. Wedekind. “A Generalization of the System Mean Void Fraction Model for Transient Two-Phase Evaporating Flows”. In: *Journal of Heat Transfer* 103.1 (Feb. 1981), pp. 81–85. ISSN: 1528-8943. DOI: 10.1115/1.3244436. URL: <http://dx.doi.org/10.1115/1.3244436>.
- [39] M. L. Huber et al. “The NIST REFPROP Database for Highly Accurate Properties of Industrially Important Fluids”. In: *Industrial & Engineering Chemistry Research* 61.42 (June 2022), pp. 15449–15472. ISSN: 1520-5045. DOI: 10.1021/acs.iecr.2c01427. URL: <http://dx.doi.org/10.1021/acs.iecr.2c01427>.
- [40] F. Casella and C. Richter. “ExternalMedia: A Library for Easy Re-Use of External Fluid Property Code in Modelica ExternalMedia: A Library for Easy Re-Use of External Fluid Property Code in Modelica”. In: *Proceedings 6th International Modelica Conference* (Sept. 2010).
- [41] P. Fritzson. “The Modelica Standard Library”. In: *Introduction to Modeling and Simulation of Technical and Physical Systems with Modelica*. Hoboken, NJ, USA: John Wiley & Sons, Inc., Apr. 2012, pp. 157–168.
- [42] T. L. McKinley and A. G. Alleyne. “An advanced nonlinear switched heat exchanger model for vapor compression cycles using the moving-boundary method”. In: *International Journal of Refrigeration* 31.7 (Nov. 2008), pp. 1253–1264. ISSN: 0140-7007. DOI: 10.1016/j.ijrefrig.2008.01.012. URL: <http://dx.doi.org/10.1016/j.ijrefrig.2008.01.012>.
- [43] A. F. Mills. “Convection fundamentals and correlations”. In: *Heat and Mass Transfer*. Routledge, May 2018, pp. 243–370.
- [44] D. Lee et al. “Evaporation heat transfer coefficient and pressure drop of R-1233zd(E) in a brazed plate heat exchanger”. In: *Applied Thermal Engineering* 130 (Feb. 2018), pp. 1147–1155. ISSN: 1359-4311. DOI: 10.1016/j.applthermaleng.2017.11.088. URL: <http://dx.doi.org/10.1016/j.applthermaleng.2017.11.088>.
- [45] M. M. Shah. “Comprehensive correlations for heat transfer during condensation in conventional and mini/micro channels in all orientations”. In: *International Journal of Refrigeration* 67 (July 2016), pp. 22–41. ISSN: 0140-7007. DOI: 10.1016/j.ijrefrig.2016.03.014. URL: <http://dx.doi.org/10.1016/j.ijrefrig.2016.03.014>.
- [46] Y.-J. Chang and C.-C. Wang. “A generalized heat transfer correlation for louver fin geometry”. In: *International Journal of Heat and Mass Transfer* 40.3 (Feb. 1997), pp. 533–544. ISSN: 0017-9310. DOI: 10.1016/0017-9310(96)00116-0. URL: [http://dx.doi.org/10.1016/0017-9310\(96\)00116-0](http://dx.doi.org/10.1016/0017-9310(96)00116-0).
- [47] A. J. Glassman. *Turbine Design and Application*. Technical Report 19950015924. Lewis Research Center Cleveland, OH, USA: NASA, June 1994.
- [48] P. P. Walsh and P. Fletcher. *Gas Turbine Performance*. en. 2nd ed. Chichester, England: Wiley-Blackwell, Apr. 2008.
- [49] F. Casella and A. Leva. “Modelling of thermo-hydraulic power generation processes using Modelica”. In: *Mathematical and Computer Modelling of Dynamical Systems* 12.1 (Feb. 2006), pp. 19–33. ISSN: 1744-5051. DOI: 10.1080/13873950500071082. URL: <http://dx.doi.org/10.1080/13873950500071082>.
- [50] *Flow Equations for Sizing Control Valves*. ANSI/ISA-75.01.01. Research Triangle Park, NC: International Society of Automation, Nov. 2007.
- [51] Danfoss. *Electric expansion valve, ETS 12C*. <https://store.danfoss.com/en/Climate-Solutions-for-cooling/Valves/Expansion-valves/Electric-Expansion-Valves/Electric-Expansion-Valves-for-HVAC-R/Electric-expansion-valve-%20ETS-12C/p/034G7502?documenttype=Brochure>. Accessed: 2024-12-17.

- [52] P. Muroi. *Valvole di regolazione per processi industriali*. PEG, 1991. ISBN: 9788870670745. URL: <https://books.google.nl/books?id=nzvp0AEACAAJ>.
- [53] X.-D. He. “Dynamic modeling and multi-variable control of vapor compression cycles in air conditioning systems”. PhD thesis. Cambridge, MA: Massachusetts Institute of Technology, Department of Mechanical Engineering, June 1996.
- [54] L. R. Petzold. “A description of dassl: a differential/algebraic system solver”. In: *Proceedings of the 10th International Association for Mathematics and Computers in Simulation (IMACS) World Congress*. 1982. URL: <https://api.semanticscholar.org/CorpusID:208868027>.
- [55] A. Outtagarts, P. Haberschill, and M. Lallemand. “The transient response of an evaporator fed through an electronic expansion valve”. In: *International Journal of Energy Research* 21.9 (July 1997), pp. 793–807. ISSN: 1099-114X. DOI: 10.1002/(sici)1099-114x(199707)21:9<793::aid-er297>3.0.co;2-p. URL: [http://dx.doi.org/10.1002/\(SICI\)1099-114X\(199707\)21:9%3C793::AID-ER297%3E3.0.CO;2-P](http://dx.doi.org/10.1002/(SICI)1099-114X(199707)21:9%3C793::AID-ER297%3E3.0.CO;2-P).
- [56] C. V. Halbe et al. “A Numerical Analysis of the Effects of Liquid Carryover on the Performance of a Two-Stage Centrifugal Compressor”. In: *Volume 2B: Turbo-machinery*. GT2018. American Society of Mechanical Engineers, June 2018. DOI: 10.1115/gt2018-77015. URL: <http://dx.doi.org/10.1115/GT2018-77015>.
- [57] J. E. Pacheco and H. A. Kidd. “Assessing Liquid Droplet Erosion Potential In Centrifugal Compressor Impellers.” In: *Proceedings of the 38th Turbomachinery Symposium*. 2009. URL: <https://api.semanticscholar.org/CorpusID:16408138>.
- [58] S. Skogestad and I. Postlethwaite. *Multivariable Feedback Control: Analysis and Design*. Hoboken, NJ, USA: John Wiley & Sons, Inc., 2005. ISBN: 9780470011676. URL: <https://books.google.nl/books?id=97iAEAAAQBAJ>.
- [59] E. Bristol. “On a new measure of interaction for multivariable process control”. In: *IEEE Transactions on Automatic Control* 11.1 (Jan. 1966), pp. 133–134. ISSN: 0018-9286. DOI: 10.1109/tac.1966.1098266. URL: <http://dx.doi.org/10.1109/TAC.1966.1098266>.
- [60] S. Estrada-Flores et al. “Simulation of transient behaviour in refrigeration plant pressure vessels: mathematical models and experimental validation”. In: *International Journal of Refrigeration* 26.2 (Mar. 2003), pp. 170–179. ISSN: 0140-7007. DOI: 10.1016/S0140-7007(02)00081-6. URL: [http://dx.doi.org/10.1016/S0140-7007\(02\)00081-6](http://dx.doi.org/10.1016/S0140-7007(02)00081-6).
- [61] H. Qiao et al. “An advanced switching moving boundary heat exchanger model with pressure drop”. In: *International Journal of Refrigeration* 65 (May 2016), pp. 154–171. ISSN: 0140-7007. DOI: 10.1016/j.ijrefrig.2016.01.026. URL: <http://dx.doi.org/10.1016/j.ijrefrig.2016.01.026>.

Appendices

A Full Heat Exchanger Derivations

To support the discussion on the heat exchanger model equations in Section 2.2.1, the full derivation of the equations presented in the paper are provided here. Starting from the general differential forms of the conservation of mass and energy given by

$$\frac{\partial \rho}{\partial t} + \frac{\partial \rho u}{\partial x} = 0 \quad (1)$$

$$\frac{\partial \rho h}{\partial t} + \frac{\partial \rho u h}{\partial x} = \frac{\partial P}{\partial t} + \frac{\dot{Q}}{A_c}, \quad (2)$$

the following sections will focus on finding the integral forms for the working fluid, glycol-water side and air side. Additionally, the derivation of the wall temperature energy equation will be discussed separately.

A.1 Working Fluid

For the Moving Boundary (MB) method, (1) and (2) are integrated with respect to the spatial coordinate x for the distinct control volumes in the heat exchanger, separated by the phase transitioning boundary. In general, starting with (1), integrating over a time-varying control volume length $L(t)$ yields

$$\int_{L(t)} \left(\frac{\partial \rho_f}{\partial t} + \frac{\partial \rho_f u_f}{\partial x} \right) dx = 0. \quad (50)$$

When multiplied by the constant cross-sectional area A_c , this length integral becomes a volume integral, where the volume, $V(t)$, is a function of time. The resulting expression is given by

$$\int_{V(t)} \left(\frac{\partial \rho_f}{\partial t} \right) dV + \int_{V(t)} \left(\frac{\partial \rho_f u_f}{\partial x} \right) dV = 0, \quad (51)$$

where the single integral is split into two. The first term represents the change of mass within the control volume and the second term represents the convection of mass in and out of the control volume. Using the Leibniz rule for the first term and the Gauss theorem for the second, the following is obtained:

$$\frac{d}{dt} \left(\int_{V(t)} \rho_f dV \right) - \int_{\partial V} \left(\rho_f \frac{dL}{dt} \right) \cdot \mathbf{n} dA_c + \int_{\partial V} (\rho_f u_f) \cdot \mathbf{n} dA_c = 0. \quad (52)$$

Here, ∂V represents the outer surface of the volume, and \mathbf{n} is the orthonormal direction pointing out of the control volume. Noting that only one-dimensional flow is considered with its properties assumed uniform over the cross-sectional area, the surface integrals can be simplified to only the inlet and outlet surfaces of the control volume. This yields

$$\begin{aligned} \frac{d}{dt} \left(\int_{V(t)} \rho_f dV \right) &= A_c \rho_{f,in} \left(u_{f,in} - \frac{dL}{dt} \Big|_{in} \right) - A_c \rho_{f,out} \left(u_{f,out} - \frac{dL}{dt} \Big|_{out} \right) \\ \implies \frac{d}{dt} (A_c L \bar{\rho}_f) &= \dot{m}_{f,in} - \dot{m}_{f,out} \\ A_c \left(L \frac{d\bar{\rho}_f}{dt} + \bar{\rho}_f \frac{dL}{dt} \right) &= \dot{m}_{f,in} - \dot{m}_{f,out}, \end{aligned} \quad (53)$$

where $\bar{\rho}_f = \frac{1}{A_c L} \int_V \rho_f dV$. The mass flow rates in and out of the volume, $\dot{m}_{f,in}$ and $\dot{m}_{f,out}$, include the effects of moving boundaries, i.e. $\frac{dL}{dt} \Big|_{in}$ and $\frac{dL}{dt} \Big|_{out}$. Depending on which control volume is considered, these boundary velocities are either equal to those of phase transition boundaries, or zero at the inlet and outlet of the heat exchanger. Since both the average density $\bar{\rho}_f$ and control volume length L are functions of time, the chain rule is applied to find the final form of (53). The derivational steps presented

above for the conservation of mass can also be applied to the energy equation. Doing so yields

$$\begin{aligned}
\frac{d}{dt} \left(\int_{V(t)} \rho_f h_f dV \right) - A_c L \frac{dP_f}{dt} &= A_c \rho_{f,in} h_{f,in} \left(u_{f,in} - \frac{dL}{dt} \Big|_{in} \right) \\
&\quad - A_c \rho_{f,out} h_{f,out} \left(u_{f,out} - \frac{dL}{dt} \Big|_{out} \right) + \dot{Q}_f \\
\Rightarrow \frac{d}{dt} \left(A_c L \overline{(\rho h)}_f \right) - A_c L \frac{dP_f}{dt} &= \dot{m}_{f,in} h_{f,in} - \dot{m}_{f,out} h_{f,out} + \dot{Q}_f \\
A_c \left(L \left(\frac{d \overline{(\rho h)}_f}{dt} - \frac{dP_f}{dt} \right) + \overline{(\rho h)}_f \frac{dL}{dt} \right) &= \dot{m}_{f,in} h_{f,in} - \dot{m}_{f,out} h_{f,out} + \dot{Q}_f.
\end{aligned} \tag{54}$$

Note that the final forms of (53) and (54) are directly reflected by (3) and (4), respectively, and the further derivation of the working fluid equations is explained in the main content of the paper.

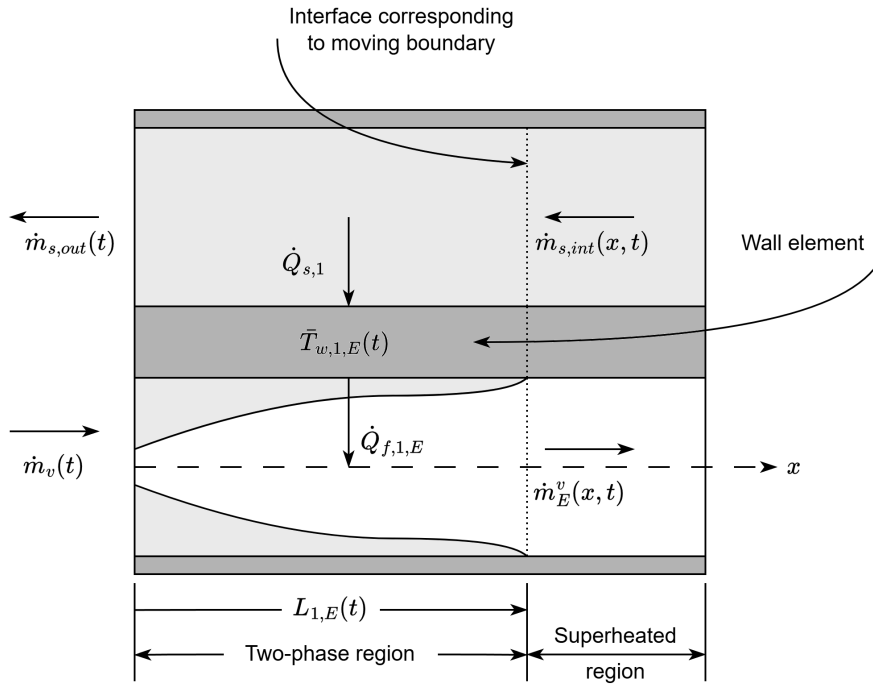


Figure 32: Evaporator schematic of Figure 4 including counter-flow glycol-water stream. The liquid phase is indicated in light gray, while the wall element is dark gray.

A.2 Glycol-water Side

The evaporator is shown once more schematically in Figure 32, where the wall element and glycol-water stream are included. Here it is important to note that the flow direction of the glycol-water is opposite to that of the refrigerant. The hot side of the glycol-water is thus on the right and the cold side on the left. For the evaporator, two control volumes of the glycol-water can be seen, which are separated by an interface that corresponds to the moving boundary of the working fluid. For each of these control volumes, the differential form of the conservation equations (1) and (2) can be integrated analogously to the method presented for the working fluid equations in the previous section. As such, these integral equations for the glycol-water are given by

$$\begin{aligned}
\frac{d}{dt} (A_c L \bar{\rho}_s) &= \dot{m}_{s,in} - \dot{m}_{s,out} \\
\frac{d}{dt} \left(A_c L \overline{(\rho h)}_s \right) - A_c L \frac{dP_s}{dt} &= \dot{m}_{s,in} h_{s,in} - \dot{m}_{s,out} h_{s,out} + \dot{Q}_s.
\end{aligned} \tag{55}$$

The chain rule can then be applied to the left hand sides for each of the time-varying variables. This results in

$$A_c \left(L \frac{d\bar{\rho}_s}{dt} + \bar{\rho}_s \frac{dL}{dt} \right) = \dot{m}_{s,in} - \dot{m}_{s,out} \quad (56)$$

$$A_c \left(L \left(\frac{d(\overline{\rho h})_s}{dt} - \frac{dP_s}{dt} \right) + (\overline{\rho h})_s \frac{dL}{dt} \right) = \dot{m}_{s,in} h_{s,in} - \dot{m}_{s,out} h_{s,out} + \dot{Q}_s.$$

The dynamic states are chosen as P_s and $h_{s,out}$. Given that $\bar{h}_s = \frac{1}{2}(h_{s,in} + h_{s,out})$ and $\bar{\rho} = f(P_s, \bar{h}_s)$, further expanding to the time derivatives of the dynamic states then yields

$$\frac{d\bar{\rho}_s}{dt} = \left(\frac{\partial \rho_s}{\partial P} \right)_h \frac{dP}{dt} + \left(\frac{\partial \rho_s}{\partial h} \right)_P \frac{d\bar{h}_s}{dt}$$

$$\frac{d\bar{h}_s}{dt} = \frac{1}{2} \left(\frac{dh_{s,in}}{dt} + \frac{dh_{s,out}}{dt} \right) \quad (57)$$

$$\frac{d(\overline{\rho h})_s}{dt} = \bar{\rho}_s \frac{d\bar{h}_s}{dt} + \bar{h}_s \frac{d\bar{\rho}_s}{dt}$$

In contrast with the derivation of the working fluid equations, $\frac{dL}{dt}$ is now known from the working fluid equations. This means that the system in (56) can be solved for the time derivatives of the dynamic states, i.e. $\frac{dP_s}{dt}$ and $\frac{dh_{s,out}}{dt}$, given $\frac{dh_{s,in}}{dt}$ and $\frac{dL}{dt}$ as inputs, using the methods described in Section 2.2.1.

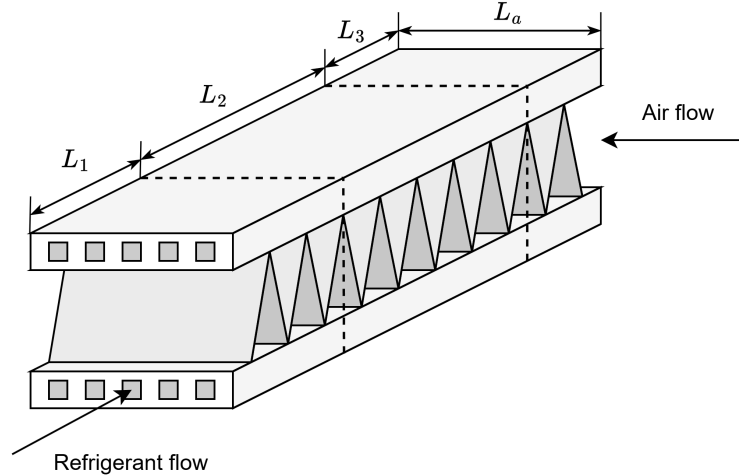


Figure 33: Schematic of condenser section with cross-flow orientation.

A.3 Air Side

For the air side equations, the condenser section in Figure 33 is considered. Since the boundaries of the working fluid control volumes change based on the phase transitioning, the cross-sectional area of the air flow changes accordingly. The integral energy conservation equation is then, recalling the assumption of uniform mass flow rate and constant pressure, given by

$$\frac{d}{dt} \left(\frac{L}{L_{tot}} A_{c,a} L_a (\overline{\rho h})_a \right) = \dot{m}_a \frac{L}{L_{tot}} (h_{a,in} - h_{a,out}) - \dot{Q}_a. \quad (58)$$

Expanding the time derivative on the left hand side then yields

$$\frac{A_{c,a} L_a}{L_{tot}} \left(L \frac{d(\overline{\rho h})_a}{dt} + (\overline{\rho h})_a \frac{dL}{dt} \right) = \dot{m}_a \frac{L}{L_{tot}} (h_{a,in} - h_{a,out}) - \dot{Q}_a. \quad (59)$$

Given that $\bar{h}_a = \frac{1}{2}(h_{a,in} + h_{a,out})$, $\bar{\rho}_a = f(P_a, \bar{h}_a)$, and that the pressure is assumed constant, the time derivative of the average product of density and enthalpy is given by

$$\begin{aligned}\frac{d\bar{\rho}_a}{dt} &= \left(\frac{\partial \rho_a}{\partial h}\right)_P \frac{d\bar{h}_a}{dt} \\ \frac{d\bar{h}_a}{dt} &= \frac{1}{2} \left(\frac{dh_{a,in}}{dt} + \frac{dh_{a,out}}{dt}\right) \\ \frac{d(\bar{\rho}h)_a}{dt} &= \bar{\rho}_a \frac{d\bar{h}_a}{dt} + \bar{h}_a \frac{d\bar{\rho}_a}{dt}.\end{aligned}\tag{60}$$

With $\frac{dh_{a,in}}{dt}$ being an input and $h_{a,out}$ as dynamic state, this means that the only unknown is the time derivative of the dynamic state, i.e. $\frac{dh_{a,out}}{dt}$. Solving the system of equations for the air side is then done as explained in Section 2.2.1.

A.4 Wall Energy

The wall energy equation follows from the Lumped Thermal Capacity (LTC) approach for transient heat transfer [43]. Starting from the differential form, the general wall energy equation is given by

$$\frac{\partial(\rho_w c_w T_w)}{\partial t} = \frac{\dot{Q}_{in}}{A_w} - \frac{\dot{Q}_{out}}{A_w}.\tag{61}$$

Integrating along the heat exchanger length, assuming constant cross-sectional wall area A_w , yields

$$\int_{V(t)} \left(\frac{\partial(\rho_w c_w T_w)}{\partial t}\right) dV = \dot{Q}_{in} - \dot{Q}_{out}.\tag{62}$$

Next, applying the Leibniz rule results in

$$\frac{d}{dt} \left(\int_{V(t)} \rho_w c_w T_w dV\right) - \int_{\partial V} \left(\rho_w c_w T_w \frac{dL}{dt}\right) \cdot \mathbf{n} dA_w = \dot{Q}_{in} - \dot{Q}_{out},\tag{63}$$

which, considering that the wall density and specific heat capacity are uniform throughout the wall, further simplifies to

$$\rho_w c_w A_w \left(L \frac{d\bar{T}_w}{dt} + \bar{T}_w \frac{dL}{dt}\right) - \rho_w c_w A_w \left(T_w|_{down} \frac{dL}{dt}\Big|_{down} - T_w|_{up} \frac{dL}{dt}\Big|_{up}\right) = \dot{Q}_{in} - \dot{Q}_{out}.\tag{64}$$

Here, the up and $down$ subscripts denote conditions at the upstream and downstream boundaries of the wall element. Considering that $\frac{dL}{dt} = \frac{dL}{dt}\Big|_{down} - \frac{dL}{dt}\Big|_{up}$, it follows that

$$L \frac{d\bar{T}_w}{dt} = (\bar{T}_w - T_w|_{up}) \frac{dL}{dt}\Big|_{up} - (\bar{T}_w - T_w|_{down}) \frac{dL}{dt}\Big|_{down} + \frac{\dot{Q}_{in} - \dot{Q}_{out}}{\rho_w c_w A_w}.\tag{65}$$

From this expression, the two additional terms on the right hand side account for the moving upstream and downstream boundaries of the wall element, respectively. Since for the evaporator the upstream boundary of the two-phase wall element is stationary, the above equation can indeed be recognized in (15) in Section 2.2.1.

B Model Constants

In this appendix, the model equations used for the models presented in the paper are reported. To this end, the appendix contains four sections: constants regarding the fluid models, heat exchangers, compressor, and expansion valve.

B.1 Fluid Models

In total, three fluid models are used. For the refrigerant fluid model, the ExternalMedia package is used, while for the glycol-water and air models, the Modelica Standard Library are used. The names of these models are listed in Table 7.

Table 7: Fluid models used in Modelica and their corresponding packages.

Fluid	Model name	Package
Refrigerant	R-1233zd(E)	ExternalMedia
Glycol-water	WaterIF97_ph	Modelica Standard Library
Air	Air_ph	Modelica Standard Library

B.2 Heat Exchangers

For the heat exchangers, different model constants are used for the evaporator and condenser. Therefore, the following subsections report on both heat exchangers.

B.2.1 Evaporator

In Table 8, the model constants of the evaporator are listed. Note that only one value for the cross-sectional flow area and channel perimeter is provided, since the channels of the glycol-water and refrigerant stream are assumed identical. The constants were computed from data sheets and drawings from the heat exchanger manufacturer.

Table 8: Evaporator constants.

Name	Symbol	Value	Unit
Total length	$L_{tot,E}$	0.530	m
Cross-sectional area flow	$A_{c,E}$	$3.96 \cdot 10^{-3}$	m ²
Flow channel perimeter	C_E	3.86	m
Cross-sectional area wall	$A_{c,w,E}$	$1.66 \cdot 10^{-3}$	m ²
Mean void fraction	$\bar{\gamma}_E$	0.996	-
Wall density	$\rho_{w,E}$	7980	kg/m ³
Wall specific heat capacity	$c_{w,E}$	500	J/(kg K)
Nominal glycol-water pressure	$P_{s,nom}$	1.01	bar

B.2.2 Condenser

In the condenser, the refrigerant flows in a two-pass configuration, as shown in the top schematic of Figure 34. Due to this flow configuration, the geometrical constants required for the model equations depend on where the phase transitioning boundaries are located, e.g. the cross-sectional area of the first pass is larger than that of the second pass. Since it is not convenient to dynamically account for this change in geometry, an equivalent single-pass configuration is used, shown in the bottom schematic of Figure 34, where the geometrical constants no longer depend on the location along the flow path. Here, all geometrical parameters, such as the cross-sectional area and flow perimeter, are averaged between the first and second pass.

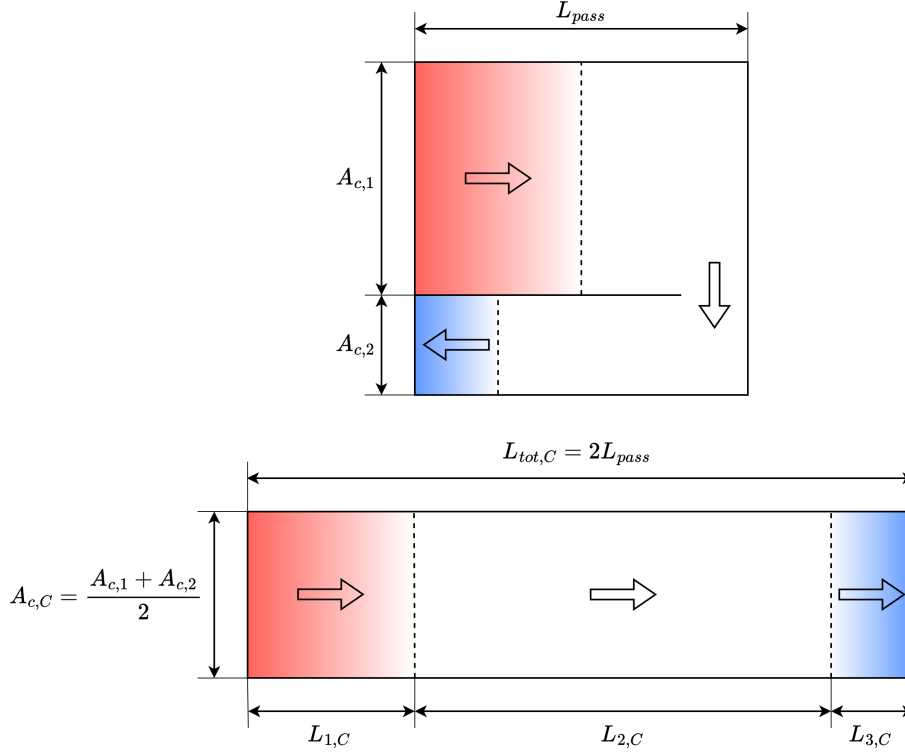


Figure 34: Schematic of real (top) and equivalent single-pass (bottom) configuration for the refrigerant flow in the condenser. The superheated control volume is indicated in red, the two-phase control volume in white, and the subcooled volume in blue. The transparent arrows indicate the flow direction.

In Table 9, the constants of the condenser model are reported, given the assumption of a single-pass refrigerant flow. The geometrical properties of the heat exchanger follow from data sheets provided by the manufacturer, where the Chang and Wang constant, Ξ , follows from the fin geometry.

Table 9: Condenser constants.

Name	Symbol	Value	Unit
Total length	$L_{tot,C}$	1.5	m
Cross-sectional area refrigerant	$A_{c,C}$	$7.86 \cdot 10^{-4}$	m ²
Refrigerant flow perimeter	\mathcal{C}_C	3.01	m
Cross-sectional area wall	$A_{c,w,C}$	$1.46 \cdot 10^{-3}$	m ²

Mean void fraction	$\bar{\gamma}_C$	0.944	-
Wall density	$\rho_{w,C}$	2710	kg/m ³
Wall specific heat capacity	$c_{w,C}$	900	J/(kg K)
Total cross-sectional area air side	$A_{c,a}$	0.399	m ²
Fin efficiency	η_{fin}	0.6	-
Total heat transfer area air side	$A_{h,a}$	21.9	m ²
Total area fins	A_{fin}	19.3	m ²
Chang and Wang constant	Ξ	0.369	-
Air pressure	P_a	1.01	bar

B.3 Compressor

In Table 10, the compressor constants are given. Note that the performance maps are also constant, constructed from experimental data provided by the manufacturer.

Table 10: Compressor constants.

Name	Symbol	Value	Unit
Reference temperature	T_{ref}	25.0	°C
Reference pressure	P_{ref}	0.720	bar
Reference speed	Ω_{ref}	80.0	kRPM

B.4 Expansion Valve

In Table 11, the Electronic Expansion Valve constants are shown. The nominal valve flow area follows from the steady-state conditions at the initialisation point, i.e. the model equations presented in Section 2.2.3 are solved at the initialisation point for A_v with the nominal mass flow rate from the steady-state solution.

Table 11: Expansion valve constants.

Name	Symbol	Value	Unit
Nominal valve flow area	A_v	$4.07 \cdot 10^{-5}$	m ²
Recovery factor	F_L	0.9	-

C Loop Shaping

Given the diagonal control structure depicted in Figure 22, the individual Single Input Single Output (SISO) control loops of the VCC are shaped using a loop shaping approach. The key idea of loop shaping is to design controller K such that the loop transfer function $L = GK$ has desirable magnitude and phase characteristics over a range of frequencies. In general, three main goals are to be achieved [58]:

- For good reference tracking and disturbance rejection, the loop gains $|L|$ should be large at low frequencies. Additionally, $L(s)$ should contain at least one integrator for each integrator in the reference signal $r(s)$.
- To reduce the effects of noise, the loop gains $|L|$ should be small at high frequencies, with a typical roll-off rate of 2, i.e., the slope of $|L|$ should be -2 at high frequencies.
- To ensure stability and robustness, the slope of $|L|$ should be -1 around the crossover frequency (the frequency where $|L|$ first crosses 1), with sufficient gain and phase margins of at least 2 dB and 30 degrees, respectively.

Examining the diagonal elements of the transfer function G of the VCC, several key observations can be made, as shown in blue in Figure 35.

The phase plot of the first element of G (mapping air mass flow rate to condenser pressure) shows a 180-degree phase shift at low frequencies, meaning that an increase in input results in a decrease in output. To ensure negative feedback and prevent instability, the first loop therefore requires a negative proportional gain. All diagonal elements exhibit steady-state gains smaller than 1 with a slope of 0, requiring integral controllers to achieve sufficient steady-state gains. Since a slope of -1 at low frequencies is sufficient for the setpoint tracking of the compressor map reconstruction, Proportional-Integral (PI) controllers are used for all control loops.

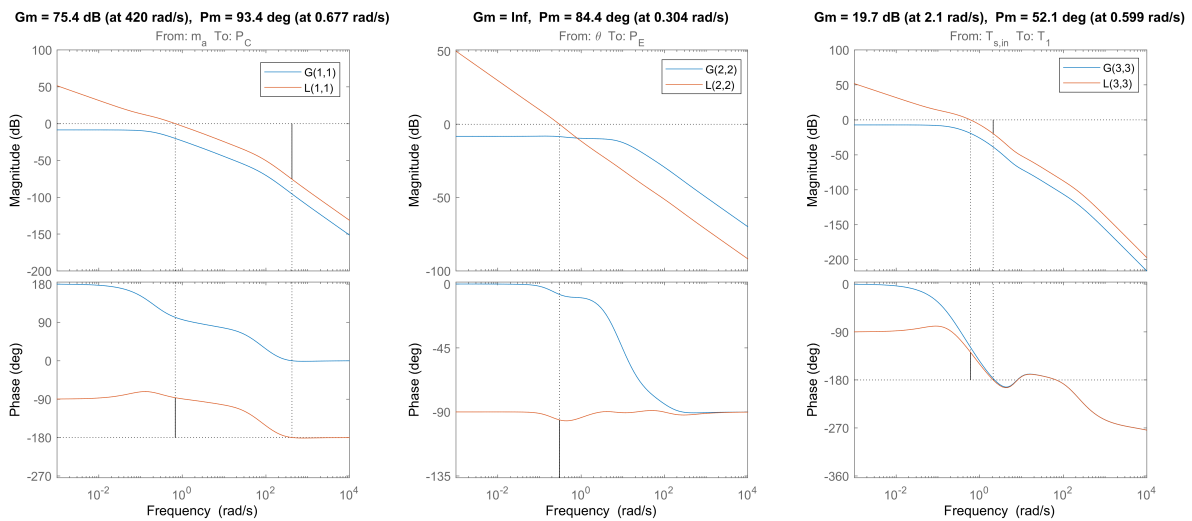


Figure 35: Bode diagrams of diagonal plant elements, G , and loop transfer function elements, L , with decentralized controller K . From left to right, the panels show the mapping from the air mass flow rate \dot{m}_a to the condenser pressure P_C , the valve opening θ to the evaporator pressure P_E , and the air inlet temperature $T_{a,in}$ to the compressor inlet temperature T_1 .

The first step in tuning the PI controllers is selecting the integral time constants. The integral time constant τ_I determines the frequency $\omega_I = \frac{1}{\tau_I}$ up to which integral action dominates. At frequencies much lower than ω_I , the PI controller's magnitude slope is -1 , while at higher frequencies, it flattens to 0.

A naive approach would be to set τ_I very low, making the frequency range over which integral action dominates very large. However, this means the 90-degree phase lag introduced by integral action occurs at higher frequencies, reducing the phase margin at the crossover frequency and potentially leading to instability. To ensure adequate phase margin (preferably above 30 degrees), τ_I values are therefore chosen based on the frequencies where G transitions from 0 to negative slope. Respectively, they are $\tau_{I,1} = 10$

s/rad, $\tau_{I,2} = 0.1$ s/rad, and $\tau_{I,1} = 10$ s/rad, as listed in Table 6. These values ensure proper low-frequency behaviour without excessive phase lag close to the crossover frequency.

To increase system bandwidth, proportional gains are adjusted iteratively. While increasing K_I improves bandwidth, it also reduces gain and phase margins, requiring careful balancing. The final proportional gains are $K_{I,1} = -10$, $K_{I,2} = 0.08$, and $K_{I,3} = 9$, as shown in Table 6.

The resulting loop transfer functions L are shown in Figure 35 in orange, exhibiting gain and phase margins well beyond the required 2 dB and 30 degrees. However, analysis of the closed-loop sensitivity function S in Figure 23 reveals a peak upper singular value of $\max(\bar{\sigma}(S)) \approx 2$, which approaches the recommended limit. This discrepancy highlights a fundamental difference between SISO and Multiple Input Multiple Output (MIMO) stability considerations. While SISO margins can be defined in terms of gain and phase, MIMO stability depends on input directionality, where specific input combinations can yield significantly different responses. Consequently, tuning the proportional gains based solely on SISO loop shaping would lead to overly aggressive settings. Instead, the peak of S was therefore used as the tuning criterion for K_I , ensuring robust stability across all input directions while maintaining adequate performance.

Part II

Literature Study

Literature Study Summary

Aviation's growing contribution to greenhouse gas (GHG) emissions has intensified research into More Electric Aircraft (MEA) concepts, where electrically powered non-propulsive systems replace traditional ones to improve efficiency and reduce environmental impact. The Environmental Control System (ECS) is the main consumer of non-propulsive power, traditionally relying on the Air Cycle Machine (ACM) powered by bleed air from the main engine. In lieu of electrifying the ACM, utilization of the Vapour Compression Cycle (VCC) offers a promising alternative for the refrigeration tasks of the ECS, primarily for its higher thermodynamic efficiency. However, the implementation of the VCC in the ECS architecture introduces challenges related to excessive system mass, component complexity, and complicated dynamic operation. To address these challenges, at Delft University of Technology (TU Delft), the Inverse organic Rankine cycle Integrated System (IRIS) test facility was developed to investigate the performance of a novel VCC-based ECS configuration, and support research on integrated design optimization methods for the preliminary design of novel ECSs. Two key innovations are of particular interest in the IRIS: the use of a high-speed electric centrifugal compressor, and the use of the low Global Warming Potential (GWP) R-1233zd(E) refrigerant. Given these innovations, the main goals of the facility are threefold: evaluating centrifugal VCC performance for application in aviation, investigating the aerothermal behaviour of the heat exchangers in the VCC, and analysing the refrigeration cycle using R-1233zd(E) and other low-GWP refrigerants.

The literature study highlights that while current integrated design methods for ECSs rely solely on steady-state models, a thorough understanding of the VCC's dynamic behaviour is essential to fully exploit its potential for ECS applications. Developing a dynamic model of the IRIS provides insight into the physical principles that govern these dynamics. Since the IRIS is a test rig with a flexible component architecture, a modular modelling approach is most suitable, allowing individual components to be modelled separately before integration into a full system model. The equation-based Modelica language offers an appropriate framework for this modular approach. According to common practices in the literature, the dynamics of the compressor and expansion valve can be neglected, as they evolve on much faster time scales than the slow thermal transients of the heat exchangers. For the heat exchangers, two main modelling approaches were identified: the Moving Boundary (MB) and Finite Control Volume (FCV) methods. Both require models for key variables such as void fraction and heat transfer coefficients. For this, explicit formulations were found to be the most suitable, as implicit correlations introduce computationally expensive algebraic loops. For the compressor, steady-state off-design performance maps can be used with appropriate corrections for varying inlet conditions. The expansion valve can be modelled using static valve sizing equations based on Bernoulli expressions, with empirically adjusted correction coefficients.

Beyond developing a dynamic model of the IRIS, the literature study also examines control system design for the facility. Three main classes of control methods were identified: conventional, advanced, and intelligent controls. Most approaches aim to improve system performance metrics, such as efficiency, disturbance rejection, or actuator effort. However, given the role of the IRIS as a test facility, there is a gap in control strategies specifically designed for testing the novel high-speed centrifugal compressor in the VCC configuration. An advanced control approach is the most suitable, as it provides deeper insight into the physical principles that shape the system's control behaviour.

From the findings of the literature study, two research objectives were synthesized: the **development of a dynamic model of the IRIS** and the **design of a control system for compressor testing**.

II.1

Introduction

Global warming is expected to continue increasing Earth's surface temperature unless global policies to reduce greenhouse gas (GHG) emissions undergo substantial changes. The 2023 synthesis report by the Intergovernmental Panel on Climate Change (IPCC) indicates that rising GHG emissions from human activities have already driven an average global temperature increase of approximately 1.1 °C between 1850–1900 and 2011–2020 [1]. As can be seen in Figure II.1.1, current policies are unfortunately insufficient to flatten this trend enough to limit global warming to a maximum of 2 °C and pursue the more ambitious goal of staying below 1.5 °C, as outlined in the 2015 Paris Agreement [2]. Consequently, catastrophic weather events, such as the recent flooding in the Valencia region in Spain, are likely to occur more frequently and with increased intensity [3]. To mitigate these consequences, it is imperative to take action to reduce GHG emissions wherever possible, minimizing our collective negative impact on the environment.

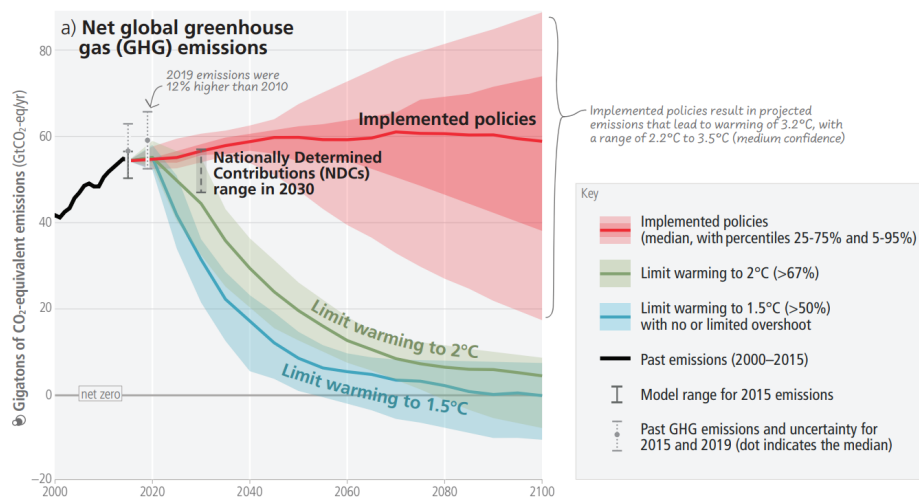


Figure II.1.1: Projections of global Greenhouse Gas (GHG) emission pathways, adapted from [1]. The red range assumes policies as implemented by the end of 2020. The green and blue ranges show pathways that limit global warming to 2 °C and 1.5 °C respectively.

GHG emissions are distributed across various sectors, with aviation currently contributing approximately 2% [4]. Alarmingly, this share is expected to rise as passenger air travel grows at an annual rate of 4%, while other sectors continue to reduce their carbon footprints [5]. A 2015 study by the European Parliament projected that the CO₂ emissions from international aviation could reach 22% of global emissions by 2050 [6]. In response to these concerning trends, the Advisory Council for Aeronautic Research in Europe (ACARE) developed the FlightPath 2050 roadmap, outlining environmental goals for aviation. These include reducing perceptible aircraft noise by 65%, cutting NO_x emissions by 90%,

and lowering CO₂ emissions by 75%, all relative to a typical new aircraft from the year 2000 [7].

To meet these ambitious targets, research in both industry and academia has shifted toward aircraft electrification, with a focus on minimizing weight and specific fuel consumption. The initial step in this transition is the More Electric Aircraft (MEA) concept, which replaces non-propulsive onboard systems with electrical alternatives while maintaining fossil-fuel-powered propulsion. This approach enhances the efficiency of the main engine and auxiliary systems but introduces unique challenges in the generation, distribution, and utilization of electrical power [8]. By focusing on overcoming these challenges, the MEA concept paves the way for the integration of hybrid and fully electric propulsion systems in Hybrid Electric Aircraft (HEA) and All Electric Aircraft (AEA), respectively.

The Environmental Control System (ECS) is the largest consumer of non-propulsive power in an aircraft, responsible for approximately 5% of the total specific fuel consumption [9]. By regulating temperature, pressure, and humidity, the ECS ensures cabin conditions that provide passenger comfort. Improving the efficiency of ECS architectures can significantly reduce fuel consumption, making this an important focus for research [10]. Traditionally, ECS designs for large aircraft rely on the Air Cycle Machine (ACM), which uses high-pressure bleed air from the main engines as its power source [11]. However, since the MEA concept eliminates this power source, alternative thermodynamic cycles are under investigation.

One promising alternative is the Vapour Compression Cycle (VCC), based on the inverse Rankine cycle [12]. The VCC uses phase changes in a working fluid to achieve a higher Coefficient of Performance (COP) compared to the ACM [11]. However, implementing the VCC introduces new challenges, including the need for specialized components and increases in system volume and mass, which may offset its performance benefits. As a result, determining the feasibility of the VCC for future electric aircraft remains a key area of research.

At Delft University of Technology (TU Delft), efforts to address these challenges include the development of novel methodologies for electrically driven VCC-based ECS designs aimed at improving efficiency and reducing environmental impact [13]. Two key innovations under investigation are the use of high-speed centrifugal compressors and a low Global Warming Potential (GWP) alternative to the state-of-the-art R-134a refrigerant. To support this research, the Inverse organic Rankine cycle Integrated System (IRIS) test facility was developed as a modular platform for validating numerical models and assessing VCC performance under experimental conditions. Since current ECS design methodologies rely solely on steady-state analysis, initial experiments focus on characterizing the IRIS under these conditions. However, ECSs inherently operate in dynamic environments, making it essential to also evaluate the transient behaviour of the system. Understanding these dynamics could provide insight into time-dependent phenomena such as thermal inertia, unstable operating regimes, and interactions between system components and control strategies; effects that cannot be fully captured in steady-state analyses. Currently, such dynamic behaviour in the IRIS can only be studied through physical testing. This approach is time-intensive, constrained by hardware limitations, and requires extensive (dis)assembly when testing different components or configurations. Furthermore, achieving consistent steady-state conditions manually has proven challenging due to oscillatory interactions between system components. This limits the flexibility of the IRIS as a testing platform. The issue is particularly significant for centrifugal compressor experiments, where strict operational limits [14] require precise and repeatable system control.

To address these limitations, two main objectives have been identified: developing a transient numerical model of the IRIS and designing a control strategy to enable consistent compressor testing. Defining precise research objectives, however, requires a thorough understanding of VCC modelling and control principles, which is best achieved through a review of existing literature. Additionally, it is important to first establish a solid foundation in ECS fundamentals, VCC technology, and the specific characteristics of the IRIS facility. To support this, the report presents an extensive literature study that provides background information, examines common methodologies, evaluates their applicability, and identifies potential research gaps. The insights gained from this study will ultimately guide the formulation of clear research goals and questions, shaping the next stages of the thesis project.

The report is structured as follows. Chapter II.2 provides background information on ECSs, covering historical developments and the challenges associated with conventional technology in MEA applications. Chapter II.3 introduces the fundamentals of VCC technology, including its thermodynamic principles,

aviation applications, and challenges for future ECS designs. Building on this, Chapter II.4 explores recent research efforts at TU Delft related to VCC-based ECS design, detailing both theoretical work and the IRIS facility.

Chapter II.5 examines the dynamic modeling of VCC systems, beginning with historical developments before discussing overall modeling paradigms and key concepts for individual component models. Chapter II.6 focuses on VCC control approaches, presenting a classification of existing methods and assessing their suitability for the IRIS.

Finally, in Chapter II.7, the insights from the literature study are summarized and used to define specific research objectives, fulfilling the report's intended purpose. As such, this chapter serves as the conclusion of the literature study, enabling the subsequent thesis project activities to commence.

II.2

Environmental Control System

This chapter provides extensive background information on Environmental Control Systems (ECSs). It begins by explaining the need for an ECS, followed by a brief overview of its historical development. Next, the current state-of-the-art technology for ECSs in large passenger aircraft, the Air Cycle Machine (ACM), is examined. Finally, the use of the ACM in More Electric Aircraft is discussed.

II.2.1. Flying at Altitude: The Need for an ECS

Commercial flights typically operate at altitudes between 9 and 12 km above sea level [15]. As shown in Figure II.2.1, temperatures and pressures at these altitudes range from -45 to -56.5 °C and 0.3 to 0.2 bar, respectively. Such conditions are extremely hazardous for humans; without protection, the time of useful consciousness is less than one minute, and prolonged exposure is fatal [16]. To mitigate these risks, Federal Aviation Administration (FAA) regulations mandate that the cabin pressure altitude of occupied areas must not exceed 8,000 feet (2.44 km) [17]. Additionally, the flight crew and passengers must have control over cabin temperature to maintain comfortable levels, typically between 18 and 30 °C. The Environmental Control System (ECS) is responsible for meeting these requirements. In addition to temperature and pressure control, maintaining air quality at high altitudes is crucial. Extremely low humidity can lead to dehydration and discomfort, while unfiltered air may carry harmful particles or contaminants that affect both passengers and sensitive equipment. These challenges underscore the critical role of the ECS in ensuring safe and comfortable flight conditions.

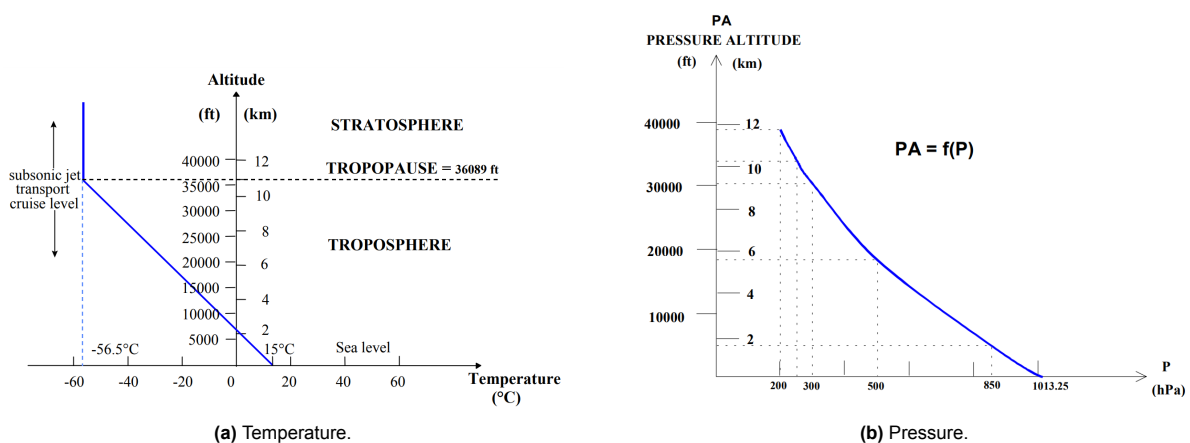


Figure II.2.1: Atmospheric conditions at altitude, based on the International Standard Atmosphere [18].

II.2.2. Historical Development

Since the early days of aviation, technological innovations have been implemented to protect humans from the harsh environmental conditions associated with flight. As Rood [19] reviewed, when flight velocities and altitudes were low, adequate clothing and goggles provided sufficient protection against weather conditions. However, during the First World War, advancements in technology enabled faster aircraft capable of operating at higher altitudes. This necessitated the use of stored oxygen, distributed to the pilots through oxygen masks during missions. Additionally, after the war, electrically heated clothing was introduced to address the extreme cold that caused discomfort for the extremities of the pilot. Although such clothing was further developed after the Second World War, cabin pressurization and heating were increasingly adopted during the Cold War era, eventually becoming the standard for civil aviation.

The first experiments with cabin pressurization date back to the early 1930s, with aircraft such as the Junkers Ju 49 and the Farman F. 1000 serving as early examples. These designs featured compact, can-shaped cabins that could be hermetically sealed for high-altitude operation. Insulation maintained suitable cabin temperatures, and at lower altitudes the cabin could be opened to improve visibility. Although technical details on the operation of these early high-altitude aircraft are limited, illustrations from contemporary publications, such as the one shown in Figure II.2.2, provide a visualization of the concepts behind their design.

As with many emerging technologies, cabin pressurization and climate control initially found use only in military applications. The first commercial airliner to feature large-scale cabin control systems was the Boeing 307 Stratoliner [20]. Designed to carry 33 passengers, the B307 featured a sealed fuselage that could withstand a significant pressure difference between the cabin and the outside environment. The aircraft was powered by four radial internal combustion engines, of which the inner two drove blower compressors that supplied pressurized air to the cabin. A novel cabin-pressure regulator was used to manage the inflow of this air and the outflow to the atmosphere through a series of mechanical control valves. These valves operated based on differential pressure, using adjustable springs to achieve the desired performance. The system activated at altitudes above 8,000 feet and maintained the cabin pressure altitude below 12,000 feet (3.66km).

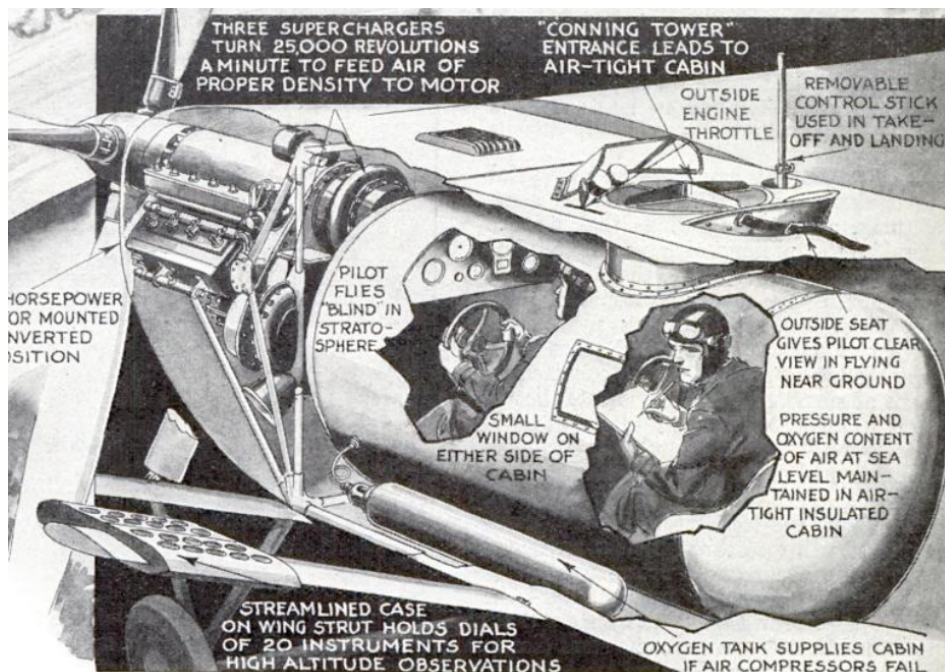


Figure II.2.2: Illustration of the first pressurized cabin concept in the Popular Science Monthly magazine, October 1932 [21].

In addition to the pressurization system, the B307 was equipped with heating and ventilation systems tailored to the operational requirements of the aircraft. At lower altitudes, fresh air could flow into the

cabin through overhead ventilators. However, when the pressurization system was engaged or external temperatures were too low, these ventilators were sealed, and the system switched to recirculating air inside the cabin. To adjust the temperature, additional air streams could pass through heat exchangers, where heat from the main engines could increase the air temperature as needed. This configuration ensured that conditions in the cabin remained controlled throughout the flight, providing comfort for passengers as the aircraft cruised at an altitude of 20,000 feet (6.10 km). At the time, operation of the pressure and temperature systems required a specialized flight engineer due to the limited automation available when the B307 entered service in July 1940.

Before 1944, refrigeration was not included in environmental control systems used in commercial airliners. Cabin ventilation relied entirely on outside air, and heaters were used to regulate temperature [22]. However, this setup often resulted in excessive temperatures inside the cabin on hot days and at low altitudes. Pressurization made this issue worse, leading to the need for a complete air conditioning system capable of fully controlling pressure, temperature, and ventilation. This need ultimately led to the development of the Air Cycle Machine (ACM). It was first introduced for civil applications in the Lockheed Constellation, which entered service in 1945 [23].

The ACM operates by compressing environmental air, cooling it, and then expanding it through a turbine to achieve temperatures well below ambient levels. Initially, compressed air for cabin pressurization and the ACM was supplied by shaft-driven compressors connected directly to the propulsion system, which consisted of reciprocating engines. However, the introduction of turbojet technology in the 1950s marked a major shift in the design of cabin conditioning systems.

Jet engines naturally produce high-pressure air as part of their operation, and this compressed air could be extracted directly from the engine compressors to supply the cabin pressurization and cooling in the ACM. This innovation eliminated the need for traditional shaft-driven compressors used with reciprocating engines, reducing the overall weight and volume of the system [22].

Despite the high power consumption of ACM systems, their seamless integration with gas turbine engines, simple design, and compact size have proven to outweigh their drawbacks. Consequently, ACMs have become the standard choice for modern airliners since the 1960s. To understand the design of current ECSs, it is thus essential to explore the ACM of today in detail. The following section is dedicated to this discussion.

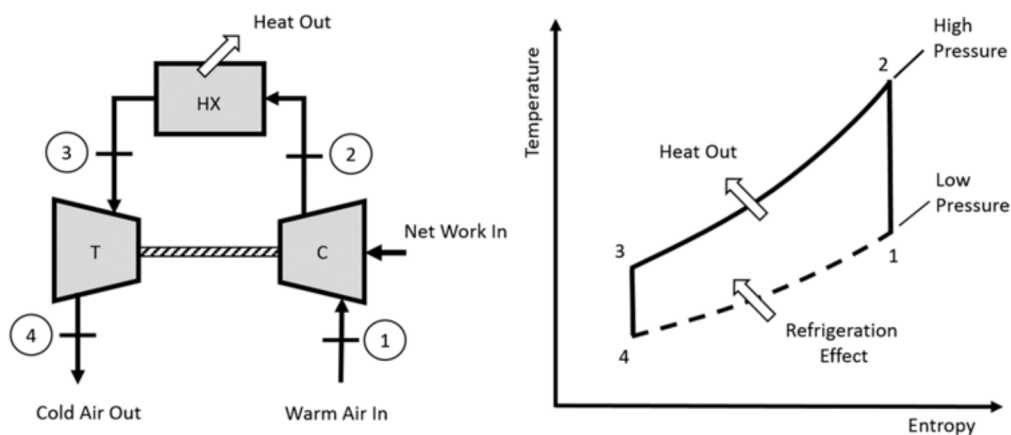


Figure II.2.3: Ideal reverse open Brayton cycle, adapted from [11].

II.2.3. Air Cycle Machine

In modern environmental control systems (ECSs), air conditioning is most commonly achieved using Air Cycle Machine (ACM) technology. Various ACM architectures exist, ranging in complexity from the simple air cycle to the bootstrap cycle, the three-wheel simple/bootstrap cycle, and the four-wheel condensing cycle. A comprehensive overview of these cycles can be found in literature, such as the review by Merzvinskas et al. [11]. For this study, only the simple-cycle ACM is discussed in detail, as it

adequately illustrates the fundamental working principles of the technology. It should be noted, however, that the simple-cycle system is predominantly used in military applications, while more complex cycles are preferred in commercial airliners to achieve lower air temperatures.

The simple-cycle ACM follows a reverse open Brayton cycle, as shown in Figure II.2.3. For simplicity, the temperature-entropy diagram illustrates the ideal cycle, omitting the complexities introduced by real-world losses. The cycle consists of four state points, marked in the figure, and involves three key thermodynamic processes: compression, cooling, and expansion. Starting at point 1, air is compressed from low to high pressure, reaching point 2. In simple air cycles, compression typically occurs in the compressor sections of the engine, although additional compressors within the ACM can increase the pressure ratio. At point 2, the air temperature is elevated due to compression. Between points 2 and 3, the temperature is reduced by passing the air through a heat exchanger, where heat is transferred to a cooling medium, such as ram air or fuel, while the pressure remains nearly constant. This process produces high-pressure, low-temperature air at point 3. Finally, the air expands in a turbine between points 3 and 4, causing its temperature to drop, potentially to levels below the inlet temperature. This expansion process extracts energy from the air as work, which can be used to power ACM components, as shown by the shaft linking the turbine and compressor in Figure II.2.3.

A schematic layout of the simple-cycle ACM is shown in Figure II.2.4. Bleed air from the primary compressor (PC) of the jet engine is directed to the ACM via a pre-cooler (PREC). Pressure regulating and flow control valves (PRV and FCV) control the pressure and flow rate of the hot air entering the ACM. A portion of the hot air is bypassed to the ACM outlet, where a temperature control valve (TCV) adjusts the air temperature supplied to the cabin. Within the ACM, the air first passes through a heat exchanger (HX), where ram air lowers its temperature. The cooled air is then expanded in a turbine, further reducing the temperature at the ACM outlet. In the simple-cycle configuration, the work generated by the turbine drives a fan in the cooling duct, ensuring adequate airflow through the heat exchanger.

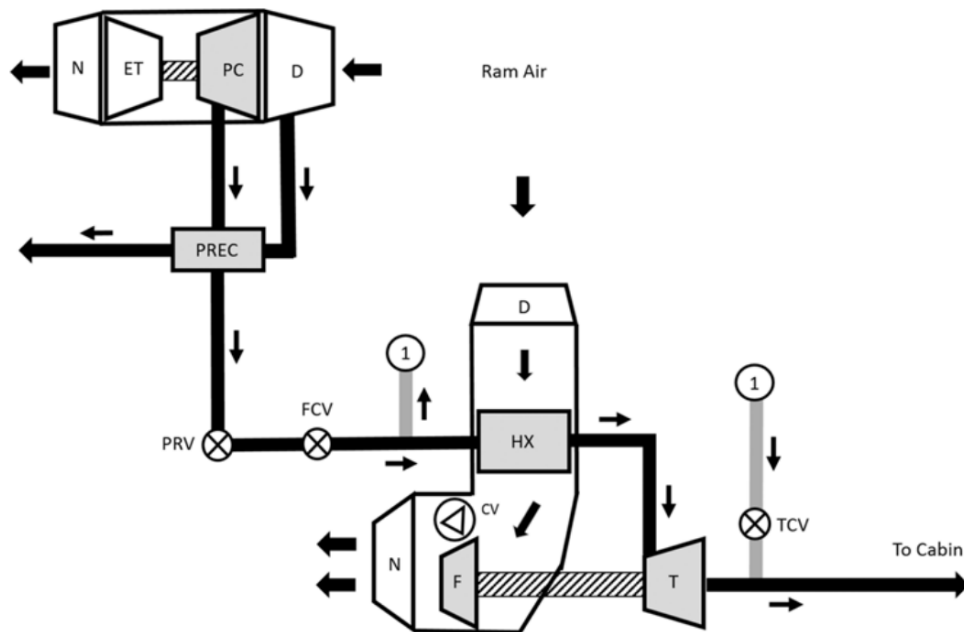


Figure II.2.4: Schematic representation of a simple-cycle ACM architecture for the ECS of an aircraft, adapted from [11].

Through these processes, the ACM accomplishes all critical functions of the ECS. It uses high-pressure bleed air for pressurization, provides ventilation with fresh, non-recirculated air, and regulates cabin temperature by mixing a bypass stream with cooled air from the reverse Brayton cycle, allowing for both heating and cooling as needed. The combination of jet engines and ACM technology thus ensures precise control of air conditions in the aircraft.

II.2.4. More Electric Aircraft and the ACM

Traditionally, non-propulsive power on aircraft includes electrical, pneumatic, hydraulic, and mechanical loads [24]. This load distribution is illustrated in Figure II.2.5a, which shows the typical power consumption of each subsystem. However, recent advances in aircraft design have led to a shift toward purely electrical loads. The core idea behind this shift is that using an electrical supply for all onboard subsystems can achieve significant gains in both efficiency and weight, which would not be possible with the traditional power supplies. Known as the More Electric Aircraft (MEA) concept, this approach seeks to replace all non-propulsive systems with electrical components, potentially resulting in a power distribution like the one shown in Figure II.2.5b.

As shown in Figure II.2.5a, the pneumatic energy extracted from the main engine for the ECS makes up the largest portion of non-propulsive power. However, modern turbofan engines are equipped with highly optimized gas generators for thrust production, and extracting air from the compressor stages for bleed purposes compromises their overall performance [25]. Consequently, eliminating the bleed system can substantially enhance aircraft performance, provided suitable alternatives for the subsystems dependent on pneumatic power can be identified. Boeing has adopted this approach in the ECS design of the 787 Dreamliner, where shaft-driven compressors have been reintroduced to supply compressed air to an ACM system. According to the company, this change results in an overall fuel saving of approximately 1 to 2 percent during cruise [8]. Similar findings were reported by Slingerland and Zandstra [26], who conducted a numerical comparison between bleed-air and electric ECSs and concluded that thrust specific fuel consumption could be reduced by 2% across the entire flight cycle.

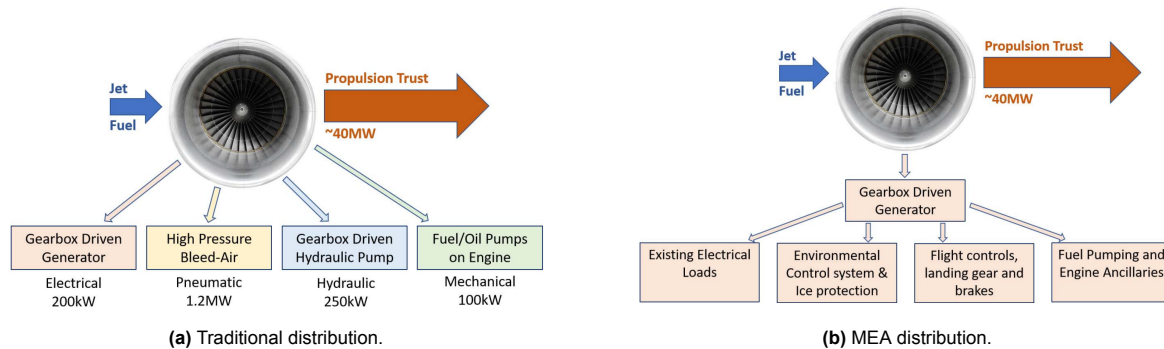


Figure II.2.5: Typical power distribution of an aero-engine [8].

While these results suggest notable fuel savings, removing the bleed air system sacrifices the simplicity provided by the integration between the ACM and the turbomachinery of the engine, as discussed in Section II.2.2. Therefore, it is not surprising that researchers have begun exploring alternative technologies that were competitive options before the widespread adoption of jet engines and ACM systems. One such alternative is the Vapour Compression Cycle (VCC), which will be the focus of the next chapter.

II.3

Vapour Compression Cycle Technology

This chapter explores the Vapour Compression Cycle (VCC) by first introducing its underlying thermodynamic principles. It then examines its historical use in aviation, highlighting key developments. Finally, the chapter discusses the challenges associated with integrating the VCC into future ECS designs.

II.3.1. Thermodynamic Principles

Before discussing the thermodynamics of the VCC, it is useful to revisit the fundamentals of refrigeration cycles, starting with the ideal Carnot cycle. This cycle consists of four reversible processes: two adiabatic and two isothermal, arranged alternately. For refrigeration purposes, the Carnot cycle can be represented by the system in Figure II.3.1. In this representation, a working fluid moves steadily in a counter-clockwise direction, undergoing the four distinct processes: compression, condensation, expansion, and evaporation. The temperature-entropy diagram illustrates the alternation between isothermal and adiabatic processes. During condensation and evaporation, the fluid undergoes phase changes at constant temperature and pressure. In contrast, during compression and expansion, the entropy remains constant, indicating that no heat is exchanged with the surroundings and no losses are generated in these two processes. The condensation and evaporation temperatures are equal to the temperatures of the regions where heat is rejected (T_H) and absorbed (T_C), respectively. Notably, when no work is supplied for compression, points 1 and 2 in the cycle collide, indicating that no temperature difference between the hot and cold regions can be established. This demonstrates that the refrigeration effect can only be realized if a non-zero amount of work is provided to the system.

In accordance with the second law of thermodynamics, the Carnot cycle achieves the maximum theoretical efficiency of any refrigeration cycle operating between regions at T_C and T_H [27]. For refrigeration systems, this efficiency is typically expressed as the Coefficient of Performance (COP), defined as the ratio of heat removed from the cold region to the net work input, i.e., $\frac{\dot{Q}_{in}}{\dot{W}_c - \dot{W}_t}$. For the Carnot cycle, the definition of the COP reduces to:

$$COP_{max} = \frac{T_C}{T_H - T_C} \quad (II.3.1)$$

This definition emphasizes the importance of discussing the Carnot cycle first, as it represents the theoretical ideal thermodynamic cycle for refrigeration. However, practical systems inevitably deviate from this ideal process, not only because truly reversible processes are impossible in nature but also due to practical constraints. Consequently, discussing the VCC requires modifying certain aspects of the Carnot cycle to address the limitations of real-world cooling equipment.

In general, there are three key adjustments to the Carnot cycle to arrive at the VCC:

- The heat transfer between the refrigerant and outside environment does not occur reversibly. As a result, the condensation temperature is always higher than the temperature of the warm

region to achieve the desired heat flow. Similarly, the evaporation temperature is lower than the temperature of the cold region.

- As can be seen in Figure II.3.1, the compression process in the Carnot cycle occurs in the two-phase liquid-vapour regime. In practice, two-phase compression is impractical, since liquid droplets can damage the internals of the compressor. Therefore, for VCC systems, the fluid is heated to (saturated) vapour conditions prior to compression.
- The expansion process generates a small amount of work, but the potential for extraction is typically minimal. When accounting for internal losses in real turbines, implementing a turbine is often uneconomical. As a result, the expansion process is usually carried out using a simple throttling device or expansion valve.

By incorporating the outlined adjustments, the Vapour Compression Cycle (VCC) is obtained, as shown in Figure II.3.2. Compared to the Carnot cycle in Figure II.3.1, several differences stand out. First, the T-s diagram clearly shows that the condensation and evaporation temperatures in the VCC are offset from the surrounding environmental temperatures, due to the irreversible nature of the heat transfer. Second, the compression process occurs entirely in the vapour phase. The ideal isentropic compression from state 1 to state 2s (solid black line) is replaced in practice by an irreversible process from state 1 to state 2 due to internal losses in the compressor. Third, the expansion valve replaces the turbine, resulting in an irreversible yet adiabatic expansion process. While this change sacrifices the ability to extract work, it significantly simplifies the system.

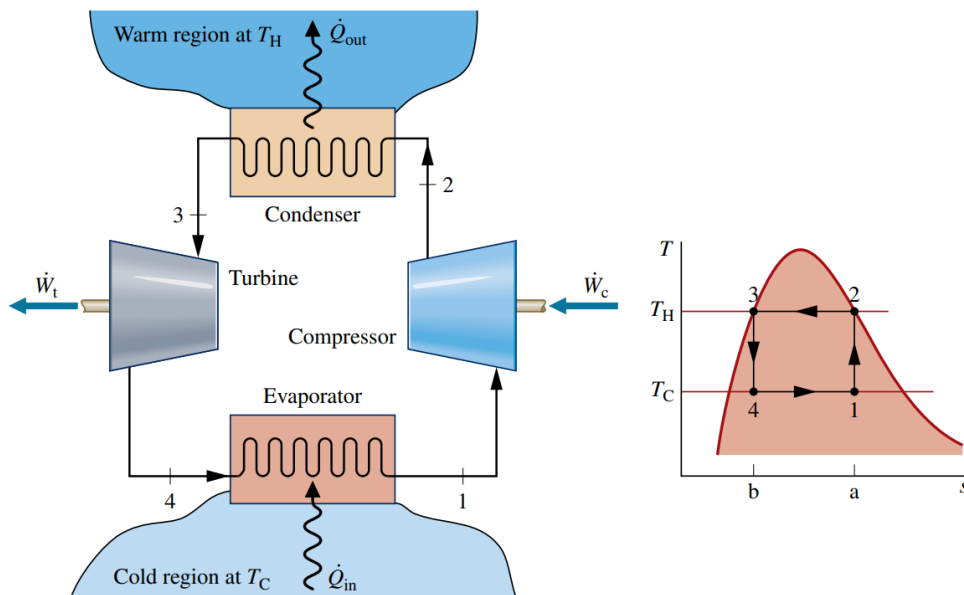


Figure II.3.1: Schematic representation of the Carnot cycle for refrigeration and corresponding temperature-entropy diagram, adapted from [27].

Finally, the heat exchangers in the VCC serve purposes beyond condensation and evaporation. After compression, the vapour must first be cooled to a saturated state in the condenser before condensation can begin. Since the superheated vapour is in a single phase state, the temperature of the fluid will decrease here. Additionally, at the ends of the process lines, the heat exchangers either cool or heat the fluid beyond saturation. This is referred to as subcooling in the condenser and superheating in the evaporator. Superheating in the evaporator is particularly important, as it ensures that no liquid enters the compressor, enabling safe operation.

The steady-state coefficient of performance (COP) of the VCC can be calculated using the specific enthalpies of the state points:

$$COP = \frac{\dot{Q}_{in}}{\dot{W}_c} = \frac{\dot{m}\Delta h_{4-1}}{\dot{m}\Delta h_{1-2}} = \frac{h_1 - h_4}{h_2 - h_1} \quad (II.3.2)$$

The COP is fundamentally limited, with the Carnot cycle providing the theoretical upper bound, as shown in Equation II.3.1.

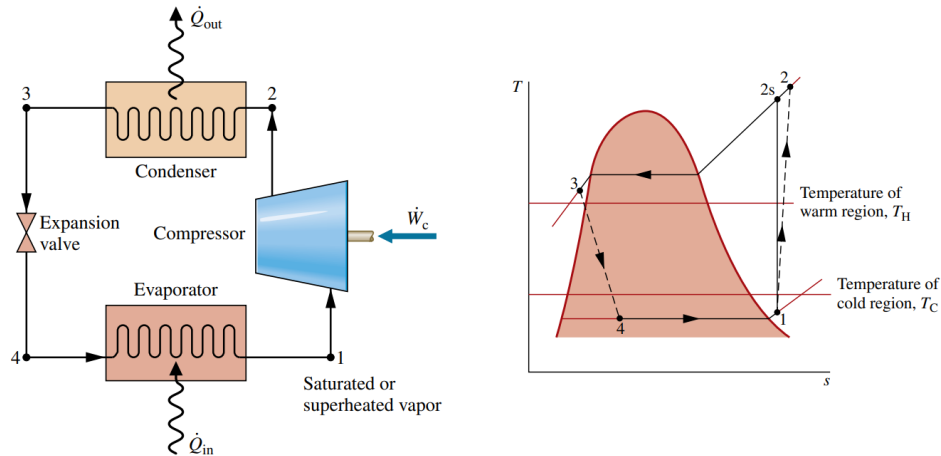


Figure II.3.2: Schematic representation of the vapour compression cycle for refrigeration and corresponding temperature-entropy diagram, adapted from [27]. For the temperature-entropy diagram, the dashed black lines indicate irreversible processes.

II.3.2. Historical Development in Aviation

The application of VCC technology in aviation has historically been limited. While VCC systems generally offer superior thermodynamic efficiency, their core components, such as compressors and heat exchangers, were traditionally large and heavy, making them unsuitable for aircraft use. As a result, the ACM concept, discussed in Section II.2.3, became the more widely adopted solution. Nonetheless, early developments did explore VCC systems, with the first aircraft applications dating back to before the 1960s [28]. Examples of early aircraft featuring VCC packs include the Boeing 707, the Douglas DC-8, and the Convair 880/990 [22]. However, technical details on the performance of these early systems are scarce in open literature.

Although VCC systems saw limited adoption in large airliner ECSs, they found more extensive use in smaller aircraft and rotorcraft. This is largely due to the limited availability of bleed air in such aircraft, which renders the ACM concept impractical [11]. Furthermore, when refrigeration demands are high, the large COP of VCC systems can outweigh the simplicity of ACMs. Modern examples of aircraft using VCC-based ECSs include the Piaggio Avanti, the Socata TBM, and the Cessna Citation family [13].

With the ongoing shift toward electrification, driven by the More Electric Aircraft (MEA) and All Electric Aircraft (AEA) concepts, research and industry are increasingly focusing on novel ECS configurations for future aircraft. This renewed interest has brought VCC technology back into consideration for large passenger aircraft. For example, in 2015, Airbus patented an ECS design that integrates ACM and VCC technologies [29]. These novel ECS designs are inherently complex, requiring advanced optimization techniques to properly design thermodynamic cycle characteristics and component dimensions. As a result, current research on VCC-based ECSs primarily focuses on developing such optimization methodologies. Notable contributions in this field can be found in the dissertations of Ascione and Giuffr  [13, 30].

Before discussing the complexities of multi-objective optimization for future ECS designs, it is important to first examine the key challenges that must be addressed to enhance the performance and efficiency of next-generation aircraft. The following section will explore these challenges in detail.

II.3.3. Challenges in Future ECS Design

It is widely recognized that the design of any aircraft subsystem should aim to minimize weight and maximize efficiency. Both objectives contribute to the broader goal of reducing fuel consumption, which provides environmental and economic benefits. However, designing ECSs involves additional com-

plexities, such as ensuring reliability and safety, simplifying maintenance, and integrating the system within existing frameworks [31]. When critically evaluating VCC technology, several challenges arise in large scale aircraft applications.

The first significant challenge is that, unlike the ACM, which uses air as a working fluid, the VCC requires a phase-changing working fluid in a closed-loop cycle. This fluid must evaporate and condense within specific temperature ranges while meeting strict safety standards, such as low flammability and toxicity. Historically, the hydrofluorocarbon R-134a became an industry standard, replacing the earlier R-12 refrigerant due to its high ozone depletion potential. However, R-134a has a relatively high Global Warming Potential [32], and the Kyoto Protocol mandates its eventual replacement with more environmentally friendly alternatives [33]. Identifying and developing suitable alternative refrigerants for VCC systems in aviation remains a critical area for future research.

A second challenge relates to compressor technology. Compressors are typically large and heavy, significantly contributing to the total weight of VCC-based ECSs. In current applications, such as business jets and helicopters, the compression process is often achieved using scroll compressors [34]. These compressors function with two spirals, one stationary and one moving eccentrically, creating sealed compartments that compress the refrigerant as its volume decreases. Scroll compressors offer several advantages over reciprocating compressors, including greater compactness, fewer components, lower vibration levels, and higher volumetric and isentropic efficiencies [35]. Despite these benefits, scroll compressors also have drawbacks. Continuous movement of the spirals requires an oil system to reduce wear on internal components [36], which increases weight and complexity. Additionally, the intricate geometry of the spirals can make maintenance challenging and costly.

The design of heat exchangers in VCC systems presents another major challenge. Efficient heat transfer requires a large surface area, but increasing the size of the heat exchanger also results in penalties in weight, drag, and pressure drop. This creates a trade-off between efficiency and the mentioned penalties. Recent research has focused on highly compact heat exchangers with area to volume ratios exceeding 700 square meters per cubic meter [37]. These designs often include complex geometries, such as high fin densities and microchannels, to enhance performance. Additive manufacturing, a relatively new technique, shows great potential for improving compact heat exchanger performance. As reviewed by Careri et al. [38], the ability of additive manufacturing to create intricate and thin features could revolutionize the aerospace industry as the technology matures.

To summarize, while the VCC presents a promising alternative to conventional ECS architectures, its successful integration into future aircraft requires overcoming key design challenges related to efficiency, weight, and component optimization. To address these challenges, researchers at TU Delft have been developing novel ECS configurations that leverage advanced optimization techniques and experimental validation. The following chapter explores these efforts, detailing innovative approaches to ECS design and the role of the IRIS test facility in bridging the gap between theory and practical implementation.

II.4

Novel ECS Designs: From Theory to Practice

As highlighted in Section II.3.2, addressing the challenges outlined in Section II.3.3 requires advanced optimization techniques for ECS design. This chapter explores the relevant research conducted at Delft University of Technology (TU Delft) in this area. The first part focuses on theoretical advancements, emphasizing ongoing developments in novel optimization methods for electric ECS design. The second part provides an in-depth discussion of the experimental test facility known as the Inverse Organic Rankine Cycle Integrated System (IRIS), which is designed primarily to validate the theoretical models and provide better insight into the operational characteristics of VCC-based cooling systems.

II.4.1. Key Advancements

Designing an ECS is a complex process. It involves selecting thermodynamic characteristics that define system-level performance (e.g., the COP) and determining the size of individual components (e.g., heat exchanger dimensions). Complicating matters further, aircraft systems face strict limitations on efficiency and weight. As a result, the ECS must maximize efficiency, minimize weight, and avoid large drag penalties. To achieve this balance, design procedures often include multi-objective mathematical optimization to determine the design variables that influence both the performance and the size of the system.

The strong coupling between system-level performance and component sizing means that optimization of one inherently affects the other. This has led to a growing focus on simultaneous optimization in ECS design [39]. An early exploration of this concept is found in the work of Vargas and Bejan [40]. Using an exergy destruction analysis, they showed that the ECS design affects global aircraft performance in two ways. First, the irreversibilities within the ECS directly influence overall system efficiency. Second, the size of the ECS impacts the power required to sustain flight associated with drag penalties. This approach has inspired extensive research on integrated design optimization for ECS development. While much of this research focuses on ACM-based systems [41–44], some studies also consider hybrid ACM-VCC architectures [45, 46].

At TU Delft, integrated design optimization has been employed to develop innovative electric ECS concepts aimed at meeting the cooling demands of a typical single-aisle, short-haul passenger aircraft. The progress in this research is captured in the dissertations of Giuffr  [30] and Ascione [13], which introduce several notable advancements:

- The adoption of the VCC as the primary cooling system for the ECS, with both standalone VCC configurations and hybrid systems incorporating the ACM explored.
- The integration of electric centrifugal compressors as an alternative to conventional scroll compressors, driven by their potential to be lighter, more compact, and more efficient.
- The evaluation of alternative working fluids to replace the widely used R-134a refrigerant, focusing

on options with significantly lower Global Warming Potential (GWP) to minimize environmental impact.

To further explore these novelties, a detailed review of the approaches and findings documented in the dissertations of Giuffré and Ascione follows next.

The work of Giuffré [30] places particular emphasis on the implementation of low-weight, high-speed electric centrifugal compressors with gas foil bearings. These compressors achieve the required pressure ratio using specially designed impellers, as shown in Figure II.4.1. The impellers are mounted on a rotating shaft driven by an electric motor. Fluid enters through the eye of the rotor and is forced radially outward by the impeller, providing the energy needed for compression [34].

A novel design methodology for centrifugal compressor stages has been developed based on earlier work by Rush and Casey [47]. This methodology represents the compressor in a simplified manner using a low-order, lumped-parameter model with a limited number of stream-wise stations. By reducing the degrees of freedom of the compressor design, this approach ensures that numerical optimization of the design variables remains computationally feasible. The predictive capabilities of the model have been validated using test cases from open literature and Computational Fluid Dynamics (CFD) simulations, demonstrating strong agreement between the results.

The low-order compressor model is subsequently used in a system-level integrated design optimization. This methodology simultaneously optimizes the design of the centrifugal compressor and the geometry of the compact heat exchangers in the ECS. Additionally, an alternative approach has been developed where a data-driven compressor model is used instead of the low-order model. These integrated optimization techniques demonstrate that VCC-based ECS designs with high-speed centrifugal compressors can outperform the efficiency and weight performance of existing ACM technology, and a (conservative) theoretical reduction in fuel weight penalty of 20% is reported.

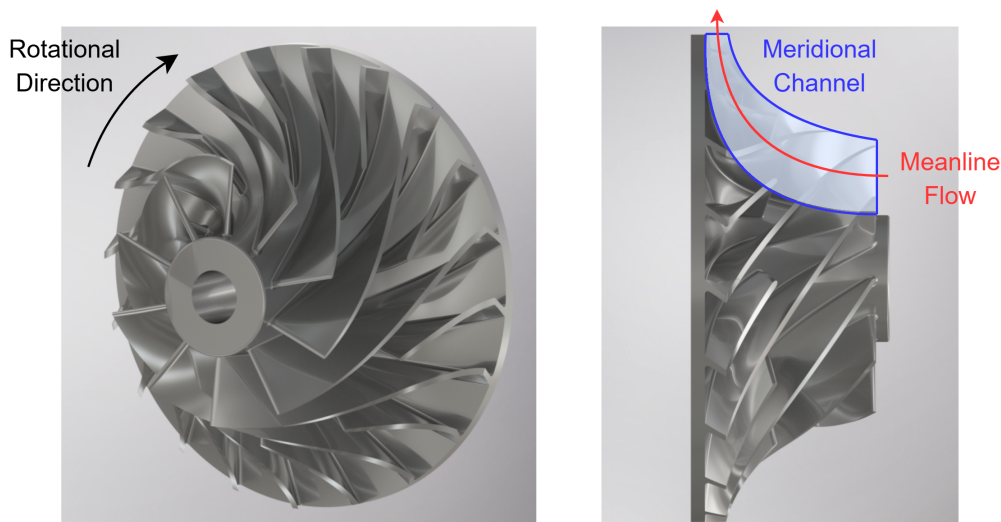


Figure II.4.1: Three-dimensional rendering of a centrifugal compressor impeller, adapted from [30], with isometric and side views shown on the left and right, respectively. The rotational direction of the impeller is shown with a black arrow, the blue region indicates the meridional flow channel, and the red arrow denotes the mean flow direction.

The dissertation by Ascione [13] closely relates to the work of Giuffré, with significant overlap between the two. While Giuffré focused on electric ECS configurations in general, including ACM, VCC, and hybrid setups, Ascione concentrated specifically on systems based on the VCC. This narrower focus likely reflects the superior performance of VCC systems demonstrated in Giuffré's work. Ascione advanced the earlier framework by introducing a method for selecting the optimal working fluid during the preliminary design phase, replacing the fixed use of R-134a in the original procedure. The study examined four integrated design optimization approaches for determining the compressor design, heat exchanger configurations, and system parameters. A fifth optimization method targeted the selection of the working fluid. All methods relied on a modular steady-state model of a VCC-based ECS.

Ascione demonstrated the effectiveness of the five optimization methods by designing ECS configurations for two applications: a single-aisle, short-haul passenger aircraft, and a large helicopter with a capacity for 20 passengers and two pilots. The set of possible working fluids was limited, such that they complied with the Kigali Amendment to the Montréal Protocol [48], promoting natural refrigerants, haloolefins, and blends. For the single-aisle aircraft, a full multi-point multi-objective optimization method was applied, including a pseudo-fluid optimization for the working fluid. The results indicated that 1-butene and 1-butyne were the most suitable fluids for this application. While these refrigerants achieved similar performance to R-134a, they exhibited significantly improved environmental properties. For the helicopter application, potential drop-in replacements for R-134a from the haloolefin family were considered. These included R-1233zd(E), R-1224yd(Z), R-1234ze(Z), and R-1336mzz(Z), all of which have a lower GWP compared to R-134a. Although these refrigerants can pose risks to aquatic life, they are still regarded as good short-term replacements for R-134a [49]. The resulting designs achieved lightweight, high-efficiency ECS configurations suitable for helicopter applications, with feasible centrifugal compressor designs showing total-to-total efficiencies of up to 80 %.

To summarize, the work of Giuffré and Ascione has significantly advanced the field of integrated optimization for the preliminary design of novel ECSs for future aircraft. The three novelties that stand out are the adoption of the VCC in such systems, the use of high-speed electric centrifugal compressors, and the exploration of environmentally friendly working fluids. The results of the studies clearly indicate the potential of these solutions in improving the performance of the ECS.

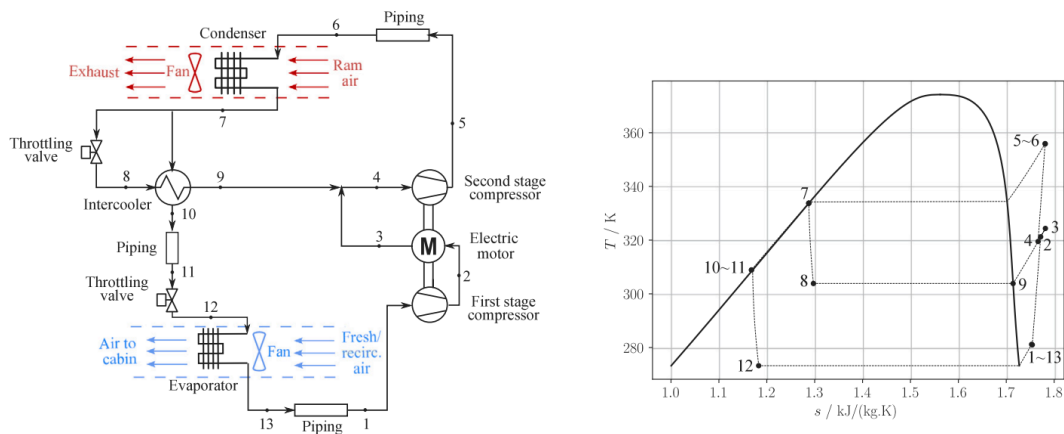


Figure II.4.2: Typical layout of a VCC-based ECS for large rotorcraft and corresponding temperature-entropy diagram [50].

II.4.2. The IRIS Experimental Facility

To support their theoretical work discussed in the previous section, Giuffré [30] and Ascione [13] developed the IRIS test facility. Designed to mimic the typical cooling requirements of a large helicopter, this facility features a high-speed centrifugal compressor and the R-1233zd(E) refrigerant as working fluid. The choice for this working fluid was based on the analysis of the helicopter use case in the work of Ascione [13], as discussed in Section II.4.1. The IRIS serves as a modular platform designed to support a wide range of component and system-level experiments, providing valuable insights into the operation of VCC-based cooling systems for aviation applications. Its objectives can be summarized as follows:

- Evaluating the performance of (centrifugal) compressors within VCC systems for aviation use.
- Investigating the aerothermal behaviour of heat exchangers, particularly the condenser.
- Analysing the refrigeration cycle using R-1233zd(E) and other low-GWP refrigerants.

As the IRIS is central to the activities outlined in this thesis, its development and layout are examined in detail in this section. This is done in three parts. First, the typical ECS configuration of a large helicopter is explained, which formed the inspiration for the layout of the IRIS. Subsequently, deviations from the original conceptual design are discussed, since practical limitations have resulted in a change of architecture. Finally, the current architecture of the IRIS is presented in detail.

II.4.2.1. Typical Helicopter ECS

The typical layout of a VCC-based ECS for large rotorcraft is presented in Figure II.4.2. Comparing this with the simple cycle in Figure II.3.2, it is clear that the compression process is divided into two separate stages, with an additional heat exchanger (intercooler) placed between the high-pressure and intermediate-pressure levels. Known as an economized configuration [51], the intercooler increases both the cooling capacity and the efficiency of the compression process. By bypassing part of the fluid exiting the condenser and allowing it to expand to the intermediate pressure level (from 7 to 8), the fluid temperature is reduced. This cooler fluid serves as a heat sink to lower the temperature of the main stream (from 7 to 10), beyond the temperature reached at the condenser outlet. As a result, the expansion to the evaporator pressure (from 11 to 12) results in lower vapour quality at the evaporator inlet compared to direct expansion from the condenser outlet to the evaporator pressure (from 7 to the evaporation temperature between 12 and 1), allowing more heat to be absorbed during evaporation for a given rotational speed of the compressor. Regarding the compression process, the introduction of cooler fluid at the intermediate pressure level effectively cools the fluid (mixing between 3 and 9 to reach 4). Since the isentropic lines diverge more at higher degrees of superheating, this leads to greater efficiency when the fluid is further compressed to the high-pressure level. The combined effect of increased cooling capacity and more efficient compression ultimately results in a higher COP (see Equation II.3.2).

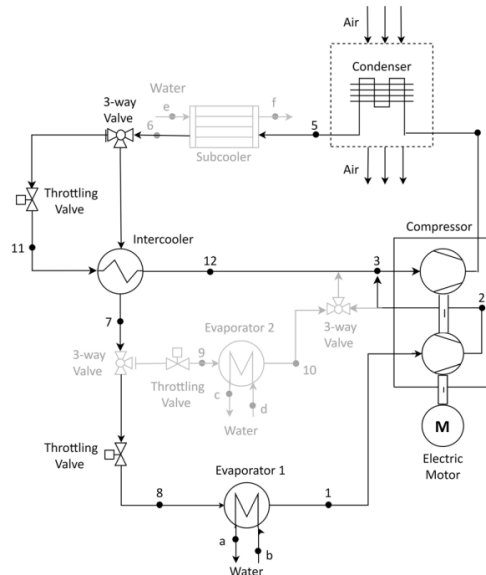


Figure II.4.3: Configuration of the IRIS, based on the typical helicopter ECS in Figure II.4.2, adapted from [52]. The shaded components are to be implemented in a later phase of the project.

In Figure II.4.3, a conceptual representation of the process flow diagram of the IRIS facility is shown. The layout closely resembles the typical architecture of Figure II.4.2, but some differences are noticeable. First, instead of the air-to-refrigerant evaporator used in the typical ECS configuration, the IRIS employs a water-to-refrigerant heat exchanger. The supply of warm water allows for more precise temperature control, resulting in better regulation of the cooling load [52]. Second, while not depicted in the figures, the conventional ECS uses a mechanically powered scroll compressor with interstage refrigerant injection (i.e., to mix in the cooler fluid from the economized configuration) to achieve the desired compression. In contrast, the IRIS features a two-stage electric centrifugal compressor, with the stage design optimized through the integrated methods discussed in Section II.4.1. Interstage cooling is implemented, meaning the compressor's electric motor is cooled by refrigerant flow between the outlet of the first and inlet of the second stage (from 2 to 3). Finally, the shaded components included in the IRIS layout are intended for a future phase of the research, which will explore cooling avionics using a second evaporator at a higher temperature level. Thus, the IRIS serves as a modular facility designed to evolve alongside the research project, offering flexibility through its adaptable architecture. Its two test sections allow for easy swapping of the condenser and compressor of different types, en-

abling component comparisons at various stages of the project. This adaptability also extends to the working fluid, facilitating the exploration of haloolefins with properties similar to R-1233zd(E) and further enhancing the facility's versatility.

II.4.2.2. Deviations from the Conceptual Design

The experimental activities of the IRIS began with the setup commissioning, as documented by Ascione et al. [53]. The system architecture during this phase is depicted in the schematic in Figure II.4.4. This design notably differs from the conceptual layout shown in Figure II.4.3, making it essential to examine the reasons behind these deviations to gain a comprehensive understanding of the facility.

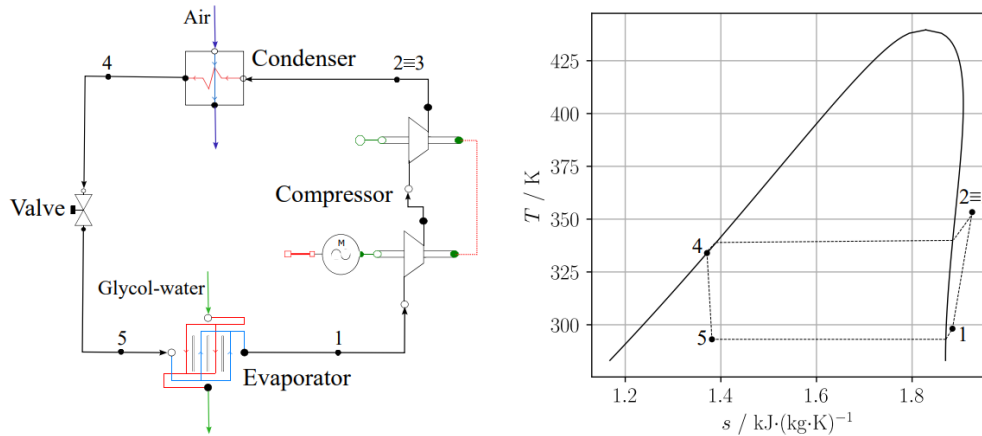


Figure II.4.4: Schematic representation of the component architecture of the IRIS at the time of commissioning, including the corresponding temperature-entropy diagram [13].

During the construction of the facility, unforeseen delays in producing the two-stage centrifugal compressor required an alternative approach. To move forward, a different compressor was temporarily installed, with plans to replace it later with the intended centrifugal machine. Since the compressor section is designed for testing and replacement, this adjustment aligns with the modular capabilities of the IRIS. However, the implementation of haloolefins in refrigeration systems is relatively recent, and the associated component technologies, including compressors, are still under development [54]. As a temporary solution, a reciprocating compressor was selected due to its availability for R-1233zd(E) and its well-established technology [55].

However, reciprocating compressors have strict lower limits on suction pressure to ensure safe operation, which prevents the inlet pressure from dropping below atmospheric levels [13]. This limitation imposes a corresponding lower bound on the evaporation temperature, as this temperature depends on the evaporator pressure, which is approximately equal to the compressor inlet pressure. For R-1233zd(E), the evaporation temperature corresponding to atmospheric pressure at sea level is $T_{evap}|_{P_{atm}} = 18.26 \text{ }^\circ\text{C}$, or 291.41 K. The evaporation temperature indicated in Figure II.4.2 (between points 12 and 1) is well below this threshold, necessitating modifications to the IRIS architecture.

Since the evaporation temperature in the intercooler (between points 8 and 9 in Figure II.4.2) lies above the lower limit, the decision was made to construct only the high-pressure cycle of the VCC. This adjustment involved removing the intercooler, shifting the evaporator pressure up to the intermediate pressure level, and implementing only a single expansion valve. The resulting temperature-entropy diagram in Figure II.4.4 thus corresponds to the upper cycle in Figure II.4.2, with condensation and evaporation temperatures that closely match. To achieve this cycle, the IRIS includes three distinct loops of the which the component layouts are described in detail in Chapter III.1.

Although the current IRIS configuration was successfully commissioned, the setup suffers of significant limitations: the system is not fully adaptable to test a wide range of operating conditions and does not fully reflect the configuration of the system it aims to represent, due to the practical adjustments to the conceptual design. Consequently, the current configuration is the result of a trade-off between to

opposites; it serves as both a test facility for specific VCC components and a prototype that loosely mirrors a future ECS for larger aircraft. This dual role means that while the IRIS can test up to certain operating conditions, it cannot offer the full flexibility of a specifically designed test rig, nor does it provide a perfect representation of a VCC as implemented in a real ECS.

Despite these limitations, the IRIS remains a valuable tool in the advancement of novel ECS research. The variety of measurement equipment of the facility allows the acquisition of crucial experimental data that complement the numerical optimization studies, aiding in the refinement of theoretical models. Although it may not be fully adaptable to every possible VCC configuration, the IRIS is particularly effective in testing conditions that closely resemble those found in actual aircraft operations. This capability helps address knowledge gaps in the behaviour of components such as the high-speed centrifugal compressor, which has not been extensively tested.

Furthermore, the modular nature of the IRIS implies that it can be continuously updated and improved as the project progresses. The planned replacement of the reciprocating compressor with the high-speed centrifugal compressor, for example, will bring the test rig closer to the specifications of a fully functional ECS, thus enhancing its relevance and accuracy in simulating future systems for electric aircraft. Additionally, the flexibility of the facility allows for further adaptations, such as the integration of an intercooler or other critical components that could expand its testing capabilities. By enabling these updates, the IRIS serves not only as a test bed but also as a dynamic research platform capable of supporting the ongoing development and optimization of environmentally sustainable ECS designs.

This concludes the background information on the IRIS and its role in novel ECS designs. Building on the knowledge from the previous chapter, the next chapter will provide a more detailed exploration of modelling techniques for VCC systems.

II.5

Dynamic Modelling of VCC Systems

With a solid foundation in novel VCC-based ECS designs developed in the previous chapters, this chapter explores the modelling methods for the IRIS. It begins with a review of the historical development of VCC modelling, followed by an introduction to different modelling paradigms, focusing on modularity and causality. The use of the Modelica programming language is then presented as an effective approach for constructing modular models. Finally, key aspects of individual component models are examined, covering the heat exchangers, compressor, expansion valve, and liquid receiver.

II.5.1. History of VCC Modelling

Before exploring the development of transient models for VCC systems, it is worth noting that early research largely concentrated on steady-state analyses, which nowadays can be found in standard thermodynamics textbooks [27]. The intricate dynamics of VCC systems, including two-phase flow, flash evaporation in the expansion valve, compressor behaviour, and the complexities of predicting active charge, posed significant challenges to transient modelling, especially prior to the widespread adoption of computer technology. Nevertheless, early efforts to describe the refrigerant's transient behaviour emerged, and since the modern modelling methods of today were derived from these original methods, it is imperative to understand their development. The current section aims to address this topic and provide a historical review of the relevant research regarding dynamic VCC modelling.

In transient modelling of a full VCC system, individual component models are typically developed and integrated. This modular approach reflects the differing time scales of the cycle's components. As noted by several authors [56] [57] [58], most modelling efforts focus on heat exchangers, while the expansion valve and compressor are often treated as static. For reciprocating compressors, common in most refrigeration applications, mass flow rate and discharge enthalpy are typically derived from volumetric and adiabatic efficiencies interpolated from performance maps. Centrifugal compressors, however, additionally require detailed transient modelling to effectively capture stall and surge dynamics [59]. Expansion valve modelling typically relies on simple orifice equations, with experimental data used to refine mass flow predictions. While Thermostatic Expansion Valves (TEVs) were conventionally employed to regulate superheating at the evaporator outlet, recent developments have shifted toward Electronic Expansion Valves (EEVs) for enhanced control flexibility.

Early attempts at transient heat exchanger modelling date back to the 1940s, employing spatial discretization through simple lumped parameter methods. Although limited information on these approaches is available in the open literature, it is reportedly known that they were unsuitable for laminar flows or scenarios involving phase transitions [60], which limited their applicability to VCC systems. A key advancement came in 1965 with Wedekind's pioneering work on two-phase heat exchanger modelling [60]. His research focused on a horizontal tube evaporator, as shown in Figure II.5.1, aiming to predict outlet conditions for superheated vapour and the tube wall temperature. Wedekind introduced a model that divided the heat exchanger into distinct regions, each corresponding to a different phase of the refrigerant. The transition point between two-phase and single-phase regions was represented

as a time-varying length variable. By spatially integrating the partial-differential conservation equations, Wedekind formulated lumped conservation equations for each region, expressed as a system of Ordinary Differential Equations (ODEs) with pressure and enthalpy as state variables. Later known as the Moving Boundary (MB) method, this approach became foundational for multi-phase heat exchanger modelling. Its advantages and limitations are further discussed in Section II.5.4.1.

In the 1980s, improved computational power enabled the adoption of alternative numerical approaches for heat exchanger modelling. Among these, the Finite Difference (FD) and Finite Control Volume (FCV) methods gained significant traction. Unlike the MB method, which tracks moving phase boundaries, these approaches divide the heat exchanger into fixed-length sections and assign dynamic states to each of them. The FD method numerically approximates the derivatives in the conservation equations, while the FCV method, displayed in Figure II.5.2, integrates across the volumes of each section, treating the fluid properties as lumped parameters [57]. One of the earliest applications of the FCV method was demonstrated by MacArthur and Grald [61], who modelled a dynamic heat pump. Their simulations showed good agreement with experimental data, though the approach required implicit time-stepping and fine temporal resolution, inherently resulting in higher computational demands. Despite these challenges, FD and FCV methods became widely adopted for their ability to capture detailed spatial variations in refrigerant properties and their improved robustness during large transients [62] compared to the MB method. A detailed comparison between the MB and FD/FCV methods is provided in Section II.5.4.1.

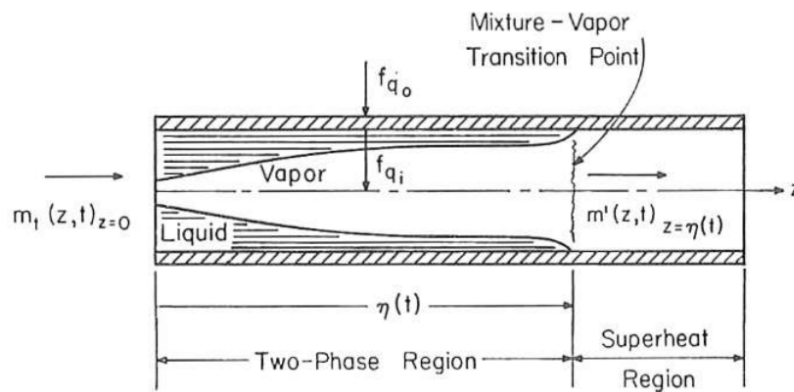


Figure II.5.1: Moving Boundary model of a horizontal evaporator, based on the approach developed by Wedekind [63].

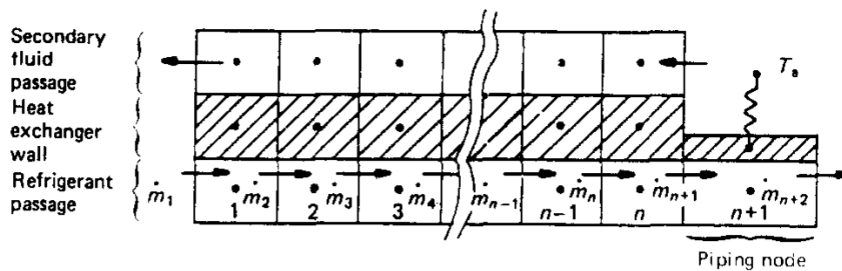


Figure II.5.2: Finite Control Volume model of the heat pump heat exchanger, as proposed by MacArthur and Grald [61].

In addition to physics-based models, data-driven approaches have also been explored for dynamic VCC modelling. These methods use generic sets of modelling equations and fit specific parameters within these equations to experimental data, achieving good quantitative agreement. However, they may lack reliability when system features change, requiring re-identification for each modification. Selecting the appropriate model structure, dynamic order, and input excitation also requires significant expertise. As reviewed by Rasmussen [57], Single Input Single Output (SISO) systems are typically captured using simple process control models (e.g., first-order transfer functions) or discrete time methods like autoregressive moving-average (ARMA) and subspace methods. However, linear models are

typically valid only within narrow operating ranges. To extend this range, nonlinear approaches such as Hammerstein, Wiener, and linear parameter-varying models have been explored. Additionally, artificial neural networks and fuzzy logic models have been developed to capture transients and improve control. While these methods have been applied to model dynamic VCC behaviour, their relevance to the IRIS is limited, as the research focuses on understanding the physical principles driving the system. Moreover, the modular configuration of the IRIS aligns better with the physics-based methods described earlier. As a result, further discussion of data-driven methods is not included in this report.

To summarize the previous discussion, the dynamic modelling methods for heat exchangers are presented schematically in Figure II.5.3. The data-driven methods are shown in gray to highlight their lesser relevance to the current study. Since a decision must be made between the MB and FD/FCV methods, Section II.5.4.1 will provide a more detailed discussion of these approaches.

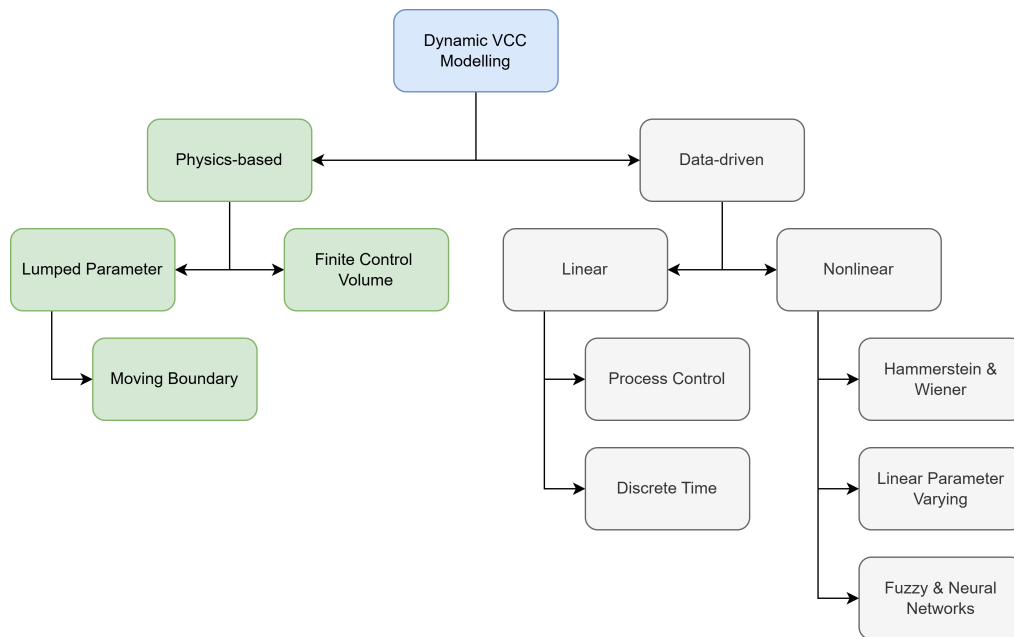


Figure II.5.3: Graphical representation of modelling approaches for the dynamic modelling of VCC systems, based on the review of Rasmussen [57].

II.5.2. Modelling Paradigms

Having covered the origins of dynamic VCC modelling, particularly regarding heat exchangers, it is now useful to take a broader view of the modelling process. In any modelling task, the first step is to understand and select the most appropriate modelling paradigm. To establish a solid foundation on modelling paradigms, this section will explore the concepts of modularity, followed by a discussion on causal and non-causal modelling approaches.

II.5.2.1. Modularity

In the context of system modelling, a common choice exists between a monolithic or modular approach [64]. The former, where the entire system is treated as one module, proves effective for problems with a limited number of equations solvable in closed form, offering insights into the general solution's characteristics. However, as systems grow larger and more complex, closed-form solutions often become more difficult to obtain. Additionally, modifying a small subset of system equations may render the original solution obsolete, as the inter-dependencies among all equations must be reconsidered to derive a new solution. To address these issues, complex system modelling frequently employs a modular approach.

Modular methods offer several advantages over simultaneous approaches. Firstly, modular problems are designed to be solved numerically, accommodating unlimited model complexity since the solution procedure is not determined by the existence of a closed-form solution. Secondly, as components are

defined independently, more detailed information can be incorporated within each individual module, and modules can be easily added, modified, or swapped without affecting other components. Finally, library packages can be built to facilitate module reuse, significantly reducing modelling efforts when constructing new systems.

Splitting a system into individual modules requires information exchange between these modules. To this end, a module is usually assigned specific ports, where the module can interact with other components via connections. Depending on the modelling goals, different variables can be used at these ports, however in physical modelling it is often convenient to use power ports, which are represented by dynamically conjugated variables called effort and flow [65]. Note that the concept of inputs and outputs is deliberately avoided here, since these definitions imply a direction of the information flow, explained in the next section.

II.5.2.2. Causal versus Non-causal

The flexibility associated with modular modelling is not always an advantage. The freedom of selecting the inputs and outputs of the system, and thereby fixing the direction of the information flow between the modules, may lead to unnecessarily complicated model structures. To prevent this, it is important to understand the difference between causal and non-causal modelling. Therefore, these two approaches will be explained briefly, including their respective advantages and disadvantages.

Causal Modelling

The basis for causal modelling is formed from Newton's paradigm that nature is not instantaneous; a specific cause leads to a corresponding effect. In the context of modular modelling, this translates to specifying the input and output variables at the ports of the modules according to a set of causality rules. Firstly, the modeller must ensure that each individual module is locally balanced, i.e. the number of unknown variables is equal to the number of equations of the module. Finally, the causal modelling principle requires that a module must be able to act and react with respect to neighbouring modules. Hence, the variables at the ports of the modules must be bilaterally coupled, such that input-output pairs are formed.

For physical models, where the connection variables at the module ports are effort and flow pairs, the causality rules can be used to identify two types of fundamental modules; storage and flow modules. These modules capture behaviour that is generally observed in various physical domains. A storage module has its connection ports oriented such that all flow variables are inputs and the effort variables are outputs. The difference between the in- and outflow of the module is equated to the change of an internal state with respect to time. The effort variables are related to this state via constitutive equations, which can be solved sequentially to obtain the outputs. Typically, storage modules follow from mass and energy balances with dynamic terms. Flow modules use effort variables as inputs and provide flow variables as outputs. Lacking internal states, the resistive modules define the flow between storage modules based on their difference in the effort variable. Often, flow modules result from conservation equations such as mass, momentum, and energy balances.

Causal models are constructed by coupling storage and flow modules in an alternating pattern. This ensures that the inputs and outputs of each consecutive module matches with its neighbouring modules, ultimately resulting in a globally well-posed model. The equations of all modules can be re-ordered such that they can be solved sequentially, and the resulting set of equations are always in an ODE form. As such, causal models are computationally attractive in comparison with higher-index Differential-Algebraic Equation (DAE) representations [66].

The causal modelling approach, while valuable as it guarantees index one models, does come with its limitations and drawbacks. One significant issue is the inability to directly connect two storage or flow modules without violating causality rules. To circumvent this, additional "dummy" modules must be inserted between the homogeneous modules to maintain the required alternating pattern. However, this introduces extra dynamics or flow resistances that may not be the focus of the analysis. Moreover, in some cases, it can even lead to high model stiffness if the time scales of the dummy modules differ from those of the main dynamics [67]. Furthermore, adhering to the alternating pattern requirement poses challenges at a system level. When constructing system models from networks of fundamental modules, modellers must manually ensure compatibility between the boundaries of different compo-

nents before they can be interconnected. This necessitates the construction of different models for various boundary conditions, ultimately limiting the modularity of the approach.

Non-causal Modelling

To overcome the rigidity of pre-defining a model's causality, non-causal modular modelling methods have been developed starting in the late 1970s [68] [69] [70]. Fundamentally inspired by bond graph modelling, as invented by Henry Paynter [71] in the early 1960s, these methods refrain from specifying the direction of information between the modules of a modular system. Instead, the unknown variables are defined symbolically, such that they can be used for implicit model representations.

When a connection is made between two modules, the port variables are classified as across variables or through variables. Two additional equations are introduced, of which the first equates all the across variables, and the second ensures that the summation of all through variables is equal to zero. The physical interpretation of the across and through variables is identical to that of effort and flow and hence the connection equations simply represent balance equations at the boundaries between subsystems, e.g. Kirchhoff's circuit laws, conservation of mass, internal force balance, Pascal's law, et cetera. If the modules are locally balanced, i.e. the number of dynamically conjugated variable pairs and inputs is equal to the degrees of freedom of the module, globally balanced models can be constructed through interconnections. Once assembled, these models can be used for simulation, which involves a solver carrying out two steps; elimination and causalization. At the elimination step, all trivial equations are removed from the system and symbolic substitution is performed if parameters can be expressed as an explicit function of other unknown variables. Next, at the causalization step, the remaining equations are re-ordered and solved for the algebraic variables and state derivatives, allowing the solver to perform a numerical integration with respect to time.

In comparison with the causal method, non-causal modelling offers a greater level of modularity, since the alternating pattern of storage and flow modules is not a prerequisite. Therefore, large dynamical models can be constructed easily without the worry of adhering to the strong causality rules at the boundaries between components. Additionally, non-causal models can be used for various types of analysis, as the causality within the model follows automatically from the boundary conditions and initial states. However, the increase in modularity and flexibility associated with non-causal modelling come at a cost. Due to the automatic assignment of causality, the modeller is not prevented from creating implicit algebraic equations or unnecessarily high-index models by inappropriately providing boundary conditions or initial states. As shown by Gani and Cameron [72], a small change in the selection of the design variables can lead to a higher index problem, even when the global balance of the model remains unchanged. Though not always possible, high-index models should be avoided as much as possible, since they are significantly more difficult to solve and can therefore make the model computationally demanding.

In summary, non-causal modelling offers a significant advantage over causal modelling, as it eliminates the need for prior assumptions regarding the causality within the model. Therefore, this modelling approach is identified as the most suitable method for modelling the VCC components of the IRIS. However, it is crucial to carefully choose the dependent and independent variables to ensure the resulting model maintains the lowest possible index and avoid unnecessary sets of implicit algebraic equations. Proper analysis of the final model is essential to confirm these criteria are met.

II.5.3. Modelica

For non-causal modelling approaches, arguably the most famous programming language is called Modelica [73]. Modelica is the result of an international effort to develop a global open source unified language for equation-based modelling of physical systems. Since its first release, a lot of work has been done on creating and improving libraries for a wide range of engineering fields, such as the automotive industry, power electronics, hydraulics, thermo-dynamic systems [74] and many more. Fortunately, libraries dedicated to modelling VCCs have also been developed [75], and even libraries specifically targeted at ECS modelling exist [76] [77]. To assess and use these libraries effectively, it is imperative to understand the basic ideas behind the Modelica language and get familiar with its semantics.

From the example shown in the original publication of Modelica [73], it can be seen that systems can be formed by hierarchically structuring lower level models. The most fundamental models are called

connectors and they are used to represent the physical ports where the general balance equations for effort and flow can be applied. Within a connector, three types of variables can be declared; potential, flow and stream variables. The latter of these variables is used if the variable is dependent on the direction of the flow. If two connectors are coupled using the connect feature, equations are introduced to ensure that the potential variables are equal, the sum of the flow variables is zero, and the sum of the product of flow and stream variables is zero.

If several components have a similar port structure, it is convenient to define a “shell” model, where only the connector instances are created. Then, when a new model is constructed, the properties of the shell class can be inherited to this model. This allows for very efficient programming, since general models can be re-used as needed. After inheriting a lower level model, additional parameters, variables and equations can be introduced within the higher level model. Modelica supports a wide range of operators and functions, e.g. the `der(·)` function indicates the derivative of a variable with respect to time, which can be used to symbolically define differential equations. Thus, by hierarchically layering sub-models and adding equations where necessary, components can be modelled in detail. Subsequently, system level models can be made by creating instances of the desired components and then using the connect feature to create the necessary balance equations for the variables at the boundaries between the components. Since the resulting model is fully described by a set of DAEs, a non-causal solver strategy as described in Section II.5.2.2 can be used to run simulations with respect to time.

Although Modelica is specifically designed to simplify the exchange and reuse of model libraries, challenges emerge for VCC-based ECS modelling. These challenges primarily stem from the complexity of heat exchanger models and the numerous details required to accurately capture their behaviour. For instance, the ThermoFluid Stream library developed by DLR [75] provides components designed for broad applicability across various fields. However, this general approach results in a limited selection of heat exchanger models, offering only an FD/FCV-based methodology. Additionally, heat transfer coefficients are often correlated with fluid properties using experimentally derived coefficients, necessitating empirical data fitting for specific systems. Similar limitations are found in other libraries, such as the one developed by Ablanque et al. [77], where heat exchanger models rely on experimentally constructed performance maps, or the library by Jordan and Schmitz [76], which exclusively adopts a finite volume approach.

It is clear that no single open-source library can fully address the dynamic modelling needs of this project. Instead, a combination of libraries must be utilized, which introduces challenges in reconciling differences between their interfaces. As a result, developing a dynamic model for the IRIS will likely require significant manual effort to carefully select and integrate appropriate submodels, ultimately creating an accurate representation of the system.

II.5.4. Individual Component Modelling

After exploring the history of VCC modelling and examining the fundamental concepts behind various modelling paradigms and the Modelica language, this section focuses on the specific approaches used for modelling the individual components of the VCC. The aim is to understand the key principles that have shaped the development of existing models, while maintaining a clear connection to the overarching non-causal modelling paradigm and features of Modelica.

II.5.4.1. Heat Exchangers

Given the complexity of the mathematics involved in modelling heat exchangers, this section begins with an exploration of some of their intricacies. Several key aspects will be addressed. First, the significance of the void fraction will be introduced, along with a review of approaches in the literature to capture this parameter. Next, correlations for heat transfer coefficients in heat exchanger models will be examined. Finally, a comparison of the MB and FCV methods will be presented.

Void Fraction

Describing the transport of mass, momentum, and energy in a two-phase mixture requires accounting for the behaviour of both the liquid and vapour phases. However, modelling these phases individually is highly complex. Instead, it is more practical to average the properties of the mixture to capture the

contributions of both phases. The concept of void fraction is central to this approach. To explain its importance for both the MB and FD/FCV methods, an introduction to the concept is provided, followed by a discussion of modelling strategies in the literature for predicting void fraction.

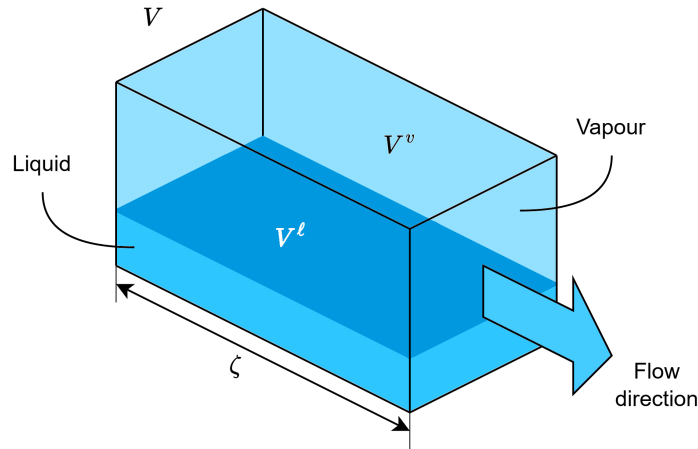


Figure II.5.4: Volume associated with a two-phase liquid-vapour mixture flow. The length of the volume ζ is defined along the flow direction.

The void fraction can be intuitively understood by considering a volume V containing a total mass M of a two-phase fluid, as shown in Figure II.5.4. This volume can represent either a two-phase region in the MB method or a fixed section of a heat exchanger with two-phase flow in the FD/FCV method. The mixture consists of saturated liquid and vapour phases, leading to the following expression:

$$M = \bar{\rho}V = \rho^\ell V^\ell + \rho^v V^v \quad (\text{II.5.1})$$

Here, the $^\ell$ and v superscripts refer to properties of the liquid and vapour phases, respectively, while $\bar{\rho}$ represents the average density of the mixture. Since the volumes of the phases sum to the total volume ($V = V^\ell + V^v$), the equation can be rewritten as:

$$\begin{aligned} \bar{\rho} &= (1 - \bar{\gamma}_V) \rho^\ell + \bar{\gamma}_V \rho^v \\ \bar{\gamma}_V &= \frac{V^v}{V^\ell + V^v} \end{aligned} \quad (\text{II.5.2})$$

The parameter $\bar{\gamma}_V$, known as the volumetric void fraction, represents the relative contribution of the vapour phase volume to the total volume. This concept extends beyond density and can be applied to other fluid properties, such as viscosity and velocity, highlighting its significance in two-phase flow modelling [78].

While Figure II.5.4 provides a simplified visualization, real two-phase flows are rarely this straightforward. Determining the relative contributions of the phases based on measurable quantities is a complex task. Researchers have devoted significant effort to developing simplified average expressions for two-phase properties, such as $\bar{\rho}$ in Equation II.5.2, that align closely with observed behaviour. Various versions of the void fraction concept have been proposed, depending on modelling applications and measurement methods [79]. Among these, the cross-sectional void fraction is particularly popular:

$$\gamma_A = \frac{A^v}{A^\ell + A^v} \quad (\text{II.5.3})$$

This represents the area occupied by vapour divided by the total cross-sectional area perpendicular to the flow. It allows for spatial variation along the flow path, making it well-suited for one-dimensional flow models typically used in heat exchangers. Consequently, the cross-sectional void fraction, from here on referred to simply as the void fraction γ , has been extensively studied in the literature.

As noted by Vijayan et al. [80], void fraction correlations in the literature can be categorized into four groups: slip ratio models, $K\varepsilon_h$ models, drift-flux correlations, and miscellaneous models. Slip ratio and

$K\varepsilon_h$ models are closely linked to the simpler Homogeneous Equilibrium Model (HEM), a foundational approach in void fraction modelling. The HEM assumes equal flow velocities for both phases [79], i.e., $u^\ell = u^v$, where:

$$u^\ell = \frac{\dot{m}^\ell}{\rho^\ell A(1-\gamma)}, \quad u^v = \frac{\dot{m}^v}{\rho^v A\gamma} \quad (II.5.4)$$

Using the relationships $\dot{m}^\ell = (1-x)\dot{m}$ and $\dot{m}^v = x\dot{m}$, the void fraction under the HEM can be expressed as:

$$\gamma_{HEM} = \frac{1}{1 + \frac{1-x}{x} \left(\frac{\rho^v}{\rho^\ell} \right)} \quad (II.5.5)$$

Although the assumption of equal phase velocities is not always realistic, the HEM highlights the void fraction's dependence on vapour quality and the density ratio of the phases. Cioncolini and Thome [78] identified these two parameters as the most critical factors in void fraction modelling. More complex models often build on this foundation by incorporating additional parameters to enhance accuracy or predictive capability. For a detailed discussion of such models, readers are referred to comprehensive reviews, such as the one by Pietrzak and Płaczek [81].

Since the void fraction depends on various flow and fluid parameters, calculating its time derivative often involves complex mathematical derivations. To address this challenge, several researchers have sought to simplify the modelling of dynamic void fraction behaviour in two-phase flows. One of the earliest contributions to this effort came from Wedekind [60], who proposed a relatively simple approach to tackle the time-varying void fraction problem in the context of his early work on MB methods. In his PhD dissertation, he circumvented the need to track temporal variations in the void fraction by assuming that the mean void fraction within the two-phase region of a heat exchanger remains approximately constant over time. This assumption was later formalized and further analysed in a subsequent paper [82], where the concept of the system mean void fraction was introduced, $\bar{\gamma}_s$. This parameter represents an alternative averaging of the cross-sectional void fraction, γ_A , along the length of the two-phase region, ζ , as follows:

$$\bar{\gamma}_s = \bar{\gamma}_s(t) \equiv \frac{1}{\zeta} \int_{z=0}^{\zeta} \gamma_A(z, t) dz \quad (II.5.6)$$

While the system mean void fraction is, by definition, time-dependent due to variations in the two-phase region, Wedekind and collaborators demonstrated through experimental validation that assuming a time-invariant mean void fraction is reasonable across a wide range of flow configurations, provided that the transients are sufficiently slow [63, 82, 83]. This finding proved pivotal for the adoption of MB methods, and the assumption of a constant mean void fraction has since been widely implemented [57].

However, while the time-invariant void fraction assumption works well for small transients, its validity diminishes under large transients, particularly when phase regions appear or disappear within the heat exchanger. To address such scenarios, researchers have developed alternative methods known as Switched Moving Boundary (SMB) approaches. These methods dynamically adjust the set of governing equations based on the configuration of the phase regions [84]. Zhang and Zhang [85] demonstrated that by incorporating the transient behaviour of the mean void fraction in the two-phase region, more robust switching criteria could be formulated compared to assuming a constant mean void fraction. Similarly, McKinley and Alleyne [86] developed their approach by including both the lengths of phase regions and the mean void fraction in their switching criteria. Qiao et al. [87] later generalized McKinley and Alleyne's strategy, showing that their method offered higher model accuracy compared to the work of Zhang and Zhang [85]. Across these studies, researchers emphasize the importance of including a dynamic mean void fraction to ensure numerical robustness and model integrity under large transients that cause phase zones to appear or disappear within the heat exchanger.

Heat Transfer Correlations

In addition to modelling the mass and energy transport of refrigerant and cooling/heating fluids, heat exchanger models also account for heat transfer. This heat transfer typically comprises three components: convection from the primary fluid to the heat exchanger's solid wall, conduction through the wall,

and convection from the wall to the secondary fluid. The convective heat transfer between the fluid and the wall is described by the general equation:

$$\dot{Q} = \alpha A_h (T_w - T_f) \quad (\text{II.5.7})$$

Here, A_h is the heat transfer area, α represents the convective heat transfer coefficient (HTC), and the subscripts w and f refer to the wall and fluid temperatures, respectively. In this formulation, the positive heat flow direction is defined as moving from the wall to the fluid. While the heat transfer area is generally derived from the heat exchanger's geometry, which is known or measurable, and the wall and fluid temperatures are either dynamic states or functions of them, the main challenge in determining convective heat flow lies in estimating appropriate values for the HTC.

The HTC reflects the local interactions driving heat transfer between the fluid and the solid surface. Since these interactions depend on complex flow parameters and fluid properties, HTC values are typically determined using empirical correlations. These correlations, derived from non-dimensional groups such as the Reynolds and Prandtl numbers, are well-established for single-phase flows. Comprehensive lists of such correlations for various flow conditions and fluids are readily available in standard textbooks [88].

For two-phase flows, however, selecting suitable HTC correlations is more application-specific. In these flows, heat transfer arises not only from convection due to fluid motion along the wall but also from phase change phenomena, such as boiling or condensation. These processes introduce complex thermo-fluid interactions that are challenging to generalize. Despite these complexities, researchers have developed simplified correlations for two-phase flows that resemble those for single-phase flows.

Two-phase flows are generally classified into two categories: boiling and condensing flows. As noted by Shah [89], a key consideration in two-phase heat transfer is the scale of the flow geometry. While most predictive methods were originally developed for large tubes (macrochannels), they often fail in smaller channels due to increased flow restrictions and the prominence of small-scale phenomena, such as the increased dominance of surface tension related effects [90, 91]. Given the compact heat exchangers used in the IRIS, correlations for mini- and microchannels are particularly relevant.

For condensing flows in mini- and microchannels, extensive research is available, as summarized by El Kadi et al. [92]. The authors highlight that the large number of correlations stems from the many parameters influencing heat transfer and pressure drop, leading to significant variation in predictions across models. Nonetheless, several general correlations for a wide range of condensing flows have been proposed. One notable example is the work by Shah [93, 94], which categorizes flow regimes into three types, Regimes I, II, and III, and considers the following heat transfer correlations:

$$\begin{aligned} \alpha_I &= \alpha_{LO} \left(1 + \frac{3.8}{Z^{0.95}} \right) \left(\frac{\mu_L}{14\mu_G} \right)^{(0.0058+0.557p_r)} \\ \alpha_{Nu} &= 1.32 \text{Re}_{LO}^{-1/3} \left[\frac{\rho_L (\rho_L - \rho_G) g k_L^3}{\mu_L^2} \right]^{1/3} \\ \text{where: } \alpha_{LO} &= 0.023 \text{Re}_{LO}^{0.8} \text{Pr}_L^{0.4} k_L / D \\ Z &= (1/x - 1)^{0.8} p_r^{0.4} \end{aligned} \quad (\text{II.5.8})$$

The two-phase heat transfer coefficient, α_{TP} , is determined based on the flow regime:

$$\alpha_{TP} = \begin{cases} \alpha_I, & \text{Regime I} \\ \alpha_I + \alpha_{Nu}, & \text{Regime II} \\ \alpha_{Nu}, & \text{Regime III} \end{cases} \quad (\text{II.5.9})$$

The flow regime is identified using the dimensionless vapour velocity, J_g (not shown here for brevity). High vapour velocities correspond to Regime I, very low velocities to Regime III, and intermediate velocities to Regime II.

In the context of dynamic modelling, Shah's correlation offers a key advantage: it can be evaluated explicitly if the thermodynamic states of the saturated liquid and vapour are known. This eliminates

the need for solving implicit algebraic loops, significantly reducing computational demand compared to correlations that depend on heat flux. Although initially appearing complex, Shah's method strikes an effective balance between generality, accuracy, and computational efficiency, making it well-suited for modelling the IRIS condenser.

For boiling flows, general correlations are less common, likely because heat transfer depends heavily on specific flow conditions, and significant methodological differences exist between pool boiling, forced convection subcooled boiling, and saturated boiling with forced flow [91]. However, under normal operation, the most relevant boiling type in the IRIS evaporator is likely saturated boiling with forced flow, making this type worth examining in more detail. The review by Kim and Mudawar [95] highlights that many correlations for boiling flow HTC include a dependency on the heat flux supplied to the fluid. Consequently, implementing such a correlation in the dynamic framework of the MB or FD/FCV method, which relies on equations similar to Equation II.5.7, would require solving the heat transfer from the wall to the fluid implicitly. This approach not only increases computational demand but also requires well-defined initial guesses for the implicit solver, which can be challenging to establish beforehand. Therefore, focusing on methods that avoid implicit formulations is more practical.

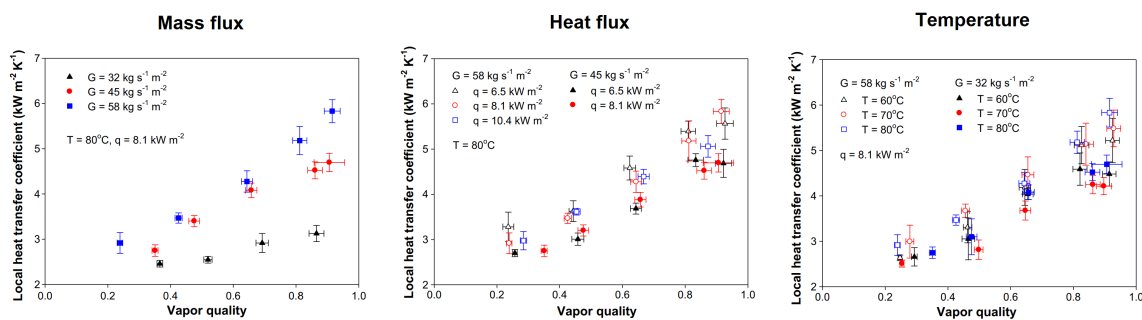


Figure II.5.5: Experimental results from Lee et al. [96] for the evaporation heat transfer coefficient as a function of the vapour quality. The effects of changing the mass flux (left), heat flux (middle), and evaporation temperature (right) are included in the diagrams.

A recent study by Lee et al. [96] provides valuable experimental data on the evaporation HTC in a brazed plate heat exchanger using R-1233zd(E) as the working fluid. Since this fluid is also used in the IRIS, and the IRIS evaporator is of the brazed plate type, the findings from Lee et al. are particularly relevant and merit further analysis.

Table II.5.1: Operating range for the experimental results presented by Lee et al. [96].

Operating conditions	Range
Evaporating temperature (°C)	60, 70, 80
Refrigerant mass flux ($\text{kg s}^{-1} \text{m}^{-2}$)	32, 45, 58
Heat flux (kW m^{-2})	3.8, 6.5, 8.1, 10.4
Vapour quality	0.17-1.00

In their study, Lee et al. conducted experiments using an isolated evaporator with two-phase refrigerant flow, where the evaporation temperature, mass flow rate, heat flux, and vapour quality were independently controlled. For various steady-state operating conditions (listed in Table II.5.1), the evaporation HTC was determined using a logarithmic mean temperature difference approach. The results are presented in Figure II.5.5, revealing that under the tested conditions, the evaporation HTC is approximately independent of heat flux and evaporation temperature, while mass flux and vapour quality exert the strongest influence. Based on these findings, the authors proposed a simplified HTC correlation

that depends only on the Reynolds and Prandtl numbers:

$$\begin{aligned}
 Nu_r &= 0.9243 Re_{eq}^{0.6151} Pr_\ell^{0.33} \\
 Re_{eq} &= \frac{G_{eq} D_h}{\mu_\ell} \\
 G_{eq} &= G \left[(1 - x_m) + x_m \left(\frac{\rho_l}{\rho_g} \right)^{0.5} \right]
 \end{aligned} \tag{II.5.10}$$

Similar to Shah's correlation for condensing flows (Equation II.5.8), the correlation by Lee et al. can be evaluated explicitly, eliminating the need for iterative procedures when calculating the heat transfer coefficient for two-phase evaporating refrigerants.

Finally, the applicability of Lee et al.'s results to the IRIS's operating conditions should be critically assessed. Comparing the range of conditions in Table II.5.1 with the temperature-entropy diagram in Figure II.4.4, the most notable difference is the significantly higher evaporation temperature in the experiments by Lee et al. (minimum 60 °C) compared to the IRIS design point (approximately 20 °C). However, since Lee et al. demonstrate that evaporation temperature has a relatively minor impact on the HTC compared to mass flux and vapour quality, the advantages of matching the working fluid and heat exchanger type outweigh the discrepancies in the evaporation temperatures for the accuracy of the correlation.

Moving Boundary versus Finite Control Volume

When comparing the FCV and MB methods for shell-and-tube heat exchangers in centrifugal chillers, Bendapudi et al. found that both models yielded very similar results [62]. The models were capable of predicting the steady-state and transient behaviour of an experimental setup reasonably well. However, the FCV model took approximately three times longer to execute compared to the MB model. For large transients, the FCV model proved to be more robust, though the significant computational demand resulted in a 20% higher execution time than real time. The authors also discuss the absence of accurate void-fraction models, leading to an under-prediction of refrigerant charge for both models. These insights are a valuable starting point for understanding the differences between the two methods. However, the system considered for their work consisted of flooded water-to-refrigerant shell-and-tube heat exchangers for both the condenser and evaporator. In the IRIS setup, different types of heat exchangers are used, and therefore the results of Bendapudi et al. should be interpreted with some caution. This is especially important for the condenser, since the flow configuration of the microchannel heat exchanger in the IRIS is of a cross-flow type, possibly leading to fundamentally different results.

In more recent work, Decideri et al. performed a similar comparison between the two modelling approaches for heat exchangers [97]. However, in contrast to the efforts of Bendapudi et al., the heat exchanger models were developed for a small-sized organic Rankine cycle unit. Two brazed plate heat exchangers were used for the condenser and evaporator, similar to the evaporator of the IRIS. First, the MB and FCV method were compared to a highly accurate benchmark model, which was based on an FCV method with 100 control volumes. The goal of this comparison was to investigate if the conservation of mass and energy is violated in lower order models. The results indicate that the MB and FCV method both satisfy the conservation of mass and energy with only a slight numerical error. Additionally, it is shown that the accuracy of the FCV method is only greater than the MB accuracy if the number of control volumes exceeds 20. However, the computation time for the 20 control volume FCV method was over 18 times greater than the MB computation time, which is in line with the conclusions of Bendapudi et al.. It must be noted however, that the significantly lower computation time of the MB method comes at the cost of modelling detail, as can be seen in the temperature distribution profiles along the heat exchanger in Figure II.5.6.

Decideri et al. tried to validate the models using a small organic Rankine cycle test rig. The results shown are limited and the experimental data contains a lot of noise. Additionally, the considered range of transients is relatively small. Nonetheless, both models show very good agreement and the authors suggest that the MB method is preferred for small-scale organic Rankine cycle purposes, due to its high accuracy and low computational cost. Through a parametric analysis, a final note is given on the limitations of the constant void fraction assumption in the MB method. To accurately model fast

transients associated with pressure and mass flow changes, the authors suggest using an average void fraction as function of pressure and boundary enthalpies. Doing so resulted in better agreement with the experimental results.

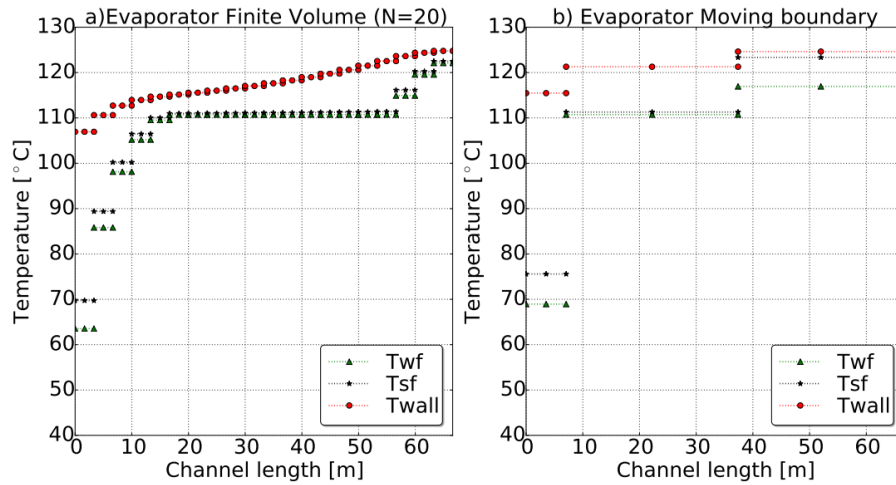


Figure II.5.6: Temperature profiles along an evaporator for the FCV model (a), and the MB model (b) [97].

Though applicable for the evaporator of the IRIS, the results of Decideri et al. may be questionable for the cross-flow condenser. Luckily, Pangborn et al. have investigated the differences between the FCV method and a switched MB method for cross-flow refrigerant-to-air heat exchangers [98]. The models were validated against an experimental test facility, of which documentation can be found in the work of Li and Alleyne [99]. The results of the comparison show that the MB model can be executed much faster than the FCV model and both models provide similar accuracy, as was also reported by Bendapudi et al. and Decideri et al.. However, Pangborn et al. conclude that though the FCV method is significantly slower in simulation, its simpler discretization is more convenient for reconfiguration to other heat exchanger types and flow configurations. Additionally, the FCV model provides a high number of thermodynamic properties in each control volume, resulting in more detailed distributed information along the length of the heat exchanger. Finally, the authors argue that the level of fidelity of the FCV model can be easily altered by changing the number of control volumes. As a result, the choice between the MB and FCV method should also be based on the required modelling flexibility of the heat exchanger.

From the above comparisons, it can be argued that the MB method is most suitable for modelling the evaporator of the IRIS. Although the robustness of the FCV method can be superior for large transients, the relatively low computational cost of the MB method is very favourable, especially in the context of control-oriented modelling. Additionally, since both models show comparable accuracy, it is expected that the MB method will provide satisfactory predictions for the evaporator properties. For the condenser, both the MB and FCV method have important advantages. For control-oriented modelling, where computational cost should be as low as possible, the MB method is likely more suitable. However, for future research, different condensers can be installed in the IRIS facility, favouring the flexibility of the FCV method.

II.5.4.2. Compressor

In most publications on dynamic VCC modelling, the dynamics of the heat exchangers are the only dynamics considered. As discussed in Section section II.5.1, this methodology follows from the fact that the slowest dynamics of the system are contained within the heat exchangers, and the transients associated with auxiliary components evolve on a much faster time scale. Following this ideology, it is not surprising that in most dynamic VCC research, the compressor is modelled as a static component. This implies that as the dynamics of the heat exchangers slowly evolve, the internal dynamics of the compressor are essentially infinitely fast, causing the compressor to reach its individual steady-state conditions with respect to its surroundings instantly. As reviewed by Rasmussen [57], this approach has been applied to almost all dynamic VCC models in literature. With no dynamic states within the

compressor model, the remaining objective is to find appropriate steady-state expressions that state the mass flow rate through, and specific enthalpy at the outlet of the compressor, as a function of the compressor speed and upstream and downstream pressure, and the inlet conditions [100] (i.e. given that the refrigerant at the inlet of the compressor is typically a single-phase superheated vapour, the thermodynamic state can be fully defined if apart from the inlet pressure, either the inlet temperature, density, or specific enthalpy is known). Depending on the type of compressor, the form of these expressions differs slightly, but in general they are given in the following form:

$$\begin{aligned}\dot{m} &= f(P_2/P_1, \omega, T_1) \\ h_2 &= h_1 + \frac{1}{\eta} (h_{2s} - h_1) \\ \eta &= f(P_2/P_1, \omega, T_1)\end{aligned}\tag{II.5.11}$$

where: $h_{2s} = g(P_2, s_1)$
 $s_1 = g(P_1, T_1)$

The outlet specific enthalpy is determined using the isentropic efficiency, η , while the isentropic outlet enthalpy, h_{2s} , is derived from the inlet entropy and outlet pressure. In the equation above, the $g(\cdot)$ functions represent fluid property relations, and the $f(\cdot)$ functions describe performance relations that depend on the type of compressor. It is worth reiterating that steady-state models for these performance relations can be used, greatly simplifying the complexity of the overall compressor model.

As discussed in Section II.4.2, the modelling of centrifugal compressors is particularly relevant for the IRIS. While it may seem intuitive to apply the steady-state modelling techniques used during the integrated design optimizations in Section II.4.1, these models are tailored for adjusting the compressor's geometrical features during the design process. For dynamic simulations, however, these geometrical adjustments are irrelevant, as the machine design and corresponding parameters remain fixed. Instead, models for such simulations focus on the compressor's off-design performance, ultimately allowing for the use of much simpler methods.

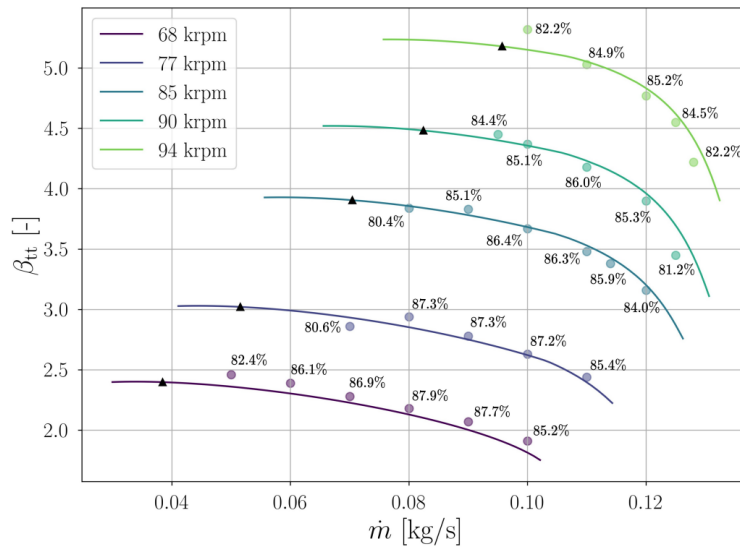


Figure II.5.7: Off-design performance map of a centrifugal compressor stage, adapted from Giuffr  [30]. Solid lines represent speed lines obtained from a mean-line model, while the dots correspond to mass-averaged CFD calculations. The percentages at the dots indicate the isentropic efficiency.

A widely used method for modelling the steady-state off-design performance of centrifugal compressors involves performance maps. These maps typically plot the compressor's pressure ratio and efficiency as functions of the mass flow rate for various constant speeds, of which an example is shown in Figure II.5.7. Often described in the form of two-dimensional tables, computing the mass flow rate and efficiency from these maps involves numerical interpolation, i.e. the $f(\cdot)$ functions in Equation II.5.11 represent the interpolation of the compressor map tables, for instance through the well-known β -method

[101]. Note that each speed line on the map has two limits: on the left, it ends at low mass flow rates and high pressure ratios, and on the right, at high mass flow rates and low pressure ratios. The left limit is known as the surge point, where the mass flow rate becomes too low to sustain the high pressure ratio, causing flow separation and reattachment at certain frequencies. This results in violent oscillations and a sharp performance drop.

The right limit corresponds to choke conditions, where high mass flow rates cause the internal velocities to reach the fluid's local speed of sound. Under these sonic conditions, further increases in mass flow rate are impossible, regardless of the pressure difference, and the compressor's efficiency typically decreases. In standard operation, VCC compressors are not designed to run under surge or choke conditions for extended periods. Unlike other applications, such as turbocharged engines in cars [102], where modelling these phenomena is critical, they are not of particular interest here. Standard performance maps are therefore sufficient for modelling the off-design compressor performance within the IRIS.

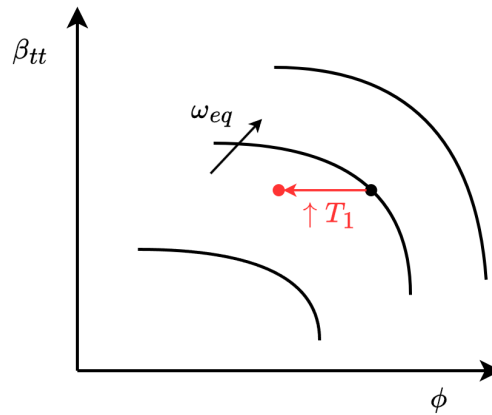


Figure II.5.8: Simplified corrected compressor map showing the effects of increased inlet temperature at constant pressure ratio (red) relative to the design point, marked by a black dot.

Compressor performance maps are typically derived from experimental data or detailed modelling methods. A common implicit assumption during this process is that the compressor's inlet conditions remain constant. However, in off-design operation, most practical applications involve varying inlet conditions, which cause the shape of the performance maps to change. Constructing separate compressor maps for every possible set of inlet conditions is not practical. Instead, these maps can be corrected to account for changing inlet conditions using a dimensionless analysis of compressor performance metrics. As described by Glassman [103], one approach for this is to assume ideal gas behaviour, which leads to the following equivalences:

$$\begin{aligned} \frac{\dot{m}\sqrt{T_1}}{P_1} &= \frac{\dot{m}_{eq}\sqrt{T_{ref}}}{P_{ref}} = \phi \\ \frac{\omega}{\sqrt{T_1}} &= \frac{\omega_{eq}}{\sqrt{T_{ref}}} \end{aligned} \quad (II.5.12)$$

These equivalences indicate that expressing compressor maps in terms of the flow number ϕ and corrected speed ω_{eq} accounts for variations in inlet temperature and pressure. To illustrate this, consider the compressor operating at the design point, marked by the black dot in Figure II.5.8. When the inlet temperature increases while maintaining a constant pressure ratio and actual compressor speed, the corrected speed and corresponding flow number decrease, as follows from Equation II.5.12. This can be intuitively explained by the reduction in fluid density caused by the temperature increase: at lower densities, the compressor must rotate faster to move the same fluid mass. The decreased flow number can be used with Equation II.5.12 to compute the actual mass flow rate at the off-design point. However, within the expression for the flow number, the inlet temperature appears again, and as a result, the increase in inlet temperature leads to an even lower actual mass flow rate. Similarly, a decrease in inlet pressure also reduces the actual mass flow rate, corresponding to the lower fluid density at reduced pressures.

While ideal gas corrections are commonly applied to compressor performance maps, their validity for the IRIS is not guaranteed due to the use of R-1233zd(E). This fluid does not always behave as an ideal gas, which can result in inaccuracies when applying the correction method described above. Fortunately, alternative correction methods have been proposed to account for deviations from ideal gas behaviour. For example, in Glassman's derivation [103], where the ideal gas corrections in Equation II.5.12 were established, an alternative approach was presented for cases where the specific heat ratio is not constant. This approach incorporates the effect of varying specific heat ratios by using the fluid's sonic conditions. Another example is provided by Pham et al. [104], who studied a centrifugal compressor for supercritical CO₂. In this application, where compression occurs near the fluid's critical point and the ideal gas law does not apply, the authors developed a correction method that extends the ideal gas corrections to include the isentropic volume exponent γ_{Pv} [105].

$$\gamma_{Pv} = -\gamma \frac{v}{P} \left(\frac{\partial P}{\partial v} \right)_T \quad (\text{II.5.13})$$

For an ideal gas, where $P = RT/v$, the isentropic volume exponent simplifies to the specific heat ratio. The authors demonstrate that their method, though more complex, can accurately correct compressor performance across a wide range of inlet temperatures and pressures, with minimal discrepancies between the corrected parameters at different conditions. However, since the inlet conditions in the IRIS are unlikely to approach the fluid's critical point, the trade-off between improved accuracy and increased complexity may make this method less suitable.

II.5.4.3. Expansion Valve

Similar to the compressor, the expansion valve is typically modelled as a static component [57]. In this approach, the model calculates the mass flow rate through the valve and the outlet enthalpy based on the inlet enthalpy, as well as the upstream and downstream pressures.

In nearly all dynamic modelling efforts, the expansion process is considered adiabatic, meaning no heat exchange occurs between the fluid and its surroundings [100]. Additionally, the change in kinetic energy between the inlet and outlet of the valve is neglected. As a result, the first law of thermodynamics dictates that the process is isenthalpic:

$$h_{in} = h_{out} \quad (\text{II.5.14})$$

To compute the mass flow rate, most models use a form of the Bernoulli equation, incorporating corrections for irreversibilities and compressibility effects. Generally, this Bernoulli-based expression takes the following form [100]:

$$\dot{m} = A_v C_d \sqrt{\rho_{in} \Delta P_{eff}} \quad (\text{II.5.15})$$

Here, A_v represents the valve opening, which, in the case of the IRIS, is controlled by a stepper motor, while C_d accounts for deviations from Bernoulli's principle. The effective pressure difference ΔP_{eff} is the primary driver of the mass flow rate through the valve.

A critical phenomenon to consider is valve choking, which occurs in most refrigeration cycles when the fluid undergoes a phase change while passing through the expansion valve. This process, known as flash evaporation, produces vapour with a much lower sonic velocity than the upstream liquid. The resulting shocks within the flow restriction limit the maximum achievable mass flow rate through the valve, and further increases in the pressure differential no longer lead to higher mass flow rates [106]. Capturing the thermodynamic behaviour of flash evaporation is highly complex, often requiring C_d to be determined by fitting experimental data to the valve model. Nevertheless, first-principle approaches have been developed to represent the key physics of choked flows, and some of these yield relatively simple expressions.

For example, Muroi [107] proposed a method based on defining a critical pressure ratio ΔP_{crit} using the recovery factor F_L and a critical pressure ratio factor F_F derived from the Homogeneous Equilibrium Model (HEM). In this framework, the effective pressure difference for Equation II.5.15 can be

determined as follows:

$$\begin{aligned}
 F_F &= 0.96 - 0.28 \sqrt{\frac{P_{in}^\ell}{P_c}} \\
 \Delta P_{crit} &= F_L^2 (P_{in} - F_F P_{in}^\ell) \\
 \Delta P_{eff} &= \begin{cases} \Delta P & \Delta P < \Delta P_{crit} \\ \Delta P_{crit} & \text{otherwise} \end{cases}
 \end{aligned} \tag{II.5.16}$$

Here, P_{in}^ℓ represents the liquid saturation pressure corresponding to the inlet temperature. Notably, as a result of the HEM, the critical pressure ratio factor depends solely on the saturation pressure P_{in}^ℓ and the critical pressure P_c of the fluid. This formulation provides a relatively simple way to model valve choking, allowing the mass flow rate to be explicitly computed as a function of known variables and parameters.

II.5.4.4. Liquid Receiver

In typical refrigeration systems, the liquid receiver is positioned directly after the condenser and upstream of the expansion valve. It serves as a passive component for regulating the mass flow through the cycle, also referred to as the active charge [108]. Its operation depends on the application, but the most common configuration involves maintaining both liquid and vapour in the receiver while ensuring that only liquid exits through an outlet positioned at the bottom. When the cycle operates under off-design conditions, the liquid level in the receiver adjusts accordingly. Since the liquid's density is significantly greater than that of the vapour, changes in the liquid level reflect corresponding variations in the total mass circulating through the cycle.

In most VCC modelling efforts, the liquid receiver is neglected. This simplification assumes a constant active charge and negligible mass and thermal dynamics of the receiver [57, 109]. In contrast, for heat recovery systems based on the Organic Rankine Cycle (ORC), which operates as the reverse of the VCC [27], the liquid receiver has been studied in greater detail because of its critical role in preventing cavitation in the liquid pump [110]. Moradi [111], for instance, reviews various modelling approaches for the liquid receiver in ORC systems. In most studies, the liquid receiver is assumed to be fully flooded when the condenser outlet is subcooled or to contain both liquid and vapour when the condenser outlet is in the two-phase regime.

This modelling approach is thermodynamically reasonable, as the presence of vapour in the liquid receiver implies a steady-state equilibrium between the liquid and vapour phases. Ideally, in the absence of external heat transfer, this equilibrium is only possible if the liquid and vapour have equal temperatures. Given their shared pressure, the liquid and vapour must then be saturated. However, because the pressure drop between the condenser and liquid receiver is typically very small, the saturated conditions within the receiver would force the fluid exiting the condenser to also be at saturated conditions. As a result, condensation would only progress to the point of saturated liquid, preventing subcooling. Subcooling, therefore, is only achievable when the receiver is fully flooded, which explains why most researchers adopt this assumption.

In practice, subcooling degrees greater than zero have been observed in systems where the liquid receiver contains vapour. For example, during the commissioning of the IRIS facility, a subcooling degree of approximately 4 K was recorded [53], even though sight glasses confirmed that the receiver was not fully flooded. Similar results have been reported in the experimental works of Moradi et al. [112] and Oh et al. [113] on ORC systems. Moradi [111] explores this phenomenon to some extent, identifying potential causes such as non-condensable gases accumulating at the receiver's top, lubricant contamination from the expansion valve forming a barrier between liquid and vapour, and heat exchange between the receiver and its surroundings due to temperature gradients.

These observations challenge the common assumption that receiver conditions are solely dictated by the condenser's exit state. Moradi instead highlights the dynamic interdependence between the liquid receiver and other system components. For example, an increase in the liquid level within the receiver is necessarily paired with a decrease in the condenser's liquid content, which reduces the degree of subcooling at the condenser outlet. Conversely, a drop in the receiver's liquid level leads to an increase in the condenser's liquid content and subcooling. This interplay underscores the deep

connection between subcooling and receiver dynamics, demonstrating that these phenomena cannot be accurately modelled in isolation.

Supporting this, Oh et al. [113] argue that the thermodynamic state of the liquid receiver cannot be explained through conventional thermodynamics alone but must instead be derived from a system-wise mass balance. This conclusion is based on experimental observations of the liquid receiver in an ORC system, where the receiver contained both liquid and vapour at equal temperatures, yet exhibited significant subcooling. The authors suggest that the vapour in the receiver can effectively be treated as a noncondensable gas.

In summary, the findings of Moradi et al. and Oh et al. highlight the limited understanding of the liquid receiver's behaviour, emphasizing the need for further research to clarify its role in both VCC and ORC systems.

II.6

Control

This chapter reviews control methods for VCC systems. It begins by categorizing existing approaches found in the literature and highlighting their key characteristics. Then, these methods are evaluated in relation to the overall objectives of the IRIS, identifying the most suitable candidates for the control goals of this thesis.

II.6.1. Classifying VCC Control Methods

In the context of refrigeration, the goal of a control system is to achieve a specified cooling load or temperature of the enclosed region, given that disturbances in outside temperatures and cooling demand can occur. Additionally, the control goal can include optimal performance, meaning as little energy is consumed as possible or responding as fast as possible to external disturbances. The control system operates by actively varying system inputs to regulate key process variables that represent the operational state of the thermodynamic processes. Typically, these output process variables include pressures and temperatures at various points in the cycle, since these can be measured with relative ease. Since the standard VCC contains two inputs that are directly integrated into the refrigerant cycle (i.e. the compressor speed and expansion valve opening), most control strategies in literature focus on manipulating these two inputs to achieve the desired behaviour [58].

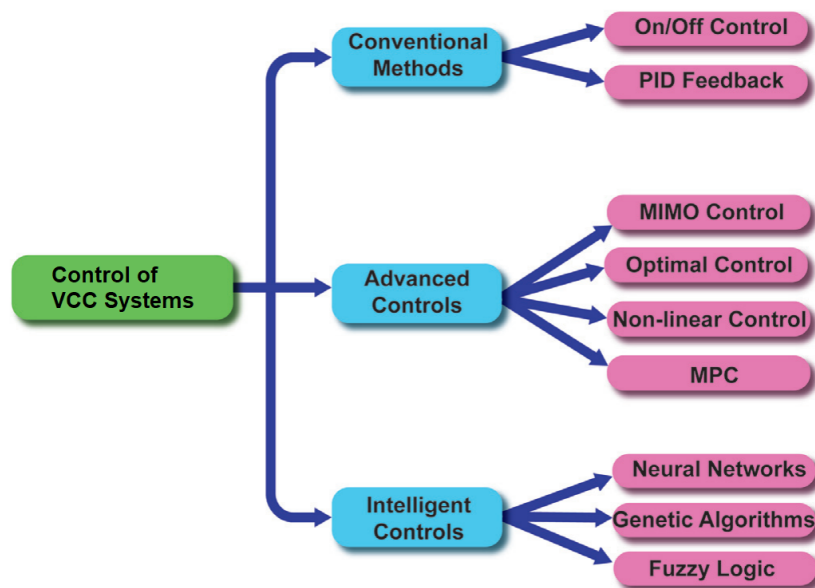


Figure II.6.1: Classification of control methods for VCC systems in literature, adapted from [58].

VCC control approaches can generally be divided into three classes: conventional methods, advanced methods, and intelligent methods. In Figure II.6.1 these classes are graphically depicted, where it can be seen that each class contains several methods. To understand the differences between these methods, each class will be discussed briefly.

II.6.1.1. Conventional Methods

Early refrigeration systems operated at a fixed steady-state point, relying on constant-speed compressors and fixed capillary tubes for the expansion process. To handle part-load cooling demands caused by fluctuations in external temperatures or cooling requirements, an on-off control strategy was commonly employed. This cyclic behavior, however, resulted in inefficiencies due to the system's thermal capacitance [114]. In the 1970s, the introduction of variable-speed compressors in refrigeration and heat pump systems marked a significant improvement in efficiency [115], as continuous operation eliminated the need for on-off cycling. However, alongside these efficiency gains came new challenges. Rapid changes in compressor speed can cause large variations in the pressure ratio, which fixed capillary devices cannot accommodate by adjusting the refrigerant flow to the evaporator. This limitation results in decreased performance at partial load, and for very large transients may shift the evaporator outlet conditions into the two-phase regime, risking liquid droplets entering the compressor and causing internal damage.

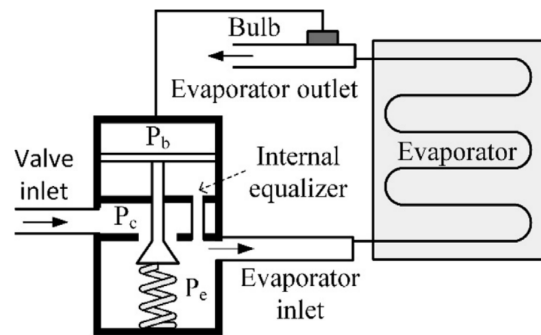


Figure II.6.2: Schematic representation of a thermostatic expansion valve [116].

To address these challenges, researchers have explored alternatives to fixed capillary throttling devices. For instance, Cohen et al. [117] recommended pairing variable-speed compressors with Thermostatic Expansion Valves (TEVs). These valves mechanically regulate their opening based on refrigerant conditions at the evaporator outlet, maintaining the refrigerant in a superheated state and protecting the compressor from liquid ingestion. As shown in Figure II.6.2, this regulation is achieved through a sensing bulb, filled with saturated refrigerant, thermally connected to the evaporator outlet and linked to the expansion valve via a pipe. Inside the valve, a diaphragm separates the refrigerant from the bulb and the refrigerant flowing through the valve. The diaphragm's displacement, which controls the valve opening, is driven by the pressure difference between the two. A drop in evaporator outlet temperature reduces the sensing bulb's pressure, causing the valve to partially close and decrease the refrigerant flow to the evaporator. This reduction limits the supply of cold fluid, increasing the evaporator outlet temperature and thereby correcting the initial temperature drop. A spring within the TEV allows adjustment of the nominal pressure differential, enabling precise regulation to maintain a consistent degree of superheating at the evaporator outlet.

Although TEVs significantly improve performance under partial loads and varying external temperatures [118], their operating range remains limited. This is primarily due to the interaction between the expansion valve and evaporator dynamics, which can lead to operational instabilities, particularly when paired with variable-speed compressors [119]. Known as hunting, these instabilities manifest as underdamped oscillations in key process variables, such as evaporator pressure and outlet temperature. Hunting poses a major challenge for VCC systems, as the oscillations can cause compressor liquid ingestion and reduce the lifespan of the expansion device [120], making it essential to avoid.

Huelle [121] observed that hunting frequently occurs when a VCC system operates at a low degree of

superheating, whether controlled by a TEV or a manually operated valve. Based on this, the author introduced the concept of Minimal Stable Superheat (MSS), which relates the stable degree of superheating to the system's cooling load, as shown in Figure II.6.3. The plot indicates that higher cooling loads require an increased degree of superheating for stability. However, maintaining low superheating is essential for optimal VCC efficiency [122]. Since TEVs can only maintain a fixed degree of superheating, VCC systems controlled by TEVs thus face a trade-off: either low efficiency at low cooling loads or instability at high cooling loads.

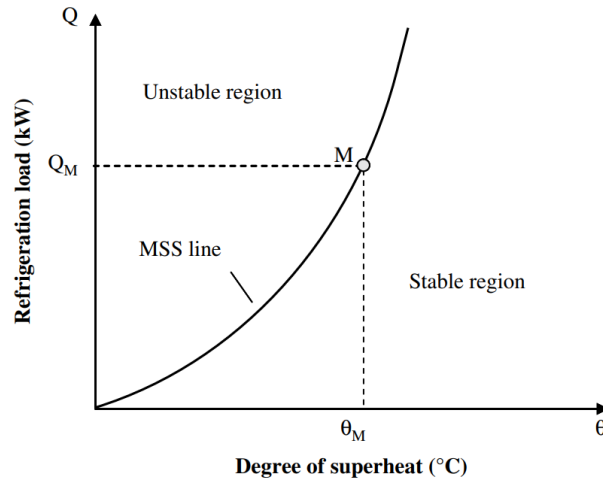


Figure II.6.3: Minimal Stable Superheat line, as proposed by Huelle [121], adapted from [119].

To address the limitations of TEVs, later research has focused on Electronic Expansion Valves (EEVs), which use a stepper motor to control the valve opening [57]. Unlike TEVs, the position of the EEV can be precisely controlled using digital signals, offering greater flexibility. For example, while the response time and setpoint of a TEV are constrained by the thermodynamic and mechanical properties of its sensing bulb and diaphragm, EEVs can be tuned more easily using Proportional Integral Derivative (PID) control. Additionally, EEVs allow the superheat setpoint to be adjusted dynamically, enabling higher efficiency at lower cooling loads compared to TEVs. Importantly, refrigerant mass flow can also be decoupled from superheat entirely with EEVs, enabling control strategies based on other process variables or their combinations.

However, the combination of variable-speed compressors and electronically controlled expansion valves also highlighted challenges in control. While PID methods are straightforward to implement, tuning separate control loops for cooling load and superheat is effective only within limited operating ranges [58]. Far from the nominal operating point, nonlinearities in the VCC system degrade controller performance and lead to stability issues. This realization prompted the development of advanced control strategies, which will be explored in the next section.

II.6.1.2. Advanced Controls

The next step beyond the Single Input Single Output (SISO) methods described in the previous section is to address the simultaneous control of multiple variables. This approach, known as Multiple Input Multiple Output (MIMO) control, not only considers the interactions between control loops but also enables the development of multivariable algorithms that compute all required inputs simultaneously based on multiple system outputs. A notable early attempt to analyse VCC dynamics as a MIMO system was made by He et al. [123]. The authors developed a low-order VCC model using Wedekind's Moving Boundary method (discussed in Section II.5.1) and numerically linearized it. A subsequent linear analysis was performed, where the Relative Gain Array (RGA) of the MIMO system was computed at steady-state. Based on the structure of the RGA, it was demonstrated that strong interactions between individual SISO loops severely limit the achievable performance of decentralized control methods in a typical VCC system with a variable-speed compressor and EEV.

Building on this, He et al. [124] designed a Linear Quadratic Gaussian (LQG) controller to optimally

and simultaneously adjust compressor speed and valve opening, where superheating and evaporation temperature were the controlled outputs. Recognizing the nonlinear nature of the VCC, the authors addressed the limitations of linear methods by designing the LQG controller at multiple steady-state operating points and applying gain scheduling to transition between them. Experimental results showed that the MIMO controller outperformed independent PID-based SISO loops in reference tracking, disturbance rejection, and overall efficiency across a wide range of operating conditions.

Subsequent researchers further developed the MIMO approach proposed by He et al.. For example, Rasmussen and Alleyne [125] employed a similar modelling strategy and confirmed, through linear analysis with the RGA, the strong interactions between SISO control loops. Unlike He et al., however, Rasmussen and Alleyne were able to directly link these findings to experimental results, since simultaneous operation of two independent SISO loops caused large oscillations of the process variables in their setup. To address these issues, they designed an \mathcal{H}_∞ controller by directly synthesizing the closed-loop frequency response to meet performance criteria under worst-case conditions. This approach inherently accounts for the interactions between the individual control loops, effectively mitigating the challenges of decentralized control. Their results demonstrated that the \mathcal{H}_∞ controller significantly outperformed PID-based decentralized methods near the initial linearization point. Additionally, to maintain robust performance across a wider operating range, the authors implemented a gain scheduling strategy between different \mathcal{H}_∞ designs at multiple other linearization points.

The analyses by He et al. and Rasmussen and Alleyne highlight the challenges of controlling VCC systems with variable speed compressors and EEVs using conventional decentralized methods. These challenges arise primarily from strong interactions between individual control loops. The Relative Gain Array (RGA) is a valuable tool for evaluating these interactions using a linear system model. Beyond the issue of loop interactions, the inherent nonlinearities of VCC systems can limit the effectiveness of linear control methods when operating far from the linearization point. However, linear multi-variable control methods have been shown to largely mitigate loop interactions, while gain scheduling can be used to transition between different linear control designs across a wide operating range.

Instead of gain scheduling, an alternative approach for extending the operating range of a controlled system is provided by nonlinear control. As the name suggests, nonlinear control methods can account for nonlinearities in system dynamics, including actuator saturation, which often occurs at the boundaries of the operating regime. However, the development of nonlinear controllers is often highly system-specific, making these methods much harder to generalize for a broad class of VCC systems [126]. Consequently, nonlinear control methods are less common in research compared to linear approaches, though some notable contributions exist in the literature. For example, Rasmussen and Larsen used a Moving Boundary-based modelling approach and, under a significant number of additional simplifying assumptions, derived a relatively simple nonlinear model. This model captured only the nonlinear relationship between the compressor speed and evaporator mass flow rate as inputs, and the degree of superheating and cooling capacity as outputs. Based on the structure resulting from their modelling approach, they developed a backstepping controller capable of regulating the degree of superheating independently of the cooling capacity. The stability of the closed-loop system was proven through a Lyapunov function analysis. Experimental validation demonstrated that this controller significantly outperformed the traditional Thermostatic Expansion Valve approach.

Although Rasmussen and Larsen's nonlinear controller demonstrates impressive performance over a large operating range, their approach highlights several common challenges associated with nonlinear control methods. Deriving the simplified nonlinear model relied on numerous strong assumptions, some of which may not hold universally for different VCC systems (for example, the assumption of negligible heat capacity in the evaporator's wall material). Furthermore, the model was tailored to a specific set of inputs and outputs. As a result, adapting the approach to different configurations would require re-deriving the entire model, a process that may not always be feasible. Identifying a suitable Lyapunov candidate for a new configuration can also pose significant difficulties. These factors illustrate why nonlinear control methods are often more case-specific compared to the more versatile and widely applicable linear approaches.

A final important control methodology within the classes of advanced controls is Model Predictive Control (MPC). Although its origins date back to the 1960s, MPC gained widespread recognition during the 1980s for its ability to handle constrained optimal control problems, particularly in the chemical industry

[127]. Over the years, its applications have expanded significantly, becoming a cornerstone for many control problems, including heating and refrigeration applications [128]. MPC is distinguished by two key features. First, it defines control actions by optimizing an objective function over a finite time horizon. This optimization relies on system response predictions generated by an internal model, with the flexibility to include constraints on states, inputs, and outputs. Second, MPC incorporates a moving time horizon to manage model inaccuracies and unknown disturbances. After computing the optimal control sequence over the time horizon, only the first control action is applied. The time window then shifts forward, and the optimization is repeated, always selecting the first action of the new sequence. This procedure continues indefinitely, allowing the system to be controlled as needed.

MPC for vapour compression systems has primarily been explored in the context of building refrigeration. Comprehensive reviews of MPC design considerations for such applications are provided, for example, by Yao and Shekhar [128]. However, the time scales of building systems are much larger than those of Environmental Control System components. For smaller-scale VCC systems, more general approaches to MPC are often more relevant, as these are less influenced by the specifics of building refrigeration.

An example of such work is provided by Jain and Alleyne [129], who developed an MPC-based controller to minimize exergy destruction in a small-scale VCC under rapidly varying cooling loads. They argue that exergy is a more suitable metric for efficiency than the conventional Coefficient of Performance (COP). While COP is fundamentally limited by the temperature difference between the VCC's hot and cold sides (see Equation II.3.1), exergy destruction relates directly to the second law of thermodynamics, capturing system irreversibilities through entropy generation. Exergy quantifies the portion of energy that can be converted to useful work, so its destruction reflects the extent to which irreversibilities reduce system efficiency.

Jain and Alleyne modeled the VCC heat exchangers using the Moving Boundary method, with static models for the compressor and expansion valve. Instead of traditional mass and energy conservation approaches, they derived their models from a second-law perspective, framing system dynamics in terms of entropy changes. This perspective informed their control objective function [129]:

$$J_{\text{VCS,II}} = \underbrace{(\|C_{\text{des}} - C_{\text{ach}}\|_2)}_{\text{Performance Objective}} + \lambda \cdot \underbrace{\left(\sum_{k=1}^{N_p} \dot{X}_{\text{dest,VCS}}[k] \right)}_{\text{Efficiency Objective}} \Delta t \quad (\text{II.6.1})$$

The function combines two objectives, balanced by a tuning parameter λ . The first minimizes the total error between the desired and actual cooling capacities across the time horizon, expressed as the 2-norm of the error over discrete time steps. The second minimizes total exergy destruction by integrating the exergy destruction rate over the time window. The controller aims to optimize this objective function while respecting constraints, such as limits on control actions and adherence to the second law of thermodynamics (e.g., ensuring non-negative reversible power).

Closed-loop simulations showed that the MPC achieved accurate tracking of the desired cooling load while maintaining inputs within specified limits. Comparing their exergy-based MPC with a first-law-based alternative revealed that minimizing exergy destruction reduced system irreversibilities but led to a lower COP. However, this analysis excluded the energy consumption of secondary fluid fans in the heat exchangers, and no experimental validation was conducted. Additionally, their prediction model used a single linear approximation, limiting the operating range and raising questions about the reliability of the results. Nonetheless, the work highlights the potential of MPC for VCC control, particularly for handling constrained optimization problems.

The main drawback of MPC is the computational demand of solving the optimization problem at each time step. Depending on the complexity of the objective function and constraints, finding solutions can be time-consuming, especially with detailed predictive models. As a result, online control using MPC may not always be feasible for VCC applications.

II.6.1.3. Intelligent Controls

The final category of control methods focuses on the intelligent control of VCC systems, leveraging Artificial Intelligence (AI) techniques in the control design and operation. These methods often rely on training or learning processes to establish input-output relationships. It is important to distinguish between the use of AI for system modelling and its application in control system design. This section addresses only the latter, although overlaps between the two are noted in the literature [58, 130]. Specifically, two prominent intelligent control methodologies are discussed: Artificial Neural Networks (ANNs) and fuzzy logic control.

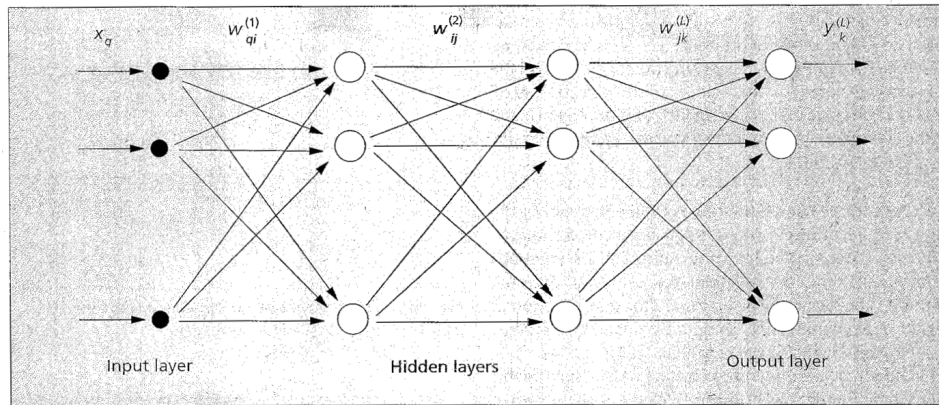


Figure II.6.4: Schematic of an Artificial Neural Network, adapted from [131].

ANNs are primarily used to map inputs to outputs, particularly when the relationship between them is complex or difficult to model mathematically. This is achieved by constructing a network of layers containing nodes, or neurons, as illustrated in Figure II.6.4. Each node applies an activation function [131], which takes the weighted sum of the outputs from the previous layer as input and produces an output passed to the next layer. By iteratively adjusting the weights between layers, the neural network is trained to align the outputs with the training data. Once trained, the network can ideally predict outputs for inputs outside the training dataset.

In the context of control, one or more ANNs can be integrated into a closed-loop system with a plant and trained to optimize a specific objective [132]. The training process aims to determine an optimal mapping between the system's observed outputs and the corresponding control inputs.

Mohanraj et al. [133] provide a comprehensive review of the application of Artificial Neural Networks (ANNs) in the control of refrigeration systems. Drawing from over ninety publications on modelling, performance prediction, and control using ANN approaches, they highlight several limitations. One major challenge is overtraining, coupled with the difficulty of selecting an optimal layer configuration and appropriate hyperparameters. To address this, the authors suggest that Genetic Algorithms offer a promising solution for optimizing network configurations. Another key limitation is the reduced reliability of ANNs when extrapolating beyond the trained dataset, which is particularly concerning for aircraft subsystems. The reliability of airborne systems must meet extremely high standards to ensure safe operation during flight, making this a critical drawback.

As an alternative to ANN-based control, fuzzy logic control offers a distinct approach. Fuzzy controllers determine control inputs using a set of fuzzy control rules, typically derived from expert knowledge or experimental validation. This heuristic method allows actions to be based on degrees of truth rather than strict binary classifications [134]. Unlike classical logic, which assigns values rigidly to categories (a value is either fully within a set or not at all), fuzzy logic permits partial membership. To illustrate this concept, Figure II.6.5 shows two bell-shaped membership functions, f_A and f_B , plotted as functions of an independent variable x . These membership functions describe how much a particular value of x belongs to two overlapping fuzzy sets. As an analogy, consider x representing room temperature. Membership function f_A might correspond to the statement "The room is cold", while f_B corresponds to "The room is hot." Instead of categorizing a temperature as strictly cold or hot, fuzzy logic allows for partial overlap: a particular temperature might simultaneously have some degree of coldness and

some degree of hotness. This gradual classification reflects real-world ambiguity more effectively than rigid boundaries.

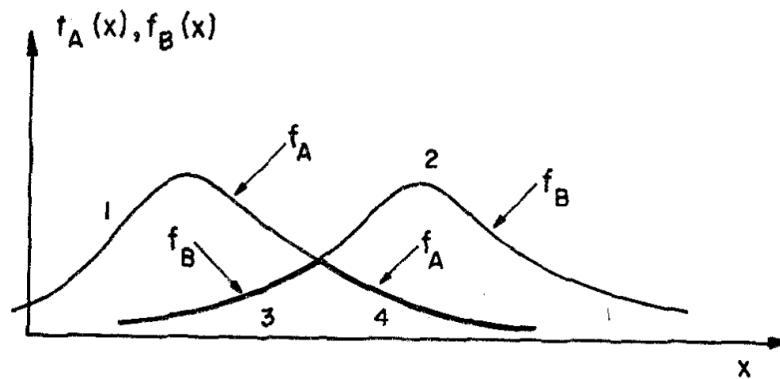


Figure II.6.5: Graphical representation of fuzzy sets, from the original paper of Zadeh in 1965 [134].

Fuzzification (interpreting observed outputs in terms of fuzzy sets) is only the first step in fuzzy logic control. The next step is to decide on a suitable action. This is typically done using logic tables, which are often constructed to mimic human decision-making processes [135]. A key advantage of this approach is its inherent nonlinearity; depending on the membership of the observed value, entirely different actions can be triggered. These actions themselves are also fuzzy, represented as membership functions rather than precise values. To generate a crisp control input for the system, a de-fuzzification step is required. One common method for this is the centre of gravity method, where the output fuzzy set's area average is computed to determine a precise value [136].

Applications of fuzzy control for VCC systems are relatively rare in the open literature. One example, however, is provided by Ekren et al. [137], who compare two intelligent controllers (fuzzy logic and ANN) with a conventional PID controller. The system under consideration regulates two outputs: the degree of superheating and the outlet temperature of the water serving as the heat source for the evaporator. To achieve this, two independent control loops are implemented: the electronic expansion valve regulates the degree of superheating, while the compressor speed controls the outlet water temperature.

For the fuzzy controller, the control rules and membership functions are derived experimentally. When comparing the performance of the PID and fuzzy controllers, the authors report that the fuzzy controller achieves a 1.4% reduction in power consumption. However, in their results it can be seen that the fuzzy controller exhibits lower stability margins compared to the PID controller. Furthermore, the authors provide limited analysis to explain the trends observed in their results, which raises questions about the credibility of the research.

II.6.2. Suitability for the IRIS

With the classification of control methods presented in the previous section, it is important to evaluate these methods in the context of the IRIS. As discussed in Chapter II.4, the primary purpose of the IRIS is to facilitate experimental research to better understand the operation of novel VCC systems, particularly for aeronautical applications. Given the lack of substantial research on state-of-the-art refrigerants and high-speed centrifugal compressors in this area, the methods employed for dynamic modelling and control should prioritize making the underlying physical principles transparent. This requirement fundamentally differs from the typical objectives in VCC control research.

Most research on VCC control focuses on improving system performance metrics, such as efficiency, robustness to disturbances, rapid transient response, or minimizing actuator effort. In contrast, the goal when testing components of the IRIS shifts to consistently regulating process variables that define the operational characteristics of the system. Additionally, the control strategy should offer insight into how the controller operates and the inputs it requires to achieve the desired behaviour. Such insights are crucial for developing control strategies for future ECS architectures, where understanding and exploiting the system's physical characteristics can play a key role. Consequently, direct implementation

of the controllers discussed in Section II.6.1 is not straightforward. Instead, control objectives must be tailored to focus on component testing and on gaining a deeper understanding of the controller's underlying decisions.

From this perspective, intelligent control methods such as Artificial Neural Networks (ANNs) and fuzzy logic controllers are less suitable. For ANNs, the mapping between system outputs and control inputs often lacks physical interpretability, making it difficult, if not impossible, to discern the reasoning behind their control actions. Furthermore, ANN-based controllers are not easily generalizable to other VCC configurations, which is problematic given the evolving nature of the IRIS. Similarly, the heuristic basis of fuzzy logic controllers makes them unsuitable for gaining structured insights into the physical nature of the system. Both methods also require extensive experimental data for training and tuning, and stability guarantees can be challenging to establish.

In contrast, advanced control approaches offer a more structured framework for understanding the physical principles governing the system. By deriving control properties from first-principle models, these methods enable the analysis of informative metrics such as stability margins, input-output interactions, and control performance limits. These capabilities are highly relevant for testing components of the IRIS and can also provide a foundation for designing control systems in future electric high-speed centrifugal VCC-based ECSs. The physically grounded nature of these methods simplifies the interpretation of results and supports drawing conclusions with broader implications. Additionally, advanced control approaches are less dependent on large datasets for tuning, making them more resilient to architectural changes in the system and reducing the time and effort needed to adapt the controller.

Considering these factors, advanced control methods are the most suitable choice for testing compressor performance in the IRIS. These methods align with the goal of understanding transient system behavior while providing deeper insights into the physical principles that characterize control challenges in novel VCC-based ECS designs.

II.7

Research Objectives

At the outset of this literature study, two main objectives were identified: (1) developing a numerical model of the IRIS and (2) designing a control strategy to enable consistent compressor testing. With the insights gained from the literature review, these objectives can now be refined into more specific research goals, which is the focus of this chapter. First, the relevance of the main objectives to the IRIS is further clarified. Next, key methodological considerations from the literature are discussed. Finally, the findings from the literature review are used to refine the research objectives of the thesis.

II.7.1. Relevance for the IRIS

A key finding from the literature is the role of the IRIS in the broader context of integrated design optimization. As a test facility, the IRIS was built to represent a novel ECS for a large helicopter, with its heat exchanger sizing, compressor dimensions, and refrigerant selection determined through integrated design optimization. The primary objectives of the facility can be summarized as follows:

- Evaluating the performance of (centrifugal) compressors within VCC systems for aviation use.
- Investigating the aerothermal behaviour of heat exchangers, particularly the condenser.
- Analysing the refrigeration cycle using R-1233zd(E) and other low-GWP refrigerants.

These objectives highlight the relevance of a dynamic model, as transient effects play a crucial role in each case. Compressor performance is most critical under dynamic conditions where surge and choke may occur, making transient analysis essential. Similarly, while steady-state studies provide valuable insights into heat exchanger behaviour at specific operating points (e.g., design point, cruise, faulty pack), their slow thermal dynamics significantly impact overall VCC performance. Understanding these dynamic effects requires a time-dependent model. Additionally, refrigerant properties, particularly in two-phase flow regions (evaporation, condensation, and expansion valve operation), exhibit transient behaviour that affects system performance, with phenomena such as hunting only observable through dynamic analysis.

Beyond aiding experimental research, a dynamic model can provide insights useful for the integrated design optimization process itself. Since the preliminary design of the IRIS was derived from steady-state optimization models, dynamic simulations may reveal system characteristics, whether beneficial or problematic, that were not captured in the optimization process. This raises the question of whether the optimality of the design holds when transient behaviour is considered. In principle, a dynamic model could be incorporated into future optimization processes to account for transient performance. However, the high computational cost of such an approach necessitates a trade-off between model fidelity and optimization feasibility.

A separate consideration from the literature review is the impact of design modifications made during the construction of the IRIS. Practical constraints led to deviations from the initial concept, resulting in a reduced operational range. Since proper component testing requires a wide operating range, it is crucial to understand these limitations. A dynamic model can aid in assessing these constraints efficiently,

providing faster, cheaper, and more flexible insights compared to experimental tests. Furthermore, while the IRIS currently operates with a reciprocating compressor, the model can be developed with the planned centrifugal machine, allowing for pre-emptive analysis of system behaviour before hardware modifications. This enables early identification of potential issues, reducing the risk of delays and additional costs in experimental campaigns.

II.7.2. Methodological Considerations

Given the planned architecture changes, a modular modelling approach is preferred, enhancing model reusability and potential integration with future optimization studies. A physics-based approach is more suitable than data-driven alternatives, as it provides greater insight into underlying system dynamics. For heat exchangers, the Moving Boundary (MB) method strikes a good balance between computational efficiency and accuracy, avoiding the high computational cost of detailed finite control volume methods. Additionally, static models for the expansion valve and compressor further reduce computational demand.

For the control system, the literature review highlights that most research focuses on optimizing efficiency or performance under standard operation, startup, or shutdown. This underscores the need for a control strategy specifically designed for compressor testing. Since a dynamic model is developed in parallel, the control system can be tuned and validated in simulation, offering deeper insights into the control properties of the IRIS and VCC systems in general.

Three main categories of control strategies were identified: conventional controls, advanced controls, and intelligent controls. Of these, advanced control methods are the most suitable, as they provide a structured framework that enhances understanding of system responses. Moreover, incorporating advanced control techniques aligns with the broader goal of integrating dynamic models into future design optimizations. Since VCC systems require active control during flight, assessing dynamic behaviour in closed-loop conditions improves the fidelity of preliminary design evaluations. This further strengthens the case for developing a control strategy for the IRIS.

II.7.3. Refined Research Objectives

Based on the considerations of the previous sections, the research objectives are refined as follows:

1. **Development of a dynamic model of the IRIS**, using a modular approach. The model will represent the future loop with the planned centrifugal compressor rather than the current loop with the reciprocating machine. To balance fidelity and complexity, heat exchangers will be modelled using the Moving Boundary method, while the expansion valve and compressor will be treated as static components.
2. **Design of a control system for compressor testing**, ensuring stable operation of the Vapour Compression Cycle across the compressor's operational range. The control method will be selected from the advanced control category, providing insights into the system's response as a Multiple Input Multiple Output plant.

In conclusion, this literature study has provided a structured overview of the background necessary to define the research objectives. By examining the evolution of Environmental Control Systems (ECSs), the principles and challenges of Vapour Compression Cycle (VCC) technology, and the methodologies used for dynamic modelling and control of these systems, a solid foundation has been established. This background has guided the formulation of the final research objectives, ensuring that they are well-grounded in existing knowledge while addressing specific gaps. These objectives will contribute to ongoing research at TU Delft on novel ECS design, supporting the development of more efficient and environmentally sustainable cooling systems for future aircraft.

Part III

Supporting Material

III.1

IRIS Detailed System Architecture

Having discussed the conceptual design and practical adjustments of the IRIS in Section II.4.2, a detailed description of the current system architecture is presented in this chapter. For this, the simplified Process & Information Diagram (P&ID) in Figure III.1.1 is considered.

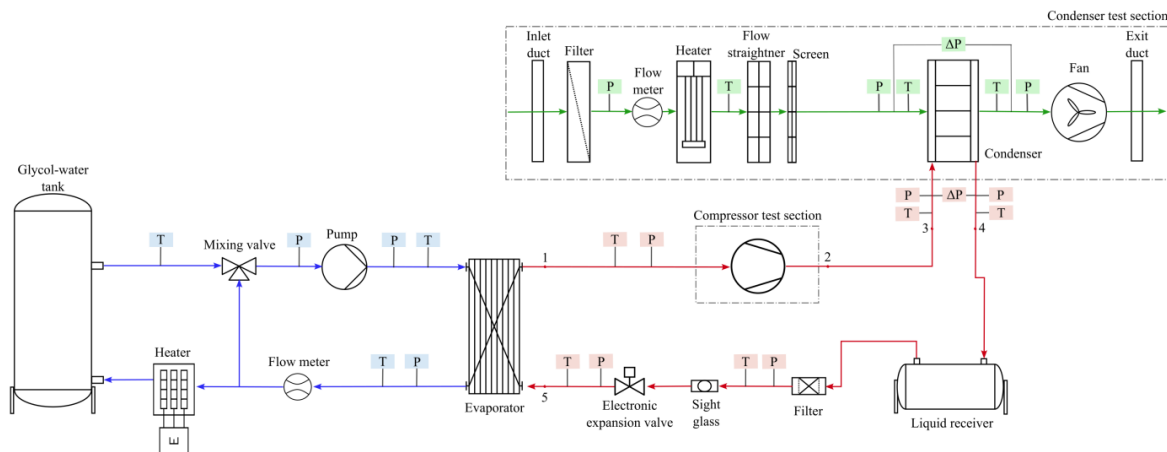


Figure III.1.1: Simplified P&ID of the IRIS facility, where the heating loop (indicated in blue) provides heat to the refrigeration loop (indicated in red) at the evaporator and heat is rejected to the cooling loop (indicated in green) at the condenser [13].

From the colours of the process lines, it can be seen that the IRIS contains three distinct loops: a heating loop, refrigeration loop, and cooling loop. To understand how these three loops work together to mimic the VCC of the helicopter ECS, the components of each loop will be discussed subsequently.

In the heating loop, a mixture of 20% ethylene glycol and 80% water is circulated by a centrifugal pump operating at a fixed rotational speed. This mixture is stored in a large insulated tank, as can be seen on the left in Figure III.1.1. From the tank, the liquid flows through a three-way mixing valve, where part of the evaporator exit stream can be fed back to the evaporator entrance. The evaporator itself consists of a single-pass brazed plate heat exchanger with a countercurrent flow arrangement. Before entering the tank again, the temperature of the liquid can be increased through an electric heater. During operation, the liquid in the heating loop is first warmed up using the electric heater. When the loop is fully heated up, the mixing valve is used to regulate the supply temperature to the evaporator inlet. In this way a constant evaporator inlet temperature can be ensured, independent of the electric heater. An expansion receiver is located downstream of the tank to protect the loop from excessive pressure build-up.

In the cooling loop, air is used as the cooling fluid to remove heat from the refrigeration loop. This air is sucked from an inlet duct through a series of components before being blown out at the exhaust duct. After being filtered, the air is first heated to the required temperature. It is then straightened

and forced through two screens to ensure a uniform stream. Subsequently, heat rejected from the refrigeration loop is transferred to the air in the condenser, which consists of a two-pass microchannel heat exchanger with a cross-flow orientation and multilouvered fins on the air side. The mass flow rate of the cooling loop is regulated through a variable speed centrifugal fan.

Concerning the refrigeration loop, the refrigerant is heated in the evaporator from a two-phase fluid to saturated vapour conditions and then superheated to the required degree. Subsequently, the superheated vapour is compressed by means of a semi-hermetic reciprocating compressor. Downstream of the compressor, the fluid passes through the condenser, where heat is rejected to the air of the cooling loop. This removal of heat causes the working fluid to desuperheat, condense to a saturated liquid, and finally reach subcooled conditions. After exiting the condenser, the fluid progresses to a horizontally placed liquid receiver, where the refrigerant charge is stored. Finally, the high pressure subcooled liquid is throttled through an electronically regulated expansion valve, allowing the fluid to depressurize and partially evaporate before entering the evaporator again.

Within each loop, several instrumentation devices are installed. This includes temperature and pressure transducers, differential pressure transducers, electromagnetic or ultrasonic flow meters, and sight glasses at different critical locations to ensure safe operation. Additionally, the IRIS is automatically regulated by a total of six independent Proportional Integral Derivative (PID) control systems. For the refrigeration loop, two of these systems control respectively the electronic expansion valve based on the evaporator superheat, and the speed of the compressor based on its suction pressure. As a backup, several warnings, alarms, and emergency shutdowns have been implemented that trigger if certain parameters exceed predefined bounds. More details on the instrumentation, control strategies, safety interlocks, and results of the commissioning of the facility can be found in the dissertation of Ascione [13].

III.2 References Literature Study

- [1] K. Calvin et al. *IPCC, 2023: Climate Change 2023: Synthesis Report. Contribution of Working Groups I, II and III to the Sixth Assessment Report of the Intergovernmental Panel on Climate Change [Core Writing Team, H. Lee and J. Romero (eds.)]. IPCC, Geneva, Switzerland.* Ed. by P. Arias et al. July 2023. DOI: 10.59327/ipcc/ar6-9789291691647. URL: <http://dx.doi.org/10.59327/ipcc/ar6-9789291691647>.
- [2] C. A. Horowitz. "Paris Agreement". In: *International Legal Materials* 55.4 (Aug. 2016), pp. 740–755. ISSN: 1930-6571. DOI: 10.1017/s0020782900004253. URL: <http://dx.doi.org/10.1017/S0020782900004253>.
- [3] World Weather Attribution. *Extreme downpours increasing in Southern Spain as fossil fuel emissions heat the climate*. Nov. 2024. URL: <https://www.worldweatherattribution.org/extreme-downpours-increasing-in-southern-spain-as-fossil-fuel-emissions-heat-the-climate/>.
- [4] H. Ritchie. "Sector by sector: where do global greenhouse gas emissions come from?" In: *Our World in Data* (2020). URL: <https://ourworldindata.org/ghg-emissions-by-sector>.
- [5] V. Grewe et al. "Evaluating the climate impact of aviation emission scenarios towards the Paris agreement including COVID-19 effects". In: *Nature Communications* 12.1 (June 2021). ISSN: 2041-1723. DOI: 10.1038/s41467-021-24091-y. URL: <http://dx.doi.org/10.1038/s41467-021-24091-y>.
- [6] M. Cames et al. *Emission Reduction Targets for International Aviation and Shipping*. The European Commission, 2015. URL: [https://www.europarl.europa.eu/thinktank/en/document/IPOL_STU\(2015\)569964](https://www.europarl.europa.eu/thinktank/en/document/IPOL_STU(2015)569964).
- [7] O. Zaporozhets, V. Isaienko, and K. Synylo. "PARE preliminary analysis of ACARE FlightPath 2050 environmental impact goals". In: *CEAS Aeronautical Journal* 12.3 (July 2021), pp. 653–667. ISSN: 1869-5590. DOI: 10.1007/s13272-021-00525-7. URL: <http://dx.doi.org/10.1007/s13272-021-00525-7>.
- [8] G. Buticchi, P. Wheeler, and D. Boroyevich. "The More-Electric Aircraft and Beyond". In: *Proceedings of the IEEE* 111.4 (Apr. 2023), pp. 356–370. ISSN: 1558-2256. DOI: 10.1109/jproc.2022.3152995. URL: <http://dx.doi.org/10.1109/JPROC.2022.3152995>.
- [9] AC-9 Aircraft Environmental Systems Committee. *Environmental control systems life cycle cost*. Tech. rep. 400 Commonwealth Drive, Warrendale, PA, United States: SAE International, 2017.
- [10] H. Schefer et al. "Discussion on Electric Power Supply Systems for All Electric Aircraft". In: *IEEE Access* 8 (2020), pp. 84188–84216. DOI: 10.1109/ACCESS.2020.2991804.
- [11] M. Merzvinikas et al. "Air conditioning systems for aeronautical applications: a review". In: *The Aeronautical Journal* 124.1274 (Dec. 2019), pp. 499–532. ISSN: 2059-6464. DOI: 10.1017/aer.2019.159. URL: <http://dx.doi.org/10.1017/aer.2019.159>.
- [12] S. K. Wang. *Handbook of Air Conditioning and Refrigeration*. en. 2nd Edition. New York: McGraw-Hill Education, 2001. ISBN: 9780070681675. URL: <https://www.accessengineeringlibrary.com/content/book/9780070681675>.
- [13] F. Ascione. "Vapour Compression Cycle Technology for Aviation: Automated Design Methods and a New Experimental Setup". English. Dissertation (TU Delft). Netherlands: Delft University of Technology, 2024. DOI: 10.4233/uuid:39ef6ce1-d97f-4197-83ab-96d1e766de61.
- [14] X. Xue and T. Wang. "Stall recognition for centrifugal compressors during speed transients". In: *Applied Thermal Engineering* 153 (May 2019), pp. 104–112. ISSN: 1359-4311. DOI: 10.1016/j.applthermaleng.2019.02.027. URL: <http://dx.doi.org/10.1016/j.applthermaleng.2019.02.027>.

- [15] P. Sforza. "Fuselage Design". In: *Commercial Airplane Design Principles*. Elsevier, 2014, pp. 47–79. ISBN: 9780124199538. DOI: 10.1016/b978-0-12-419953-8.00003-6. URL: <http://dx.doi.org/10.1016/B978-0-12-419953-8.00003-6>.
- [16] W. J. Tarver, K. Volner, and J. S. Cooper. "Aerospace Pressure Effects". en. In: *StatPearls*. Treasure Island (FL): StatPearls Publishing, Jan. 2024.
- [17] Federal Aviation Administration. *14 CFR 25.831 - 25.843*. Tech. rep. Code of Federal Regulations, Dec. 2024.
- [18] Airbus. *Getting to Grips with Aircraft Performance*. Tech. rep. Flight Operations Support & Line Assistance, Jan. 2002.
- [19] G. Rood. "A Brief History of Flying Clothing". In: *Journal of Aeronautical History* 4.2014/01 (2014), pp. 3–53.
- [20] M. Lavelle. "Boeing Model 307 Stratoliner: A Culmination of the 1930s Commercial Aircraft Design, Engineering, and Manufacturing Progress". In: *47th AIAA Aerospace Sciences Meeting including The New Horizons Forum and Aerospace Exposition*. American Institute of Aeronautics and Astronautics, Jan. 2009. DOI: 10.2514/6.2009-961. URL: <http://dx.doi.org/10.2514/6.2009-961>.
- [21] E. Teale. "High-Flying Planes to Race Sun Across Atlantic". In: *Popular Science Monthly* 121.4 (Oct. 1932), pp. 13–14.
- [22] K. Linnett and R. Crabtree. "What's Next in Commercial Aircraft Environmental Control Systems?" In: *SAE Technical Paper Series*. ICES. SAE International, July 1993. DOI: 10.4271/932057. URL: <http://dx.doi.org/10.4271/932057>.
- [23] S. Pace. *Lockheed's Constellation*. Zenith Imprint, 1998. ISBN: 9781610607308. URL: <https://books.google.nl/books?id=aANoyFe5C14C>.
- [24] P. Wheeler and S. Bozhko. "The More Electric Aircraft: Technology and challenges". In: *IEEE Electrification Magazine* 2.4 (2014), pp. 6–12. DOI: 10.1109/MELE.2014.2360720.
- [25] B. Zhao et al. "Impact of Air System Bleeding on Aircraft Engine Performance". In: *ASME-JSME-KSME 2011 Joint Fluids Engineering Conference: Volume 1, Symposia – Parts A, B, C, and D*. AJK2011. ASMEDC, Jan. 2011, pp. 553–560. DOI: 10.1115/ajk2011-22004. URL: <http://dx.doi.org/10.1115/ajk2011-22004>.
- [26] R. Slingerland and S. Zandstra. "Bleed Air versus Electric Power Off-takes from a Turbofan Gas Turbine over the Flight Cycle". In: *7th AIAA ATIO Conf, 2nd CEIAT Int'l Conf on Innov and Integr in Aero Sciences, 17th LTA Systems Tech Conf; followed by 2nd TEOS Forum*. American Institute of Aeronautics and Astronautics, Sept. 2007. DOI: 10.2514/6.2007-7848. URL: <http://dx.doi.org/10.2514/6.2007-7848>.
- [27] M. Moran et al. *Principles of Engineering Thermodynamics: SI Version*. Wiley, 2015. ISBN: 9781118960882. URL: <https://books.google.nl/books?id=zfQwBgAAQBAJ>.
- [28] P. F. Dexter, R. J. Watts, and W. L. Haskin. "Vapor Cycle Compressors for Aerospace Vehicle Thermal Management". In: *SAE Technical Paper Series*. AEROTECH. SAE International, Sept. 1990. DOI: 10.4271/901960. URL: <http://dx.doi.org/10.4271/901960>.
- [29] F. Klimpel et al. *Aircraft air conditioning system and method of operating an aircraft air conditioning system*. Jan. 2015.
- [30] A. Giuffré. "Integrated Design Optimization of Electrically-Driven Vapor Compression Cycle Systems for Aircraft: Powered by High-Speed Centrifugal Compressors". English. Dissertation (TU Delft). Delft University of Technology, 2023. DOI: 10.4233/uuid:b4f6a4a4-2e48-4bbe-9093-3f1368282f63.
- [31] M. Dechow and C. A. H. Nurcombe. "Aircraft environmental control systems". In: *The Handbook of Environmental Chemistry*. Berlin, Heidelberg: Springer Berlin Heidelberg, Aug. 2005, pp. 3–24.
- [32] C. Aprea, A. Greco, and A. Maiorino. "An experimental evaluation of the greenhouse effect in the substitution of R134a with CO₂". In: *Energy* 45.1 (Sept. 2012), pp. 753–761. ISSN: 0360-5442. DOI: 10.1016/j.energy.2012.07.015. URL: <http://dx.doi.org/10.1016/j.energy.2012.07.015>.

- [33] N. Abas et al. "Natural and synthetic refrigerants, global warming: A review". In: *Renewable and Sustainable Energy Reviews* 90 (July 2018), pp. 557–569. ISSN: 1364-0321. DOI: 10.1016/j.rser.2018.03.099. URL: <http://dx.doi.org/10.1016/j.rser.2018.03.099>.
- [34] G. Hundy, A. Trott, and T. Welch. "Compressors". In: *Refrigeration, Air Conditioning and Heat Pumps*. Elsevier, 2016, pp. 59–87. ISBN: 9780081006474. DOI: 10.1016/b978-0-08-100647-4.00004-8. URL: <http://dx.doi.org/10.1016/B978-0-08-100647-4.00004-8>.
- [35] I. Grace, D. Datta, and S. A. Tassou. "Comparison Of Hermetic Scroll And Reciprocating Compressors Operating Under Varying Refrigerant Charge And Load". In: *International Compressor Engineering Conference* 1518 (2002). URL: <https://docs.lib.purdue.edu/icec/1518>.
- [36] S. Cheng et al. "A multi-DOF tribo-dynamics analysis of scroll compressor considering wear properties of Oldham's ring". In: *Tribology International* 179 (Jan. 2023), p. 108125. ISSN: 0301-679X. DOI: 10.1016/j.triboint.2022.108125. URL: <http://dx.doi.org/10.1016/j.triboint.2022.108125>.
- [37] B. Zohuri. *Application of Compact Heat Exchangers For Combined Cycle Driven Efficiency In Next Generation Nuclear Power Plants: A Novel Approach*. Springer International Publishing, 2016. ISBN: 9783319235370. DOI: 10.1007/978-3-319-23537-0. URL: <http://dx.doi.org/10.1007/978-3-319-23537-0>.
- [38] F. Careri et al. "Additive manufacturing of heat exchangers in aerospace applications: a review". In: *Applied Thermal Engineering* 235 (Nov. 2023), p. 121387. ISSN: 1359-4311. DOI: 10.1016/j.applthermaleng.2023.121387. URL: <http://dx.doi.org/10.1016/j.applthermaleng.2023.121387>.
- [39] A. Giuffrè et al. "Data-driven modeling of high-speed centrifugal compressors for aircraft Environmental Control Systems". In: *International Journal of Refrigeration* 151 (2023), pp. 354–369. ISSN: 0140-7007. DOI: <https://doi.org/10.1016/j.ijrefrig.2023.03.019>. URL: <https://www.sciencedirect.com/science/article/pii/S0140700723000865>.
- [40] J. V. C. Vargas and A. Bejan. "Integrative thermodynamic optimization of the environmental control system of an aircraft". en. In: *Int. J. Heat Mass Transf.* 44.20 (Oct. 2001), pp. 3907–3917.
- [41] I. Pérez-Grande and T. J. Leo. "Optimization of a commercial aircraft environmental control system". In: *Applied Thermal Engineering* 22.17 (Dec. 2002), pp. 1885–1904. ISSN: 1359-4311. DOI: 10.1016/S1359-4311(02)00130-8. URL: [http://dx.doi.org/10.1016/S1359-4311\(02\)00130-8](http://dx.doi.org/10.1016/S1359-4311(02)00130-8).
- [42] D. Bender. "Integration of exergy analysis into model-based design and evaluation of aircraft environmental control systems". en. In: *Energy (Oxf.)* 137 (Oct. 2017), pp. 739–751.
- [43] X. Li et al. "Heat current method for analysis and optimization of a refrigeration system for aircraft environmental control system". en. In: *Int. J. Refrig.* 106 (Oct. 2019), pp. 163–180.
- [44] Z. Duan et al. "Multi-objective optimization of the aircraft environment control system based on component-level parameter decomposition". In: *Energy* 245 (2022), p. 123330. ISSN: 0360-5442. DOI: <https://doi.org/10.1016/j.energy.2022.123330>. URL: <https://www.sciencedirect.com/science/article/pii/S036054422200233X>.
- [45] M. Sielemann et al. "Optimization of an unconventional environmental control system architecture". en. In: *SAE Int. J. Aerosp.* 4.2 (Oct. 2011), pp. 1263–1275.
- [46] D. Schlabe and J. Lienig. "Model-based thermal management functions for aircraft systems". In: *SAE Technical Paper Series*. 2014-01-2203. 400 Commonwealth Drive, Warrendale, PA, United States: SAE International, Sept. 2014.
- [47] D. Rusch and M. Casey. "The Design Space Boundaries for High Flow Capacity Centrifugal Compressors". In: *Journal of Turbomachinery* 135.3 (Mar. 2013). ISSN: 1528-8900. DOI: 10.1115/1.4007548. URL: <http://dx.doi.org/10.1115/1.4007548>.
- [48] E. A. Heath. "Amendment to the Montreal Protocol on Substances that Deplete the Ozone Layer (Kigali Amendment)". In: *International Legal Materials* 56.1 (Feb. 2017), pp. 193–205. ISSN: 1930-6571. DOI: 10.1017/ilm.2016.2. URL: <http://dx.doi.org/10.1017/ilm.2016.2>.

- [49] M. Mohanraj and J. D. A. P. Abraham. "Environment friendly refrigerant options for automobile air conditioners: a review". In: *Journal of Thermal Analysis and Calorimetry* 147.1 (Oct. 2020), pp. 47–72. ISSN: 1588-2926. DOI: 10.1007/s10973-020-10286-w. URL: <http://dx.doi.org/10.1007/s10973-020-10286-w>.
- [50] F. Ascione, P. Colonna, and C. De Servi. "Integrated design optimization method for novel vapour-compression-cycle-based environmental control systems". In: *Applied Thermal Engineering* 236 (2024), p. 121261. ISSN: 1359-4311. DOI: <https://doi.org/10.1016/j.applthermaleng.2023.121261>. URL: <https://www.sciencedirect.com/science/article/pii/S1359431123012905>.
- [51] A. Mannini. "The Environmental Control System for a Modern Helicopter: a Blend of New Technologies." In: *Twenty First European Rotorcraft Forum*. 1995.
- [52] A. Giuffrè, P. Colonna, and M. Pini. "Design Optimization of a High-Speed Twin-Stage Compressor for Next-Gen Aircraft Environmental Control System". In: *Journal of Engineering for Gas Turbines and Power* 145.3 (Dec. 2022), p. 031017. ISSN: 0742-4795. DOI: 10.1115/1.4056022. eprint: https://asmedigitalcollection.asme.org/gasturbinespower/article-pdf/145/3/031017/6958025/gtp_145_03_031017.pdf. URL: <https://doi.org/10.1115/1.4056022>.
- [53] F. Ascione et al. "Design and Commissioning of the IRIS: A Setup for Aircraft Vapour Compression Cycle-Based Environmental Control System Testing". In: *Volume 5: Cycle Innovations*. GT2024. American Society of Mechanical Engineers, June 2024. DOI: 10.1115/gt2024-123714. URL: <http://dx.doi.org/10.1115/GT2024-123714>.
- [54] M. O. McLinden, C. J. Seeton, and A. Pearson. "New refrigerants and system configurations for vapor-compression refrigeration". In: *Science* 370.6518 (Nov. 2020), pp. 791–796. ISSN: 1095-9203. DOI: 10.1126/science.abe3692. URL: <http://dx.doi.org/10.1126/science.abe3692>.
- [55] Bitzer. *Bitzer is HFO-ready*. <https://www.bitzer.de/cs/en/press/bitzer-is-hfo-ready.jsp>. Accessed: 09-01-2025. 2016.
- [56] S. Bendapudi and J. E. Braun. *A Review of Literature on Dynamic Models of Vapor Compression Equipment*. Tech. rep. 4036-5. ASHRAE, May 2002.
- [57] B. P. Rasmussen. "Dynamic modeling for vapor compression systems—Part I: Literature review". In: *HVAC&R Research* 18.5 (Sept. 2012), pp. 934–955. ISSN: 1938-5587. DOI: 10.1080/10789669.2011.582916. URL: <http://dx.doi.org/10.1080/10789669.2011.582916>.
- [58] A. Goyal, M. A. Staedter, and S. Garimella. "A review of control methodologies for vapor compression and absorption heat pumps". In: *International Journal of Refrigeration* 97 (Jan. 2019), pp. 1–20. ISSN: 0140-7007. DOI: 10.1016/j.ijrefrig.2018.08.026. URL: <http://dx.doi.org/10.1016/j.ijrefrig.2018.08.026>.
- [59] F. K. Moore and E. M. Greitzer. "A Theory of Post-Stall Transients in Axial Compression Systems: Part I—Development of Equations". In: *Journal of Engineering for Gas Turbines and Power* 108.1 (Jan. 1986), pp. 68–76. ISSN: 1528-8919. DOI: 10.1115/1.3239887. URL: <http://dx.doi.org/10.1115/1.3239887>.
- [60] G. L. Wedekind. "Transient Response of the Mixture-Vapour Transition Point in Two-phase Horizontal Evaporating Flow". Dissertation. Michigan: University of Illinois, Sept. 1965.
- [61] J. MacArthur and E. Grald. "Unsteady compressible two-phase flow model for predicting cyclic heat pump performance and a comparison with experimental data". In: *International Journal of Refrigeration* 12.1 (Jan. 1989), pp. 29–41. ISSN: 0140-7007. DOI: 10.1016/0140-7007(89)90009-1. URL: [http://dx.doi.org/10.1016/0140-7007\(89\)90009-1](http://dx.doi.org/10.1016/0140-7007(89)90009-1).
- [62] S. Bendapudi, J. E. Braun, and E. A. Groll. "A comparison of moving-boundary and finite-volume formulations for transients in centrifugal chillers". In: *International Journal of Refrigeration* 31.8 (Dec. 2008), pp. 1437–1452. ISSN: 0140-7007. DOI: 10.1016/j.ijrefrig.2008.03.006. URL: <http://dx.doi.org/10.1016/j.ijrefrig.2008.03.006>.

- [63] G. L. Wedekind and W. F. Stoecker. "Theoretical Model for Predicting the Transient Response of the Mixture-Vapor Transition Point in Horizontal Evaporating Flow". In: *Journal of Heat Transfer* 90.1 (Feb. 1968), pp. 165–174. ISSN: 1528-8943. DOI: 10.1115/1.3597448. URL: <http://dx.doi.org/10.1115/1.3597448>.
- [64] P. Colonna and H. van Putten. "Dynamic modeling of steam power cycles." In: *Applied Thermal Engineering* 27.2–3 (Feb. 2007), pp. 467–480. ISSN: 1359-4311. DOI: 10.1016/j.applthermaleng.2006.06.011. URL: <http://dx.doi.org/10.1016/j.applthermaleng.2006.06.011>.
- [65] P. Breedveld. "Concept-Oriented Modeling of Dynamic Behavior". In: *Bond Graph Modelling of Engineering Systems*. Springer New York, 2011, pp. 3–52. ISBN: 9781441993687. DOI: 10.1007/978-1-4419-9368-7_1. URL: http://dx.doi.org/10.1007/978-1-4419-9368-7_1.
- [66] P. Amodio and F. Mazzia. "Numerical solution of differential algebraic equations and computation of consistent initial/boundary conditions". In: *Journal of Computational and Applied Mathematics* 87.1 (Dec. 1997), pp. 135–146. ISSN: 0377-0427. DOI: 10.1016/S0377-0427(97)00178-7. URL: [http://dx.doi.org/10.1016/S0377-0427\(97\)00178-7](http://dx.doi.org/10.1016/S0377-0427(97)00178-7).
- [67] E. Martinez and B. Drozdowicz. "Multitime-scale approach to real-time simulation of stiff dynamic systems". In: *Computers & Chemical Engineering* 13.7 (July 1989), pp. 767–778. ISSN: 0098-1354. DOI: 10.1016/0098-1354(89)85050-1. URL: [http://dx.doi.org/10.1016/0098-1354\(89\)85050-1](http://dx.doi.org/10.1016/0098-1354(89)85050-1).
- [68] H. Elmqvist. "DYMOLA - A Structured Model Language for Large Continuous Systems". In: *Summer Computer Simulation Conference*. Toronto, Canada, 1979.
- [69] M. Andersson et al. "OmSim-an integrated interactive environment for object-oriented modeling and simulation". In: *Proceedings of IEEE Symposium on Computer-Aided Control Systems Design (CACSD)*. CACSD-94. IEEE, 1994, pp. 285–290. DOI: 10.1109/cacsd.1994.288917. URL: <http://dx.doi.org/10.1109/CACSD.1994.288917>.
- [70] P. Piela et al. "ASCEND: an object-oriented computer environment for modeling and analysis: The modeling language". In: *Computers & Chemical Engineering* 15.1 (Jan. 1991), pp. 53–72. ISSN: 0098-1354. DOI: 10.1016/0098-1354(91)87006-u. URL: [http://dx.doi.org/10.1016/0098-1354\(91\)87006-u](http://dx.doi.org/10.1016/0098-1354(91)87006-u).
- [71] J. M.-D. Filippo et al. "A survey of bond graphs: Theory, applications and programs". In: *Journal of the Franklin Institute* 328.5–6 (Jan. 1991), pp. 565–606. ISSN: 0016-0032. DOI: 10.1016/0016-0032(91)90044-4. URL: [http://dx.doi.org/10.1016/0016-0032\(91\)90044-4](http://dx.doi.org/10.1016/0016-0032(91)90044-4).
- [72] R. Gani and I. T. Cameron. "Modelling for dynamic simulation of chemical processes: the index problem". In: *Chemical Engineering Science* 47.5 (Apr. 1992), pp. 1311–1315. ISSN: 0009-2509. DOI: 10.1016/0009-2509(92)80252-8. URL: [http://dx.doi.org/10.1016/0009-2509\(92\)80252-8](http://dx.doi.org/10.1016/0009-2509(92)80252-8).
- [73] S. E. Mattsson and H. Elmqvist. "Modelica - An International Effort to Design the Next Generation Modeling Language". In: *IFAC Proceedings Volumes* 30.4 (Apr. 1997), pp. 151–155. ISSN: 1474-6670. DOI: 10.1016/S1474-6670(17)43628-7. URL: [http://dx.doi.org/10.1016/S1474-6670\(17\)43628-7](http://dx.doi.org/10.1016/S1474-6670(17)43628-7).
- [74] H. Elmqvist. "Modelica Evolution - From My Perspective". In: *Proceedings of the 10th International Modelica Conference, March 10-12, 2014, Lund, Sweden*. Vol. 96. Modelica. Linköping University Electronic Press, Mar. 2014, pp. 17–26. DOI: 10.3384/ecp1409617. URL: <http://dx.doi.org/10.3384/ecp1409617>.
- [75] D. Zimmer, M. Meißner, and N. Weber. "The DLR ThermoFluid Stream Library". In: *Electronics* 11.22 (Nov. 2022), p. 3790. ISSN: 2079-9292. DOI: 10.3390/electronics11223790. URL: <http://dx.doi.org/10.3390/electronics11223790>.
- [76] P. Jordan and G. Schmitzm. "A Modelica Library for Scalable Modelling of Aircraft Environmental Control Systems". In: *Proceedings of the 10th International Modelica Conference, March 10-12, 2014, Lund, Sweden*. Vol. 96. Modelica. Linköping University Electronic Press, Mar. 2014, pp. 599–608. DOI: 10.3384/ecp14096599. URL: <http://dx.doi.org/10.3384/ecp14096599>.
- [77] N. Ablanque et al. "Dynamic Model of Vapor Compression Systems for Aircraft Environmental Control Systems". In: *Journal of Aircraft* 61.5 (Sept. 2024), pp. 1387–1396. ISSN: 1533-3868. DOI: 10.2514/1.c037711. URL: <http://dx.doi.org/10.2514/1.c037711>.

- [78] A. Cioncolini and J. R. Thome. "Void fraction prediction in annular two-phase flow". In: *International Journal of Multiphase Flow* 43 (July 2012), pp. 72–84. ISSN: 0301-9322. DOI: 10.1016/j.ijmultiphaseflow.2012.03.003. URL: <http://dx.doi.org/10.1016/j.ijmultiphaseflow.2012.03.003>.
- [79] J. R. Thome. *WOLVERINE ENGINEERING DATABOOK III*. Swiss Federal Institute of Technology Lausanne (EPFL), 2006. URL: <https://infoscience.epfl.ch/handle/20.500.14299/214953>.
- [80] P. K. Vijayan et al. "An assessment of pressure drop and void fraction correlations with data from two-phase natural circulation loops". In: *Heat and Mass Transfer* 36.6 (Nov. 2000), pp. 541–548. ISSN: 1432-1181. DOI: 10.1007/s002310000108. URL: <http://dx.doi.org/10.1007/s002310000108>.
- [81] M. Pietrzak and M. Płaczek. "Void fraction predictive methods in two-phase flow across a small diameter channel". In: *International Journal of Multiphase Flow* 121 (Dec. 2019), p. 103115. ISSN: 0301-9322. DOI: 10.1016/j.ijmultiphaseflow.2019.103115. URL: <http://dx.doi.org/10.1016/j.ijmultiphaseflow.2019.103115>.
- [82] G. Wedekind, B. Bhatt, and B. Beck. "A system mean void fraction model for predicting various transient phenomena associated with two-phase evaporating and condensing flows". In: *International Journal of Multiphase Flow* 4.1 (Mar. 1978), pp. 97–114. ISSN: 0301-9322. DOI: 10.1016/0301-9322(78)90029-0. URL: [http://dx.doi.org/10.1016/0301-9322\(78\)90029-0](http://dx.doi.org/10.1016/0301-9322(78)90029-0).
- [83] B. T. Beck and G. L. Wedekind. "A Generalization of the System Mean Void Fraction Model for Transient Two-Phase Evaporating Flows". In: *Journal of Heat Transfer* 103.1 (Feb. 1981), pp. 81–85. ISSN: 1528-8943. DOI: 10.1115/1.3244436. URL: <http://dx.doi.org/10.1115/1.3244436>.
- [84] M. Willatzen, N. Pettit, and L. Ploug-Sørensen. "A general dynamic simulation model for evaporators and condensers in refrigeration. Part I: moving-boundary formulation of two-phase flows with heat exchange". In: *International Journal of Refrigeration* 21.5 (Aug. 1998), pp. 398–403. ISSN: 0140-7007. DOI: 10.1016/S0140-7007(97)00091-1. URL: [http://dx.doi.org/10.1016/S0140-7007\(97\)00091-1](http://dx.doi.org/10.1016/S0140-7007(97)00091-1).
- [85] W.-J. Zhang and C.-L. Zhang. "A generalized moving-boundary model for transient simulation of dry-expansion evaporators under larger disturbances". In: *International Journal of Refrigeration* 29.7 (Nov. 2006), pp. 1119–1127. ISSN: 0140-7007. DOI: 10.1016/j.ijrefrig.2006.03.002. URL: <http://dx.doi.org/10.1016/j.ijrefrig.2006.03.002>.
- [86] T. L. McKinley and A. G. Alleyne. "An advanced nonlinear switched heat exchanger model for vapor compression cycles using the moving-boundary method". In: *International Journal of Heat and Mass Transfer* 31.7 (Nov. 2008), pp. 1253–1264.
- [87] H. Qiao et al. "An advanced switching moving boundary heat exchanger model with pressure drop". In: *International Journal of Refrigeration* 65 (May 2016), pp. 154–171. ISSN: 0140-7007. DOI: 10.1016/j.ijrefrig.2016.01.026. URL: <http://dx.doi.org/10.1016/j.ijrefrig.2016.01.026>.
- [88] A. F. Mills. "Convection fundamentals and correlations". In: *Heat and Mass Transfer*. Routledge, May 2018, pp. 243–370.
- [89] M. M. Shah. *Two-Phase Heat Transfer*. Wiley, Feb. 2021. ISBN: 9781119618652. DOI: 10.1002/9781119618652. URL: <http://dx.doi.org/10.1002/9781119618652>.
- [90] P. A. Kew and K. Cornwell. "Correlations for the prediction of boiling heat transfer in small-diameter channels". In: *Applied Thermal Engineering* 17.8–10 (Aug. 1997), pp. 705–715. ISSN: 1359-4311. DOI: 10.1016/S1359-4311(96)00071-3. URL: [http://dx.doi.org/10.1016/S1359-4311\(96\)00071-3](http://dx.doi.org/10.1016/S1359-4311(96)00071-3).
- [91] M. M. Shah. "Applicability of Correlations for Boiling/Condensing in Macrochannels to Minichannels". In: *Heat and Mass Transfer Research Journal* 2.1 (2018).

- [92] K. El Kadi, F. Alnaimat, and S. Sherif. "Recent advances in condensation heat transfer in mini and micro channels: A comprehensive review". In: *Applied Thermal Engineering* 197 (Oct. 2021), p. 117412. ISSN: 1359-4311. DOI: 10.1016/j.applthermaleng.2021.117412. URL: <http://dx.doi.org/10.1016/j.applthermaleng.2021.117412>.
- [93] M. M. Shah. "Comprehensive correlations for heat transfer during condensation in conventional and mini/micro channels in all orientations". In: *International Journal of Refrigeration* 67 (July 2016), pp. 22–41. ISSN: 0140-7007. DOI: 10.1016/j.ijrefrig.2016.03.014. URL: <http://dx.doi.org/10.1016/j.ijrefrig.2016.03.014>.
- [94] M. M. Shah. "Improved correlation for heat transfer during condensation in conventional and mini/micro channels". In: *International Journal of Refrigeration* 98 (Feb. 2019), pp. 222–237. ISSN: 0140-7007. DOI: 10.1016/j.ijrefrig.2018.07.037. URL: <http://dx.doi.org/10.1016/j.ijrefrig.2018.07.037>.
- [95] S.-M. Kim and I. Mudawar. "Review of databases and predictive methods for heat transfer in condensing and boiling mini/micro-channel flows". In: *International Journal of Heat and Mass Transfer* 77 (Oct. 2014), pp. 627–652. ISSN: 0017-9310. DOI: 10.1016/j.ijheatmasstransfer.2014.05.036. URL: <http://dx.doi.org/10.1016/j.ijheatmasstransfer.2014.05.036>.
- [96] D. Lee et al. "Evaporation heat transfer coefficient and pressure drop of R-1233zd(E) in a brazed plate heat exchanger". In: *Applied Thermal Engineering* 130 (Feb. 2018), pp. 1147–1155. ISSN: 1359-4311. DOI: 10.1016/j.applthermaleng.2017.11.088. URL: <http://dx.doi.org/10.1016/j.applthermaleng.2017.11.088>.
- [97] A. Desideri et al. "Comparison of Moving Boundary and Finite-Volume Heat Exchanger Models in the Modelica Language". In: *Energies* 9.5 (May 2016), p. 339. ISSN: 1996-1073. DOI: 10.3390/en9050339. URL: <http://dx.doi.org/10.3390/en9050339>.
- [98] H. Pangborn, A. G. Alleyne, and N. Wu. "A comparison between finite volume and switched moving boundary approaches for dynamic vapor compression system modeling". In: *International Journal of Refrigeration* 53 (May 2015), pp. 101–114. ISSN: 0140-7007. DOI: 10.1016/j.ijrefrig.2015.01.009. URL: <http://dx.doi.org/10.1016/j.ijrefrig.2015.01.009>.
- [99] B. Li and A. G. Alleyne. "A dynamic model of a vapor compression cycle with shut-down and start-up operations". In: *International Journal of Refrigeration* 33.3 (May 2010), pp. 538–552. ISSN: 0140-7007. DOI: 10.1016/j.ijrefrig.2009.09.011. URL: <http://dx.doi.org/10.1016/j.ijrefrig.2009.09.011>.
- [100] B. P. Rasmussen and B. Shenoy. "Dynamic modeling for vapor compression systems—Part II: Simulation tutorial". In: *HVAC&R Research* 18.5 (Sept. 2012), pp. 956–973. ISSN: 1938-5587. DOI: 10.1080/10789669.2011.582917. URL: <http://dx.doi.org/10.1080/10789669.2011.582917>.
- [101] P. P. Walsh and P. Fletcher. *Gas Turbine Performance*. en. 2nd ed. Chichester, England: Wiley-Blackwell, Apr. 2008.
- [102] O. Leufvén and L. Eriksson. "A surge and choke capable compressor flow model—Validation and extrapolation capability". In: *Control Engineering Practice* 21.12 (Dec. 2013), pp. 1871–1883. ISSN: 0967-0661. DOI: 10.1016/j.conengprac.2013.07.005. URL: <http://dx.doi.org/10.1016/j.conengprac.2013.07.005>.
- [103] A. J. Glassman. *Turbine Design and Application*. Technical Report 19950015924. Lewis Research Center Cleveland, OH, USA: NASA, June 1994.
- [104] H. Pham et al. "An approach for establishing the performance maps of the sc-CO₂ compressor: Development and qualification by means of CFD simulations". In: *International Journal of Heat and Fluid Flow* 61 (Oct. 2016), pp. 379–394. ISSN: 0142-727X. DOI: 10.1016/j.ijheatfluidflow.2016.05.017. URL: <http://dx.doi.org/10.1016/j.ijheatfluidflow.2016.05.017>.
- [105] P. Nederstigt and R. Pecnik. "Generalised Isentropic Relations in Thermodynamics". In: *Energies* 16.5 (Feb. 2023), p. 2281. ISSN: 1996-1073. DOI: 10.3390/en16052281. URL: <http://dx.doi.org/10.3390/en16052281>.

- [106] J. Liu, J. Chen, and Z. Chen. "Choking phenomenon and pressure drop mechanism in electronic expansion valves". In: *Energy Conversion and Management* 49.6 (June 2008), pp. 1321–1330. ISSN: 0196-8904. DOI: 10.1016/j.enconman.2008.01.003. URL: <http://dx.doi.org/10.1016/j.enconman.2008.01.003>.
- [107] P. Muroli. *Valvole di regolazione per processi industriali*. PEG, 1991. ISBN: 9788870670745. URL: <https://books.google.nl/books?id=nzvp0AEACAAJ>.
- [108] L. Rajapaksha and K. Suen. "Influence of liquid receiver on the performance of reversible heat pumps using refrigerant mixtures". In: *International Journal of Refrigeration* 27.1 (Jan. 2004), pp. 53–62. ISSN: 0140-7007. DOI: 10.1016/S0140-7007(03)00092-6. URL: [http://dx.doi.org/10.1016/S0140-7007\(03\)00092-6](http://dx.doi.org/10.1016/S0140-7007(03)00092-6).
- [109] S. Estrada-Flores et al. "Simulation of transient behaviour in refrigeration plant pressure vessels: mathematical models and experimental validation". In: *International Journal of Refrigeration* 26.2 (Mar. 2003), pp. 170–179. ISSN: 0140-7007. DOI: 10.1016/S0140-7007(02)00081-6. URL: [http://dx.doi.org/10.1016/S0140-7007\(02\)00081-6](http://dx.doi.org/10.1016/S0140-7007(02)00081-6).
- [110] R. Moradi and L. Cioccolanti. "Modelling approaches of micro and small-scale organic Rankine cycle systems: A critical review". In: *Applied Thermal Engineering* 236 (Jan. 2024), p. 121505. ISSN: 1359-4311. DOI: 10.1016/j.applthermaleng.2023.121505. URL: <http://dx.doi.org/10.1016/j.applthermaleng.2023.121505>.
- [111] R. Moradi. "Object-oriented modeling of micro-ORC systems for low-grade waste heat recovery applications". PhD thesis. Rome: Sapienza Università di Roma, May 2021.
- [112] R. Moradi et al. "Assumption-free modeling of a micro-scale organic Rankine cycle system based on a mass-sensitive method". In: *Energy Conversion and Management* 245 (Oct. 2021), p. 114554. ISSN: 0196-8904. DOI: 10.1016/j.enconman.2021.114554. URL: <http://dx.doi.org/10.1016/j.enconman.2021.114554>.
- [113] J. Oh, H. Jeong, and H. Lee. "Experimental and numerical analysis on low-temperature off-design organic Rankine cycle in perspective of mass conservation". In: *Energy* 234 (Nov. 2021), p. 121262. ISSN: 0360-5442. DOI: 10.1016/j.energy.2021.121262. URL: <http://dx.doi.org/10.1016/j.energy.2021.121262>.
- [114] S. Tassou, C. Marquand, and D. Wilson. "Comparison of the performance of capacity controlled and conventional on/off controlled heat pumps". In: *Applied Energy* 14.4 (Jan. 1983), pp. 241–256. ISSN: 0306-2619. DOI: 10.1016/0306-2619(83)90051-x. URL: [http://dx.doi.org/10.1016/0306-2619\(83\)90051-x](http://dx.doi.org/10.1016/0306-2619(83)90051-x).
- [115] T. Qureshi and S. Tassou. "Variable-speed capacity control in refrigeration systems". In: *Applied Thermal Engineering* 16.2 (Feb. 1996), pp. 103–113. ISSN: 1359-4311. DOI: 10.1016/1359-4311(95)00051-e. URL: [http://dx.doi.org/10.1016/1359-4311\(95\)00051-e](http://dx.doi.org/10.1016/1359-4311(95)00051-e).
- [116] A. Behfar and D. Yuill. "Evaluation of gray box thermostatic expansion valve mass flow models". In: *International Journal of Refrigeration* 96 (Dec. 2018), pp. 161–168. ISSN: 0140-7007. DOI: 10.1016/j.ijrefrig.2018.08.008. URL: <http://dx.doi.org/10.1016/j.ijrefrig.2018.08.008>.
- [117] R. Cohen, J. Hamilton, and J. Pearson. "Possible Energy Conservation Through Use of Variable Capacity Compressors". In: *International Compressor Engineering Conference* 97 (1974). URL: <https://docs.lib.purdue.edu/icec/97/>.
- [118] J. Jia and W. Lee. "Experimental investigations on the use of capillary tube and thermostatic expansion valve in storage-enhanced heat recovery room air-conditioner". In: *Energy and Buildings* 101 (Aug. 2015), pp. 76–83. ISSN: 0378-7788. DOI: 10.1016/j.enbuild.2015.05.007. URL: <http://dx.doi.org/10.1016/j.enbuild.2015.05.007>.
- [119] Y. Chen et al. "A study on the operational stability of a refrigeration system having a variable speed compressor". In: *International Journal of Refrigeration* 31.8 (Dec. 2008), pp. 1368–1374. ISSN: 0140-7007. DOI: 10.1016/j.ijrefrig.2008.04.012. URL: <http://dx.doi.org/10.1016/j.ijrefrig.2008.04.012>.
- [120] Y. Xia et al. "A review on the operational instability of vapor compression system". In: *International Journal of Refrigeration* 122 (Feb. 2021), pp. 97–109. ISSN: 0140-7007. DOI: 10.1016/j.ijrefrig.2020.10.024. URL: <http://dx.doi.org/10.1016/j.ijrefrig.2020.10.024>.

- [121] Z. Huelle. "Mss line-new approach to hunting problem". In: *ASHRAE Journal: American Society of Heating Refrigerating and Air-conditioning Engineers* 14.10 (1972), p. 43.
- [122] M. S. Elliott and B. P. Rasmussen. "On reducing evaporator superheat nonlinearity with control architecture". In: *International Journal of Refrigeration* 33.3 (May 2010), pp. 607–614. ISSN: 0140-7007. DOI: 10.1016/j.ijrefrig.2009.12.013. URL: <http://dx.doi.org/10.1016/j.ijrefrig.2009.12.013>.
- [123] X.-D. He, S. Liu, and H. H. Asada. "Modeling of Vapor Compression Cycles for Multivariable Feedback Control of HVAC Systems". In: *Journal of Dynamic Systems, Measurement, and Control* 119.2 (June 1997), pp. 183–191. ISSN: 1528-9028. DOI: 10.1115/1.2801231. URL: <http://dx.doi.org/10.1115/1.2801231>.
- [124] X.-D. He et al. "Multivariable Control of Vapor Compression Systems". In: *HVAC&R Research* 4.3 (July 1998), pp. 205–230. ISSN: 1938-5587. DOI: 10.1080/10789669.1998.10391401. URL: <http://dx.doi.org/10.1080/10789669.1998.10391401>.
- [125] R. Bryan P. and A. G. Alleyne. *Dynamic Modeling and Advanced Control of Air Conditioning and Refrigeration Systems*. Tech. rep. ACRC TR-244. Champaign, IL: University of Illinois at Urbana-Champaign, June 2006.
- [126] F. Behrooz et al. "Review of Control Techniques for HVAC Systems—Nonlinearity Approaches Based on Fuzzy Cognitive Maps". In: *Energies* 11.3 (Feb. 2018), p. 495. ISSN: 1996-1073. DOI: 10.3390/en11030495. URL: <http://dx.doi.org/10.3390/en11030495>.
- [127] M. Morari and J. H. Lee. "Model predictive control: past, present and future". In: *Computers & Chemical Engineering* 23.4–5 (May 1999), pp. 667–682. ISSN: 0098-1354. DOI: 10.1016/S0098-1354(98)00301-9. URL: [http://dx.doi.org/10.1016/S0098-1354\(98\)00301-9](http://dx.doi.org/10.1016/S0098-1354(98)00301-9).
- [128] Y. Yao and D. K. Shekhar. "State of the art review on model predictive control (MPC) in Heating Ventilation and Air-conditioning (HVAC) field". In: *Building and Environment* 200 (Aug. 2021), p. 107952. ISSN: 0360-1323. DOI: 10.1016/j.buildenv.2021.107952. URL: <http://dx.doi.org/10.1016/j.buildenv.2021.107952>.
- [129] N. Jain and A. Alleyne. "Exergy-based optimal control of a vapor compression system". In: *Energy Conversion and Management* 92 (Mar. 2015), pp. 353–365. ISSN: 0196-8904. DOI: 10.1016/j.enconman.2014.12.014. URL: <http://dx.doi.org/10.1016/j.enconman.2014.12.014>.
- [130] D. Adelekan, O. Ohunakin, and B. Paul. "Artificial intelligence models for refrigeration, air conditioning and heat pump systems". In: *Energy Reports* 8 (Nov. 2022), pp. 8451–8466. ISSN: 2352-4847. DOI: 10.1016/j.egy.2022.06.062. URL: <http://dx.doi.org/10.1016/j.egy.2022.06.062>.
- [131] A. Jain, J. Mao, and K. Mohiuddin. "Artificial neural networks: a tutorial". In: *Computer* 29.3 (Mar. 1996), pp. 31–44. ISSN: 0018-9162. DOI: 10.1109/2.485891. URL: <http://dx.doi.org/10.1109/2.485891>.
- [132] V. Vemuri. "Artificial Neural Networks in Control Applications". In: *Advances in Computers Volume 36*. Elsevier, 1993, pp. 203–254. ISBN: 9780120121366. DOI: 10.1016/S0065-2458(08)60272-7. URL: [http://dx.doi.org/10.1016/S0065-2458\(08\)60272-7](http://dx.doi.org/10.1016/S0065-2458(08)60272-7).
- [133] M. Mohanraj, S. Jayaraj, and C. Muraleedharan. "Applications of artificial neural networks for refrigeration, air-conditioning and heat pump systems—A review". In: *Renewable and Sustainable Energy Reviews* 16.2 (Feb. 2012), pp. 1340–1358. ISSN: 1364-0321. DOI: 10.1016/j.rser.2011.10.015. URL: <http://dx.doi.org/10.1016/j.rser.2011.10.015>.
- [134] L. Zadeh. "Fuzzy sets". In: *Information and Control* 8.3 (June 1965), pp. 338–353. ISSN: 0019-9958. DOI: 10.1016/S0019-9958(65)90241-x. URL: [http://dx.doi.org/10.1016/S0019-9958\(65\)90241-x](http://dx.doi.org/10.1016/S0019-9958(65)90241-x).
- [135] M. Sugeno. "An introductory survey of fuzzy control". In: *Information Sciences* 36.1–2 (July 1985), pp. 59–83. ISSN: 0020-0255. DOI: 10.1016/0020-0255(85)90026-x. URL: [http://dx.doi.org/10.1016/0020-0255\(85\)90026-x](http://dx.doi.org/10.1016/0020-0255(85)90026-x).

- [136] N. Mogharreban and L. F. DiLalla. "Comparison of Defuzzification Techniques for Analysis of Non-interval Data". In: *NAFIPS 2006 - 2006 Annual Meeting of the North American Fuzzy Information Processing Society*. IEEE, June 2006. DOI: 10.1109/nafips.2006.365418. URL: <http://dx.doi.org/10.1109/NAFIPS.2006.365418>.
- [137] O. Ekren, S. Sahin, and Y. Isler. "Comparison of different controllers for variable speed compressor and electronic expansion valve". In: *International Journal of Refrigeration* 33.6 (Sept. 2010), pp. 1161–1168. ISSN: 0140-7007. DOI: 10.1016/j.ijrefrig.2010.05.005. URL: <http://dx.doi.org/10.1016/j.ijrefrig.2010.05.005>.